The Dissertation Committee for Benjamin Thomas King
certifies that this is the approved version of the following dissertation:

Laboratory and Numerical Studies of Internal Wave Generation and Propagation in the Ocean

Committee:

Harry L. Swinney, Supervisor

Wendell Horton

William McCormick

Robert Moser

Robert Scott

Laboratory and Numerical Studies of Internal Wave Generation and Propagation in the Ocean

by

Benjamin Thomas King, B.S.

DISSERTATION

Presented to the Faculty of the Graduate School of

The University of Texas at Austin

in Partial Fulfillment

of the Requirements

for the Degree of

DOCTOR OF PHILOSOPHY

THE UNIVERSITY OF TEXAS AT AUSTIN

August 2010

For my mother and father, Betty and Tom.

Over there, brother Sancho Panza, we can dip our arms right up to our elbows in what people call adventures.

from *Don Quixote*, Cervantes

Acknowledgments

I would first like the acknowledge the support of my parents, Betty and Tom King, who have always been behind me in all my endeavors. They encouraged my curiosity from a young age, and their unwavering support has made this work possible. I also acknowledge my aunt, Marilynn Lynch, and the memory of my late grandmother, Billie Lynch, who is dearly missed. I also thank Naomi Trejo for companionship, encouraging words, and for broadening my horizons, and Jean and Leonard Holder for their support and encouragement to pursue a graduate degree.

Harry Swinney, to a large extent, granted me the freedom to pursue my own interests and projects, while still providing many insights into the scientific process. I credit him with teaching me how to carry a research project through from initial conception to final publication. He also taught me how to boil a complex problem down to its bare essentials, and appreciate the importance of understanding problems on a fundamental level.

Hepeng Zhang has been a friend and mentor during my entire tenure here. He is one of the most intelligent and insightful people I've had the privelege to work with, and can always find humor in otherwise serious situations.

Bruce Rodenborn is a great friend and coworker who is always willing to help out in whatever way he can. Always practical, he is equally at home

talking about internal wave reflection theory or rewiring a house.

Robert Moser and Chung-Hsiang Jiang were instrumental in getting me started doing numerical simulations when I was a complete stranger to numerical methods. Robert Scott has been a great friend and collaborator for the last couple years, offering a fresh perspective from the oceanographic community. I have also been priveleged to work on a project with Mark Stone, who has a bright future ahead of him in engineering or the sciences.

Martin Kochanczyk is one of the first people I met here, and have shared an office with for 5 years now. I've always been able to count on him, from a joke or serious debate, to setting up a workshop in his garage. Mark Monti deserves many thanks for friendship throughout the years as well, and has been a great tennis and workout partner. I also thank my other office mates, Katie Hinko and Pinyu Thrasher for companionship and many entertaining conversations. I'd also like to acknowledge Leen Alawieh, Tobias Bartsch, Avraham Be'er, Marybeth Casias, Vassili Demergis, E. L. Florin, Chieze Ibeneche, Andrea Keidel, Daniel Kiefer, Flip Kromer, Bill McCormick, Mike Marder, Vaggelis Meintanis, Matthias Schroeter, George Shubeita, Jack Swift, Katja Taute, Matthew Thrasher, Olga Vera, and the rest of the CNLD family for company, advice, and good humor.

Much appreciation is also due Olga Vera and Marybath Casias, who work tirelessly behind the scenes to make the CNLD a vibrant place to do research.

Finally, I'd like to thank my undergraduate research mentors, Donald Naugle and Wayne Saslow, who gave me early opportunities to experience research and helped inspired me to become a scientist.

Acknowledgment of financial support is made to the Graduate Continuing Education Fellowship program at the University of Texas, and the National Science Foundation, Chemical, Bioengineering, Environmental, and Transport Systems Program (Award No. 0755114). The Texas Advanced Computing Center provided a generous allotment of computational resources.

Benjamin Thomas King

Center for Nonlinear Dynamics
The University of Texas at Austin
July 2010

Laboratory and Numerical Studies of Internal Wave Generation and Propagation in the Ocean

Publication No. _____

Benjamin Thomas King, Ph.D.
The University of Texas at Austin, 2010

Supervisor: Harry L. Swinney

Internal waves are generated in the ocean by oscillating tidal flow over bottom topography such as ridges, seamounts, and continental slopes. They are similar to the more familiar surface waves, but not being constrained to move on the surface, propagate throughout the bulk of the world oceans. Internal waves transmit energy over thousands of kilometers, ultimately breaking and releasing their energy into turbulence and mixing. Where these internal waves are generated, as well as where and how they break and cause mixing, has important effects on the general circulation of the ocean, which is in turn a major component in earth's climate. As a first step in a more thorough understanding of the evolution of internal waves in the ocean, it is important to characterize their generation. The two-dimensional generation problem has been studied for four decades, with ample experimental, numerical, and theoretical results. Most of this past work has also been done using linear, inviscid approximations. However, wave generation in the ocean is three-dimensional

(3D), and in many locations, nonlinear and viscous effects can be significant. Recent advances in experimental and numerical techniques are only now making the fully nonlinear, 3D generation process accessible. We utilize these new techniques to perform both laboratory experiments and numerical simulations on internal wave generation in 3D. We find that a significant component of the internal wave field generated by tidal flow over 3D topography is radiated in the direction *perpendicular* to the tidal forcing direction. This could lead to substantial improvements of global internal wave generation models. In addition, we have developed a new method for statistical analysis of ocean data sets, and have found large regions in the deep ocean where internal waves may not propagate. This will also have important effects on the way researchers study the propagation of internal waves, which, when propagating downward, were previously thought to always reflect from the sea floor.

Table of Contents

Chapter 1

Introduction

1.1 Internal gravity waves and the global ocean circulation

Internal gravity waves are a special class of wave which exist only in continuously stratified fluids (fluids with density varying continuously with depth). For an introduction to internal waves, see *Kundu and Cohen* [2004] or *Gerkema and Zimmerman* [2008]. For a stratified fluid to be stable, the fluid must become less dense with increasing height. If a fluid parcel is displaced upward from its equilibrium height, it will be more dense than the surrounding fluid, resulting in a downward gravitational restoring force. Conversely, if a fluid parcel is displaced downward from its equilibrium height, it will feel an upward buoyant restoring force. Such a restoring force, along with inertial mass of the fluid, results in the possibility of wave motion. Subject to frequency constraints, which will be discussed later, a disturbance in a stratified fluid resulting in a vertical displacement of fluid radiates away as an internal gravity wave (hereafter referred to as an internal wave). Unlike many waves in physical systems, the restoring force is always vertical, regardless of the direction of the wave propagation. Due to this unusual restoring force, internal waves have many unusual properties (A full discussion of internal wave properties

is given in the next chapter). One of these properties is that the unique characteristic that the angle of internal wave propagation (with respect to the horizontal) depends only on the angle of the wave vector, not its magnitude. The dispersion relation for internal waves in a nonrotating fluid is:

$$\frac{\omega}{N} = \sin\theta \tag{1.1}$$

where ω is the wave frequency, θ is the angle of wave propagation with respect to the horizontal, and N is the buoyancy frequency, which quantifies the stratification:

$$N = \sqrt{-\frac{g}{\rho(z)}\frac{d\rho}{dz}}. \tag{1.2}$$

In the above expression, g is the gravitational acceleration, and $\rho(z)$ is the density as a function of depth. This neglects compressibility effects, which are discussed in more detail in the next chapter. An unusual resulting property is that all internal waves at a given frequency propagate at the same angle with respect to the horizontal. This means that 'wave packets,' or groups of internal waves at the same frequency but a range of wavenumbers can propagate together without dispersion for thousands of kilometers across the open ocean.

Many internal waves in the ocean are generated by tidal flow oscillating past under water topography. When a fluid parcel encounters an obstacle and is displaced vertically, this disturbance leads to internal waves, which propagate away from the generation site. The exact nature of the internal waves depends sensitively on details of the topography, such as the height and

maximum slope, and tidal flow details such as tidal amplitude and frequency. Many studies have been undertaken to understand how internal waves are generated, but due to the complex nature of the problem, many simplifying assumptions are normally made. Most theoretical work assumes the flow is 2D and linear. In addition, many theories also assume inviscid flow. (There are theories that are either *weakly* nonlinear or viscous, but not both.) All of these assumptions lead to a large literature applicable in very special regimes, with little work done on more general conditions. Another nearly universal assumption is that the density stratification is uniform in height, which is far from being the case in the ocean, where the buoyancy frequency N varies by more than two orders of magnitude as a function of depth.

1.2 Global ocean circulation and earth's climate

In addition to understanding where and how internal waves are generated, much effort has also focused on determining the fate of internal waves as they propagate and ultimately break and release their energy into turbulence and mixing. Internal waves play a crucial role in regulating the thermohaline circulation, which gives rise to many of the large scale flows we observe (such as the Gulf Stream). Breaking internal waves are the only currently known source of mixing energy sufficient to account for the deep water upwelling that occurs across the oceans. This upwelling is the return flow from the surface water in polar regions which cools, becomes dense, and sinks to the ocean bottom. In order for this flow to recirculate, the cool, dense, deep water must

be mixed with overlying less dense water, enabling it to slowly rise back to the surface. This mixing equates to an increase in potential energy, or equivalently, a restratification of the water column. If not for this continuous restratification using energy extracted from internal waves, the ocean would slowly fill with cool, dense water. After a time scale of order 1000 years, the entire ocean would be cold and uniform, with a very thin layer of warm water near the surface. Since this is not what oceanographers observe, we conclude that internal waves are likely responsible for transferring energy from large scale tides (and other large scale processes such as wind forcing) into small scale mixing, which is responsible for continually maintaining the ocean's density stratification.

The mechanisms through which internal waves propagate and eventually break depend on the stratification of the ocean, which varies significantly as a function of location. The stratification of the ocean has still not been carefully quantified, despite the completion more than a decade ago of the most comprehensive snapshot of water properties in the ocean ever undertaken (the World Ocean Circulation Experiment). As can be deduced from Eq. 1.1, the stratification ($N(z)$), plays an important role in determining the angle at which internal waves propagate. Internal waves propagating at shallow angles ($\omega << N(z)$, often the case in shallow waters) can travel many kilometers before encountering the ocean surface or the seafloor, where there are greatly increased chances of wave breaking through interaction with boundary layers or bottom topography. In contrast, internal waves propagating at steeper angles ($\omega \lesssim N$, often the case in the deep ocean) strike the boundaries more

often and are thus more likely to be scattered or dissipated. It is reasonable to expect, therefore, that understanding and quantifying the stratification in the ocean is important in developing a better understanding of how waves evolve in time.

1.3 Objectives of this work

In light of the foregoing discussion, we work toward several objectives. (1) Study internal wave generation in 3D, utilizing both laboratory experiments and numerical simulations. We show that understanding 3D phenomena is crucial to building a more complete picture of internal wave generation in the ocean. (2) Study the internal wave generation problem using fully nonlinear and viscous simulations. We show that the nonlinear term leads to unexpected second harmonic internal waves (internal waves at twice the tidal forcing frequency), which can account for a significant amount of the energy radiated from 3D topography. (3) Make quantitative comparisons between experiments and simulations where applicable. In suitable parameter regimes, these complementary approaches reinforce the findings, and numerical simulations can then be used to probe parameters difficult to attain in the laboratory. (4) Carefully examine the largest available set of measurements in the ocean (the World Ocean Circulation Experiment, or WOCE) to see how internal waves propagate in the ocean. In particular, a careful statistical analysis of the WOCE data is made for the first time to quantify uncertainty in measurements of the buoyancy frequency N. (5) Speculate on how these results

will affect future research and internal wave parametrizations in the ocean. As discussed previously, internal waves play a substantial role in regulating ocean circulation, and ultimately earth's climate, so understanding their generation and evolution is a priority in the oceanographic community.

1.4 Organization of this dissertation

The remainder of this dissertation is organized as follows: Chapter 2 gives a more thorough background and literature review of internal waves and their connection to the global ocean circulation and climate. Chapter 3 describes the methods used, including laboratory experiments and numerical simulations. It also details the new statistical methods developed to extract information about stratification of the ocean from observational data sets. Chapter 4 presents results of laboratory experiments and simulations on the internal waves generated by tidal flow over a three dimensional model topographic feature (a half-sphere on a plane). Chapter 5 expands this analysis to the more realistic case of a 3D Gaussian-shaped mountain, focusing on flows specific to 3D topography. Chapter 6 discusses preliminary results from a careful statistical analysis of data from the World Ocean Circulation Experiment. These results shed light on how internal waves propagate through the world oceans. Chapter 7 discusses additional connections with previous research and poses additional questions that our results have raised. Finally, the appendix contains extensive additional figures showing a global cross section of the WOCE data.

Chapter 2

Backgound and Literature Survey

2.1 Motivation

2.1.1 Thermohaline Circulation

The ocean is an integral part of the earth's climate system, continuously exchanging heat and moisture with the atmosphere. Being a large heat reservoir, the ocean also moderates climates along coastlines and transfers heat thousands of kilometers across the earth's surface [*Rahmstorf*, 2002]. To a large extent, the global ocean circulation affects how the ocean interacts with the rest of the climate system. The global ocean circulation consists of four parts: (1) Surface water near the equator is heated by sunlight. High evaporation rates result in increased salt concentrations. This warm, salty water is advected poleward primarily by wind forcing. (2) In localized regions in the arctic, this water is cooled by arctic air masses (in the process, releasing heat to the atmosphere at high latitudes), becomes denser, and sinks to the deep ocean. The local regions in which this process occurs are called 'deep water formation zones.' Estimates of deep water formation vary between 15 and 90 Sv (1 Sverdrup = 10^6 m^3/s) [*Stommel and Arons*, 1960; *Munk and Cartwright*, 1966; *Macdonald and Wunsch*, 1996], with a typical value of 30 Sv. (3) Due to subsequent deep water formation, the cool, dense water in the deep ocean

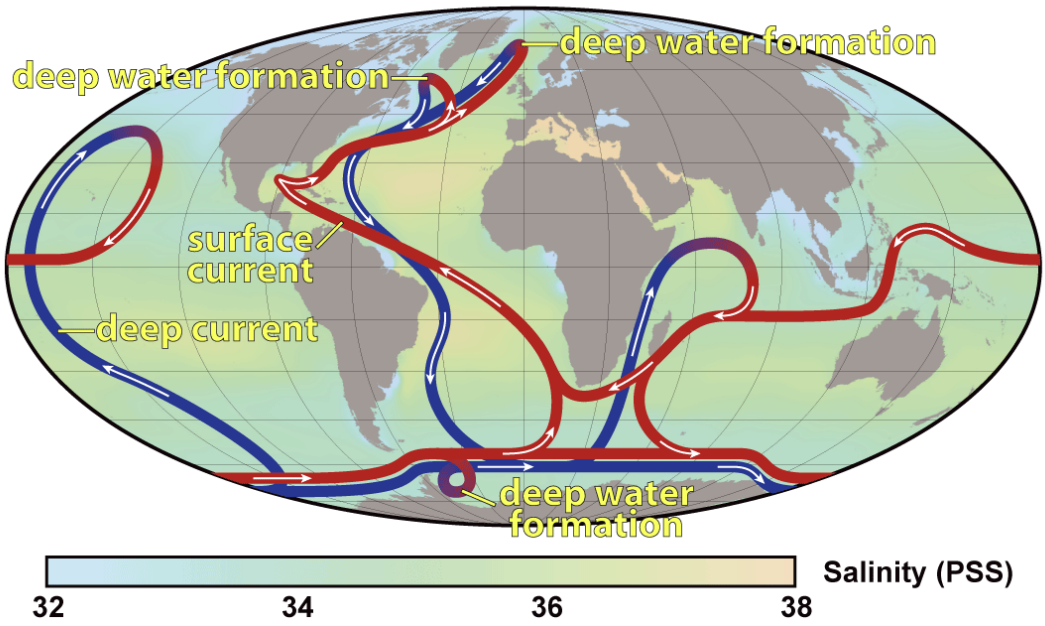

Figure 2.1: A simplified schematic diagram of the thermohaline circulation. Warm surface currents are denoted with red lines, and cold, deep currents are denoted with blue lines. So called 'deep water formation' zones are local regions where the surface water is cooled, becomes dense, and sinks to the deep ocean. Color denotes the sea surface salinity in the Practical Salinity Scale. Image courtesy of Robert Simmon, NASA.

is displaced back toward the equator. (4) To complete the circulation, this cool dense water must become less dense so that it can return to the surface. (Note that lowering the density of deep water is equivalent to raising the center of gravity of the entire water column.) Otherwise, within roughly 3000 years, the entire basin would slowly fill with cool, dense water in the 'filling box' scenario [*Baines and Turner*, 1969]. Figure 2.1 shows a very simplified schematic diagram of the thermohaline circulation, which is named after the gradients in temperature and salinity which drive the flow.

The first three components of this circulation are fairly well understood, but despite decades of study, (4) remains largely mysterious. Based on observations of the global circulation, 2.1 TW is required to power the upwelling return flow [*Munk and Wunsch*, 1998].

The more obvious mechanism which could lead to a lowering of the density of cold, deep water would be geothermal heating near the seafloor. Worldwide, heat energy is released from the earth's interior to the ocean through the seafloor at a rate of 30 TW. While this heat energy has important effects on deep currents [*Hofmann and Maqueda*, 2009], Huang [*Huang*, 1999] estimated that only 0.05 TW is utilized to restratify the water column.

2.1.2 Mixing

The other possible mechanism is mixing, whereby deep water is mixed with less dense, overlying water, raising the center of gravity of the entire water column. The exact source of the 2.1 TW of required mixing energy is not well known, but most of the energy likely comes from a combination of wind at the ocean surface and tidal motions [*Wunsch and Ferrari*, 2004]. Scientists can compute the energy dissipated by the tides from observations of the slowly evolving orbit of the earth-moon and earth-sun systems [*Dickey et al.*, 1994]. The lunar tides dissipate 3.2 TW total, with the majority (2.5 TW) being at the principle semidiurnal frequency (M_2), having a period of 12.42 hours. The solar tides dissipate 0.5 TW, resulting in a total of 3.7 TW input into the earth. 0.2 TW are dissipated by compression of the solid earth and

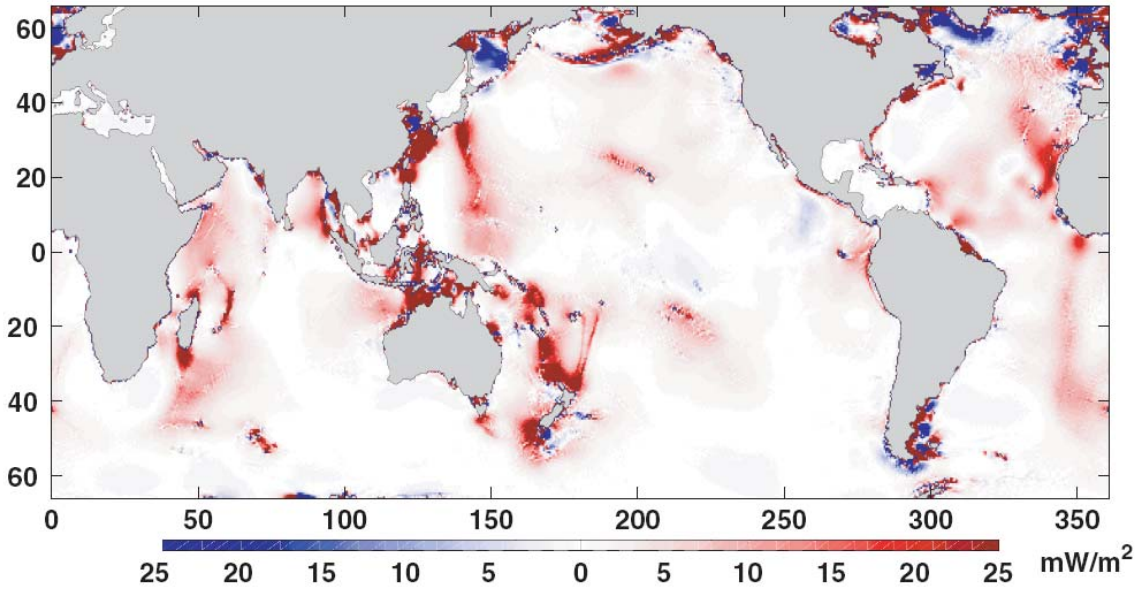

Figure 2.2: Global rate of conversion of tidal energy to internal wave energy, as inferred from sea surface height measurements. Note that most of the energy conversion takes place near rough topography, such as the Hawaiian Ridge, Mid-Atlantic Ridge, and other large features. Image from *Egbert and Ray* [2003]

0.02 TW are dissipated by atmospheric tides, leaving 3.5 TW to be dissipated in the world oceans. Accurate measurements of global sea surface elevations by the TOPEX-POSEIDON satellite altimeter have enabled oceanographers to estimate that 0.9 TW of the tidal power is scattered from large scale tidal motions into 'internal tides' at ocean seamounts, ridges, and continental slopes [*Egbert and Ray*, 2000, 2003]. Figure 2.2 shows a global map of tidal dissipation, with red denoting regions where substantial energy is being converted from the surface tides to internal waves. The remaining 2.6 TW of the tidal power is dissipated primarily in the bottom boundary layer of shallow seas

[*Kantha et al.*, 1995], where tidal velocities are larger than in the deep ocean. Internal tides (also called internal gravity waves, discussed in the next section), are generated by the oscillatory tidal motion over topographic features in the ocean. Like surface waves, they can travel long distances across the ocean, but unlike surface waves, internal gravity waves travel through the *interior* of the ocean. They eventually break, causing turbulence and mixing. Internal wave breaking is a result of instabilities [*Staquet and Sommeria*, 2002; *Staquet*, 2004, 2007], geometrical focusing [*Maas and Lam*, 1995; *Buhler and Muller*, 2007], scattering from the seafloor [*Muller and Xu*, 1992] or irregular topography [*Gilbert and Garrett*, 1989; *Johnston et al.*, 2003; *Johnston and Merrifield*, 2003; *Nakamura and Awaji*, 2009; *Peacock et al.*, 2009], or critical reflection (reflection from topography with slope similar to the slope of wave beam propagation) [*Cacchione and Wunsch*, 1974; *Ivey and Nokes*, 1989; *Slinn and Riley*, 1996, 1998; *Javam et al.*, 1999; *Legg and Adcroft*, 2003]. The often discussed 'tidal conversion rate' refers to the rate at which energy is extracted from large scale tidal motions into internal waves.

Since the simple energy budget analysis of Munk [*Munk and Cartwright*, 1966], it was widely believed that the required mixing occurred uniformly throughout the deep ocean, but many observational studies reported mixing rates too small by an order of magnitude to account for the given circulation [*Toole et al.*, 1994; *Polzin et al.*, 1997; *Ledwell et al.*, 1998]. However, several studies in the last two decades have shown that the mixing is very heterogeneous, with most of the mixing taking place in isolated regions near

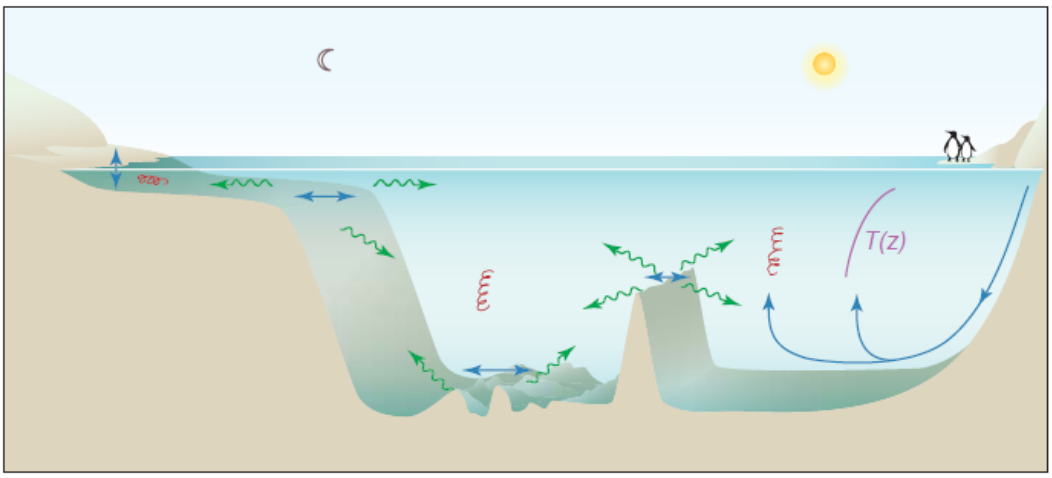

Figure 2.3: A meridional cross section of the ocean. Tides sloshing back and forth (horizontal blue arrows) generate internal waves (wavy green arrows) when the tide encounters topographic features such as ridges, bottom roughness, and continental slopes. Mixing (red spirals) occurs when the internal waves break, causing small scale turbulence and mixing. The long blue arrows on the right depict deep water formation near the poles. From *Garrett* [2003]

rough topography [*Polzin et al.*, 1997; *Toole et al.*, 1997; *Ledwell et al.*, 2000; *Mauritzen et al.*, 2002; *Garabato et al.*, 2004]. This result is consistent with internal waves being generated, and subsequently breaking and causing mixing near rough topography. Figure 2.3 shows a simplified schematic diagram of internal waves and mixing resulting from tidal motion.

Since only 0.9 TW of mixing energy is available from the tides, the remaining 1.2 TW required to mix the deep ocean is presumed to come from wind forcing at the ocean surface [*Munk and Wunsch*, 1998]. It is estimated that between 7 and 36 TW of power is transferred from the atmosphere into the ocean [*Lueck and Reid*, 1984], implying that a non-negligible fraction of the

wind energy deposited in the ocean is ultimately used to mix the deep ocean. There is currently a high-profile debate over whether biota may play some role in mixing the ocean [*Kunze et al.*, 2007; *Dewar*, 2009; *Visser*, 2007a, b], but the results are inconclusive.

2.1.3 Observations of internal waves in the ocean

Numerous recent studies have been undertaken to characterize internal waves in the ocean. Observations are too numerous to summarize in great detail, but have focused on several key areas, including the Bay of Biscay [*Pingree et al.*, 1986; *Pingree and New*, 1989, 1991], the Hawaiian Ridge [*Lee et al.*, 2006; *Nash et al.*, 2006; *Klymak et al.*, 2008; *Cole et al.*, 2009], the South China Sea [*Zhao et al.*, 2004; *Lien et al.*, 2005; *Chang et al.*, 2006; *Zhao and Alford*, 2006; *Duda and Rainville*, 2008; *Su et al.*, 2008; *Song et al.*, 2010], and various other locations of interest [*Kitade and Matsuyama*, 2002; *Althaus et al.*, 2003; *Filonov and Lavin*, 2003; *Manders et al.*, 2004; *Nash et al.*, 2004], typically near large topographic features or continental slopes.

2.2 Internal gravity waves

As discussed in Section 2.1.2, internal gravity waves (hereafter referred to simply as 'internal waves' following convention in the oceanographic literature) are the source of nearly half of the mixing energy required to maintain the global ocean circulation. A brief introduction to internal waves and some of their unusual properties follows.

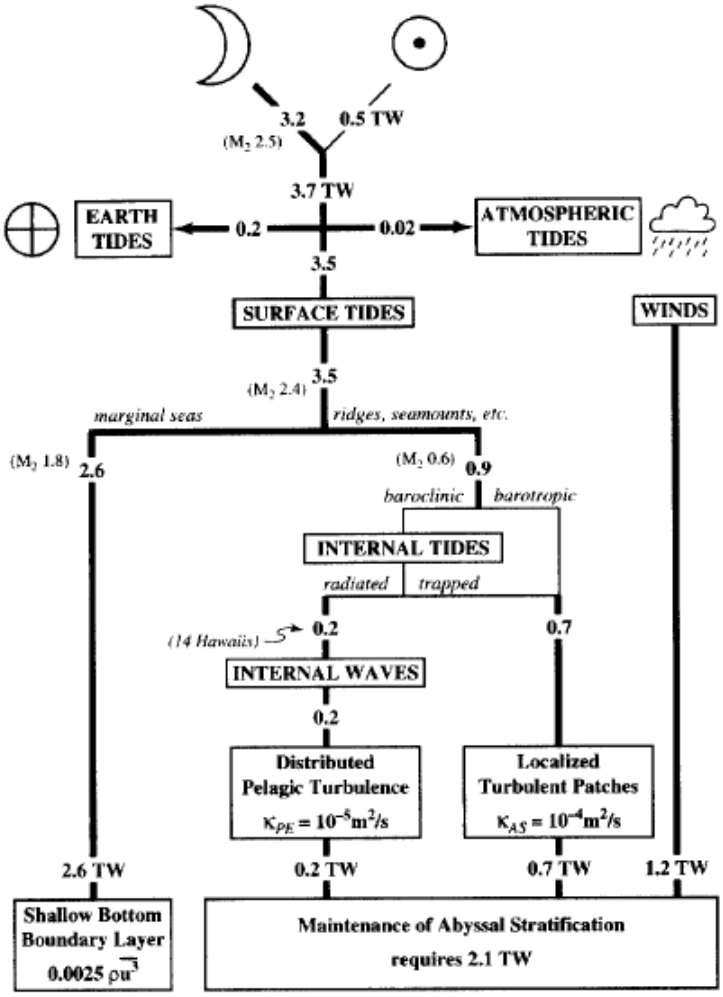

Figure 2.4: A schematic of the approximate energy budget associated with the deep sea mixing which sustains the thermohaline circulation. From *Munk and Wunsch* [1998]

2.2.1 Density Stratification

Internal waves are a general class of disturbance that occurs in a density-stratified fluid (a fluid where density varies with depth). There are two general kinds of stratification: (1) Discrete stratification, where the density changes by a finite amount over an infinitesimal height (an interface). The interface may be between two immiscible fluids, such as oil and water, or between the same kind of fluid with different concentrations of a solute, such as salt, which changes the fluid's density. The most intuitive example of such an interface is the interface between the surface of the ocean and atmosphere, which supports surface waves. The more general class of stratification is (2) continuous stratification, in which the density is a continuous function of depth. The ocean, atmosphere, and many astrophysical systems fall into this category. In a system with a discrete stratification (called a two-layer system if the density only has two values with a single interface in between), waves are confined to move along the interface between the different densities. A continuous stratification, however, lacks this constraint, resulting in rich wave dynamics and phenomena.

For a continuously stratified fluid, one might expect the extent to which the fluid is stratified to have important effects on the dynamics of the system. To this end, oceanographers introduce the buoyancy frequency [*Gerkema and Zimmerman*, 2008]:

$$N^2 = -\frac{g}{\rho(z)}\left(\frac{d\rho}{dz} + \frac{\rho(z)g}{c_s^2}\right) \tag{2.1}$$

where N is the buoyancy frequency (in older literature often called the Brunt-Vaisala frequency), g is the gravitational acceleration, $\rho(z)$ is the density as a function of depth, and c_s is the speed of sound in the fluid. N is defined as the frequency at which a fluid parcel would oscillate about its equilibrium depth if displaced vertically in a stratified fluid. For a stratified fluid to be stable, one would naively expect that:

$$\frac{d\rho}{dz} < 0 \tag{2.2}$$

which says that, for z increasing upward, the fluid must become less dense with increasing height. However, the actual stability criterion is given by the constraint $N^2 > 0$. Utilizing Eq. 2.1, the stability criterion becomes:

$$\frac{d\rho}{dz} < -\frac{\rho(z)g}{c_s^2} \tag{2.3}$$

Since $\rho(z)$, g, and c_s are positive quantities, the right hand side of Eq. 2.3 is always negative, meaning that it is not sufficient for $d\rho/dz$ to simply be negative, but it must have a negative value with a minimum magnitude.

2.2.2 Dispersion Relation

To derive the internal wave dispersion relation, we begin with the linearized, inviscid governing equations for a stratified fluid [*Kundu and Cohen*, 2004]:

$$\frac{\partial u}{\partial t} = -\frac{1}{\rho_o}\frac{\partial p'}{\partial x} \tag{2.4}$$

$$\frac{\partial v}{\partial t} = -\frac{1}{\rho_o}\frac{\partial p'}{\partial y} \tag{2.5}$$

$$\frac{\partial w}{\partial t} = -\frac{1}{\rho_o}\frac{\partial p'}{\partial z} - \frac{\rho'}{\rho_o}g \tag{2.6}$$

$$\frac{\partial \rho'}{\partial t} - \frac{N^2 \rho_o}{g} w = 0 \tag{2.7}$$

$$\frac{\partial u}{\partial x} + \frac{\partial v}{\partial y} + \frac{\partial w}{\partial z} = 0 \tag{2.8}$$

where u, v, and w are the velocity components in the x, y, and z directions, respectively. ρ_o is a constant reference density, and p' and ρ' are the perturbation pressure and density, respectively, after the hydrostatic balance

$$\frac{dp}{dz} = -\rho g \tag{2.9}$$

has been subtracted from Eqs 2.4-2.6. The governing equations then simply describe perturbations to a background equilibrium state. The Equations 2.4-2.9 are written in the Boussinesq approximation, which assumes that the density can be replaced with the constant reference density ρ_o everywhere except in front of the gravity body force term in Eq. 2.6. This approximation is valid when the stratification is weak (when the vertical length scale of a flow is small compared to the vertical length over which the density of the fluid changes appreciably), which is a valid and universally used approximation in the ocean. u, v, p', and ρ' can be eliminated from Eqs. 2.4-2.9 to obtain a single second order differential equation for the vertical velocity w:

$$\frac{\partial^2}{\partial t^2}\nabla^2 w + N^2 \nabla_H^2 w = 0 \tag{2.10}$$

where ∇_H^2 is the horizontal Laplacian operator defined as:

$$\nabla_H^2 = \frac{\partial^2}{\partial x^2} + \frac{\partial^2}{\partial y^2} \tag{2.11}$$

Assuming a plane wave solution:

$$w(x,z,t) = w_o \exp(i(kx + mz - \omega t)) \tag{2.12}$$

and plugging into 2.18 yields the dispersion relation:

$$\omega^2 = \frac{k^2}{k^2 + m^2} N^2 \tag{2.13}$$

where we have assumed, without loss of generality, that the internal wave propagates in the $x - z$-plane. Defining θ to be the angle of the wave vector $\mathbf{K} = k\hat{\mathbf{x}} + m\hat{\mathbf{z}}$ with respect to the horizontal, we can rewrite 2.13 as:

$$\frac{\omega}{N} = \sin\theta \tag{2.14}$$

This is an unusual dispersion relation because the frequency only depends on the *direction* of the wave vector, not its magnitude.

Plugging (2.12) into the continuity equation 2.9 allows one to solve for the plane wave solution for u:

$$u(x,z,t) = -\frac{m}{k} w_o \exp(i(kx + mz - \omega t)) \tag{2.15}$$

Despite solutions for u and w being derived from the linearized governing equations (2.4-2.9), the plane wave solutions for u and w are also solutions to the nonlinear governing equations, as can be seen from plugging Eqs. 2.12 and 2.15 into the nonlinear advection term $\mathbf{u} \cdot \nabla \mathbf{u}$. Plugging the plane wave solutions (2.15) and (2.12) into the continuity equation (2.9) gives $ku + mw = 0$, or $\mathbf{K} \cdot \mathbf{u} = 0$ This means that fluid motion is perpendicular to the wave vector.

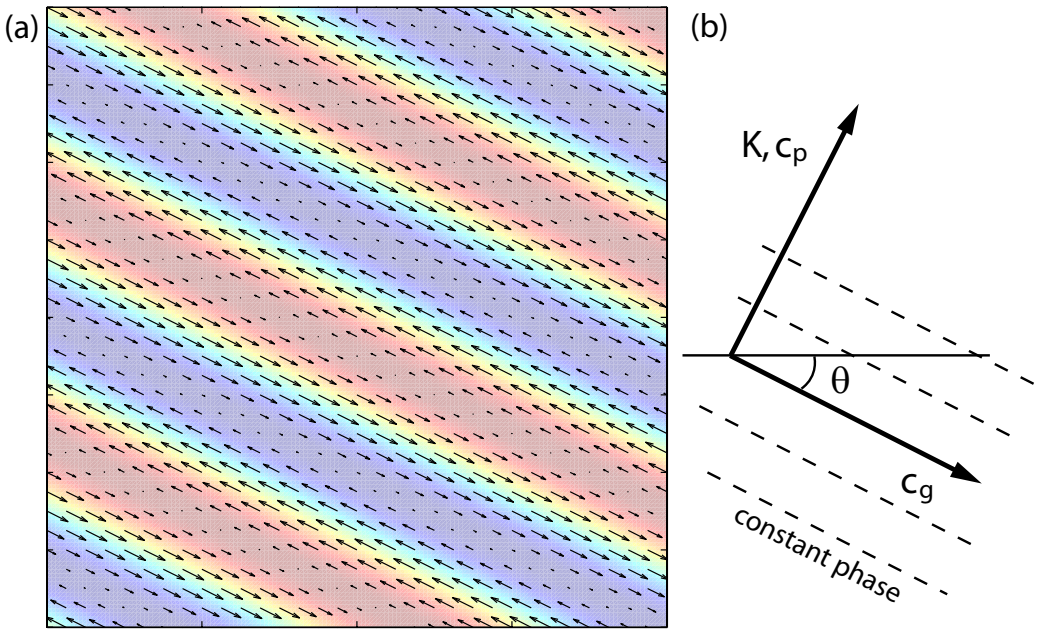

Figure 2.5: (a) An internal plane wave. Arrows give a snapshot of the velocity field, while color denotes vorticity, defined as the curl of the velocity field ($\omega = \nabla \times \mathbf{u}$). (b) Physical wave parameters group velocity ($\mathbf{c_g}$), phase velocity ($\mathbf{c_p}$), and wave vector ($\mathbf{K}$). Gravity is downward. Fluid oscillates back and forth along lines of constant phase. Lines of constant phase propagate up and to the right in (a).

Figure 2.5a shows a representation of an internal plane wave. Fluid parcels oscillate along a line from the upper left to the lower right, while the wave vector **K** is up and to the right. Further analysis [*Kundu and Cohen*, 2004] shows that the group velocity vector is along the direction of fluid motion, which implies that the group velocity and the phase velocity are perpendicular. Figure 2.5b depicts the relevant physical parameters for an internal wave graphically.

2.2.3 Properties

From Eq. 2.14, internal waves with different wavenumbers do not disperse if their wave vectors are in the same direction. This makes possible internal wave packets, called wave beams, in which internal waves made up of a series of wavenumbers travel in the same direction and remain coherent over long distances. Figure 2.6 shows an example of an internal wave beam. Since plane waves satisfy the fully nonlinear governing equations, wave packets comprised of sums of plane waves also satisfy the full nonlinear Navier-Stokes equations.

The dispersion relation (Eq. 2.14) also places limits on the frequencies at which internal waves are allowed to propagate. For Eq. 2.14 to be defined, the wave frequency must satisfy:

$$\omega \leq N \tag{2.16}$$

By Eq. 2.14, the angle of internal wave beam propagation depends on the ratio of the wave frequency ω and buoyancy frequency N. In the limit of very small

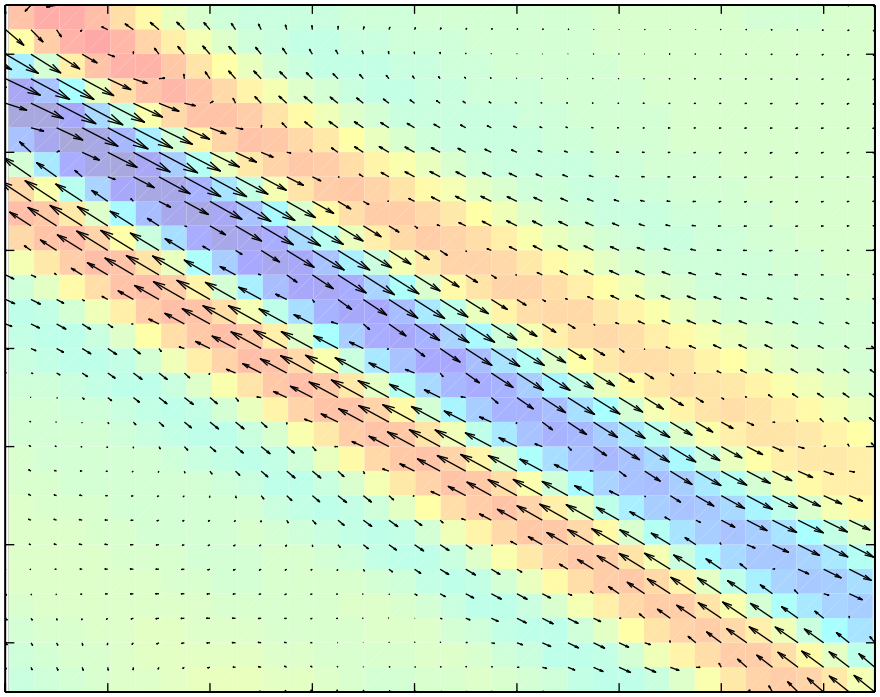

Figure 2.6: An internal wave beam. Arrows denote a snapshot of the velocity field, and color denotes vorticity. As in Figure 2.5, the group velocity and energy propagation are down and to the right, and the phase velocity is up and the right.

ω ($\omega << N$), the propagation direction is nearly horizontal. In the limit of ω approaching N, the propagation direction becomes vertical. In the ocean, N is typically much larger than ω_{M2}, the dominant tidal component. (ω_{M2} has correponding period 12.42 hours, while N typically has a period varying from roughly 10 minutes in the thermocline to several hours in the deep ocean.) However, there are notable exceptions in the deep ocean where $N \approx \omega_{M2}$, which will be discussed in great detail in Chapter 6. It is important to note that Eq. 2.14 was derived in the absence of the Coriolis force, which can be significant in certain cases. The full dispersion relation obtained without approximations, as well as implications of its use, are discussed in 6.1.

The vertical components of the phase velocity c_p and group velocity c_g of an internal wave always have opposite sign. This property is illustrated in Figure 2.5b, where the vertical components of c_p and c_g are positive and negative, respectively. For a more thorough discussion of phase and group velocity properties, see *Gerkema and Zimmerman* [2008].

Another unusual property of internal waves is due to the fact that the restoring force, gravity, is always in the vertical direction. This gives rise to unusual reflection properties of internal waves. If an internal wave is incident on a sloping surface (shown schematically in Figure 2.7), the reflected wave has the same angle with respect to the *vertical* direction instead of the surface normal direction. In the case shown in the diagram, the reflected internal wave beam is narrower than the incoming wave beam, with the consequence that the reflected beam has greater energy density. This elevated energy density

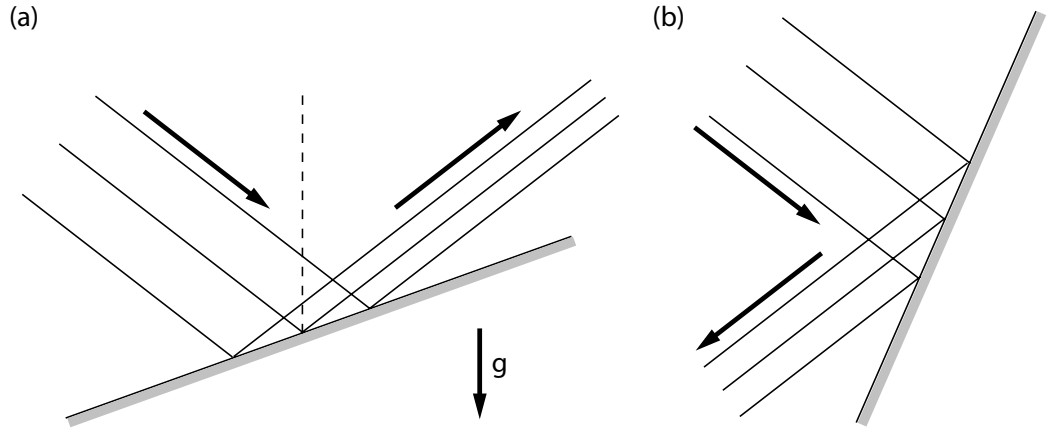

Figure 2.7: Internal wave reflection from a sloping bottom. (a) If the slope angle is smaller than the wave beam angle, the wave beam reflection is up and to the right. (b) If the slope angle is greater than the wave beam angle, the wave beam reflection is down and to the left.

corresponds to a higher shear and a larger probability of the reflected wave beam undergoing instability and breaking [*Staquet and Sommeria*, 2002]. Reflections such as these are one of the primary ways internal wave energy is transferred to smaller length scales, and ultimately leads to turbulence and mixing [*Eriksen*, 1985]).

2.2.4 Vertical mode formulation

Thus far, all discussion of internal waves has referred to internal plane waves, and internal wave beams, which are comprised of continuous distribution of plane waves in wavenumber space. Wave beams propagate in a direction defined by the dispersion relation (Eq. 2.14), and can be traced through a fluid where the buoyancy frequency $N(z)$ is known. This is the ray

tracing technique, or the method of characteristics, for internal wave propagation. (A characteristic is defined as a line along which an internal wave beam propagates). An alternate formalism which is useful for some applications is the vertical mode formalism. In this formalism, an eigenvalue problem is solved which results in standing internal waves which fill the stratified water column. Superpositions of various modes can be used to describe many phenomena more naturally than can ray tracing. A thorough treatment of vertical modes is given in *Gerkema and Zimmerman* [2008], but the problem amounts to first assuming plane wave behavior in the horizontal direction, such that the vertical velocity can be written:

$$w = W(z) \exp i(kx - \omega t) \tag{2.17}$$

w is then plugged into the governing equation for a stratified fluid (2.18 with the Coriolis correction included:

$$\frac{\partial^2}{\partial t^2}\nabla^2 w + (\vec{f} \cdot \nabla)^2 w + N^2 \nabla_H^2 w = 0 \tag{2.18}$$

where $\vec{f} = 2\Omega \sin\phi \hat{\mathbf{z}}$, Ω is the angular velocity of earth, and ϕ is the latitude. The $\hat{\mathbf{y}}$-component of the Coriolis correction, which is proportional to $\cos\phi$ is neglected here using the 'Traditional Approximation,' which is discussed in Section 6.1.) This substitution results in an eigenvalue equation for $W(z)$:

$$\frac{d^2 W}{dt^2} + k^2 \frac{N^2(z) - \omega^2}{\omega^2 - f^2} W = 0 \tag{2.19}$$

with boundary conditions

$$W(z = 0, -D) = 0 \tag{2.20}$$

where D is the ocean depth. The boundary condition at the surface ($z = 0$) is a rigid lid approximation. Eq. 2.19 can be solved numerically for an arbitrary stratification $N(z)$, wave frequency ω, and Coriolis parameter f. Once the solution for $W(z)$, and hence $w(z)$ by Eq. 2.17, is found, the vertical mode horizontal velocities can be found using the governing equations (Eqs. 2.4-2.9).

For the simple case of constant N, the problem becomes trivial, and the $W(z)$ are simply sine functions:

$$W_n = \sin\left(\frac{n\pi z}{D}\right), \quad n = 1, 2, 3, \cdots \tag{2.21}$$

where n is the mode number. Figure 2.8 shows the result of superposing multiple modes, eventually resulting in the recovery of wave beam-like behavior. Vertical modes in nonuniform ocean buoyancy profiles will be discussed in Section 6.4.3.

2.2.5 Internal tides

Internal tides are defined to be internal waves at a tidal frequency. Internal tides are the source of roughly half of the mixing energy required to sustain the global ocean circulation [*Wunsch and Ferrari*, 2004], and occur at the lunar principal semidiurnal (M2), solar principle semidiurnal (S2), and other tidal frequencies. To obtain the continuous spectrum of internal wave frequencies found in the ocean [*Garrett and Munk*, 1972], these internal tides undergo nonlinear interactions with other internal tides [*Lamb*, 2004; *Tabaei*

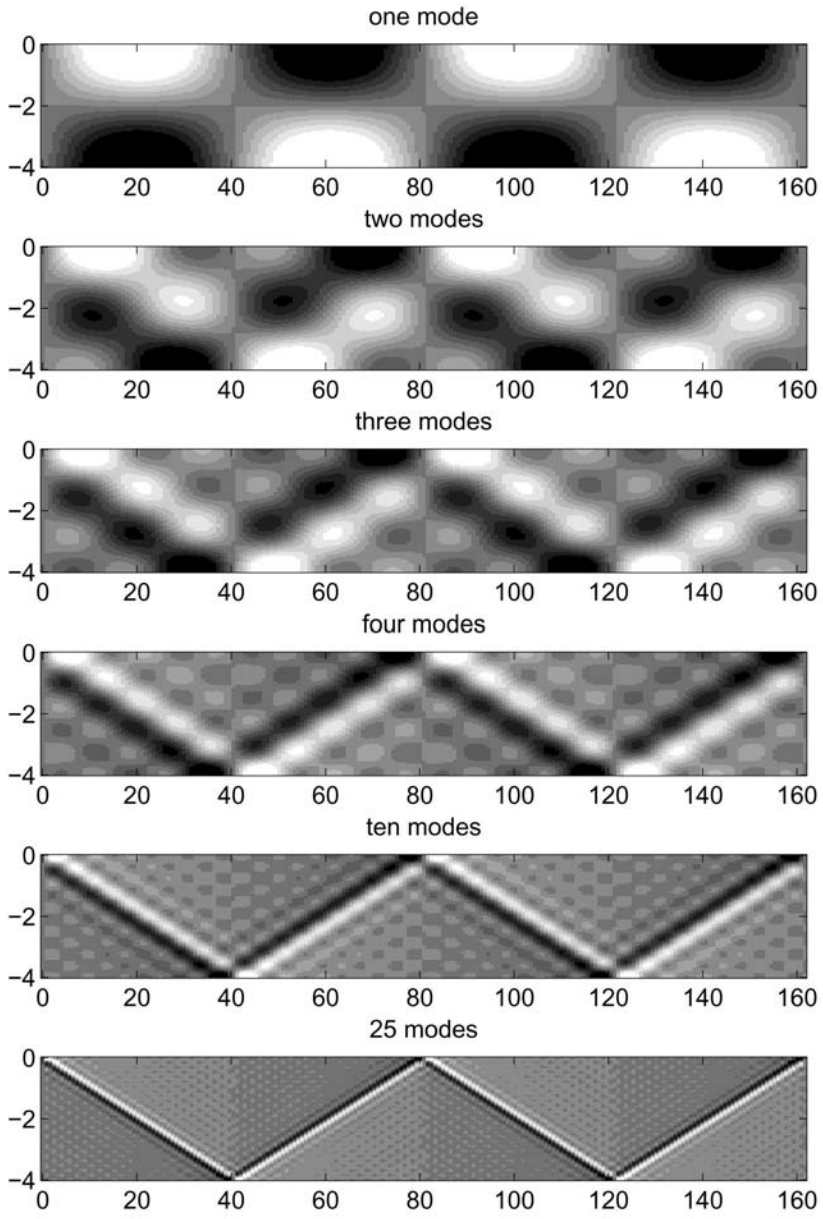

Figure 2.8: Horizontal velocities of vertical modes. The top figure shows the first vertical mode ($n = 1$). Subsequent figures show the wave field when progressively higher modes are added. When only the first four vertical modes are added (fourth plot), internal wave beam structure begins to become evident. The addition of additional vertical modes results in sharper wave beams. From *Gerkema and Zimmerman* [2008]

et al., 2005; *Thrope*, 2005], as well as wind-forced internal waves, which occur at many frequencies. These nonlinear interactions produce internal waves at sums and differences of the frequencies of the interacting waves, breaking the internal tides, which occur at discrete frequencies, into a continuous frequency spectrum of internal waves [*Staquet and Sommeria*, 2002].

2.3 Internal tides and bottom topography

Internal tides are generated when oscillating tides encounter bottom topography, which presents an obstacle to the horizontal flow. Some of the fluid impinging on the topography is forced upward, away from it's equilibrium depth, resulting in a disturbance that radiates away as an internal tide (an internal wave at tidal frequency; see section 2.2.5). The surface tides are also called *barotropic* tides, and result in sloshing of the entire water column over the ocean basins. A flow is barotropic when the surfaces of constant density (isopycnals), and the surfaces of constant pressure (isobars) coincide. The internal tides generated by the interaction of the barotropic tide with bottom topography are baroclinic, meaning that isopycnals and isobars intersect, which gives rise to vertical structure in the water column (in constrast to the vertically uniform barotropic tides). For this reason internal tides are sometimes referred to as baroclinic tides, and the generation of internal tides will often be referred to as barotropic-to-baroclinic energy conversion.

Since roughly half of the internal waves in the ocean are generated by the barotropic tide sloshing back and forth over bottom topography [*Munk and*

Wunsch, 1998], it is important to characterize the different types of bottom topography. Bottom topography is typically divided into two broad classes, depending on the ratio of maximum topographic slope to internal wave beam slope (discussed in Section 2.4). For a given tidal forcing frequency ω, if the slope of the generated internal tides (computed using Eq. 2.14) is smaller than the maximum topographic slope ($\gamma > 1$), the topography is 'supercritical.' If the internal tide slope is greater than the maximum topographic slope ($\gamma < 1$), the topography is 'subcritical.' In the special case with $\gamma = 1$, the topography is 'critical.' As will be discussed later, the criticality of a topographic slope is important in determining the nature of the generated internal tides and how effective the topography is at converting energy from the barotropic to the baroclinic tide.

2.4 Dimensionless parameters

Dimensionless parameters are often used to characterize studies of internal tide generation and interaction with bottom topography. The following have proven to be the most useful in the context of internal wave generation.
(1) Reynolds number

$$Re = \frac{UL}{\nu} \tag{2.22}$$

where U and L are typical velocity and length scales of a flow, respectively, and ν is the kinematic viscosity. This is the ratio of the nonlinear to viscous terms in the Navier-Stokes equations, and gives a measure of the importance of viscous effects. Re varies drastically in the ocean depending on the scale of

the flow, but values of $10^5 - 10^8$ are common.

(2) Froude number

$$Fr = \frac{U}{NH} = \frac{A\omega}{NH} \tag{2.23}$$

This is the ratio of the kinetic energy of impinging fluid to the potential energy required for the fluid to go over topography. This is a measure of the extent to which topography is an obstacle to incoming flow. When Fr is large, the topography does not present a significant obstacle to flow. When Fr is small, impinging flow cannot go over the topography and is blocked.

(3) Excursion parameter or tidal forcing amplitude

$$\epsilon = \frac{A}{\sigma} \tag{2.24}$$

where A is the tidal forcing amplitude when the tidal forcing velocity is given by $u(t) = A\omega \sin \omega t$, and σ is a horizontal length scale of the topography. This parameter quantifies the tidal excursion in relation to the horizontal length scale of the topography. There are two primary regimes: (1) For $\epsilon << 1$, the tidal excursion is small compared to the topography and internal tides are generated. For $\epsilon >> 1$, called the quasi-steady regime, lee waves are generated and propagate away from the topography.

(4) Ratio of maximum topographic slope to internal wave beam slope

$$\gamma = \frac{\sqrt{N^2 - \omega^2}}{\omega} \left(\frac{dh}{dx}\right)_{max} \tag{2.25}$$

where $h(x)$ is the height of the topography as a function of horizontal distance. This ratio is used to divide topographic features into classes, which are discussed in Section 2.3.

(5) Ratio of topographic height to ocean depth

$$\delta = \frac{H}{D} \tag{2.26}$$

although many early studies, which will be discussed in the next section, considered an infinitely deep ocean, recent work has shown that the height of the topography relative to the ocean depth can have an effect on the internal wave generation process [*Khatiwala*, 2003].

(6) Richardson number

$$Ri = \frac{N^2}{\left(\frac{\partial u}{\partial z}\right)^2} \tag{2.27}$$

This dimensionless number is the ratio of the stratification, which tends to suppress instabilities, to the vertical shear, which tends to destabilize the flow. This is often used to characterize the likelihood of an internal wave becoming unstable and breaking. The standard critical value of Ri is generally considered to be 1/4, below which internal waves are thought to be unstable [*Staquet and Sommeria*, 2002]. However, a recent study demonstrated internal waves which were stable at lower Richardson numbers [*Zhang et al.*, 2008], so the $Ri = 1/4$ criterion appears to be necessary but not sufficient to guarantee wave breaking.

2.5 Previous studies of internal wave generation

2.5.1 Two-dimensional studies

Studies of internal wave generation date back a half century, and vary widely in complexity. The simplest studies approximated topography by simple geometric shapes (most commonly cylinders) to understand the generation process. Flow oscillating past a cylinder is similar to flow past supercritical topography since the maximum slope of the cylinder is infinite. The only striking difference is the fact that a cylinder or similar shape lacks a bottom boundary approximating the sea floor. Despite this difference, studies of oscillating flow past cylinders have shed light on the internal wave generation process and enabled advances in more realistic models. In parallel, much work has also been done on more realistic topographic shapes, although more of this work has been theoretical in nature. These previous studies will be summarized below.

2.5.1.1 Simple model: the oscillating cylinder

2D experiments on internal wave generation date to the first shadowgraph study by *Gortler* [1943], followed by *Mowbray and Rarity* [1967], who studied the simple case of internal waves generated by a vertically oscillating cylinder using Schlieren visualization. They observed the 'St. Andrew's cross' X pattern formed by internal wave beams, shown in Figure 2.9. (In 2D, there are four possible propagation directions from a general disturbance that can satisfy the dispersion relation 2.14.) *Thomas and Stevenson* [1972] developed a viscous similarity solution for the oscillating cylinder, making the assumption

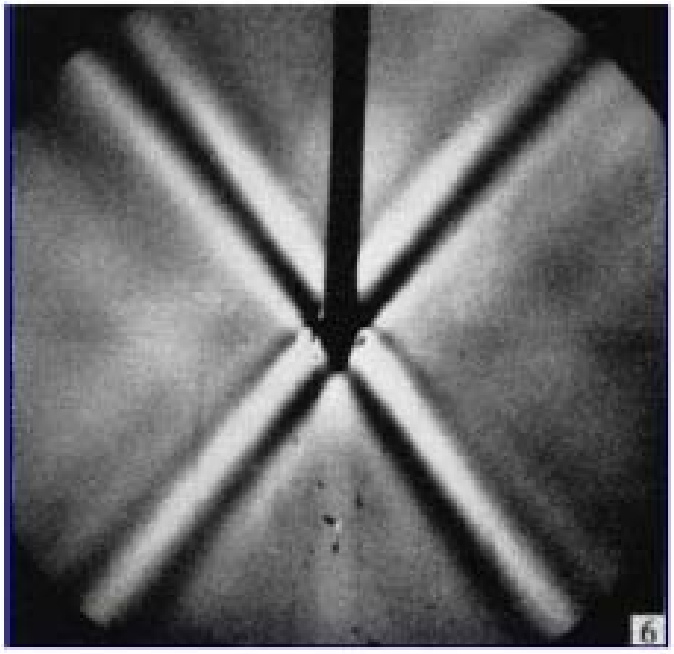

Figure 2.9: St. Andrew's cross pattern. A 2 cm diameter cylinder in the center of the image is oscillated vertically at frequency 0.35 rad/s. Internal wave beams are visualized using the Schlieren technique, which shows differences in refractive index associated with the wave motion. The vertical black bar is the supporting rod for the cylinder. From *Mowbray and Rarity* [1967]

that variations in velocity along an internal wave beam are small compared to variations across the wave beam, and obtained the first theoretical cross sections of internal wave beams. *Hurley* [1997] followed up with a linear inviscid theory without the boundary-layer type approximation, followed by an extension to viscous flows [*Hurley and Keady*, 1997], which healed the singularities that result from an inviscid treatment of the problem. This viscous theory was subsequently verified experimentally by *Sutherland et al.* [1999], who used a vertically oscillating cylinder and the new synthetic Schlieren visualization technique [*Dalziel et al.*, 2000]. A similar system was studied by us [*Zhang et al.*, 2007], utilizing a horizontally oscillating cylinder and Particle Image Velocimetry visualization for more accurate flow characterization (discussed in Section 3.1.3). *Ermanyuk and Gavrilov* [2008] also studied the oscillating cylinder, but extended the results to circular oscillations. A circular motion imitates more realistic tidal motion, as tidal oscillations in the ocean are actually elliptical due to Coriolis effects (The ellipticity of the tidal orbits depends strongly on latitude, being nearly zero at low latitudes).

2.5.1.2 Refined models: Gaussian ridges and similar topography

The pioneering theoretical studies of internal tide generation by tidal flow over more realistic bottom topography were done by *Cox and Sandstrom* [1962], *Baines* [1973], and *Bell* [1975]. In the most widely used early study, Bell solved the linear, inviscid problem in an ocean of infinite depth and constant N under the assumption of small, subcritical topography ($\delta << 1$ and

$\gamma < 1$). Under these assumptions, the bottom boundary condition can be enforced at $z = 0$ rather than at $z = h(x)$ (where $h(x)$ is the height of the topography), simplifying the calculations substantially. This method allows one to solve for the internal tide field for bottom topography of arbitrary shape by decomposing the topography into a Fourier series of solutions. The most physically relevant quantity, the rate of energy conversion from tidal motion to internal waves, can then be computed. *Baines* [1982] provided a useful summary of the early internal wave generation theories and generalized them so they could be more easily applied to estimate energy conversion rates on a global scale.

Many subsequent theoretical studies have relaxed the earlier constraints. *Balmforth et al.* [2002] studied tidal conversion for the case of finite topographic height H. This study included tidal energy conversion by sinusoidal bumps, Gaussian ridges, and random topography comprised of a series of wavelengths set to roughly match the roughness of the ocean floor in certain locations. *Smith and Young* [2002] extended Bell's result to account for depth-dependent N profiles. *Laurent et al.* [2003] studied the case of supercritical topography ($\gamma > 1$) using the simplified case of a knife-edge, and *Smith and Young* [2003] developed a theory for supercritical topography (also utilizing knife-edge geometry) using a realistic ocean N profile. *Petrelis et al.* [2006] used an integral equation method to compute tidal conversion by triangular and smooth polynomial ridges, and found that tidal energy conversion increases monotonically with topographic height and decreases monotonically with horizontal length

scale for supercritical topography. For the case of subcritical topography, the rate of energy conversion into internal waves was found to depend nonmonotonically on both the vertical and horizontal length scales of the topography.

In addition, several recent numerical studies have been advanced, the main advantage being that numerical simulations can more easily accommodate the nonlinear terms in the governing equations. *Khatiwala* [2003] developed a fully nonlinear numerical model for comparison with the linear analytic wave generation models. He found that accounting for a finite depth generally reduced the energy converted from surface tides into internal tides. *Lamb* [2004] used a nonlinear, inviscid model to study nonlinear interactions between internal tides generated by tidal flow over a flat-topped ridge, and showed that wave beam interactions could have a significant effect on the flow field near the topography. *Di Lorenzo et al.* [2006] used a primitive equation model to estimate conversion rates at steep ocean ridges, and compared results with previous theoretical results. An important finding was that in many cases, the energy estimates derived from linear wave generation models are still reasonable even when used outside the linear flow regimes in which they are technically applicable. This primarily refers to the well known problem that the velocity fields in linear theories diverge along the wave beams as topographic slopes become critical. Despite the divergence in the flow field, the integrated energy flux remains finite. [*Aguilar et al.*, 2006; *Aguilar and Sutherland*, 2006] have undertaken laboratory experiments on rough topography and sinusoidal periodic topography, and shown that the topographic

boundary layer can sometimes have appreciable effects on the generated internal wave field. *Legg and Huijts* [2006] and *Legg and Klymak* [2008] have performed numerical simulations using the MITgcm model [*Marshall et al.*, 1997] on internal wave generation by realistic topography. They focused on flow features near the topography that may lead to increased local mixing. *Legg and Klymak* [2008] studied four different Gaussian-shaped topographic features with widely varying heights and slopes. All features were designed to approximate observed topographic features in the ocean, such as the Mid-Atlantic Ridge, Hawaiian Ridge, etc.

2.5.2 Three-dimensional studies

Previous three-dimensional studies are limited to a few special cases, and have only been visualized in two dimensions in experiments. In addition, previous theoretical work has been linear, which eliminates the possibility of having harmonic internal waves, which we later show to be very important in understanding the internal wave generation process. In the ocean, many waves have high amplitudes [*Holloway*, 1980], resulting in the likely breakdown of most linear theories, and the assumption that oceanic flows should be well characterized by 2D studies is debatable. However, recent advances in computational methods and observational techniques have led to increased research on 3D internal wave generation.

2.5.2.1 Simple model: the oscillating spheroid

The first theoretical study of the oscillating sphere was undertaken by *Hendershott* [1969], solving the linear, inviscid, axisymmetric (vertically oscillating sphere) problem. The slightly more general case of the oscillating spheroid was studied theoretically by *Sarma and Krishna* [1972]; *Lai and Lee* [1981]. *Appleby and Crighton* [1987] solved the linear inviscid problem for a *horizontally* oscillating sphere, which is more relevant to tidal forcing in the ocean. They derived the azimuthal dependence of the generated internal wave field, showing that wave beam velocity amplitude should fall off as the cosine of the azimuthal angle (defined as the horizontal angle measured from the tidal forcing direction). Our experimental and numerical verification of the functional form of this theory is discussed in Chapter 4, where we also determine the tidal forcing amplitude at which the theory begins to break down. *Voisin* [1991] solved the linearized viscous problem, following up later [*Voisin*, 2003] with better characterization of the generated internal wave field. *Flynn et al.* [2003] performed the only previous experimental study on an oscillating sphere, using the synthetic Schlieren method [*Sutherland et al.*, 1999] to measure perturbations of the background density gradient for the vertically oscillating case. They also combined the analytic results of *Appleby and Crighton* [1987] and *Voisin* [1991] with the boundary layer approximation of *Stevenson and Thomas* [1974] to include viscous dissipation in the propagation of the generated internal waves. However, the agreement between the viscous theory and experiment was poor. In particular, the predicted and observed internal

wave amplitudes differed by up to a factor of 2.

2.5.2.2 Refined models: 3D mountains

Two key numerical studies have been undertaken on 3D Gaussian shaped topography. *Holloway and Merrifield* [1999] used the Princeton Ocean Model (POM) to study the 3D, fully nonlinear internal tide generation by Gaussian-shaped seamounts and islands. Inclusion of the free surface was found to affect the amount of energy converted from tidal motions into the internal wave field. In addition, the tidal forcing was elliptical, resulting in a more realistic internal wave field. The horizontal aspect ratio (defined as the ratio of the longer to the shorter horizontal length scales of the topography) was found to have a substantial effect on internal wave generation, with longer topography (aspect ratio 3:1) converting nearly ten times the energy into internal waves as symmetric topography (aspect ratio 1:1). In agreement with previous work, internal tides were found to be more strongly generated when the topographic slope was critical or supercritical. *Munroe and Lamb* [2005] also used POM to study the role of topographic height on internal tide generation. They found that for subcritical topography, the energy conversion was proportional to the square of the topographic height, while the relationship becomes more complex for supercritical topography. In addition, the energy conversion increases more rapidly with height for elongated (large aspect ratio topography) than for symmetric topography. *Baines* [2007] developed a linear inviscid theory for internal tide generation by tidal flow past pillbox-shaped topography and

characterized the azimuthal dependence of the wave field. The pillbox is intended to mimic steep topography, but with infinite slope and a horizontal top, there is not a large correspondence with most actual topography.

2.5.2.3 Numerical studies of actual bottom topography

Since the advent of several 3D codes dedicated to oceanic studies [*Blumberg and Mellor*, 1987; *Marshall et al.*, 1997; *Fringer et al.*, 2006], there have been many recent studies of internal tide generation by tidal flow over measured bottom topography. These studies simulate realistic tidal flow over actual bottom topography using measured oceanic stratifications, resulting in accurate models of internal tide generation and propagation in regions of interest. Several such regions are the East China Sea [*Niwa and Hibiya*, 2004], South China Sea [*Wu et al.*, 2005], Monterey Bay [*Jachec et al.*, 2006], the Mid-Atlantic Ridge [*Zilberman et al.*, 2009], and a generalized continental slope [*Katsumata*, 2006]. In order to make fluid problms on these scales soluble with current computing resources, exaggerated effective viscosities must be utilized. These viscosities are typically on the order of 0.1-1.0 m^2/s [*Legg and Huijts*, 2006], with the effective viscosities often being different in the vertical and horizontal directions (This is reasonable since stratification, which inhibits vertical flow, introduces anisotropy into the problem). Since the molecular viscosity of water is 10^{-6} m^2/s, these effective viscosities are exaggerated by a factor of roughly 10^5-10^6. The implicit assumption when using these artificial viscosities is that flows with length scales smaller than the grid (subgrid flow

features) can be safely ignored.

2.5.3 Global models of internal tide generation and mixing

To predict internal tide generation on a global scale, three components are needed: (1) A detailed model of the astronomical tides, (2) Detailed knowledge of bottom topography on a global scale, and (3) a model to combine the tidal and topographic information at each location of interest and to determine the energy conversion rate.

The global tides have been characterized with high accuracy by the TOPEX/Poseidon project, which consists of a satellite altimeter capable of determining sea surface height to sub-centimeter accuracy [*Ray*, 2001; *Ray et al.*, 2001]. From careful measurements of sea surface height worldwide over the course of many years, scientists have developed an accurate picture of the global tides. Figure 2.10 shows a global surface tide map, with color denoting changes in sea surface height, and white lines denoting lines of constant phase, separated by 1 hour. Using this sea surface height data and the continuity equation (Eq. 2.9), modelers can infer the horizontal tidal flow at any location with reasonable accuracy.

The highest resolution bottom topography information available comes from a combination of sonar soundings and gravity anomaly computations based on the TOPEX/Poseidon satellite altimeter data. Bottom depths are available on a global grid with 2 minute resolution [*Smith and Sandwell*, 1997] and, very recently, 30 second resolution [*Becker et al.*, 2009]. These angular

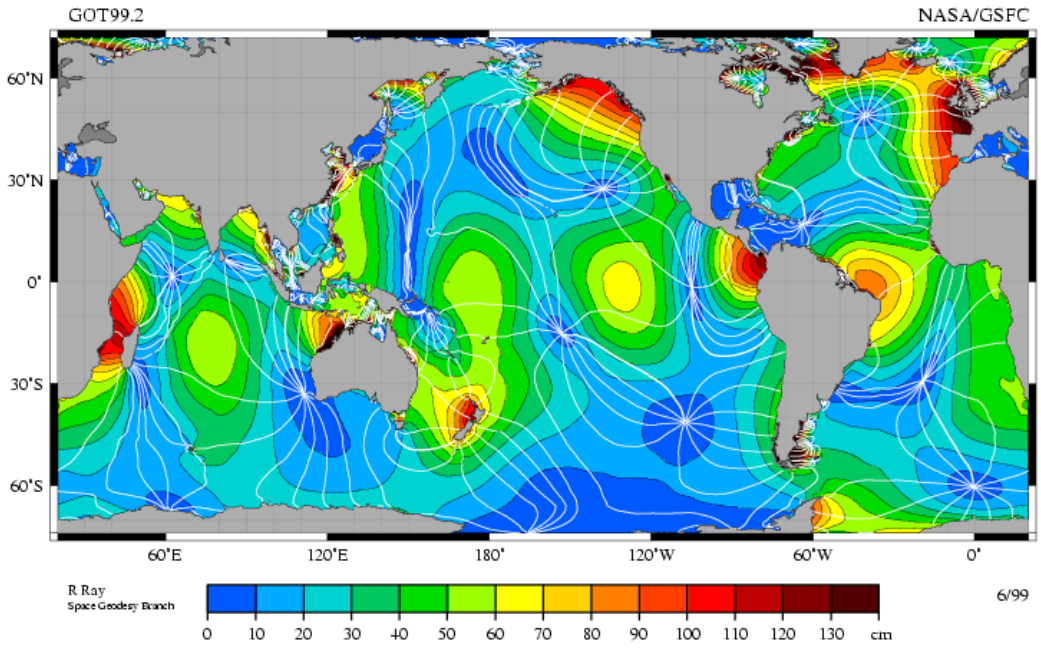

Figure 2.10: Global map of the surface tides. Tidal motion becomes complex due to Coriolis effects and interaction with landmasses. Image courtesy of R. Ray and NASA.

resolutions correspond to spatial resolutions at the equator of 3.7 km and 0.9 km, respectively. (Note that these data are not measured directly, but inferred from anomalies in sea surface height due to the gravitational influence of the spatially variable sea floor.) Based on these high resolution sea floor maps, the slope of the seafloor can be estimated at all locations.

Since tidal motion and bottom topography can be estimated on a regular grid, many of the available internal wave generation theories can be used to characterize internal wave generation on a global scale. *Morozov* [1995] applied the linear internal wave generation theory developed by *Baines* [1982] to estimate the energy conversion at many large topographic features. *Niwa and Hibiya* [2001] integrated a primitive equation model over much of the Pacific ocean and found that the locations of conversion from surface tide to internal tide energy matched well with the results inferred from satellite altimetry [*Egbert and Ray*, 2000]. *Simmons et al.* [2004] performed a similar analysis on the entire global ocean, except they utilized a simple discrete stratification model (with the water column being comprised of either 2 or 10 uniform layers) to estimate internal wave generation and propagation over the entire global ocean. Most recently, *Nycander* [2005] utilized a linear internal tide generation model similar to that used by *Morozov* [1995], combined with the newly available global sea floor data of [*Smith and Sandwell*, 1997], to estimate internal tide generaition throughout the global ocean.

2.6 Current study

We extend the previous work on internal tide generation by tidal flow over 3D topography using numerical simulations and laboratory experiments in tandem. In particular, we focus on the spatial character of the 3D internal tide fields, and are careful to include nonlinear effects, which give rise to unexpected mean flows and higher harmonic internal waves (internal waves at integer multiples of the tidal forcing frequency). We use a Direct Numerical Simulation (DNS) of a laboratory scale system to ensure that viscous flows are fully resolved. For the first time, 3D experiments and numerical results are carefully compared to ensure good agreement. The numerical simulations are fully viscous, and convergence studies ensure that our numerical grids are sufficient to fully resolve all components of the flow fields (including the viscous boundary layer around the topography). Our objective is to demonstrate the importance of considering the 3D, fully nonlinear internal tide generation problem. As will be discussed in the following chapter, we choose two simple geometries: a half-sphere on a plane, and an axisymmetric Gaussian mountain. These topographies share the important features of topography in the ocean, namely slopes with both subcritical and supercritical components. We hope that the result will help refine the next generation of global internal tide generation models.

Once internal tides have been generated, we are also concerned with their evolution and eventual breaking. An important new possibility is that there might be large regions in the deep ocean where the stratification is

insufficient to support internal tides at the semidiurnal (M2) frequency (as well as internal waves at higher frequencies). We present the results of two analysis schemes devised to systematically check the most thorough ocean database available (World Ocean Circulation Experiment (WOCE) database) for regions where internal waves may not propagate. This would be a startling result, as internal waves are thought to be ubiquitous throughout the world oceans [*Munk*, 1981], with an empirically derived frequency-wavenumber spectrum (often called GM72) [*Garrett and Munk*, 1972, 1975]. Our first method for analyzing the WOCE data to obtain buoyancy frequency profiles $N(z)$ uses a simple filtering scheme, and the second method utilizes a more rigorous statistical averaging scheme to place error bars on the resulting buoyancy frequency profiles. Regions where M2 internal waves cannot penetrate are bounded by 'turning points' (or 'turning depths'), with incident internal waves reflecting from the interface. We conduct the first systematic analysis of the more than 18,000 WOCE (Conductivity-Temperature-Depth) CTD casts, and have discovered (1) the ubiquity of turning points in the deep ocean, (2) that below the thermocline, the stratification of the ocean is remarkably stable over time periods on the order of a decade, and (3) stratification does not vary significantly over great distances in the open ocean, but varies substantially near large or abrupt bottom topography. We perform DNS simulations on internal waves reflecting from turning points to determine if energy is lost in the reflection process. We also solve for the vertical modes in the presence of a turning point to see how the structure of these waves might be modified by

very weakly stratified regions in the deep ocean.

Chapter 3

Methods

3.1 Laboratory Experiments

3.1.1 Experimental Apparatus

Laboratory experiments were performed in a 250 L glass tank. The tank dimensions are 90 cm wide × 45 cm deep × 60 cm high.

Stratifying agent

Sodium Chloride (NaCl, ordinary salt) was chosen as the stratifying agent, although we also successfully utilized sucrose ($C_{12}H_{22}O_{11}$) in an earlier study [*Zhang et al.*, 2007]. The primary advantage of salt over sucrose is that the salt solution inhibits the growth of algae and other organic matter in the tank, which quickly becomes a problem when dealing with concentrated sugar solutions. In addition, when using sugar solutions, buildup of organic material occurs in tubing and eventually affects flow rates. Sugar tends to also get tracked around the laboratory near the apparatus. The only disadvantage of the salt solution is its corrosive properties, but suitable choices of materials used near the lab apparatus can minimize this problem. In addition, flushing all pumps and plumbing with fresh water after use helps slow the corrosion process.

Table salt could not be used in these experiments because it normally contains iodides, which don't dissolve in water, and result in a cloudy fluid solution with poor optical clarity. The best source of salt we found was salt used in swimming pools, which is sold in 40 lb bags at relatively low cost.

3.1.1.1 Obtaining a stratified fluid

We use the double bucket technique [*Oster*, 1965] to obtain a stratified fluid in the lab. Two reservoirs are used. The first reservoir, called the storage reservoir, is initially filled with salt water with density equal to the maximum density desired in the lab tank. In our experiments, the density of the salt water is 1.15 g/mL. The second reservoir, called the mixing reservoir, is initially filled with fresh water. Two pumps are also used; pump 1 moves fluid from the storage resevoir into the mixing reservoir, and pump 2 moves fluid from the mixing reservoir into the laboratory tank. The mixing reservoir also conains a stirring mechanism which vigorously stirs the fluid to ensure that the denser fluid being pumped in is quickly mixed into the bulk of the fluid. As dense fluid is pumped into the mixing reservoir and thoroughly mixed by the stirring mechanism, the fluid in the mixing reservoir becomes progressively denser. This fluid is in turn pumped into the laboratory tank through 1/8 inch ID copper tubing, with the tubing outlets located at the *bottom* of the tank. In this way, progessively denser fluid is continuously pumped into the bottom of the lab tank. Fluid entering the tank displaces the lighter fluid above it, with the result being a continuous density stratification in the lab tank. For

a linear density stratification, as is used in this study, the flow rate of pump 2 must be exactly twice the flow rate of pump 1, so that the water level of the two identical reservoirs decreases at the same rate. In principle, the flow rates of the two pumps can be varied with time using a computer controller to obtain an arbitrary density profile, but this was not done here.

In practice, the flow rate of pump 2 was maintained at 1.5 L/min, and pump 1 was operated at 0.75 L/min. These flow rates give an approximate fill time of 3 hours. Due to the changing head on the pumps as the relative water levels in the reservoirs and lab tank change, measurements were typically made every 10-20 minutes to ensure that the water levels in the two reservoirs were decreasing at the same rate. Discrepancies in water level between the two reservoirs meant that manual adjustments had to be made to the flow rates to keep them close to their nominal values. In the lab tank, small discrepancies in the density profile tend to be smoothed over very quickly due to two processes: (1) mixing as the fluid enters the lab tank and comes to equilibrium, and (2) molecular diffusion of the stratifying agent (salt). To give an example of the second mechanism, consider a vertical interval of 0.5 cm over which the density profile differs from the surrounding profile (which would correspond to a deviation from the nominal pump rates for 1 minute). The diffusive length scale is defined to be:

$$L = 2\sqrt{DT}, \tag{3.1}$$

where D is the diffusion constant of the stratifying agent and T is the diffusion time scale. For sodium chloride in water, D is roughly 10^{-5} cm^2/s. For the

0.5 cm length scale irregularity in the density profile, the relevant time scale is roughly one hour. After the tank has been filled and allowed to settle for an hour or so, we expect that most small irregularities have been smoothed over by diffusive action. Using the same analysis of diffusion time and length scales, we can show that the stratification, once established, would be very robust over long time periods in the absence of stirring. Plugging in the height of the tank, 60 cm, to the above relation, gives a time scale for diffusive mixing of the entire tank of about 10^8 seconds, or roughly 3 years. In practice, however, a single stratification can only be used for up to 5 days. Beyond that time, the repeated act of inserting and removing apparatus from the tank causes excessive mixing, and the linear density profile can no longer relied on.

In all experiments discussed in Chapters 4 and 5, the maximum density at the bottom of the tank is 1.15 g/cm^3, and the resulting buoyancy frequency is $N = 1.5$ rad/s. The density is not measured directly, but the extent to which N is constant can be inferred from the angle of the generated internal wave beams using Eq. 1.1. Deviations from a constant propagation angle would correspond to deviations in N. Measurements of internal wave beams over distances of 20 cm show negligible amounts of variation from a constant propagation angle, so we conclude that the constant stratification is satisfactory for the studies presented here.

Oscillatory flow

As discussed in Chapter 1, many internal waves are generated in the ocean by tidal flow oscillating past topography such as submerged ridges, mountains, and continental slopes. It would be very difficult and impractical to oscillate an entire body of fluid in the laboratory. However, since the important effect is the *relative* motion between the background fluid and topographic features, we can oscillate the topographic features in a stationary fluid instead. This amounts to a straightforward transformation of reference frame. In much of the literature, results are discussed in the reference frame of the bottom topography since this is more intuitive. However, in the laboratory, it is far more convenient to discuss results in the frame of the oscillating tide.

We use a simple translation stage driven by a stepper motor to oscillate a model topographic feature back and forth in the lab tank. The stepper motor is controlled by Labview, and enables us to specify both the forcing frequency and amplitude of the oscillatory motion. This makes available a large phase space for a given topography and stratification.

Various model topographic features (i.e. cylinders, spheres, Gaussian-shaped mountains, etc.) are suspended from the translation stage into the lab tank. In mounting the topography, it is important to avoid overly complicated support structures in the tank, as these support structures excite additional unwanted motion in the fluid when the topography is oscillated. Typically, a single 1 inch aluminum square tube was found to be sufficient. In some cases, where the forcing object (and hence the hydrodynamic drag on the forcing

object when oscillating) was small, a single 1/4-20 threaded rod could be used to suspend the object instead.

3.1.2 Model topographic features

We employed two different types of topographic features in these studies. Both topographic features are three-dimensional objects, and result in rich dynamics that are not observed in simpler two-dimensional flows.

3.1.2.1 Sphere

The simpler of the two 3D geometries was a nylon sphere. Two diameters were used: 6.5 cm and 10 cm. The smaller sphere was utilized when looking at far field features such as internal waves generated by the oscillating sphere. The larger sphere was used to look at near field features like the boundary layer around the sphere. Both spheres were painted black to avoid unwanted scattering of the laser light sheet used for visualization (discussed in Section 3.1.4.

3.1.2.2 Axisymmetric Gaussian mountain

As a more realistic model of bottom topography, an axisymmetric Gaussian-shaped mountain was used. The mountain used had functional form:

$$h(r) = H \exp(-r^2/\sigma^2), \tag{3.2}$$

where $h(r)$ is the height of the mountain as a function of radial distance from the origin, $H = 7$ cm is the maximum height, and $\sigma = 2.85$ cm is the 1/e half-

width of the mountain. The Gaussian mountain was machined from Delrin on a CNC machine, which enables the machining of smooth curves. The Gaussian mountain was bolted to a 16 inch thick black aluminum plate and suspended in an inverted position from the traverse mechanism. Mounting the mountain in an inverted position has no effect on the resulting flow field (after a proper reflection of the processed data), but results in less extraneous support structure being present in the tank since the mountain can be mounted higher in the water column. In addition, the shorter mounting apparatus that results from mounting the mountain higher in the tank results in a shorter torque arm associated with the hydrodynamic drag on the mountain as it is oscillated. This allowed us to further reduce the cross section of the supporting material and introduce still fewer unwanted disturbances in the tank.

Both topographic features needed to be removed from the laboratory tank after experiments were performed and reinserted in preparation for additional experiements over the course of the five days in which a given stratification could be used. The main reason for removing the model topographic features was to minimize the aggressive corrosion that takes place in a concentrated salt solution. In addition, the need to obtain experimental data necessitated removal of the topography and shifting of the traverse mechanism on a regular basis. As discussed in Section 3.1.1.1, the stratification is remarkably robust to perturbations, and molecular diffusion on the scale of the laboratory tank is a very slow process. Regardless, we used extreme care when moving objects within the stratified fluid. Excess motion causes stirring

of the fluid, and through the stretching and folding of the isopycnal (constant density) surfaces, significant density gradients form, which locally decrease molecular diffusion time scales from months to minutes. It is therefore important to minimize unnecessary movement of objects in the laboratory tank. When removing or inserting forcing objects and their associated support structures, we tried to keep speeds of movement below roughly 1 cm/s, especially when dealing with large plates such as the one used to mount the Gaussian mountain.

3.1.3 Flow Visualization

To visualize flow, the fluid was seeded with small, reflective passive tracers. We used titanium dioxide (TiO_2) particles, with a typical size distribution between 1 and 10 μm. Particles of this size are excellent tracers of the fluid flow, but the high density (4.2 g/cm^3), means that the particles sediment out of the fluid. Sedimentation speed can be determined utilizing Stokes' Law to determine the terminal settling velocity at which the effective weight (gravitational force minus the buoyancy force) of a tracer particle of a given size equals the Stokes drag:

$$mg = 6\pi\mu r v_s \tag{3.3}$$

where m is the effective mass of the tracer particle (the mass of the particle minus the mass of the fluid it displaces, to compensate for the buoyancy term), μ the dynamic viscosity of the fluid, r the radius of the tracer particle (assuming a spherical tracer), and v_s the sedimentation velocity. Writing the

mass of the particle in terms of its density ρ_p, the density of the fluid ρ_f, and particle volume $4/3\pi r^3$, and solving for v_s gives:

$$v_s = \frac{2gr^2(\rho_p - \rho_f)}{9\mu} \tag{3.4}$$

Using this relation, 1 μm titanium dioxide particles sediment at a speed of 7×10^{-4} cm/s, giving a characteristic time scale of 24 minutes to descend 1 cm. On the larger side of the tracer size distribution, the 10 μm titanium dioxide particles sediment at 7×10^{-2} cm/s, descending 1 cm in only 14 s. The larger particles therefore settle to the bottom of the tank quickly, leaving the smaller (1-2 μm) particles to be used to visualize the flow.

It is important to note that the foregoing analysis is only valid for small Reynolds number ($Re << 1$). For a typical 0.1 cm/s relative flow around a tracer particle of size 5 μm, $Re = 5 \times 10^{-5}$, so the small Re assumption is satisfied.

Illumination of the tracer particles is achieved using a Coherent Inc. (www.coherent.com) Verdi 5 W green laser. The beam is passed through a speader which converts the beam into a vertical light sheet 0.5 cm thick. The light sheet illuminates a vertical plane in the laboratory tank, typically passing through the center of the forcing object. This results in flow visualization in the midplane of the system. In principle, the spreader lens can be rotated 90° to create a horizontal light sheet, which can be photographed from above, but this wasn't utilized in this study. It is important that all forcing objects as well as support structures suspended in the tank be painted black to avoid

unwanted reflections from reaching the camera.

3.1.4 Data Acquisition

A 12-bit CCD camera with 997 × 1004 pixel resolution is used to photograph the setup from the front. A 35 mm lens is used, resulting in a field of view of between 10-20 cm^2, depending on the distance of the camera in front of the visualization plane. A Labview program captures frames from the camera at a specified interval in time. The exact time interval between snapshots is not critical, but tracer particles need to move roughly 4 pixels or more between subsequent images for the particle tracking software to establish velocity vectors with confidence. An empirically determined maximum interval between snapshots is one twentieth of an oscillation period. This upper limit is due to the fact that particle tracking algorithms work under the assumption that the velocity is roughly constant between subsequent snapshots. Equivalently, one could say that the flow is approximately steady. However, this assumption breaks down when studying periodic motion with longer intervals between snapshots.

3.1.5 Data Analysis

To determine the flow field from the raw images, we use the Correlation Image Velocimetry (CIV) algorithm developed by Fincham and Delercy [*Fincham and Delerce*, 2000]. Rather than tracing individual particles, which is sometimes done, this algorithm tracks groups of particles, which is a more

robust procedure as individual particles are very small and sometimes move out of the light sheet. Each snapshot is divided into a 50×50 grid, and the pattern of particles within each grid box is characterized using a Fourier transform of the pixel intensity. For each box, the algorithm then looks for a similar pattern displaced a short distance in the following snapshot (The algorithm maximizes the correlation between the original box and many trial boxes nearby in the following snapshot). The end result is that the program outputs a 50×50 velocity field, as well as a measure of confidence based on the quality of the correlations. The 50×50 grid with a 10 cm square window size corresponds to a maximum spatial resolution of 0.2 cm.

To reduce error, images are actually taken in pairs, typically separated by 0.035 s, with images in pairs having a modifier 'a' or 'b' after the image name. To give an example, a single interval in time then has two pairs of images: sample_1a and sample_2a, and sample_1b and sample_2b. The time intervals of these two pairs of images overlap almost completely, which means that the velocity fields extracted from each pair can be averaged to reduce error. This procedure amounts to taking twice as many measurements of the velocity field to, in principle, reduce error by a factor of $\sqrt{2}$.

Before the raw images can be passed through the CIV software, the 12-bit grayscale images from the camera must be converted into 8-bit images. This task is performed with the Matlab script 'fileProcSuper.m,' which loops over all png images in a user-specified directory. and converts them into 8-bit images, saved into a new subdirectory. These images can then be loaded into

the CIV software.

When the CIV analysis is complete, the Matlab script 'readallncfile-sav.m' loads the data and averages the appropriate pairs of velocity fields, outputting the final velocity field at every time step. To convert the processed velocity fields, which have units of pixels per time separation between images, into physical units, a calibration image is necessary to establish the scale in the images. This is done by submerging a metal ruler in the same plane as the light sheet. An image is then captured with the camera in the same position as during the experimental runs. Using this image, a direct conversion from pixels to centimeters can be made. Since we know the time separation between images, we can then convert the velocity fields into physical units (cm/s) for analysis and comparison with numerical simulations.

3.2 Numerical Simulations

3.2.1 CDP

CDP is a powerful numerical flow solver developed by Frank Ham (fham@stanford.edu) and collaborators at the Center for Turbulence Research at Stanford University [*Ham and Iaccarino*, 2004; *Ham et al.*, 2006]. It is a finite-volume based solver which utilizes a fractional step method for implicit time marching [*Mahesh et al.*, 2004]. The solver works on both structured and unstructured grids, enabling the user to solve a wide variety of problems with different geometries. CDP includes a subgrid scale model (Smagorinsky), but we run the code strictly in Direct Numerical Simulation (DNS) mode, meaning

that there is no allowance for subgrid scale flow features. This means that the specified value of viscosity is simply the molecular viscosity of the fluid, and grids must be small enough to resolve all flow features in the region of interest (see section 3.2.6 for details on grid generation). CDP solves the governing equation system:

$$\frac{\partial u}{\partial t} + u\frac{\partial u}{\partial x} + v\frac{\partial u}{\partial y} + w\frac{\partial u}{\partial z} = -\frac{1}{\rho_o}\frac{\partial p}{\partial x} + \frac{\mu}{\rho_o}\left(\frac{\partial^2}{\partial x^2} + \frac{\partial^2}{\partial y^2} + \frac{\partial^2}{\partial z^2}\right)u \tag{3.5}$$

$$\frac{\partial v}{\partial t} + u\frac{\partial v}{\partial x} + v\frac{\partial v}{\partial y} + w\frac{\partial v}{\partial z} = -\frac{1}{\rho_o}\frac{\partial p}{\partial y} + \frac{\mu}{\rho_o}\left(\frac{\partial^2}{\partial x^2} + \frac{\partial^2}{\partial y^2} + \frac{\partial^2}{\partial z^2}\right)v \tag{3.6}$$

$$\frac{\partial w}{\partial t} + u\frac{\partial w}{\partial x} + v\frac{\partial w}{\partial y} + w\frac{\partial w}{\partial z} = -\frac{1}{\rho_o}\frac{\partial p}{\partial z} + \frac{\mu}{\rho_o}\left(\frac{\partial^2}{\partial x^2} + \frac{\partial^2}{\partial y^2} + \frac{\partial^2}{\partial z^2}\right)w + \frac{\rho}{\rho_o}g \tag{3.7}$$

$$\frac{\partial u}{\partial x} + \frac{\partial v}{\partial y} + \frac{\partial w}{\partial z} = 0 \tag{3.8}$$

$$\frac{\partial \rho}{\partial t} + u\frac{\partial \rho}{\partial x} + v\frac{\partial \rho}{\partial y} + w\frac{\partial \rho}{\partial z} = D\left(\frac{\partial^2}{\partial x^2} + \frac{\partial^2}{\partial y^2} + \frac{\partial^2}{\partial z^2}\right)\rho \tag{3.9}$$

The boundary conditions depend on the particular geometry being solved and are discussed later. Equations 3.5-3.7 are the Navier-Stokes equations written in the Boussinesq approximation, Eq.n 3.8 is the continuity equation, and Eq. 3.9 is the density advection-diffusion equation. The density of the fluid is ρ, and ρ_o is a reference density, taken to be 1 g/cm^3. For the dynamic viscosity μ, we use the value for water at 20° C, μ = 0.01 g·cm^{-1}s^{-1}. (For comparison purposes with laboratory experiments later, the temperature in the lab is between 20-22° C, which results in variations in viscosity of less than 4% from the value used in numerical simulations.) The density diffusion coefficient D, taken to be 10^{-5} cm^{2}s^{-1} (the approximate salt diffusivity in

water) for all simulations discussed in this study, is so small as to make the diffusion timescale many orders of magnitude longer than a typical simulation (see Section 3.1.1.1 for a more complete discussion of diffusion time scales).

Variables are stored on a collocated grid, with velocity components u_i and pressure p stored at control volume centers and face-normal velocities U_f stored at faces between adjacent control volumes. All physical quantities of interest are therefore computed in the centers of the control volumes, but the values of pressure and velocity are staggered in time, hence the so-called fractional step method where velocities are determined at integer time steps and pressures are determined between the integer time steps.

For initial conditions at time step n given by u_i, p, and U_f, the velocities and pressure at time $n+1$ are computed using the following: (1) Use the Adams-Bashforth second order method to predict the face-normal velocities at $n+1$

$$U_f^{n+1} = 2U_f^n - U_f^{n-1}, \tag{3.10}$$

(2) Solve the momentum equation for the intermediate velocity $\hat{u}_{i,p}$ corresponding to each cell p

$$\frac{\hat{u}_{i,p} - u_{i,p}^n}{\Delta t} + \frac{1}{2}(\hat{H}_{i,p} + H_{i,p}^n) = -\frac{\partial p}{\partial x_i}\bigg|_p^{n-1/2}, \tag{3.11}$$

where the index i runs over the three spatial dimensions, n is the time step index, and H_i is the discretization of the convective and viscous terms, given by:

$$H_i = \sum_f U_f^{n+1/2} \left(\frac{u_{i,p}^{n+1/2} + u_{i,nb}^{n+1/2}}{2} \right) A_f \tag{3.12}$$

where the sum is over the faces surrounding each control volume, A_f is the surface area of each face, and the subscript nb denotes a value from a neighboring control volume. Note that the intermediate velocity and convective and viscous operator are solved implicity while the pressure term is solved explicity. This step is an approximate guess of the new velocity using the previous pressure field.

(3) The old pressure gradient is removed to obtain u_i^*:

$$\frac{u_{i,p}^* - \hat{u}_{i,p}}{\Delta t} = \left.\frac{\partial p}{\partial x_i}\right|_p^{n-1/2}, \tag{3.13}$$

This results in an approximate velocity field computed using all the terms in the Navier-Stokes equation except for the updated pressure term, which has not yet been computed.

(4) The u_i^*, which are located at the control volume centers, are interpolated to the faces between control volumes:

$$U_f^* = \frac{1}{2}(u_{i,p}^* + u_{i,nb}^*)n_{i,f}, \tag{3.14}$$

where $u_{i,nb}^*$ is the velocity at the center of the control volume that control volume p shares face f with, and $n_{i,f}$ is the boundary unit normal pointing toward the neighboring control volume nb.

(5) Pressure $p^{n+1/2}$ is obtained at the midpoint of the current timestep using:

$$\sum_f \frac{U_f^{n+1} - U_f^*}{\Delta t} A_f = -\sum_f \left.\frac{\partial p}{\partial n}\right|_f^{n+1/2} A_f, \tag{3.15}$$

This is why the current method is called a fractional step scheme; the pressure and velocity fields are not obtained simulatanously, but in a leapfrogging

pattern in time.

(6) The previous approximate velocity is then corrected using the new pressure field:

$$\frac{u_{i,p}^{n+1} - u_{i,p}^{*}}{\Delta t} = -\frac{\partial p}{\partial x_i}\bigg|_{p}^{n+1/2}, \tag{3.16}$$

3.2.2 Configuring CDP on Lonestar

Most of the following is applicable to running CDP on a desktop computer with a single CPU, but we focus on implementation of the code on the Lonestar Cluster at the Texas Advanced Computing Center (TACC), as most of the problems studies here are too complex to be solved on a PC. The Lonestar cluster consists of 5840 processors grouped into nodes of 4 cpus, with InfiniBand interconnects. Peak performance of the cluster is 62 TeraFLOPS (62×10^{12} floating point operations per second). All details given below apply directly to running on Lonestar, but most of the instructions would apply to other clusters at TACC (i.e. the 62,976 cpu Ranger cluster), or clusters elsewhere, as long as the appropriate libraries are installed. The only libraries that are crucial to the operation of CDP are HYPRE (a library for inversion of large matrices), blas (a linear algebra package), and an MPI package, which provides a structure for the processors to communicate with one another during the computation.

The primary way to interact with the CDP solver is through the use of 'hooks' files, which customize the solver to each specific problem. The user must provide a grid corresponding to the physical geometry of the system, as

well as two input files which specify initial conditions, boundary conditions, output options, and solver parameters. The steps for configuring, compiling, and executing a simulation on the Lonestar cluster are contained in the following subsections.

msh2cdp preprocessor

All grid file formats are basically lists of grid nodes and connectivity lists that tell the processor which nodes are connected to which other nodes. This enables the solver to identify faces, and by extension, control volumes. The msh2cdp preprocessor is part of the CDP software package and converts a grid file in .cas format to an input file readable by CDP (.cdp format). The input file for the preprocessor is called msh2.cdp.in. An example is given below:

```
# the input msh file
MSH = sample_grid.cas

# Initialize periodic boundary conditions
front-7 = periodic_front-7
periodic_front-7.DY -10.0
back-9 = periodic_back-9
periodic_back-9.DY 10.0
```

The first command tells the preprocessor the name of the input grid to use. The remaining commands let the user specify periodic boundary conditions, if desired. In this example, front-7 and back-9 are the names of the left and right boundaries of the sample domain contained in sample_grid.cas. The names of the boundaries are assigned during creation of the grid in the grid generation software, which is discussed in more detail in Section 3.2.6. To enforce the periodic boundary conditions, they are renamed 'periodic_front-7' and 'periodic_back-9,' respectively. The next commands tell the solver how to connect the periodic boundaries to each other. If a fluid parcel moves out of the domain through periodic_back-9, it re-enters the domain through periodic_front-7, which in this example, is 10.0 units in the positive y-direction. In this way, the user specifies all periodic boundary conditions and their connectivity.

The preprocessor is compiled and run using:

```
bsub -I -q development -n 1 -W 0:10 ibrun ../cdp2.4/src/
    msh2cdp/msh2cdp
```

'bsub -I' submits the job. '-q development' requests an allocation in the development queue on Lonestar, which is designed for debugging and small tasks, such as preconditioning the compuational grid, as in our case. '-n 1' specifies that the job is to run on a single processor. This is a requirement for the msh2cdp preprocessor as this code is not parallelized. The maximum number of processors that can be requested in the development queue on Lonestar is

currently 16. '-W 0:10' requests ten minutes of wall clock time. The maximum amount that can be requested in the development queue is 15 minutes. However, most of the grids used in this dissertation require substantially less wall clock time. 'ibrun ../cdp2.4/src/msh2cdp/msh2cdp' gives the path of the msh2cdp executable relative to the current working directory. When cdp2.4 is unzipped and installed, the default path is '/cdp2.4/src/msh2cdp/msh2cdp.'

Executing msh2cdp produces an output file called 'result.cdp,' which needs to be renamed to 'restart.cdp.' For CDP to run, it must be able to find a restart.cdp file containing grid information in its running directory. Since boundary conditions are specified in the preprocessor, if the user wishes to run an identical domain with and without periodic boundary conditions, he must create two separate restart.cdp files.

Initialization files

Two input files need to be modified before CDP can be compiled and executed. Examples of input files will be given for the physical case of a sinusoidally oscillating flow in the x (left-right) direction. This is relevant to the tidal forcing studies discussed in Chapters 3 and 4. The first input file is 'cdp_if2.in':

```
# fluid properties...
FLUID.NU = 0.01


# solver controls...
```

```
DT = 0.01
NSTEPS = 4900

ADD_SCALAR Z
Z.DIFF = 0.00000001

# boundary conditions...
bottom-4 = SLIP
top-8 = SLIP
left-5 = HOOK
right-6 = HOOK

# statistics...
STATS = U P
RESET_STATS = .TRUE.

# output...
WRITE_STEP TECPLOT sample_output 100 ALL U P
```

The first command defines the viscosity. When simulation units are taken to be cgs, as is convenient for most of the numerical studies here, the units of viscosity are centipoise (cP). The following lines define the time step 'DT' and the number of steps 'NSTEPS' desired. 'ADD_SCALAR Z' adds the passive tracer that cdp uses to determine the fluid density. This is equivalent to

adding a stratifying agent in the experimental system. The molecular diffusivity 'Z_DIFF' of the stratifying agent is set very small so that diffusion does not have time to act significantly on the time scale of a simulation. (This is also the case in the laboratory setup.) Next, boundary conditions not addressed in the msh2cdp preprocessor are set. In this case, 'SLIP' makes the boundaries into free slip boundaries. The user can also specify 'WALL' to satisfy a no-slip condition at the boundaries, or 'HOOK' to tell CDP to see the other input file, discussed below, for a more general specification of the boundary condition. The '# statistics' section establishes output statistics and does not need to be changed. The final command specifies the desired output. 'sample_output' is the prefix that will appear in front of the output files, which are numbered based on time step and processor number. '100' tells CDP to output the desired variables every 100 time steps. 'ALL' outputs the variable at every control volume. Alternatively, the user can specify a certain plane on which to output data by entering 6 numbers in a sequence which contains the three coordinates of a point on the plane followed by three coordinates describing a unit vector normal to the plane. 'U P' tells cdp to output both the velocity and pressure variables.

The second input file 'cdp_if2_hooks.f90' specifies custom boundary and initial conditions and allows the user to add terms to the right hand side of the Navier Stokes equations. In this study, this powerful feature has been utilized to add buoyancy effects, Coriolis corrections, Rayleigh damping, and body forcing terms. An example of one of the hooks files is broken into its

relevant subroutines and explained below:

```
 subroutine initial_hook(if2)
   if (myrank == 0) &
     write(*,*) 'initial_hook...'
   if (if2%step == 0) then
5    if (myrank == 0) &
       write(*,*) 'initial_hook: setting initial condition...'
     gp => if2%gp
     salt => get_r1('Z',gp)
     do ino = 1,gp%nno_ib
10     x = gp%node_cc(1,ino)
       y = gp%node_cc(2,ino)
       z = gp%node_cc(3,ino)
       if2%u(1,ino) = 0.0_WP
       if2%u(2,ino) = 0.0_WP
15     if2%u(3,ino) = 0.0_WP
       salt(ino) = 1.1035_WP - 0.0023_WP*z
     end do
   end if
 end subroutine initial_hook
```

This subroutine specifies the initial conditions of the simulation. Lines 13-15 determine the initial velocity distribution, which can be functions of the

spatial coordinates x, y, and z. 'salt' is the name of the passive tracer that determines the density of the fluid. Line 16 defines the density stratification, which in this example is a linear function of depth (z).

```
 subroutine scalar_bc_hook(phi_bc,bc_type,scalar,zone,if2)
   if (zone%name == 'left-5') then
     if (scalar%name == 'Z') then
        gp => if2%gp
5       do i = 1,zone%n_nodelist
           ino = zone%nodelist(i)
           y = gp%node_cc(2,ino)
           phi_bc(ino) = 1.1035_WP - 0.0023_WP*z
        end do
10      bc_type = PENALTY_BC
     end if
   else
     if (scalar%name == 'Z') then
        gp => if2%gp
15      do i = 1,zone%n_nodelist
           ino = zone%nodelist(i)
           y = gp%node_cc(2,ino)
           phi_bc(ino) = 1.1035_WP - 0.0023_WP*z
        end do
20      bc_type = PENALTY_BC
```

```
      end if
    end if
  end subroutine scalar_bc_hook
```

The 'scalar_bc_hook subroutine specifies the value of the density (or any other scalar quantity the user has defined) at any boundary that the user specified as a 'HOOK' boundary in the 'cdp_if2.in' file. In this example, the density is specified at both the left and right boundaries.

```
  subroutine momentum_bc_hook(u_bc,bc_type,zone,if2)
    if (zone%name == 'left-5') then
      gp => if2%gp
      do i = 1,zone%n_nodelist
5       ino = zone%nodelist(i)
        u_bc(1,ino) = 0.4275_WP*sin(omega*if2%time)
        u_bc(2,ino) = 0.0_WP
        u_bc(3,ino) = 0.0_WP
      end do
10    bc_type = INJECT_BC
    else
      gp => if2%gp
      do i = 1,zone%n_nodelist
        ino = zone%nodelist(i)
15      u_bc(1,ino) = 0.4275_WP*sin(omega*if2%time)
```

```
      u_bc(2,ino) = 0.0_WP
      u_bc(3,ino) = 0.0_WP
    end do
    bc_type = INJECT_BC
20 end if
 end subroutine momentum_bc_hook

 subroutine momentum_source_hook(Au,bu,if2)
   ! ------------------------------------------------------
   ! modify the momentum system with a source if needed:
   ! [Au]{u} = {bu}
5  ! ------------------------------------------------------
   if (myrank == 0) &
     write(*,*) 'applying Boussinesq gravity term to RHS...'
   gp => if2%gp
   salt => get_r1('Z',gp)
10 do ino = 1,gp%nno_ib
     y = gp%node_cc(2,ino)
     drho = salt(ino) - (1.1035_WP - 0.0023_WP*y)
     bu(2,ino) = bu(2,ino) - 980.0_WP*drho*gp%no_local_volume(ino)
   end do
 end subroutine momentum_source_hook
```

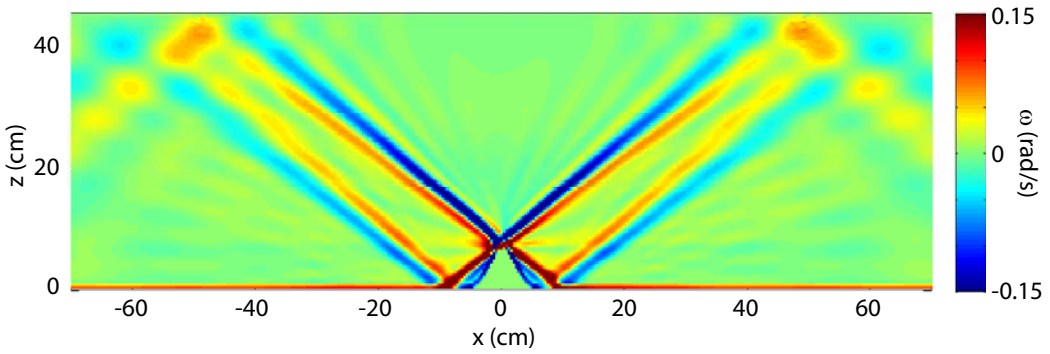

Figure 3.1: Vorticity field from a sample 2D computation in which an oscillating tidal flow is forced over a Guassian ridge (bottom center). The internal waves radiate away as beams toward the upper left and right.

3.2.3 Internal wave generation in CDP

There are four methods used in this study to generate internal waves in the numerical simulations. They are described briefly below and code excerpts from the hooks file for each case follow.

(1) The simplest way to generate internal waves is to force an oscillatory flow back and forth over bottom topography, as is discussed in Chapters 3 and 4. Flow at the left and right boundaries is vertically uniform:

$$u(x = 0, L, t) = A \sin(\omega t) \tag{3.17}$$

where L is the width of the domain. An example of implementing the oscillatory flow at the left and right boundaries is in the subroutine 'momentum_bc_hook' displayed above.

(2) Internal wave beams can be generated using suitably chosen (divergence-

free) body forcing terms. We use (private communication with CH Jiang):

$$\vec{F}(x,z) = \nabla \times \nabla \times \Phi \hat{z} \tag{3.18}$$

$$\Phi(x,z) = Aexp\left(\frac{-(x-x_o)^2}{2\sigma_x^2}\right) exp\left(\frac{-(z-z_o)^2}{2\sigma_z^2}\right) \tag{3.19}$$

where x is the horizontal direction and z the vertical. This 'wavemaker' has the advantage that, rather than generating four internal wave beams of equal strength, as are generated in the case of an oscillating object [*Mowbray and Rarity*, 1967], and for an oscillating flow past a ridge (Figure 3.1), two of the four generated beams are very weak, resulting in fewer unwanted internal waves in the computational domain. Figure 3.2 shows the resulting body forcing vectors.

Figure 3.3 shows this wavemaker in a stratified system with constant buoyancy frequency N. An example of implementation is given below:

```
amp = 0.7_WP
omega = 0.843_WP
s1 = 1.0_WP
s2 = 2.0_WP
x0 = 150.0_WP
z0 = 63.6_WP
theta = -78*3.1415926_WP/180
a = cos(theta)
b = sin(theta)
```

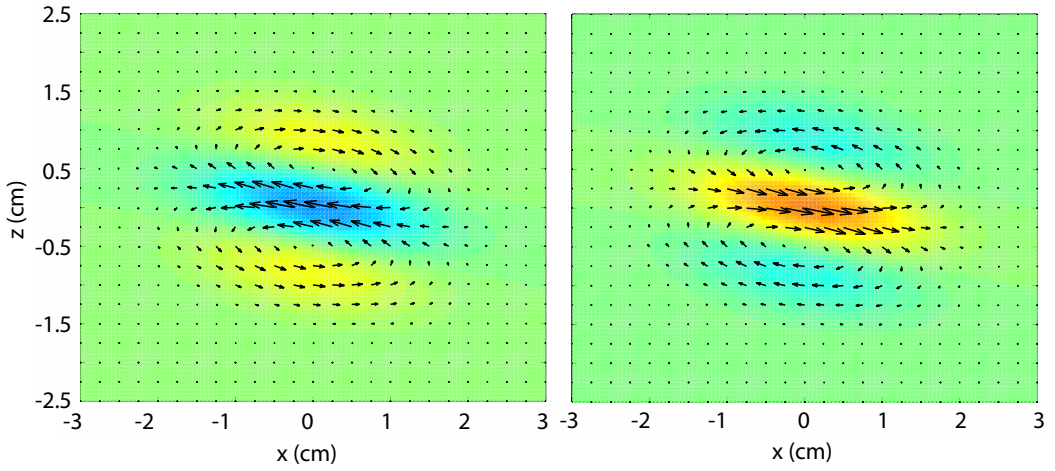

Figure 3.2: The body forcing wavemaker discussed above. The vector fields represent the body forcing term at two different phases: 0° and 180°. Color denotes the horizontal component of the body forcing term. The vectors oscillate back and forth with the forcing frequency. The entire beam wavemaker is tilted 78° with respect to the vertical (This wavemaker angle is used in Section 6.4.2). Since velocity is in the direction of the wave vector, which is also the wave propagation direction, this wavemaker would generate wave beams propagating up and to the left, and down and to the right.

```
10 do ino = 1,gp%nno_ib
     x = gp%node_cc(1,ino)
     z = gp%node_cc(3,ino)
       u1 = amp*((((x-x0)*a-(z-z0)*b)*((x-x0)*b+(z-z0)*a))&
         /(s1**2*s2**2*exp(((x-x0)*a-(z-z0)*b)**2/(2*s1**2))&
15       *exp(((x-x0)*b+(z-z0)*a)**2/(2*s2**2))))
       w1 = amp*(1/(s1**2*exp(((x-x0)*a-(z-z0)*b)**2/(2*s1**2))&
         *exp(((x-x0)*b+(z-z0)*a)**2/(2*s2**2))) - ((x-x0)&
         *a-(z-z0)*b)**2/(s1**4*exp(((x-x0)*a-(z-z0)*b)**2&
         /(2*s1**2))*exp(((x-x0)*b+(z-z0)*a)**2/(2*s2**2))))
20   uprime = u1*cos(-theta) - w1*sin(-theta)
     wprime = u1*sin(-theta) + w1*cos(-theta)
     bu(1,ino) = bu(1,ino) + uprime*sin(omega*if2%time)&
     *gp%no_local_volume(ino)
     bu(3,ino) = bu(3,ino) + wprime*sin(omega*if2%time)&
     *gp%no_local_volume(ino)
   end do
```

In this example, 's1' and 's2' represent σ_x and σ_z, respectively. These variables determine the length scale of the wavemaker along and perpendicular to the wave beam. 'x0' and 'z0' are the coordinates of the center of the wavemaker, and 'theta' gives the angle of the generated wave beam with respect to the vertical. Lines 20-21 rotate the spatial coordinates to coincide with angle 'theta,' and lines 22-23 rotate the resulting body force term accordingly. In lines 22-23,

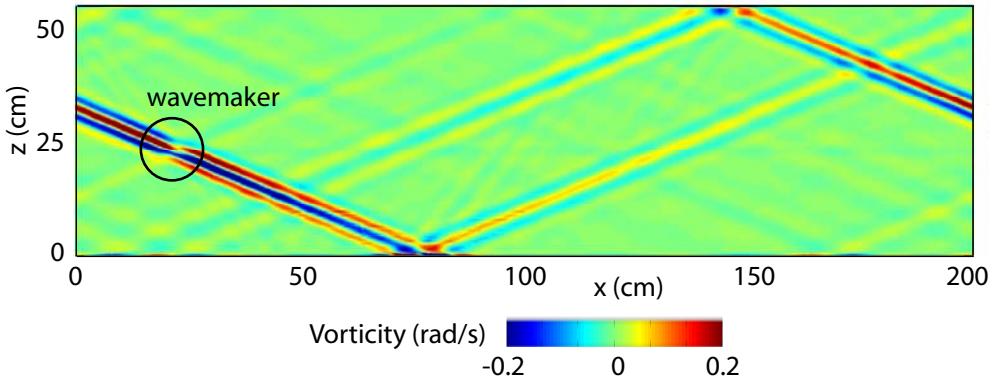

Figure 3.3: A snapshot of vorticity showing the internal wave field produced by the wavemaker (enclosed by black circle) pictured in Figure 3.2. The primary wave beams propagate down and to the right, and up and to the left. The left and right boundaries are periodic, so wave beams wrap around the domain.

note that it is important in general to multiply any additional body forcing term by the volume of each control volume the body forcing term is being applied to. In CDP, the volume of element 'ino' is 'gp%no_local_volume(ino).'

(3) Similar internal wave beams can be generated by using physical forcing at one of the boundaries to mimic the laboratory wavemaker developed by [*Gostiaux and Dauxois*, 2007]. A vertically-propagating sinusoidal wave is enforced at the desired boundary:

$$u(x = 0, z, t) = A \sin(m(z - z_o) - \omega t) \tag{3.20}$$

where $u(x = 0, z, t)$ is the x-velocity at the boundary, A the desired velocity amplitude, m the vertical component of the wavenumber, and ω the frequency. In this example, the phase velocity is traveling upward. Recall from chapter 1 that if the vertical component of he phase velocity is positive, the vertical

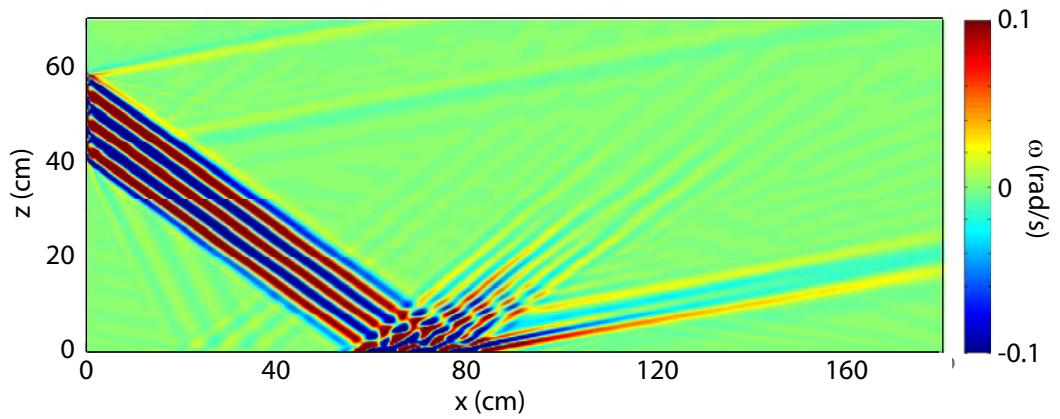

Figure 3.4: An example of a physical wavemaker implemented at the left boundary (Color denotes vorticity $\omega = \nabla \mathbf{u}$). An arbitrary number of wavelengths can be generated. In this example, the gravity vector has been rotated 12° clockwise to show the effects of internal wave reflection from a sloping bottom.

component of the group velocity, and hence wave propagation direction, must be negative, and vice versa. Therefore if the above boundary forcing was used on the left boundary, the internal wave would propagate down and to the right. Conversely, if the above forcing was used on the right boundary ($x = L$), the internal wave would propagate up and to the left. Unlike the previous body-forcing wavemaker, this wavemaker allows the user to excite internal wave beams with an arbitrary number of wavelengths. An example is shown in Figure 3.4, which shows an internal wave with three wavelengths generated at the left boundary and reflecting from the domain bottom.

Note that this boundary forcing is localized on the z-axis to include an integer number of wave periods. This is necessary for mass to be conserved in the computational domain. Failure to restrict this forcing accordingly causes

the code to diverge.

An example of implementing this code is given below. The following excerpt is added to the subroutine 'momentum_bc_hook':

```
omega = 0.628_WP
if (zone%name == 'left-5') then
   gp => if2%gp
   do i = 1,zone%n_nodelist
     ino = zone%nodelist(i)
     y = gp%node_cc(2,ino)
     if (y >= 40 .AND. y <= 58) then
        u_bc(1,ino) = 0.25_WP*sin(1.0472_WP*(y-40.0_WP)&
        -omega*if2%time)
     else
       u_bc(1,ino) = 0.0_WP
     end if
     u_bc(2,ino) = 0.0_WP
     u_bc(3,ino) = 0.0_WP
   end do
   bc_type = INJECT_BC
 end if
```

The above parameters were used to produce the wave field in Figure 3.4.

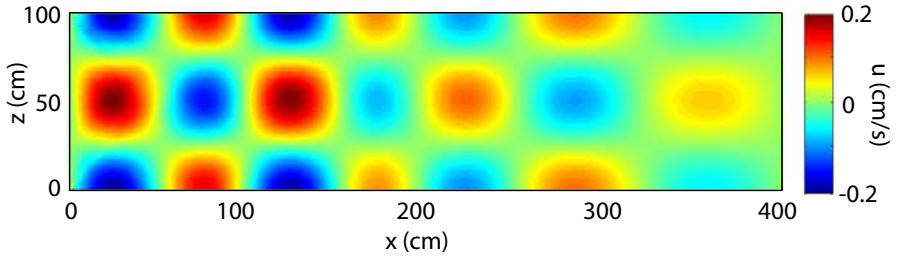

Figure 3.5: A mode 3 internal wave generated by horizontal forcing at the left boundary. Color denotes horizontal velocity. This snapshot was taken wave periods after the forcing began.

(4) Boundary forcing similar to that in (3) above can be used to generate vertical modes as well. Instead of localizing the forcing in the z-direction, the standing wave is enforced along the entire z-axis:

$$u(x = 0, z, t) = A \sin\left(\frac{2\pi n}{H}\right) \sin(\omega t) \tag{3.21}$$

where n is the number of the vertical mode desired, and H is the height of the domain. The wavelengths are constrained such that an integer number of wavelengths fits along the z-axis. An example showing a mode 3 wave generated using this technique is shown in Fig. 3.5.

3.2.3.1 Rayleigh damping

When internal waves are generated and allowed to propagate through the computational domain, it is often necessary, especially in 2D, to intro-

duce damping near boundaries to reduce unwanted internal wave reflections. Rayleigh damping is performed by adding a negative term to the momentum equations which depends linearly on the fluid velocity. In the following example, which is from simulations in Chapter 6, the damping is only in the x-direction, and serves to damp out the predominantly horizontal internal wave motion near the left and right boundaries $x = 0$ and $x = 400$. The following code is embedded within the control volume loop in the 'momentum_source_hook' subroutine in 'cdp_if2_hooks.f90':

```
if (x > 320) then
   bu(1,ino) = bu(1,ino) - 0.005_WP*(tanh(0.1_WP*(x-360.0_WP))&
   +1.0_WP)*if2%u(1,ino)*gp%no_local_volume(ino)
end if
if (x < 80) then
   bu(1,ino) = bu(1,ino) - 0.005_WP*(tanh(-0.1*(x-40.0_WP))&
   +1.0_WP)*if2%u(1,ino)*gp%no_local_volume(ino)
end if
```

The damping consists of a negative x-dependent coefficient multiplying the x-component of the velocity within a predefined distance from the boundaries. As is required for momentum sources, the damping terms are multiplied by the volume of each control volume ('gp%no_local_volume(ino)'), so that the force each fluid parcel experiences is proportional to its mass. The 'tanh' function is ideal for the damping coefficient for two reasons: (1) The increase in

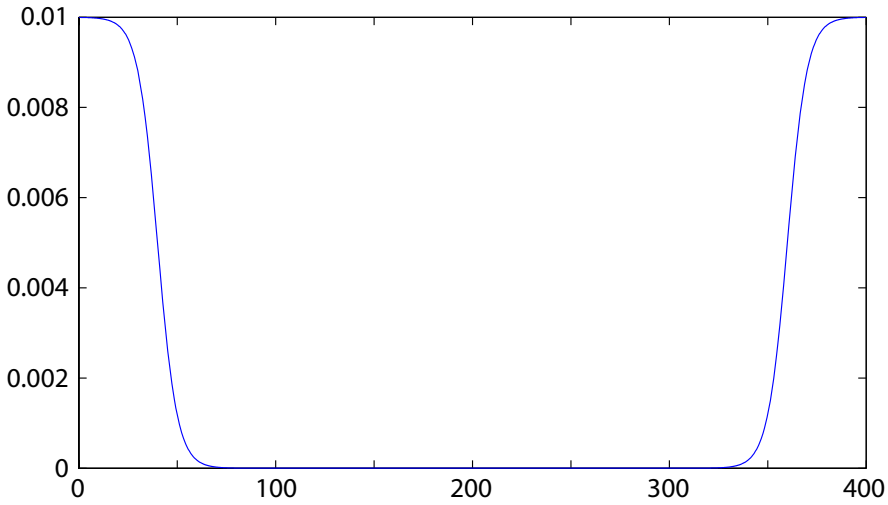

Figure 3.6: Rayleigh dampign coefficient as a function of x. The large damping at the left and right boundaries attenuates internal waves at the edges of the domain, preventing unwanted reflected internal wave beams from reentering the region of interest.

damping strength can be controlled so that the damping function takes several wavelengths to reach its maximum. If an incident internal wave encounters strong damping without a gradual transition, the internal wave can reflect from the damped region. (2) This function reaches is constant after reaching its maximum value, giving precise control of the spatial scale over which the damping takes place. Figure 3.6 shows the damping coefficient as a function of x for a domain defined between 0 and 400 cm.

3.2.4 Executing CDP

Typing 'make' at the Lonestar command prompt runs Makefile, which reads the initialization files and restart.cdp and creates the executable 'cdp_if2.'

Typically, a job script (named 'job_script' in this example) is used to specify the desired parameters for running the executable.

```
#!/bin/tcsh          # first line specifies shell
#BSUB -J job_name    #name the job
#BSUB -o out.o%J      #output->   out.o&ltjobID>
#BSUB -e err.o%J      #error -> error.o&ltjobID>
#BSUB -n 64 -W 6:00     #64 CPUs and 6 hours max runtime
#BSUB -q normal         #Use normal queue.
set echo                #Echo all commands.
cd $LS_SUBCWD           #cd to directory of submission
ibrun ./cdp_if2         #use ibrun for "pam -g 1 mvapich_wrapper"
```

The job script is submitted using:

```
bsub < job_script
```

CDP outputs diagnostics that assist the user in determining whether the simulation was successful. The most useful diagnostics are the residuals from the solution of the pressure Poisson equation (Equation 3.15). CDP uses an iterative scheme to solve the Poisson equation at every time step, with the error being reduced at every step of the iterative solver. The pressure Poisson system is a system of linear equations of the form:

$$\mathbf{A}\mathbf{x} = \mathbf{b} \tag{3.22}$$

where $\mathbf{x}$ is the exact solution for the pressure field. Since numerical analysis yields an approximate pressure field $\mathbf{x}'$, where $\mathbf{A}\mathbf{x}' = \mathbf{b}'$, it is important to define a method for quantifying the difference between the exact and approximate pressure fields $(\mathbf{x} - \mathbf{x}')$. The exact solution $\mathbf{x}$ is not known, so the exact error $\mathbf{x} - \mathbf{x}'$ is also unknown, but the *residual*, defined as $\mathbf{b} - \mathbf{b}' = \mathbf{b} - \mathbf{A}\mathbf{x}'$, or the difference in the right hand sides of the equations with the exact and approximate solutions [*Moin*, 2001], can be easily computed. The relative residual is the residual normalized by the right hand side of the equation ($\mathbf{b}$), so that:

$$R = \frac{\mathbf{b} - \mathbf{A}\mathbf{x}'}{\mathbf{b}} \tag{3.23}$$

By default, CDP iterates over the pressure Poisson equation at each time step intil the relative residual drops below 10^{-5}. The default maximum number of iteractions is 20. Typically, if the relative residual is not below 10^{-5} within 20 iterations, the solution will not converge and numerical results cannot be trusted. The most common cause of this lack of convergence is the time step being too large. In many cases, a reduced time step corrects the problem. The other commonly encountered problem which causes convergence not to be reached is a discrepancy in the forcing mechanism. Usually this occurs when an error is made in the boundary forcing (discussed in Section 3.2.3), the most common being when an error in one of the boundary forcing terms causes mass conservation to be violated. Since the pressure Poisson equation enforces the continuity equation, and hence mass conservation, a lack of mass conservation will necessarily cause problems with the pressure Poisson system.

3.2.5 Data Analysis

Each processor used in the computation creates its own output file at the interval in time specified by the user in 'cdp_if2.in.' Output files have the format sample_output.xxxxxx.xxx.dat, where the first 6-digit number is the step number (up to 999,999 can be output without modifying the code) and the 3-digit number is the processor number (up tp 999 processors). To change the number of digits output, changes must be made to the 'dump_flagged_tecplot' subroutine in the file '/cdp2.4/src/cdp/gp_io_m.F90.'

To analyze the data, all output files must be downloaded to a local machine with Matlab. The Matlab script 'read_raw_data2.mat' reads all raw data files in a user-specified folder and saves the data into a single mat file for further analysis. For visualization, the data are interpolated to various surfaces, as shown in Chapters 3 and 4.

An important component of the results discussed in the following two chapters is the direct comparison between numerical simulations and laboratory experiments. Since simulation flow fields are obtained in the tidal reference frame, and experimental flow fields are obtained in the topographic reference frame, a reference frame transformation must be made to compare numerical and experimental results. As the tidal flow is oscillating, the reference frame transformation is non-Galilean. In general, non-Galilean transformations have complex effects on dynamical quantities, but simply comparing kinematic quantities such as velocity between accelerated reference frames is straightforward. The background tidal flow is simply subtracted from the

velocity fields obtained from numerical simulations, which enables a direct comparison with experiments.

3.2.6 Computational Grids

One of the most challenging aspects of numerical computations is the creation of suitable grids on which to solve the governing equations. Velocities and pressures are solved for in the center of every control volume, so control volumes must be very dense in regions where the flow is expected to have very small features (such as boundary layers or regions where wave breaking or turbulence might occur). It is better to err on the side of too much resolution than too little. However, numerical simulations can still be quite costly, so grids need to be created which offer sufficient spatial resolution where required without being wasteful. There are several consequences that arise from higher resolution, the simplest being rapidly increasing processing time. In the simulations discussed here, which are mostly 3D, compuational time increases as resolution to the 4th power. This is because doubling the number of control volumes (CVs) along a linear dimension results in a factor of 8 increase in the total number of CVs. In addition, decreasing the size of the smallest CV normally necessitates a corresponding decrease in the time step, resulting in another power of 2 (To simulate a given interval in time now takes twice as long). So every successive increase of resolution by a factor of 2 results in an increase by a factor of 16 in computational time. This is why efficiency is so important in creating a computational grid.

Another often overlooked complication is that processing of output data becomes more cumbersome, especially if velocity vectors are output at every CV in the domain, as is sometimes necessary. The burgeoning output files quickly reach file size limits, especially on 32-bit computers. If simulations are being run to obtain a very specific result, one can often reduce file sizes by only outputting a subset of the data, or by outputting statistical quantities. However, to examine other quantities, the simulation must be run again with different output options.

Pointwise Gridgen (www.pointwise.com) was used to create all computational grids. This software allows for the creation of both structured and unstructured grids, and gives the user fine control over the control volume density at different locations within the domain. Grid files are output in cas format, which is compatible with the 'msh2cdp' preprocessor. Boundaries are also assigned names, which are also recognized by the preprocessor. Brief descriptions of the computational domains uused to obtain the results in Chapters 4 and 5 follow.

Half Sphere

Figure 3.7 shows the computational grid utilized to study tidal flow over a half-sphere (results discussed in Chapter 4). The half-sphere has radius $R = 6.5$ cm and is situated with its center at the origin in a computational domain that is 100 cm long $\times$ 100 cm wide $\times$ 45 cm high. The conical wave propagation region is modeled with a rectangular structured grid rotated about the vertical

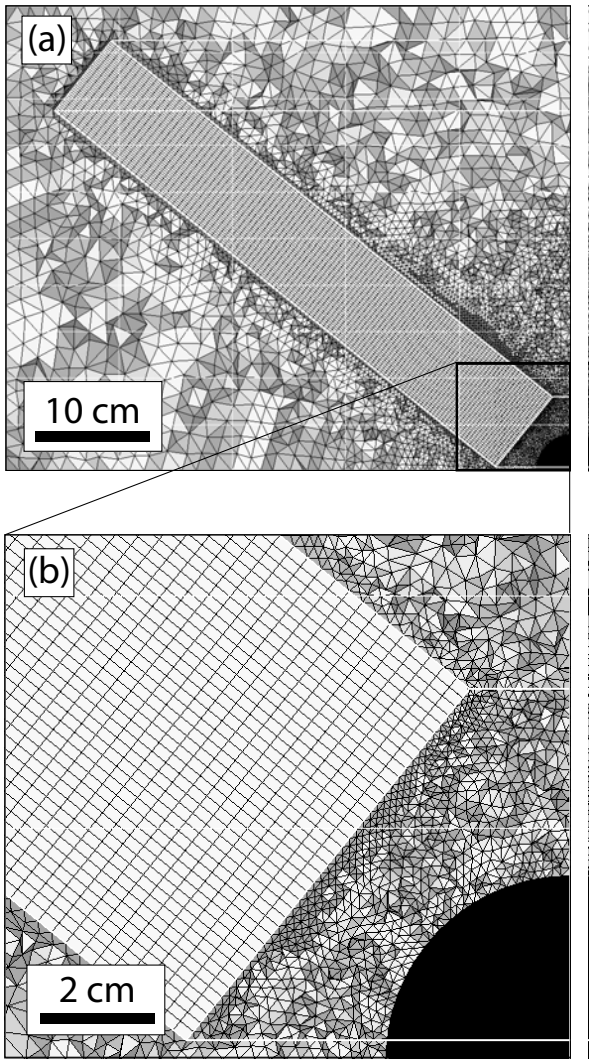

Figure 3.7: A 2D slice through the 3D computational domain for the half-sphere geometry, where the shading corresponds to a 3D rendering of the computational tetrahedra nearest the vertical midplane. (a) A 2D cross section through the vertical midplane $y = 0$. Only the left half of the domain ($x < 0$) is shown; the right half is essentially a reflection about the vertical axis. The entire computational domain is 100 cm long $\times$ 50 cm wide $\times$ 45 cm high. The region with rectangular cells wraps around the vertical axis to create a conical region. (b) A closeup of the region surrounding the half-sphere. Grid size is 0.2 cm near the sphere (radius $R = 3.25$ cm) and increases to 2 cm far from the generation region and wavebeams.

axis, and the generation region surrounding the sphere is modeled with an unstructured tetrahedral grid. The remaining volume, which consists mainly of the background barotropic flow, is also made up of unstructured tetrahedra with a characteristic size of up to 2 cm. The control volumes can be made very large in this region because the flow is uniform and large scale. The structured grid in the wave propagation region enables very fine control over the cross- and along-beam resolution. Since the wavebeam flow velocity varies much more rapidly in the cross-beam direction than in the along-beam direction, we can use different spatial resolutions in the two directions to maximize accuracy and minimize computational time. The unstructured grid in the generation region adapts the grid from the structured beam propagation zone to the curved boundary of the sphere. Despite all flows being laminar, high resolution is needed to accurately capture the flow field, where velocity can change markedly over a distance of a few percent of the sphere radius. the cross-beam resolution is 0.2 cm and the along-beam resolution varies from 0.3 cm near the generation region to 1 cm in the far field. The unstructured grid in the generation region is more difficult to characterize, but there is a typical separation of 0.2 cm between computational nodes. This grid contains roughly 5 million control volumes. This grid was used to generate all results in Chapter 4. A highly refined version of this grid was created to characterize the convergence of the CDP code, and is discussed in Section 3.2.7.

Gaussian Mountain

Figure 3.8 shows part of the computational grid used to study a Gaussian mountain geometry. The full domain is 100 cm long $\times$ 80 cm wide $\times$ 45 cm high. The structured boundary layer region was created by meshing triangular cells with typical separation 0.15 cm on the surface of the Gaussian mountain. These triangular surface cells were then extruded outward normal to the surface. The initial thickness was 0.02 cm and was gradually increased to a surface-normal thickness of roughly 0.2 cm. The structured region in the upper left of Figure 3.8 has a typical grid spacing of 0.5 cm, and is rotated about the vertical to create a cylindrical structured region. All other parts of the domain are structured, with grid apacing increasing to 2 cm far from the Gaussian mountain. A careful convergence study of results obtained using the Gaussian mountain grid was not performed as the grid resolution and flow parameters were nearly identical to those of the half-sphere. The convergence study perfomed on the half-sphere is discussed in Section 3.2.7.

Symmetry considerations

Both the half-sphere and Gaussian geometries are axisymmetric. It is therefore reasonable to expect symmetry in the flow field about the tidal forcing direction. Invoking a symmetry argument and only simulating half of the domain allows all computational grids to be reduced in size by a factor of two, greatly facilitating numerical computations and data analysis. Figure 3.9 shows cross sections of internal wave velocities generated by tidal flow over the

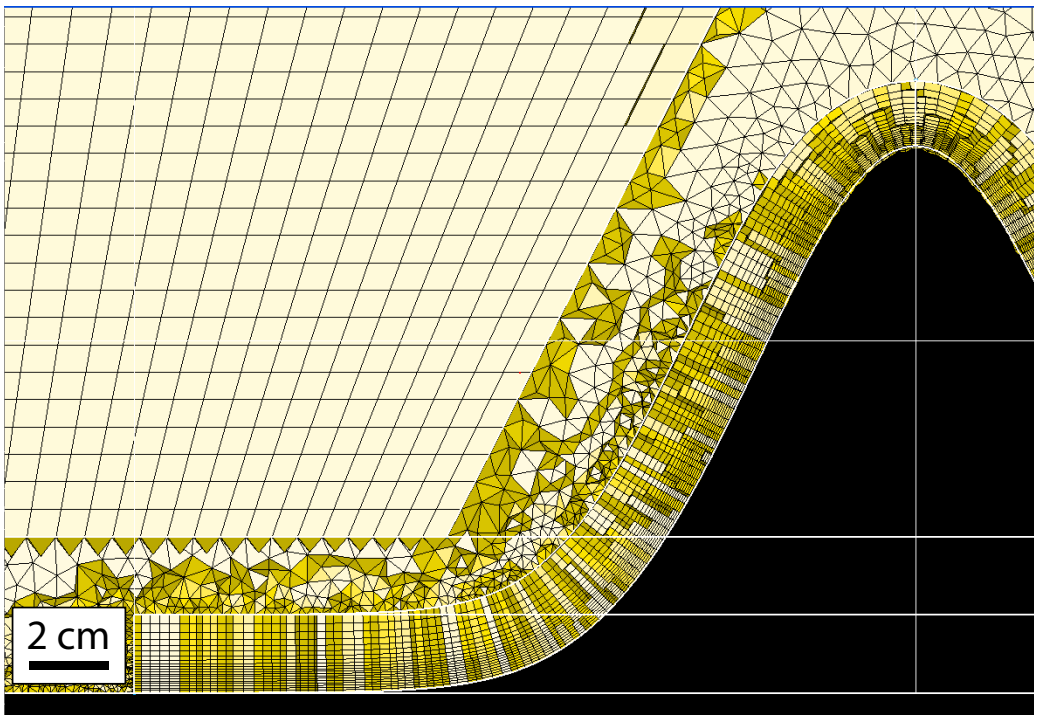

Figure 3.8: A 2D slice through the $y = 0$ vertical midplane of the Gaussian geometry, where the shading corresponds to a 3D rendering of the computational tetrahedra nearest the vertical midplane. The entire domain is 100 cm long $\times$ 80 cm wide $\times$ 45 cm high. The boundary layer is resolved with a high resolution structured grid with minimum surface normal resolution 0.02 cm.

half-sphere at various azimuthal angles measured with respect to the forcing direction. The solid red lines are at the specified azimuthal angles, measured *clockwise* (as viewed from the positive z-axis) from the negative x-axis. For comparison, the blue circles are at the specified azimuthal angles, measured *counterclockwise* from the negative x-axis. The flow fields about the tidal forcing directions are, to within numerical error, mirror reflections of each other, and only considering half of the full domain is a reasonable strategy for decreasing computation time and complexity.

3.2.7 Grid Convergence

CDP has been verified and validated in different contexts [*Mahesh et al.*, 2006; *Shunn and Ham*, 2007]. We validated the code by comparison with experiment (results of direct comparison of simulations and experiments for both the half-sphere and Guassian geometries are presented in Chapters 4 and 5). In addition, we undertook a grid convergence study on the simulations for the case of the half-sphere geometry. Convergence studies are not easy with an unstructured grid, as grid spacing is nonuniform, and simple refinements such as increasing grid resolution everywhere by a given factor are not trivial. Of primary interest is the extent to which the boundary layers were resolved. The thickness of the Stokes boundary layer on the half-sphere is $\delta = \sqrt{2\nu/\omega} \backsimeq 0.15$ cm. To ensure full resolution of this boundary layer, we covered the half-sphere surface with triangles with 0.05 cm characteristic nodal separation instead of the 0.2 cm nodal separation depicted in Figure 3.7. We then extruded the

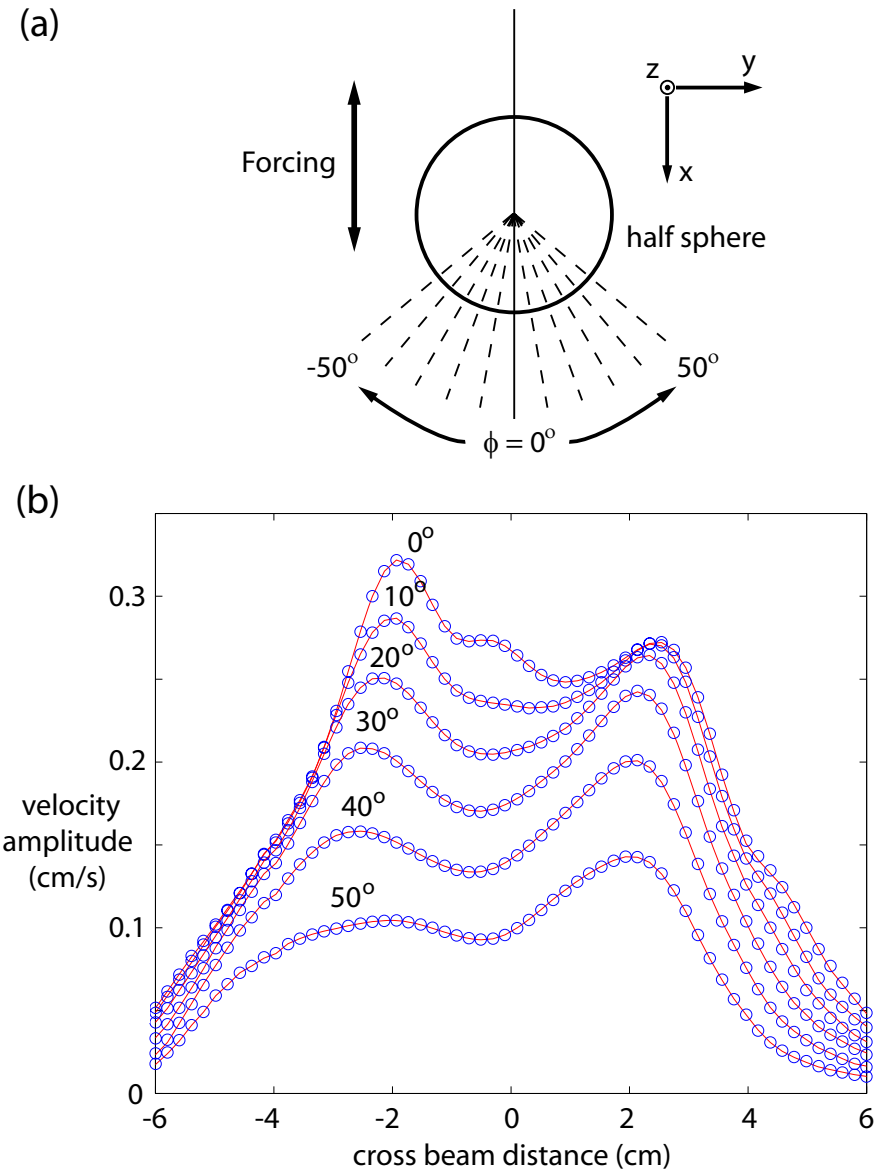

Figure 3.9: (a) A schematic diagram of the half sphere, pictured from above, showing the locations of internal wave cross sections at different azimuthal angles. (b) Internal wave beam cross sections on either side of the tidal forcing direction. The angles labeled are the azimuthal angles measured clockwise (red lines) and counterclockwise (blue circles) from the negative x-axis. Flow is symmetrical about the forcing direction.

0.05 cm mesh outward in the sphere-normal direction at intervals of 0.015 cm, resulting in about 10 control volumes within the Stokes boundary layer. An example of the boundary layer flow computed with this mesh is shown in Fig. 3.11.

Additional grids were generated with the boundary layer resolution getting progressively coarser: the grids had sphere-normal resolutions of 0.015 cm, 0.030 cm, and 0.060 cm (0.5%, 1%, and 2% of R, respectively). Other than the differing resolutions in the sphere boundary layer, the three grids were nearly identical. In particular, the structured grid in the wave propagation region remained unchanged. Simulations were run on all three grids at a relatively high forcing amplitude ($A = 0.4R = 1.3$ cm) at the same frequency used in the rest of this study ($\omega = 0.942$ rad/s). To ensure numerical stability, a time step of $\Delta t = T/2000$ was used for all three simulations, where $T = \frac{2\pi}{\omega}$ is the forcing period.

We use a single scalar quantity to compare between grids, the along-beam velocity amplitude integrated over conical surfaces which encompass the entire internal wave field radiated from the half-sphere. The integrated scalar quantity corresponds to a total material flux amplitude per period associated with the wave motion. For the cases of the three grids, integrating over the velocity amplitude at radial distance $r = 4R$ yields the following results:

$Grid$	$Coarse$	$Medium$	$Fine$
$Value$	92.117	94.214	95.620

Although the integrated velocity amplitude is converging with increased

resolution, the convergence is not rapid enough to be second order in space. This is not surprising, however, since we only refined the grid in the region immediately surrounding the sphere, rather than refining the grid by progressive factors of two at all locations in the domain.

To check the numerical results obtained using the less refined grid shown in Fig. 3.7, we compare cross sections of the internal wave beams in this grid and with the grids with highly refined boundary layers. At forcing amplitude $A/R = 0.4$, near the wave ampitude peaks, the internal wave velocity amplitudes differ by at most 4%. From this we conclude that fully resolving the boundary layer around the sphere is not critical to understand the generated internal waves.

3.2.8 Reynolds number and runtime considerations

An important aspect of numerical simulations is balancing the need for greater spatial and temporal resolution with the constraint of limited computational resources. To produce results which most closely resemble ocean scale flows, it is natural to increase Re as much as possible, but in 3D, small increases in Re can be very costly. For the 3D studies presented in Chapters 4 and 5, Re is varied between 100 and 1000. For the studies of tidal flow past bottom topography, Re is varied by varying the tidal forcing amplitude A, which, for fixed forcing frequency ω, results in maximum velocity $A\omega$. Amplitude was increased as much as possible until the onset of the 'quasi steady' regime was encountered at around $A/\sigma = 1$ [*Garrett and Kunze*, 2007]. Further increases

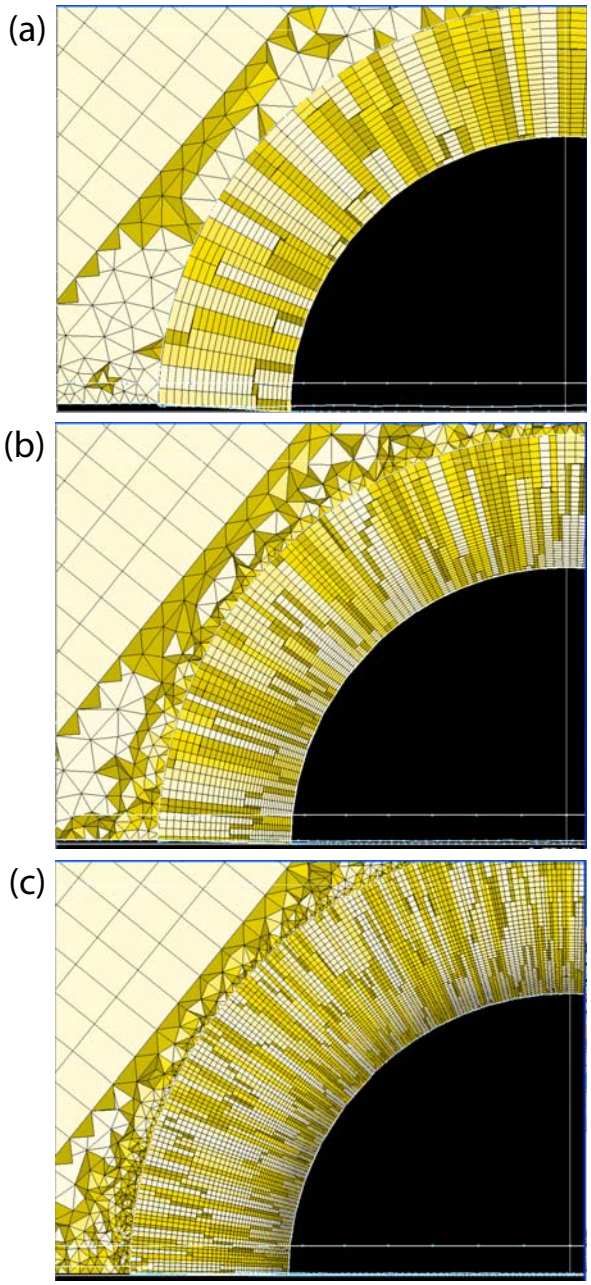

Figure 3.10: The three computational grids used in the convergence study. The surface normal grid spacings are (a) 0.060 cm, (b) 0.030 cm, and (c) 0.015 cm.

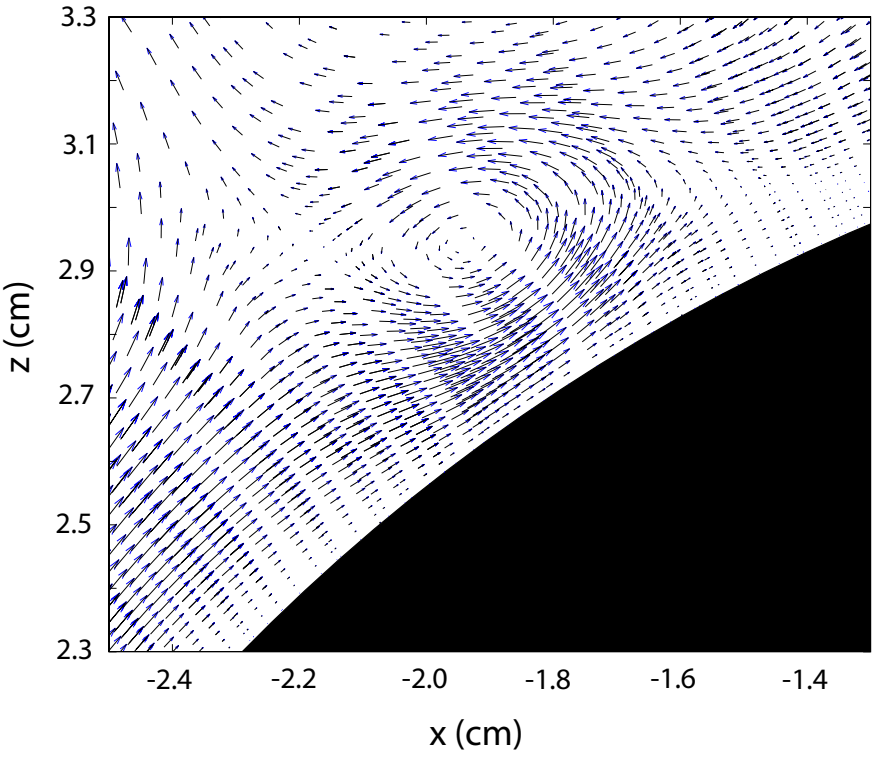

Figure 3.11: Instantaneous velocity field in the $y = 0$ plane, when the sphere was at its right-most position at zero velocity. There are about 10 vectors in the boundary layer; the grid used in computing this flow is shown in Fig. 3.10c. The vortex is a short-lived structure that forms when the flow in the generation region changes direction. The vectors are not regularly spaced since the data have not been interpolated to a regular grid.

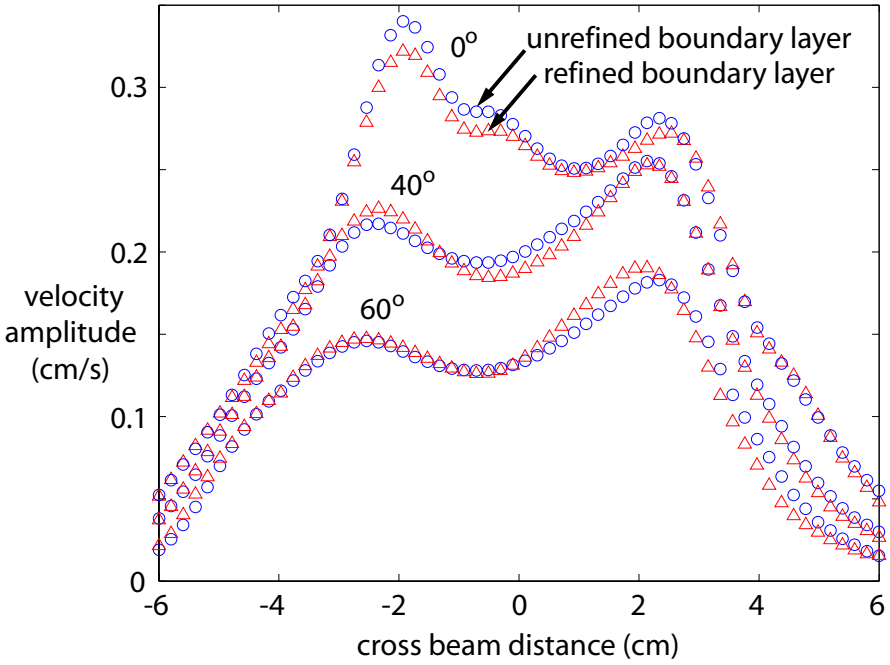

Figure 3.12: Internal wave velocity profiles at three azimuthal angles (defined as the horizontal angle relative to the tidal forcing direction) for the simple grid with unrefined boundary region as in Figure 3.7 (blue circles) and the grid with the highly refined boundary region as in 3.10c (red triangles). Not fully resolving the boundary flow causes s slight overprediction (at most 4% near the velocity peaks) of the velocity amplitude.

in Re require a larger computational domain or reduced viscosity. Since the flow solver results are dimensionless, these two options are actually identical, and depend only on the units ascribed to the simulation results. In our experience, it is easier, however to consider the Re increase obtained by reducing viscosity. For a more detailed discussion on increases in grid size, see Section 3.2.6. The end result is that increasing Re by a factor of X requires X^4 times the computational power. (For a 2D system, this would only require an increase in computational power by X^3.)

To give a concrete example of resolution and runtime on Lonestar, one of the high tidal forcing amplitude cases studied in chapter 5 ($A/\sigma = 0.5$) required a grid with approximately 5×10^6 control volumes. The time step was T/1000, where T is the period of the tidal forcing. This scenario was evaluated for 7 tidal forcing periods and took 787 cpu hours to complete (This corresponds to just over 6 hours of wall clock time on 128 processors). For this run, $Re \approx 500$; to increase Re to 10,000 (a factor of 20 increase) would likely require a $20^4 = 160,000$-fold increase in computational time. A single 7-period run at this elevated Re would require 1.26×10^8 cpu hours. For comparison purposes, our typical yearly allotment of cpu hours on the Lonestar cluster is 250,000 cpu hours.

Clearly, computational resources are not unlimited, but careful grid construction can maximize the resolution in areas of interest while minimizing computational time. Figure 3.7 shows the computational grid utilized in Chapter 4, which contains 5×10^6 control volumes. The highest spatial res-

olution in the boundary layer of the half sphere is 2 mm. For an identical domain with this high resolution everywhere, there would be 2.8×10^7 control volumes, so in this example of grid refinement, the number of control volumes was reduced by more than a factor of 5. Careful grid refinement can easily reduce the size of a uniform grid by an order of magnitude or more, but it is important to remember that the smallest control volumes typically constrain the time step.

As was previously discussed in Section 3.2.6, another complicating factor in large increases in Re is the increase in data storage and processing time (usually due to interpolating results on unstructured grids to desired visualization surfaces). At Reynolds number much higher than those studied here, outputting full velocity and pressure fields at regular time intervals becomes impractical, and only a subset of the output can be saved. This is not a strict limitation, but it requires careful planning before each simulation to ensure that all data required for some particular method of analysis will be available.

3.3 World Ocean Circulation Experiment data analysis

The World Ocean Circulation Experiment (WOCE) was conducted as a component of the World Climate Research Program (WCRP) between 1990 and 1998 (although data from as early as 1985 has been incorporated into the dataset). The objective was to provide a large range of insitu measurements of many physical quantities on a grid crossing the entire world ocean. The program included Conductivity-Temperature-Density (CTD) scans, cur-

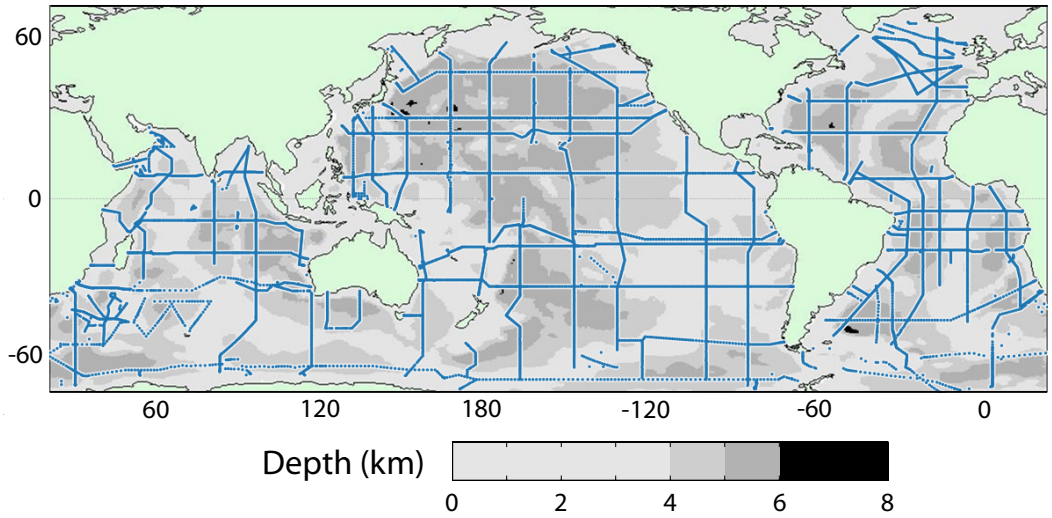

Figure 3.13: map of the WOCE one time cruises. Coverage is fairly uniform, with higher measurement density in regions of interest to oceanographers. Individual casts are denoted with blue dots, which appear as continuous lines except in areas of high distortion due to the map projection (high latitudes)

rent meters, sea-level measurements, and Acoustic Doppler Current Profiler (ADCP) measurements. Most of our analysis was performed on the WOCE One Time survey, which consists of an elaborate series of zonal (east-west) and meriodional (north-south) coast-to-coast cruises across the world oceans. The goal of the One Time survey was to obtain a snapshot of the state of the ocean taken within a single decade. (Later repeat cruises and time series stations seeked to address questions related to temporal variability of ocean quantities.) While a 10 year period may not seem like a snapshot compared to the other time scales discussed in this dissertation, this is a very brief window when considering the general ocean circulation, which evolves over time scales of order 10^3 years [*Wunsch and Ferrari*, 2004]. The WOCE data were taken

on many cruises, with individual 'casts' being taken with a typical spacing of 60 km along the route of each cruise. To produce a cast, the research vessel stopped and lowered sensors on a cable, taking measurements as the sensors were lowered through the water column. Typical vertical resolution for the measurements we utilized is 2 m, although some coarser casts only have data every 4 m or 6 m. In total, there are roughly 18,000 casts spread across the world oceans.

The primary objective of this component of our research was to determine if there are regions in the ocean where $N(z) < \omega_{M2}$, where $\omega_{M2} = 1.405 \times 10^{-4}$ rad/s = 1.93 cycles per day, and $N(z)$ is the local buoyancy frequency. Since the definition of N (Eq. 2.1) involves taking the derivative of vertical density gradient, measurement error assocated with determining the fluid density is quickly amplified. We developed two methods, discussed in the following subsections, for smoothing the data so that meaningful results could be extracted.

3.3.1 A simple analysis scheme

3.3.1.1 Filtering

In the simpler of the two analysis schemes, the raw data are filtered before being passed to the function which computes N. In practice, density is very difficult to measure in the ocean, so oceanographers typically calculate the density from measurements of temperature, salinity, and pressure using the International Equation of State of Seawater (EOS-80) [*UNESCO*, 1981]. The

raw temperature and salinity data are filtered using an unweighted moving filter with total window size 100 m. $N^2(z)$ is then calculated using the 'sw-bfrq' Matlab routine from the Seawater package (www.cmar.csiro.au). The sw_bfrq routine actually uses the EOS-80 relation to compute *potential density* in the process of determining $N^2(z)$. Potential density is the density a fluid parcel would have if it was raised adiabatically to a given reference depth. Using potential density in computations accounts for compressibility effects, enabling the use of the simpler definition of N (Eq. 1.2) rather than Eq. 2.1. For a rigorous discussion of potential density and its use in the calculation of sea water properties, see *Gerkema and Zimmerman* [2008].

The Seawater routine 'sw_bfrq' outputs $N^2(z)$. In cases where $N^2(z) < 0$, $N^2(z)$ is set to zero, and then the square root is taken to obtain $N(z)$. Since the computation of $N^2(z)$ requires taking a derivative of measured quantities that have already been filtered, the output must be filtered again. Results with the least scatter are obtained by filtering the resulting $N(z)$ using a low pass third order Butterworth filter with cutoff vertical wavelength of 200 m. The resulting curve is shown in Figure 3.14, along with more crude filters for comparison. Of primary interest is deep region where N^2 drops below ω_{M2}^2, with the result that semidiurnal (ω_{M2}) internal waves would not be allowed to propagate below roughly 5 km. Without extensive filtering, it is more difficult to establish with great confidence whether or not N^2 ever crosses below ω_{M2}^2.

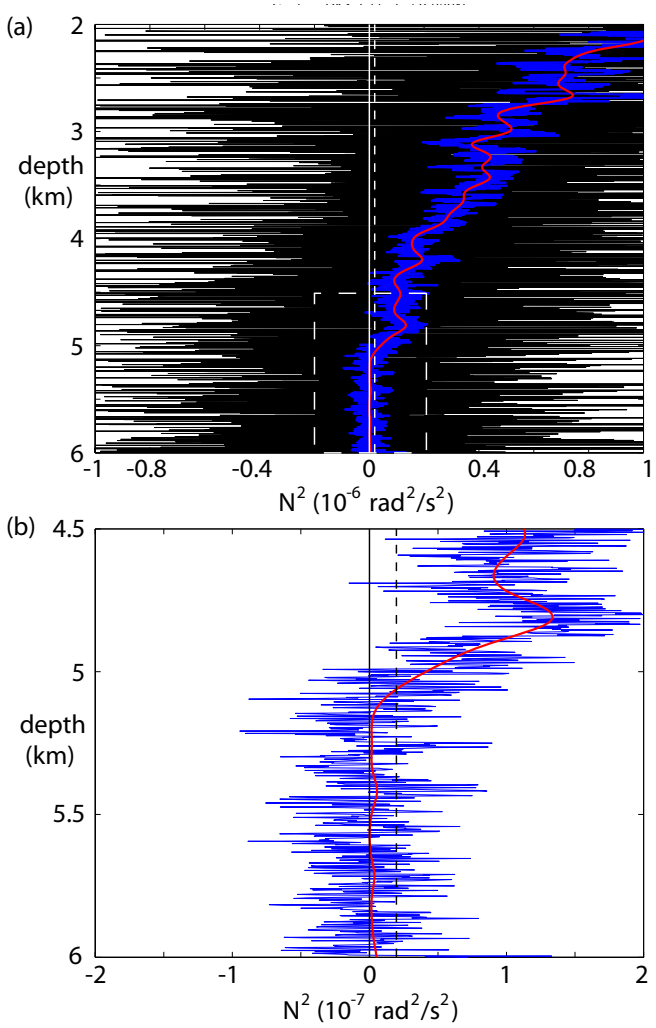

Figure 3.14: (a) $N^2(z)$ calculated from plugging raw oceanic measurements (cast P14N_325023_1_24, 50.2390° N, 179.1315° E) into the sw_bfrq routine (black lines), subsequently applying an unweighted moving average with window size 20 m (blue lines), and applying the pre- and post-filters discussed in Section 3.3.1. The blue line is similar to the result obtained by *Gerkema and Zimmerman* [2008]. The vertical white lines denote $N^2 = 0$ (solid) and $N^2 = \omega_{M2}^2$ (dashed), and the dashed white rectangle shows the location of the close up in (b). (b) Similar to (a) except with greater detail near the bottom of the profile, where N^2 aproaches zero. For clarity, the black trace without any filtering has been removed. The vertical black solid and dashed lines denote $N^2 = 0$ and $N^2 = \omega_{M2}^2$, respectively.

3.3.1.2 Determination of turning points

$N(z)$ is highly variable along a single cast. The raw data is filtered to the greatest extent possible, but there are still locations where assigning a single turning depth is ambiguous. At many locations, $N(z)$ is very close to ω_{M2}, and crosses back and forth multiple times, resulting in many narrow bands where internal waves, in principle, would not be allowed to propagate. These crossing events, where $N(z)$ is very close to ω_{M2} are disregarded as they are inferred from a single snapshot of heavily filtered WOCE data. Placing error bars on the $N(z)$ profiles is nontrivial as the errors depend on the particular instruments used on each cruise. Instead, we focus on turning depths where $N(z)$ drops below ω_{M2} for a certain minimum depth interval.

For the simpler filtering scheme and subsequent results, presented in Section 6.2, we use the fairly relaxed constraint that $N(z)$ must be smaller than ω_{M2} for a minimum contiguous depth interval of 50 m. When this criterion is met, the shallowest depth of the deepest contiguous interval where $N(z) < \omega_{M2}$ is called the turning depth at a particular location. In this way, for casts which have multiple locations where $N(z)$ drops below ω_{M2}, the deepest such point is identified as the turning point. To eliminate the arbitrary nature of simply choosing a minimum crossing interval, we characterize turning depths by the largest contiguous depth interval over which $N(z) < \omega_{M2}$. In this classification scheme, the minimum interval remains at 50 m, which constitutes a 'weak' crossing event, and increases in some cast locations to an interval larger than 1 km, constituting 'strong,' or very convincing crossings where $M2$ internal

waves would be unlikely to penetrate.

The turning depth calculation is automated to search for turning depths over the entire WOCE data set. It is possible that isolated casts contain more than one contiguous depth interval over which $N(z) < \omega_{M2}$. These casts would cause a turning depth to be returned even though there are deeper regions where internal waves are allowed to propagate. However, based on inspection of many individual casts, several of which are shown in Section 6.4, this event is rare in the WOCE data, and we do not expect this to change the results noticeably. The primary objective of this component of the study is to give a qualitative description of the locations and prevalence of turning points in the ocean, not a quantitative analysis, which would require substantially more data than are available.

3.3.1.3 Cruise transects

Since the WOCE casts are located along cruises, it is reasonable to compare all the buoyancy frequency profiles along individual cruises. This provides a high spatial resolution snapshot of the buoyancy frequency along a large zonal or meridional slice of the ocean. Although the casts are not simultaneous, they are typically seperated in time by order 10 hours. As will be shown in Section 6.4, variation of the buoyancy frequency in the deep ocean, where we are concerned, is small even over timescales of years. To arrive at these plots, shown in Section 3.2, the data analysis proceeds as for the individual casts discussed in Section 2.1. Salinity and temperature data

are interpolated to a uniform 2 m vertical depth vector, and then filtered using a moving average with window size 100 m. Buoyancy frequency is then computed using the Seawater routine 'sw-bfrq,' with the output being run through a third order low pass Butterworth filter with cutoff wavelength 200 m.

The Smith and Sandwell bathymetry [*Smith and Sandwell*, 1997] is then interpolated to the exact latitude and longitude of each cast, as well as at 7 equally spaced points along a line connecting adjacent casts. Since the WOCE cruises usually deviate slightly from exact zonal or meridional paths, this is the best way to maximize the accuracy of the bathymetry between casts. The frequency at which the Smith and Sandwell bathymetry is sampled between casts is chosen to maximize the detail of the bathymetry displayed in a large figure. This gives a qualitative sense of the bottom roughness everywhere along a WOCE cruise and makes use of the higher resolution available in the Smith and Sandwell set (3.7 km resolution as opposed to typical WOCE data resolution on the order of 60 km).

Finally, the buoyancy frequency data is interpolated to a uniform grid along the transect direction and overlaid on the bathymetry data. For the case of a meridional cruise, the uniform grid is located at the average longitude of the casts in the cruise, with begin and end points at the same latitudes as those of the cruise. The number of points in the uniform grid is equal to the number of casts in the cruise, so the average spatial resolution of the transect is preserved.

Due to the large variation of $N(z)$ in the ocean, a logarithmic colorbar is chosen for the quantity $N(z) - \omega_{M2}$, with a sharp color transition when $N(z) - \omega_{M2} = 0$, denoting a turning depth.

3.3.2 Statistical analysis

We have developed, in collaboration with Prof. Michael Marder (UT Austin), a sophisticated WOCE data analysis scheme to enable the determination of error bars on the processed $N(z)$ profiles. This is an important advance, as error quantification allows us to reinforce the results obtained with the simple filtering analysis and to establish greater confidence in the presence of turning depths.

3.3.2.1 Bin sorting and error propagation

This more refined analysis uses standard statistical tools applied for the first time to the WOCE data set. Analysis on a single cast begins with sorting the data (pressure, temperature, and salinity) into bins of constant depth interval (Effects of varying bin size will be discussed in Section 6.3.1). The sorting procedure is performed from the top of the data (the sea surface) downward, as this ensures that bins on neighboring casts align, facilitating visualization later. Each of the measurements is averaged in each bin, resulting in an average pressure, temperature, and salinity in each bin [*Marder*, 2009]:

$$\bar{x} = \sum_{i=1}^{N_b} \frac{x_i}{N_b} \tag{3.24}$$

where x_i are the individual pressure, temperature, or salinity measurements, $\bar{x}$ represents the averaged quantities, and N_b is the number of samples in each bin. The notation N_b is used for the number of samples in each bin instead of the more common notation N to avoid confusion with the buoyancy frequency. Standard deviation of temperature and salinity in each bin is obtained:

$$S = \sqrt{\sum_{i=1}^{N_b} \frac{(x_i - \bar{x})^2}{N_b - 1}} \tag{3.25}$$

and standard error is computed for the temperature and salinity of each bin:

$$\Delta x = \frac{S}{\sqrt{N_b}} \tag{3.26}$$

The raw data have now been averaged into bins, with each bin having an average pressure, and averaged temperature and salinity measurements with their associated standard errors. This analysis assumes that the measurements in each bin are independent measurements. This may not be entirely accurate as we expect that passing internal waves and other flow features might result in correlations between data. However, further analysis on many WOCE casts shows that the correlation lengths of the salinity and temperature profiles is typically less than 5 m, meaning that statistics can be performed on the bin-sorted data under the reasonably good assumption that the data are uncorrelated.

In order to continue using the standard 'sw_bfrq' script from the seawater routines (see Section 3.3.1.1), a numerical method was devised to propagate standard error through the computation of N. Rather than simply passing the

bin-averaged T and S to 'sw_bfrq,' which computes N^2, noise is first added to the bin-averaged T and S values by randomly sampling from a normal distribution with standard deviation equal to the standard error of the bin-averaged quantities. A cubic spline is then fitted to the perturbed T and S data and sampled at the same vertical resolution of the unaveraged data (This enables a more accurate computation of derivatives in the 'sw_bfrq' routine). N^2 is then computed using the 'sw_bfrq' routine and the spline-fitted data. Repeating this computation many times (typically on the order of 1000), with newly sampled noise and a new spline fit at each iteration, results in a range of N^2 values that reflects the standard error in the input T and S. Since the spline-fitted data is passed to the buoynacy frequency routine at a much higher spatial resolution than the bin-sorted data, the resulting N^2 curve must be downsampled to appropriately reflect the vertical resolution of the bin-sorted data. Once the resulting family of N^2 curves is downsampled, an average N^2 and standard deviation is computed at each bin. This effectively propagates the error through the computation of N^2, resulting in a final N^2 curve with error bars. Figure 3.15 shows an example of an N^2 profile obtained using this statistical method. This method of establishing confidence intervals on the $N(z)$ profiles is the only way to rigorously prove the existence of turning depths in the deep ocean, which will be discussed in 6.3.4

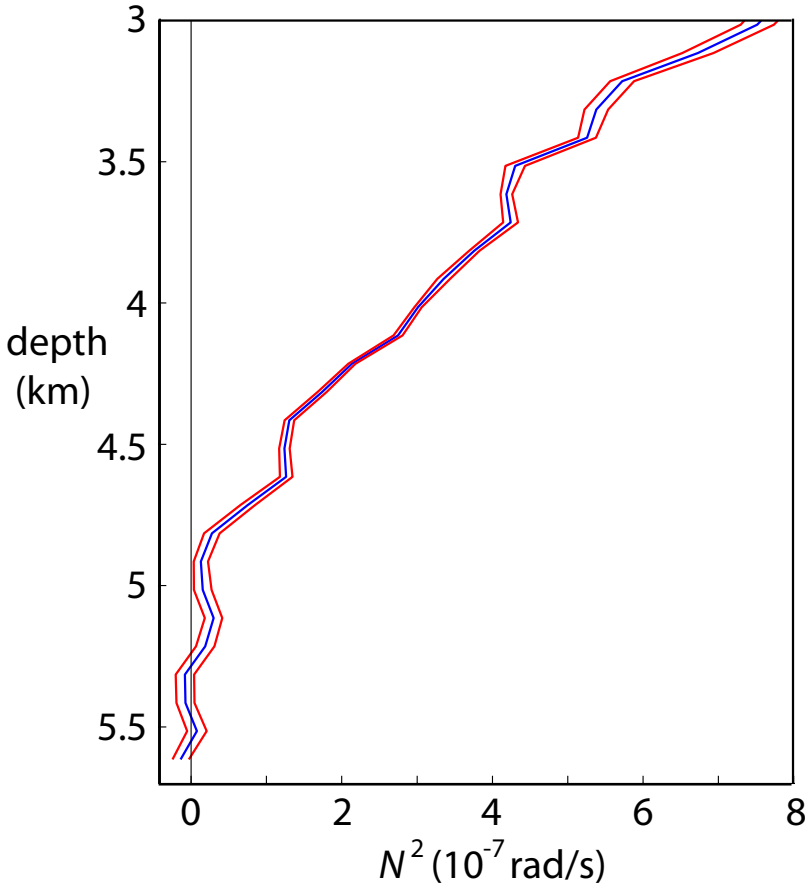

Figure 3.15: Example of a bin averaged N^2 profile from the P14 cruise (cast P14N_325023_1_32, 46.4992° N, 179.0052° E). The blue profile is the average N^2 and the red lines on either side denote the 68% confidence interval determined from the numerical error propagation. Bin size is 50 m, and adjacent bin averages and error bars are connected with straight lines. Note that for clarity only a part of the profile is shown.

3.3.2.2 Variable bin size

Variable bin size has the advantage that an optimum bin size can be selected based on statistical criteria at each depth. In our implementation, the size of the first bin is set, and the neighboring bin is initially set to contain a predefined number of points (minimum bin size). A simple T-test is performed between the first two bins [*Marder*, 2009], whereby the following quantity is evaluated:

$$T = |\bar{x}_1 - \bar{x}_2| - \gamma(\Delta x_1 + \Delta x_2) \tag{3.27}$$

where $\bar{x}_1$ and $\bar{x}_2$ are the average values of the first and second bins, respectively, Δx_1 and Δx_2 are the standard errors of the first and second bins, respectively, and γ is a user-defined number that determines how stringent the test for statistical distinguishability of the two bins is. If $T > 0$ (this correponds to the absence of overlap of the error bars between the adjacent bins), the bins are determined to be statistically distinguishable, and the size of the second bin is fixed. A similar analysis is then performed on the second bin and a new third bin, and so on. If $t < 0$ (corresponding to overlapping error bars between the adjacent bins), the error bars of the adjacent bins overlap and the bins are statistically indistinguishable. Another data point is added to the second bin, and the T-test is performed again, incrementing the second bin until statistical significance is obtained, before beginning the analysis again on the second and third bins. In this way, the entire water column from a cast is sorted into bins where the T-test is used to determine bin sizes.

In the variable bin size analysis, there are three tunable parameters: (1)

the minimum bin size, (2) the size of the first bin, and most importantly, (3) γ in Eq. 3.27, which determines the confidence intervals to be used in the T-test ($\gamma = 1$ corresponds to 68% confidence, $\gamma = 2$ corresponds to 95% confidence, etc.). We have found that the resulting bin sorting depends very sensitively on these three parameters and decided not to pursue the variable bin size algorithm in preparation of the results presented here. Another difficulty is that the temperature and salinity data for a given cast will in general have different bin size distributions when using the variable bin size scheme, which makes choosing the depths at which to evaluate N^2 nontrivial. The bin analysis could be performed on density (after density is computed from the raw salinity and temperature data). but the standard 'sw_bfrq' routine takes salinity and temperature as inputs.

3.3.2.3 Spatial and temporal averaging

In certain regions, additional averaging can be utilized to reduce the size of the error bars on the computed $N(z)$ profiles. Typically, neighboring casts from a particular cruise can be averaged so long as the casts are qualitatively similar. The $N(z)$ profiles are simply averaged, with the resulting standard deviation as a function of depth used to quantify the uncertainty.

In addition, casts from different cruises that pass through a given area at different times can be averaged to quantify the extent to which $N(z)$ profiles vary over time. These averages can often span 10 years in time, and in this case, the standard deviation is a measure of temporal variability $N(z)$. Results

from this further averaging are discussed in Section 6.3.3.

3.4 Numerical solution of vertical modes

To determine the effects of turning depths on internal waves, we also consider the alternate method of describing internal waves: the vertical mode decomposition. In this formalism, internal waves are decomposed into a series of vertical modes, which form a spanning set of solutions to the internal wave eigenvalue equation in a stratified fluid [*Gerkema and Zimmerman*, 2008]:

$$\frac{\partial^2 w}{\partial t^2} + k^2 \frac{N^2(z) - \omega^2}{\omega^2 - f^2} w(z) = 0 \tag{3.28}$$

where $w(z)$ is the vertical velocity and the $z-$dependent buoyancy frequency profile $N(z)$ makes the problem nontrivial. Localized internal wave beams can then be written as a sum of many vertical modes. Near topography such as ridges and seamounts where internal tides are generated, the internal tides are typically beam-like, indicating the presence of many vertical modes with large vertical wavenumber. However, with increasing distance from the generation site, the higher vertical modes decay, leaving most of the remaining internal tidal energy in the lowest several vertical modes [*St Laurent and Garrett*, 2002].

We use the built-in Matlab solver 'eig' to numerically solve the eigenvalue problem for a typical ocean $N(z)$ profile. 'eig' can solve large systems of coupled differential equations, and it automatically breaks the system of equations where the sign of the coefficient of the second term in Eq. 3.28 changes. When this term changes sign (as would occur when $N(z)$ drops below ω_{M2},

the solutions of the system have a different nature, requiring the solution of separate problems with appropriate matching conditions at the boundaries.

The scripts used to solve for the vertical modes are modified versions of codes originally developed by Sam Kelly at Oregon State University (skelly@coas.oregonstate.edu). They can be adapted to solve for any desired mode(s) for an arbitrary $N(z)$ profile, and vertical resolution was set to 1 m.

Chapter 4

3D Topography: Sphere

We examine the generation of internal waves by 3D topography for a system that shares qualitative features with supercritical topography on the ocean floor: a horizontally oscillating flow over a half-sphere (Figure 4.1a). This work has been published, and this chapter follows closely the publication *King et al.* [2009]. The half-sphere is taken to be centered at the origin; z is in the vertical direction (antiparallel to the gravity vector), x is in the forcing direction, and y is the remaining coordinate in the right-handed triad. The azimuthal angle ϕ is measured from the x-axis. The polar angle ψ (not to be confused with the angle of wave beam propagation θ in Eq. 1.1) is measured from the vertical. Internal waves are generated most intensely when the slope of wavebeam propagation is near the slope of the topography (This occurs when the wave beam angle θ nearly equals the topographic polar angle ψ). As in recent work, we define a *near-critical* region to be where the topographic slope differs from $\cot\theta$ by no more than 0.09 [*Zhang et al.*, 2008].

As can be seen in Figure 4.1b, the wave beam propagation angles selected by the dispersion relation (Eq. 1.1) sweep out characteristic cones in three dimensions (in contrast to the four possible angles, the St. Andrews

Cross, in two dimensions). The characteristic cones are axisymmetric, but the horizontal tidal motion breaks the axisymmetry. Our experiments and numerical simulations yield internal waves that are more intense in the forcing direction ($\phi = 0$) than in other directions, which is not surprising. However, it was surprising to find, perpendicular to the forcing direction, a strong non-linear flow that arises from higher harmonic oscillations in the boundary layer around the half-sphere. This flow is absent in unstratified flows, as well as in stratified flows where $\omega > N$ and internal waves do not propagate. As discussed more fully in Section 3.2, simulations are performed on the Lonestar cluster at the Texas Advanced Computing Center, typically using blocks of 128 processors. All simulations are run for at least 7 forcing periods to ensure that steady state is reached. By the seventh period, the internal wave fields are within 1.3% of their asymptotic values; this is determined by examining the time series of velocity at points in the internal wave field. Consequently, all analysis is done on the seventh through tenth periods. At these times, reflections from boundaries have not had time to set up and interfere with the results. The shape and extent of the computational domain (Figure 3.7)was chosen such that unwanted wave reflections would be in the regions below the conical wave characteristics, where they would not interfere with the analysis presented here. In addition, wave reflections are much weaker than in similar 2D studies because there is a $1/r$ geometrical spreading factor associated with 3D internal waves emanating from a localized source. This spreading factor, in addition to normal viscous dissipation and a suitably chosen domain, ensures

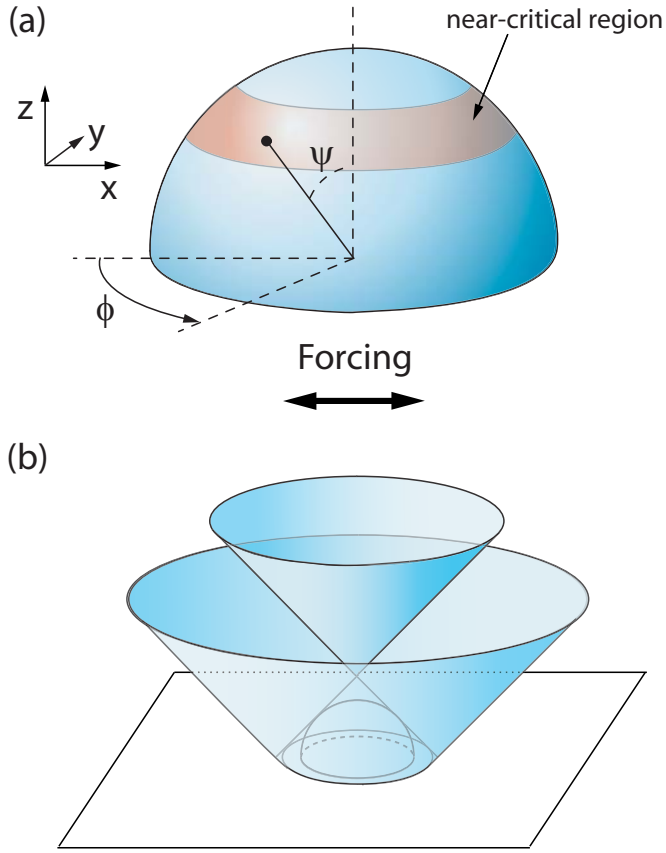

Figure 4.1: (a) Horizontally oscillating tidal flow (in the x direction) impinges on a half-sphere. The azimuthal angle ϕ is measured from the x-axis and the polar angle ψ from the vertical. The red band denotes the near-critical region where the internal wave generation is most intense. (b) Internal waves are allowed by the dispersion relation (Eq. 1.1) to propagate along two nested cones, the upper one corresponding to waves propagating upward from the near critical region, and the lower cone corresponding to waves that propagate downward from the near critical region and are reflected from the horizontal plane ($z = 0$).

that reflections do not interfere with the internal wave field.

Corresponding experiments are performed utilizing the experimental apparatus described in Section 3.1.1, with the nylon sphere described in 3.1.2.1.

4.1 Linear Internal Waves

The forcing frequency for all results presented in this chapter is $\omega = 0.942$ rad/s. The nondimensionalized tidal forcing amplitude is fixed at $A/R = 0.092$ until noted later when the effects of varying amplitude are discussed.

4.1.1 Flow in the forcing direction.

For simplicity, the internal wave field is first visualized in the tidal forcing direction, where we expect the generated wave to be most intense.

Figure 4.2 shows an example of the good agreement found between the experimental and numerical flow fields in the tidal forcing direction. The waves are bimodal near the sphere and are (in the plane defined by the forcing direction and the vertical axis through the center of the half-sphere) similar to the internal wave field generated by a horizontally oscillating cylinder [*Zhang et al.*, 2007]. In Figure 4.2 (c) and (d), the σ-axis is defined to be perpendicular to the wave propagation direction, with positive sigma toward the upper right. The origin of the σ coordinate is along a line extending from the center of the half-sphere along the wave propagation angle.

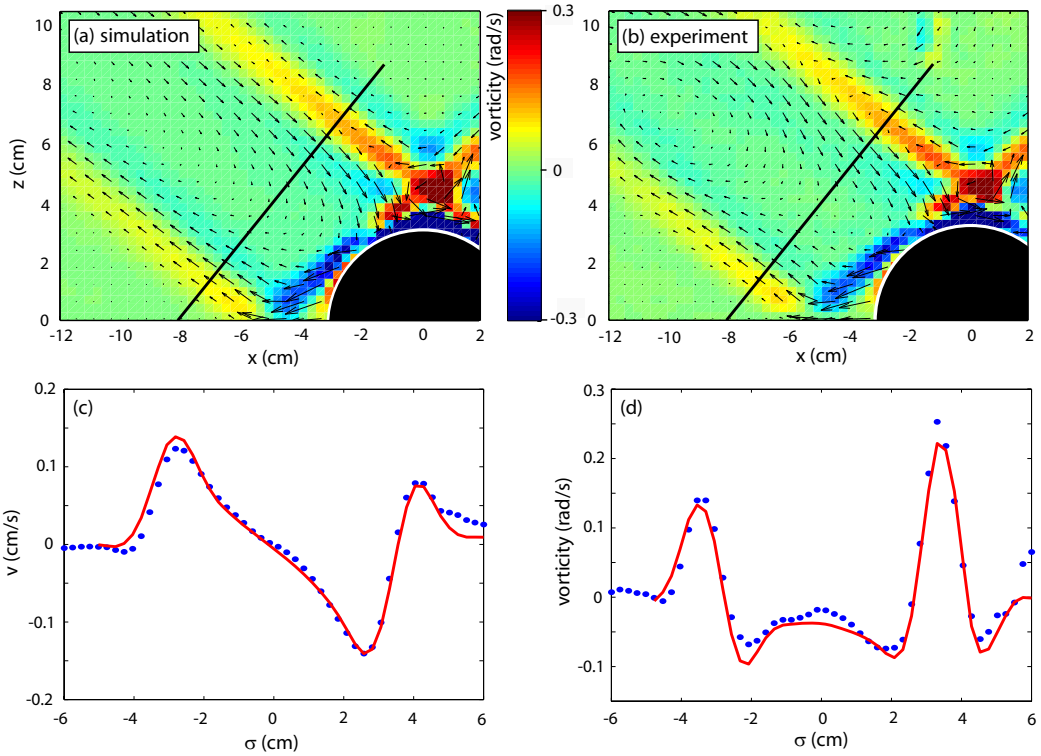

Figure 4.2: Instantaneous velocity field (arrows) and vorticity field (color) in the vertical midplane $y = 0$ from (a) simulation and (b) experiment. These fields are displayed when the flow is moving to the right, 5% of a period after the velocity maximum. The lower graphs compare simulation (red lines) and experiment (blue dots) at $r/R = 2$ for instantaneous profiles of (c) velocity and (d) vorticity, along the black diagonal lines in (a) and (b). σ is the cross-beam coordinate, defined to be zero between the two wavebeams, and becoming positive toward the upper right.

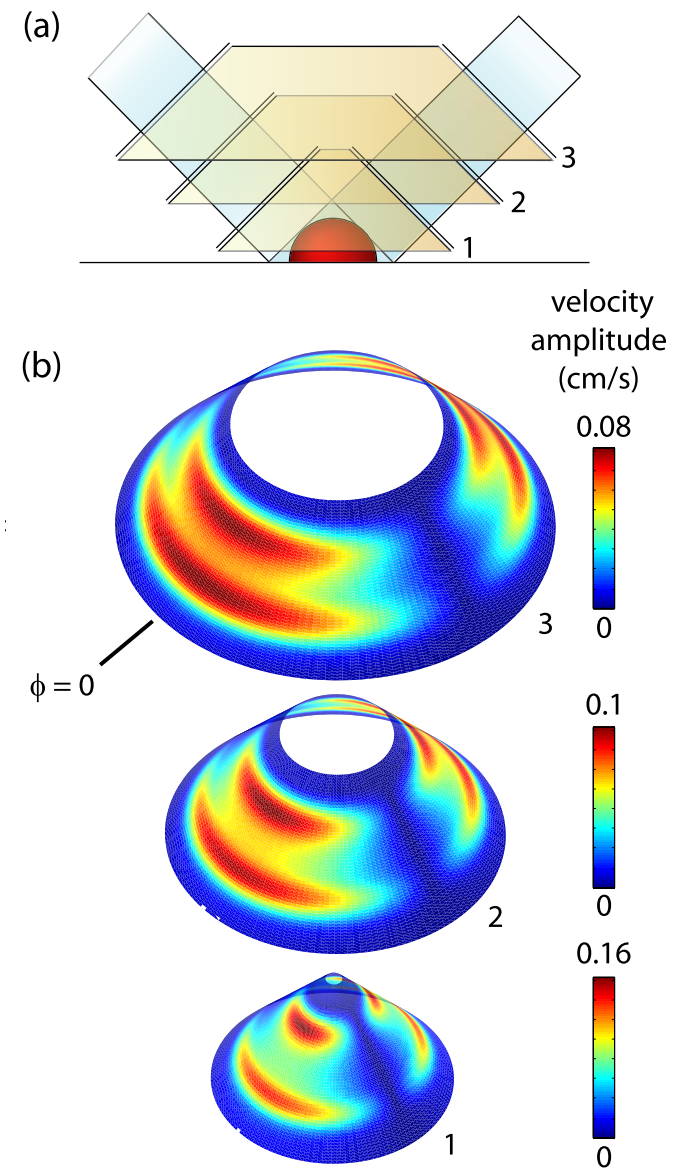

Figure 4.3: (a) A 2D cross section of conical surfaces where the wave amplitude is visualized at r = (1) $2R$, (2) $3.5R$, and (3) $5R$ from the center of the half-sphere, for forcing amplitude $A/R = 0.092$. (b) The velocity amplitude on the three conical surfaces (displaced vertically for visualization) is denoted by color ranging from dark red (high) to deep blue (low); the color map is different for each surface to enhance the visibility of the wave structure at each distance.

4.1.2 Wave Structure

Figure 4.3 is an example of a flow field visualized in three dimensions, on a conical surface so that wave strength can be seen at all azimuthal angles for a given distance from the center of the half-sphere. These results are obtained by fitting a sine wave with frequency ω to the time series of the along-beam velocity component at every point on each surface. As expected, the internal waves are radiated most strongly in the forcing direction, with the waves becoming less intense with increasing azimuthal angle. Near the sphere the wavebeam is bimodal; the top beam propagates directly outward from the half-sphere, while the bottom beam is reflected from the bottom boundary. Further from the sphere, viscous effects begin to smear these two distinct waves. By $r = 5R$ the waves already have significant overlap, and at large r the structure becomes unimodal.

To characterize the azimuthal dependence of the internal wave field, we plot the maximum along-beam velocity amplitude of the upper beam as a function of azimuthal angle for three forcing amplitudes (Figure 4.4). For the smallest forcing, the wave amplitude is described well by a cosine dependence, as predicted by the linear inviscid analysis of *Appleby and Crighton* [1987]. For higher forcing, the behavior departs from linear theory: a higher proportion of the wave energy is radiated in the forcing direction. To quantify the energy radiation as a function of azimuthal angle, we evaluate energy flux associated with the internal waves in the far field. For low wave amplitude, we use the linear energy flux term $p'\mathbf{u}'$, where $\mathbf{u}'$ is the baroclinic velocity and p' is the

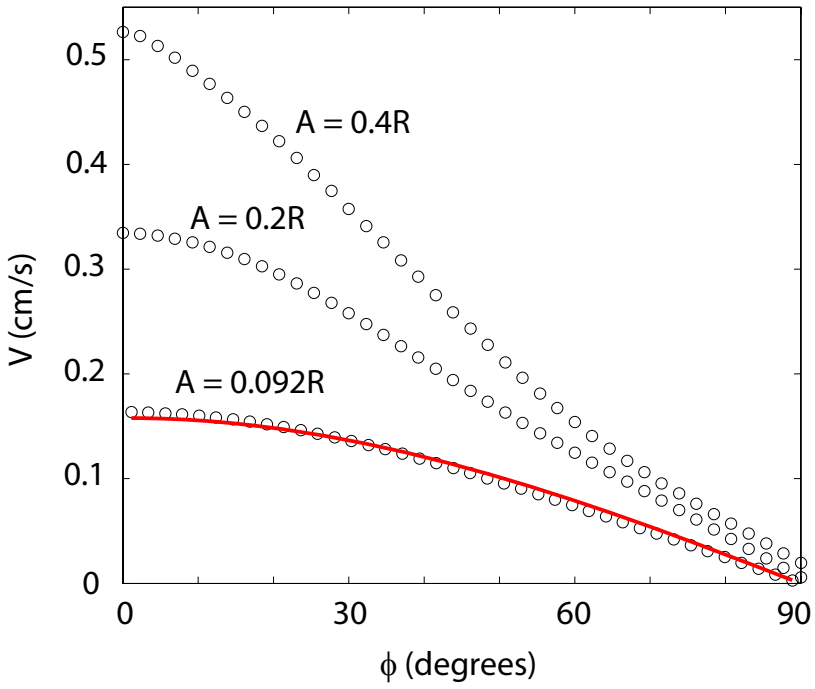

Figure 4.4: The azimuthal dependence of the wave field at $r = 2R$ simulated at low forcing amplitude ($A/R = 0.092$) follows the $\cos\phi$ prediction of inviscid theory (solid curve). For higher forcing, the wave beams become stronger in the forcing direction ($\phi = 0$) and there is large deviation from the linear inviscid theory.

baroclinic component of the pressure perturbation. Near the half-sphere, it is unclear how to distinguish between the barotropic and baroclinic components of the velocity and pressure fields. However, in the far field ($r >> R$), we use the fact that the barotropic tidal flow is, to first order, unperturbed by the presence of the half-sphere. For a spatially uniform oscillatory background flow, $u(t) = A\omega \sin(\omega t)$, it can be shown using the Navier-Stokes equation that the barotropic component of the pressure perturbation is a function only of x and t:

$$p'_{bt}(x) = (-A\omega^2 \cos \omega t)x \tag{4.1}$$

This barotropic pressure is subtracted from the pressure perturbation from the simulations to obtain the baroclinic pressure perturbation associated with the internal waves. When multiplied by the baroclinic velocity, this gives the energy flux at a point in the internal wave. Energy flux is summed in the cross-beam direction and averaged over a single period to obtain the average energy radiation as a function of the azimuthal angle ϕ. At low amplitude ($A/R = 0.1$) the ϕ-dependence of the radiated energy is described well by a $\cos^2 \phi$ function, as would be expected since the beam velocity and barotropic pressure perturbation should both scale as $\cos \phi$; 50% of the radiated energy is within 23° of the forcing direction. At higher amplitudes, a greater fraction of the total radiated energy is closer to the forcing direction (cf. Figure 4.4).

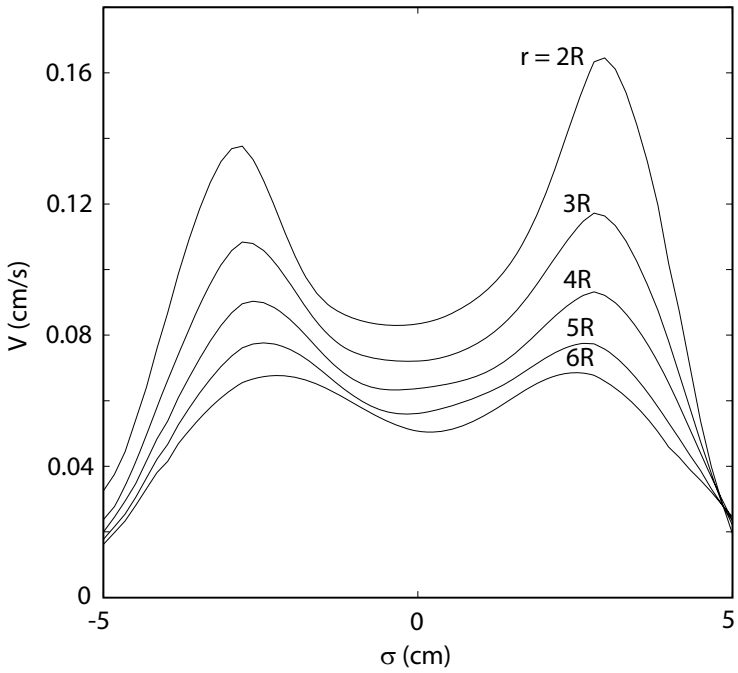

Figure 4.5: Cross-beam profiles of the along-beam velocity component at $r/R = 2$, 3, 4, 5, and 6, where R is the radius of the half-sphere. These profiles are taken in the forcing direction ($\phi = 0$) at a forcing amplitude of $A/R = 0.092$. At distance $2R$ from the center of the half-sphere, the ratio of velocity amplitudes in the two beams is 1.23, but this ratio drops with distance along the beam, and the beams are equal in amplitude by $r = 5R$.

4.1.3 Asymmetry between the upper and lower wavebeams

Simulations and experiments both show an asymmetry between the upper and lower wavebeams generated by the sphere (Figure 4.5), as can be seen in Figure 8a of the paper on experiments by *Flynn et al.* [2003]. The asymmetry appears to be a 3D effect because no 2D studies have reported any asymmetry. The asymmetry in the velocity amplitudes of the two wave beams follows from a geometrical argument. A half-sphere (or any super-

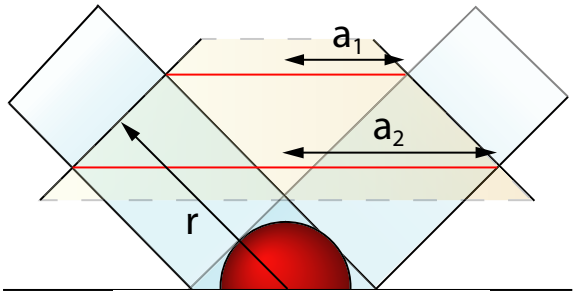

Figure 4.6: A 2D cross section illustrating the observed wavebeam asymmetry. For a given cross section distance, the energy in the top beam is concentrated in a smaller area (a circle with radius a_1) than the energy in the lower beam (a circle with radius a_2). The upper wavebeam therefore has a higher energy density and, consequently, a higher amplitude than the lower beam. As r becomes larger, the ratio of a_1 to a_2 approaches 1, and the asymmetry decreases corrspondingly.

critical topography) generates internal wave beams along two nested conical characteristics, as in Figure 4.1b. Waves along the inner characteristic cone propagate upward from the near-critical regions on the half sphere, and waves along the outer characteristic also propagate upward after being reflected from the bottom boundary. By symmetry, equal amounts of energy go into each wavebeam.

A cross section such as those in Figure 4.3 intersects each characteristic surface in a circle. Viewed from the side, the circles of intersection are the horizontal red lines in Figure 4.6. In the inviscid limit (with attenuation neglected), the energy flux in each wavebeam should be inversely proportional to the circumference of the circle of intersection of the cross section and the characteristics. This is a consequence of the wavebeam spreading out in

three dimensions, similar to the geometrical focusing discussed in [*Buhler and Muller*, 2007]. This relationship between energy fluxes F_1 and F_2 in the two wavebeams can be written as

$$\frac{F_1}{F_2} = \frac{a_2}{a_1}, \tag{4.2}$$

where the radii a_1 and a_2 are defined in Figure 4.6. Geometrical considerations allow us to rewrite this as

$$\frac{F_1}{F_2} = \frac{r/R + \tan\theta}{r/R - \tan\theta}, \tag{4.3}$$

where θ is again the wave beam propagation direction. This function has the expected qualitative behavior: the ratio of energy fluxes approaches 1 for large r/R and diverges as r/R approaches $\tan\alpha$. To make a quantitative comparison to simulation data, we use the result that wavebeam energy flux is related to energy density by the expression [*Kundu and Cohen*, 2004]

$$\vec{F} = \vec{c_g} E \tag{4.4}$$

where $\vec{c_g}$ is the group velocity and E is the energy density of the wave. In general, wavebeams are comprised of a spectrum of wavenumbers with different group velocities, but in both simulations and experiments, we observe a distinct wave front propagating outward from the half-sphere after the onset of oscillation, implying a sharply peaked wavenumber spectrum around a dominant wavenumber, which determines the group and phase velocities of the waves. It is assumed that the two wavebeams under consideration have the

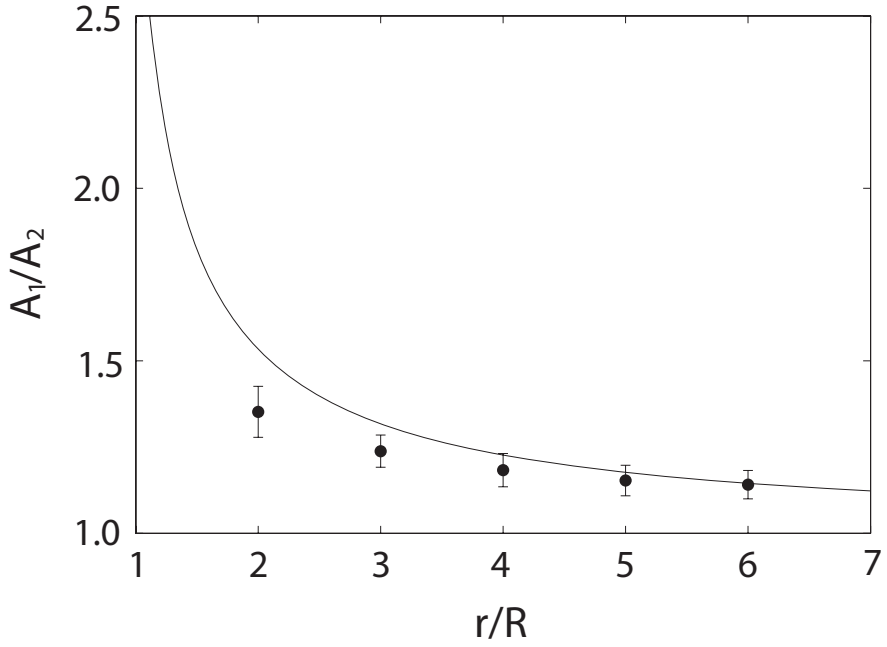

Figure 4.7: Comparison of measurements (solid dots) of the wavebeam asymmetry (ratio of the upper to lower wavebeam amplitudes) from a simulation with the prediction (Eq. 4.5) from the geometrical argument (solid curve). ($A/R = 0.4$)

same dominant wavenumber, and therefore the same group velocity $\vec{c_g}$. Eq. 4.4 is used in the second equality to show that the ratio of beam amplitudes is then

$$\frac{A_1}{A_2} = \sqrt{\frac{E_1}{E_2}} = \sqrt{\frac{r/R + \tan\theta}{r/R - \tan\theta}} \tag{4.5}$$

To compare Eq. 4.5 to numerical results, we compute the ratio of beam strengths using the maximum beam amplitudes of the upper and lower wave beams at several distances from the center of the half-sphere. The error bars are based on the standard error associated with fitting a sine function at the

forcing frequency to a time series of beam velocities at an output of 20 points per period. We find that Eq. 4.5 predicts the asymmetry well for large r/R (Figure 4.7), where linear inviscid theory applies, but the measurements depart from the prediction for small r/R where beam-beam and beam-boundary layer interactions can be important. As discussed in [*Flynn et al.*, 2003], the interactions between the generated internal waves and the viscous boundary layer around the half-sphere are not well understood, and we show in the next section the importance of nonlinear effects near the half-sphere. In the near field, both of the above complicating factors reduce the validity of the symmetry assumptions used to derive the geometrical argument Eq. 4.5.

4.2 Nonlinear Out-of-Forcing-Plane Flow

The experiments and simulations both reveal a strong flow *perpendicular* to the forcing direction (i.e., in the y direction); we refer to this as the nonlinear flow. Fluid immediately above the sphere is pushed downward along the $\phi = 90^o$ directions in narrow boundary layers. This flow departs near $\psi = \theta$ from the boundary layer and propagates outward in the y direction. Snapshots from experiment and simulation show the same out-of-forcing-plane flow (Figure 4.9). The speed of the downward flow in the boundary layer (at $\phi = 90^o$) is roughly equal to the maximum forcing speed, Aω.

We verify that the flow perpendicular to the forcing direction is unique to internal waves by performing experiments with a forcing frequency higher than the buoyancy frequency, so internal waves do not propagate. Then the

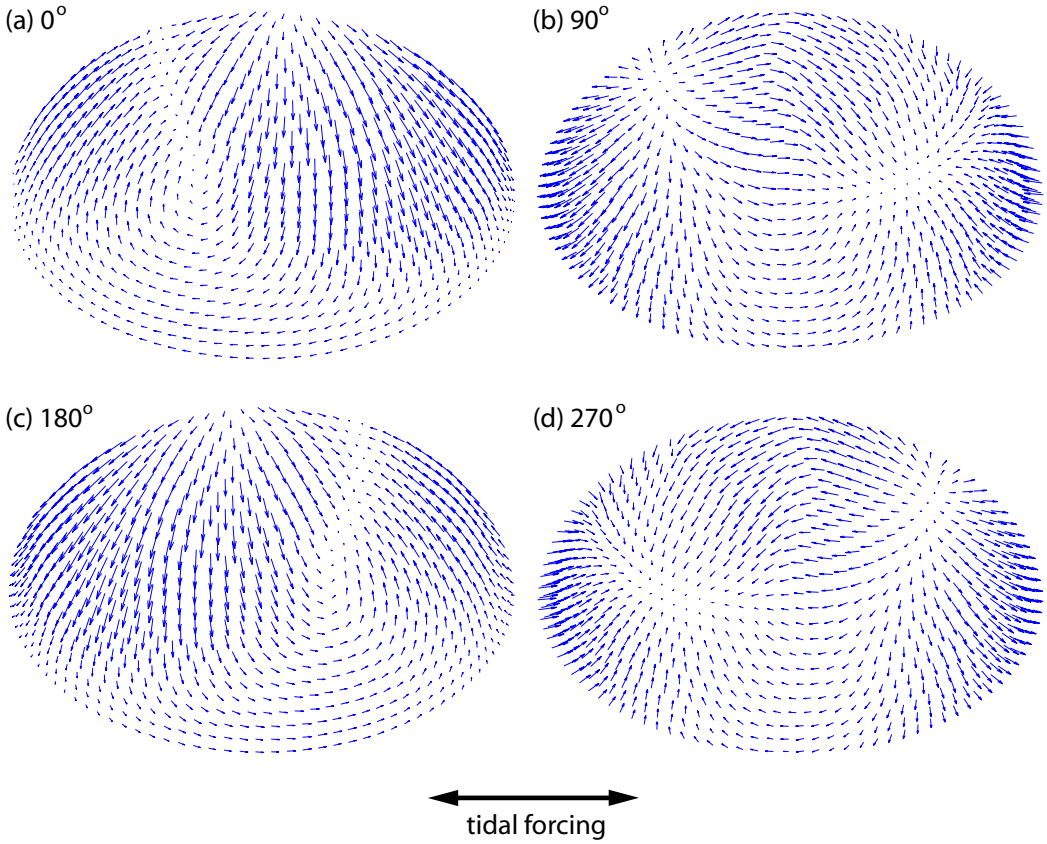

Figure 4.8: Velocity vectors 0.25 cm above the surface of the sphere at forcing phases (a) 0°, (b) 90°, (c) 180°, and (d) 270°. In these figures, only half of the spherical boundary layer ($y > 0$) is shown for clarity. Forcing is in the left-right direction, and 90° phase corresponds to tidal flow having its maximum value to the right.

flow simply deforms around the oscillating sphere. The out-of-forcing-plane flow arises from wavefronts that travel in the $y = 0$ plane and collide near the top of the sphere, generating a flow that is predominately at twice the forcing frequency. Figure 4.8 illustrates this 2ω boundary flow, with a series of snapshots of the boundary layer at 90° increments in tidal forcing. (a) and (c) show the boundary layer when the background tidal flow is zero. (b) and (d) show the boundary layer when the tidal flow is at its maximum value to the right and left, respectively. Note in (a) and (c), when the background tidal flow is changing direction, there is a strong flow down the sphere in the $\phi = 90°$ direction. The downward flow occurs twice per forcing period, whenever the background flow changes direction. Figure 4.10 shows a time series of the y-component (perpendicular to the forcing plane) of this boundary flow; the y-component of velocity is always positive, meaning that the flow is moving down the side of the sphere at all times.

In this study, we have intentionally made $2\omega > N$, so that second harmonic waves are not allowed to propagate. However, as can be seen in Figure 4.10, strong motion at twice the forcing frequency is still present near the half-sphere. Thus a large amount of energy cannot propagate away from the half-sphere, resulting in trapped energy that may contribute to local mixing near the sides of the topography. The trapped energy can be estimated using the wave saturation data (circles) in Figure 4.11. The internal wave field begins to saturate at $A/R = 0.3$, so the wave energy remains roughly fixed at higher forcing amplitudes even though more energy is being supplied by the

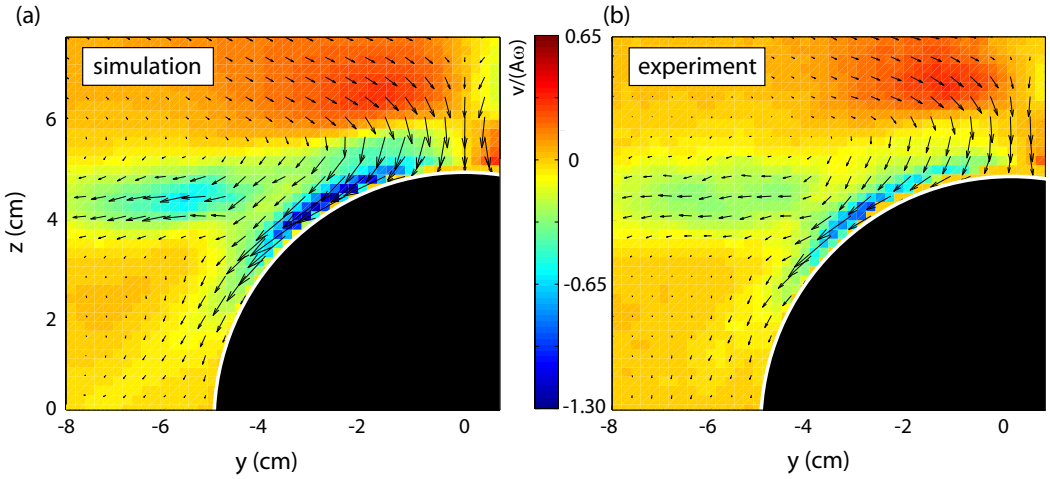

Figure 4.9: (Color online) An intense boundary layer current and an outflow perpendicular to the forcing direction is revealed by these snapshots, where the forcing is normal to the page ($R = 5$ cm and amplitude $A/R = 0.2$). The color maps represent the y component of velocity relative to the maximum forcing velocity, $A\omega$.

forcing. At $A/R = 0.6$, the maximum wave amplitude is 0.32 cm/s, which is only 70% of the value extrapolated from lower forcing amplitudes in the linear regime (black line in Figure 4.11). Since kinetic energy is proportional to the square of velocity, roughly 50% of the energy extracted from the tide is not propagating away in the form of internal waves.

The zero frequency component of the flow perpendicular to the forcing direction is plotted as a function of forcing amplitude in Figure 4.11. For small forcing amplitude ($A/R \lesssim 0.2$), the velocity amplitude is proportional to the square of the forcing amplitude, as would be expected for a nonlinear process. For comparison, the figure also shows the internal wave amplitude in the forcing plane; this velocity depends linearly on the forcing amplitude (for

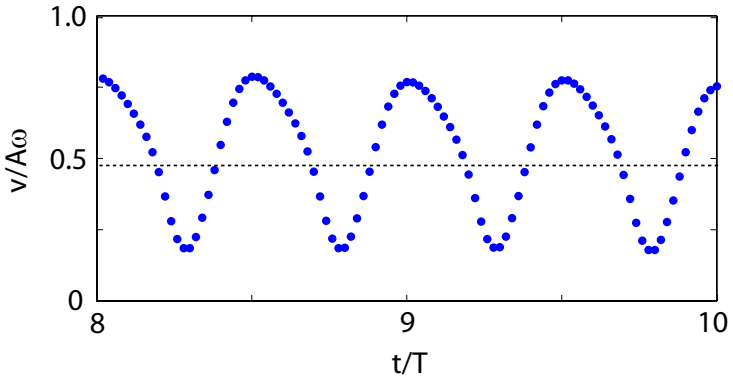

Figure 4.10: The flow perpendicular to the forcing direction varies in strength periodically at frequency 2ω. The y component of velocity is plotted here for a position 0.2 cm above a half sphere of radius $R = 3.25$ cm at $\phi = 90^o$ and $\theta = 38.9^o$; this is the center of the near-critical region, where the motion perpendicular to the forcing direction is strongest. Note that the average of the y component of velocity (given by the dashed line) is nonzero.

low forcing).

The average nonlinear flow in both the the vertical forcing plane through the sphere center and through a horizontal plane above the sphere center is shown in Figure 4.12. Strong flow down the sides of the sphere in the direction perpendicular to the forcing is evident in Figure 4.12(a); the velocity amplitude is comparable to the forcing velocity amplitude, $A\omega$. Most of the boundary flow splits off and moves in the y direction. This outward flow, viewed from above in Figure 4.12(b), recirculates in the horizontal plane, impinging on the half-sphere from the $\phi = 0$ direction. This circulation is not entirely within the horizontal plane, but the vertical length scale of the circulation is very small compared to the horizontal length scale (roughly 0.5 cm and 10 cm, re-

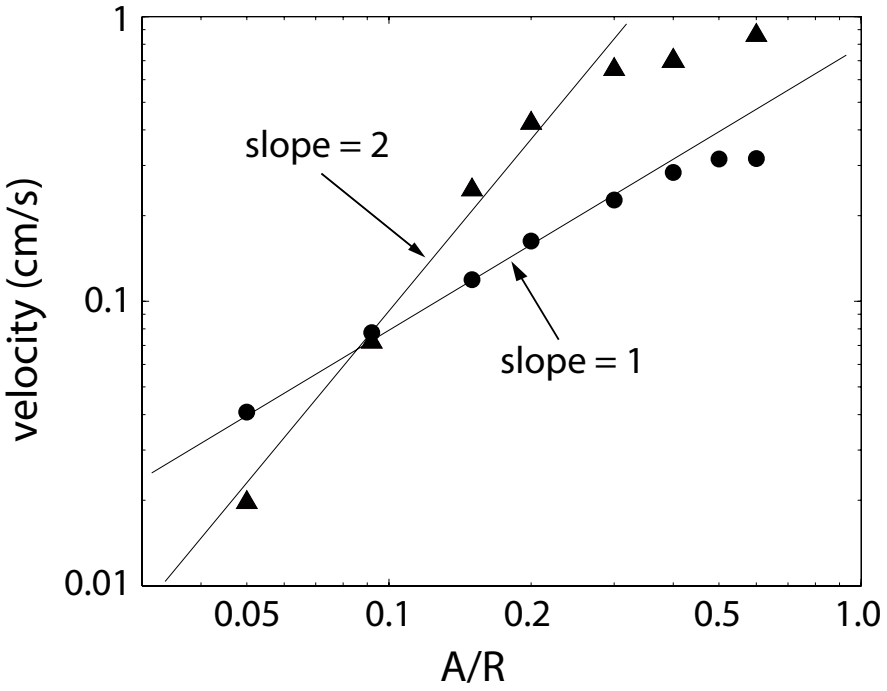

Figure 4.11: At low forcing amplitude, the flow velocity perpendicular to the forcing direction (triangles) varies as the forcing amplitude squared, indicating this flow arises from nonlinear interactions. In contrast, the internal wave velocity amplitude (circles) in the forcing plane increases linearly with forcing amplitude, as expected from linear inviscid theory, while for higher forcing ($A/R \gtrsim 0.3$), the velocity amplitude saturates (at 0.32 cm/s). The mean flow is computed 0.2 cm above the surface of the half-sphere at azimuthal angle $\phi = 90°$ and polar angle $\psi = \theta$. The wave amplitudes are the maximum along-beam velocity amplitudes of the top wave beams at $r/R = 5$. ($R = 3.25$ cm.) The uncertainties (less than 3%) are small compared to the size of the data points.

spectively). This is expected due to the suppression of vertical motion by the stratification.

4.3 Discussion

We have studied the internal wave generation process in numerical simulations and experiments for a model for tidal flow over three-dimensional seamounts. Our model is a horizontally oscillating stratified flow past a half-sphere on a plane.

In the forcing plane ($\phi = 0$), we find that the internal wave field is qualitatively similar to the 2D internal wave field generated by an oscillating cylinder. For flow over a half-sphere, the wave amplitude decreases with increasing angle ϕ away from the forcing direction and becomes zero perpendicular to the forcing direction. For low forcing amplitude, the wave field follows the angular dependence of the linear inviscid theory of Applyby and Crighton [*Appleby and Crighton*, 1987]. However, for $A/R > 0.2$ there are large deviations from that theory, and a larger fraction of the radiated energy is in the forcing direction. This is consistent with the previous work of Munroe and Lamb [*Munroe and Lamb*, 2005] and Holloway and Merrified [*Holloway and Merrifield*, 1999], who found that, despite the three dimensionality of the topography, most of the internal wave energy is radiated in the tidal forcing direction.

Wave radiation at large angles to the forcing direction is weak, but we have discovered that the 3D topography produces, surprisingly, a strong flow

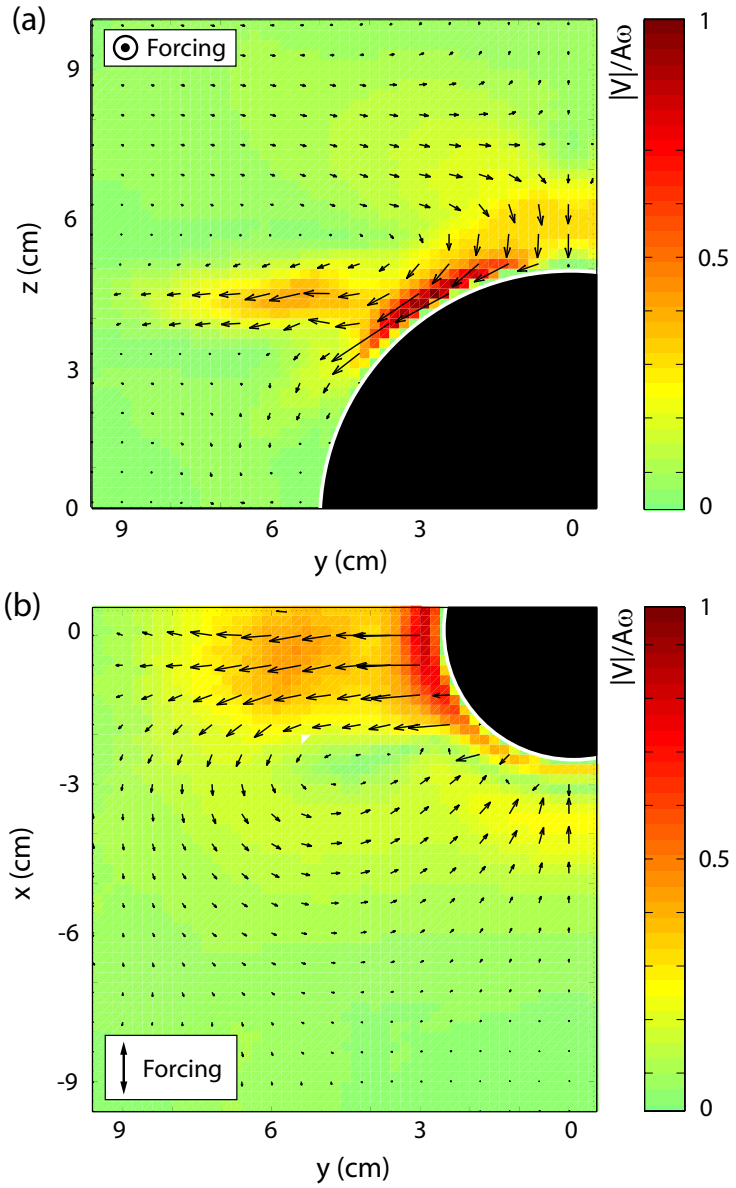

Figure 4.12: (a) Flow perpendicular to the vertical forcing plane is revealed by this plot of the average velocity field in the plane through the sphere center ($x = 0$). There is a strong flow outward along the y-axis. (In this figure, in-plane velocities are denoted by vectors and in-plane speeds by color.) (b) In the horizontal plane at $z = 4.25$ cm, one can see that the flow forms a closed circulation, returning to the sphere in the forcing direction. ($R = 5$ cm.)

in the plane *perpendicular* to the oscillating tidal flow. This perpendicular flow is a prominent effect, producing flow speeds comparable to the tidal flow speed. For low forcing, the perpendicular flow speed is proportional to the square of the forcing amplitude, indicating that this flow is a result of nonlinear interactions, probably between the internal waves being generated or between internal waves and the viscous boundary layer. In the ocean, strong flow perpendicular to a tidal flow could enhance material transport and mixing near bottom topography. Since the perpendicular flow is proportional to the square of the forcing amplitude, this flow will be especially strong near topography with small features (where the excursion parameter A/R will be large). In addition to a nonzero mean component, the nonlinear flow has a large component that oscillates at twice the forcing frequency, leading to the possibility of strong out-of-forcing-plane second harmonics when $2\omega < N$. This suggests that a significant fraction of the energy converted from the barotropic tide by bottom topography could be radiated in the direction perpendicular to the forcing.

Although linear theory and 2D simulations are good predictors of linear internal wave generation, we find that strong flows arise due to the three dimensionality of bottom topography. Our results should apply widely because even quasi-2D topographic features such as ridges have 3D roughness and ends where 3D effects can be significant. These effects manifest themselves across the entire excursion parameter range examined in this work, $0.05 < A/R < 0.6$, with the lower end of the range applying to large bottom topography, and the

higher end being more relevant to small topography or to 3D roughness on large topography.

Chapter 5

3D Topography: Gaussian Mountain

This work has been accepted for publication, and this chapter follows closely the article *King et al.* [2010]. There are two natural extensions of the work on tidal flow past the half sphere: (1) move to a more realistic model of bottom topography, and (2) generalize to the frequency regime $2\omega < N$ where second harmonics (internal waves at twice the tidal forcing frequency) are allowed by the dispersion relation Eq. 1.1.

We examine tidal flow past 3D topography for the case $2\omega < N$, and we find the boundary flow generates second harmonic internal tides that propagate away from the topography in the direction *perpendicular* to the tidal forcing. Again, we make the simplifying assumption that the Coriolis parameter $f = 0$. The model system is an axisymmetric Gaussian mountain of height 7 cm and $1/e$ half-width $\sigma = 2.85$ cm (see Figure 5.1a). This model geometry is chosen so that the maximum topographic slope is greater than the slope of both fundamental and second harmonic internal tide propagation. Two additional model topographic slopes (discussed in Section 5.1.2) are utilized to determine the effect of varying topographic slope on second harmonic generation. The axes are oriented in the same manner as in Chapter 4, with tidal forcing in

the x-direction, and z being the vertical direction. The buoyancy frequency $N = 1.5$ rad/s is independent of depth, and the tidal forcing frequency $\omega = 0.6$ rad/s. Inserting these values into Eq. 1.1 gives propagation angles of 23.6° for the fundamental internal tides at the tidal forcing frequency ω and 53.1° for second harmonic internal tides at 2ω.

Like the half-sphere, the Gaussian mountain studied here is supercritical (with respect to both the fundamental and second harmonic internal waves), but the Gaussian has the added advantage that it transitions smoothly into the sea floor. This is more realistic than the half-sphere, which has discontinuous slope where it meets the ocean bottom.

Three primary aspects of internal wave generation by tidal flow over the 3D Gaussian mountain are studied. The first aspect is the structure of the generated internal wave field, with emphasis on waves generated *perpendicular* to the tidal forcing direction. Included are detailed comparisons of numerical simulations and laboratory experiments for identical parameters. The second topic is the dependence of the generated internal wave field on the maximum slope of the Gaussian mountain. The final section presents the results from two methods of computing the power radiated into the internal wave field. The power radiated as internal waves *perpendicular* to the tidal forcing direction is shown to be a significant fraction of the total radiated power.

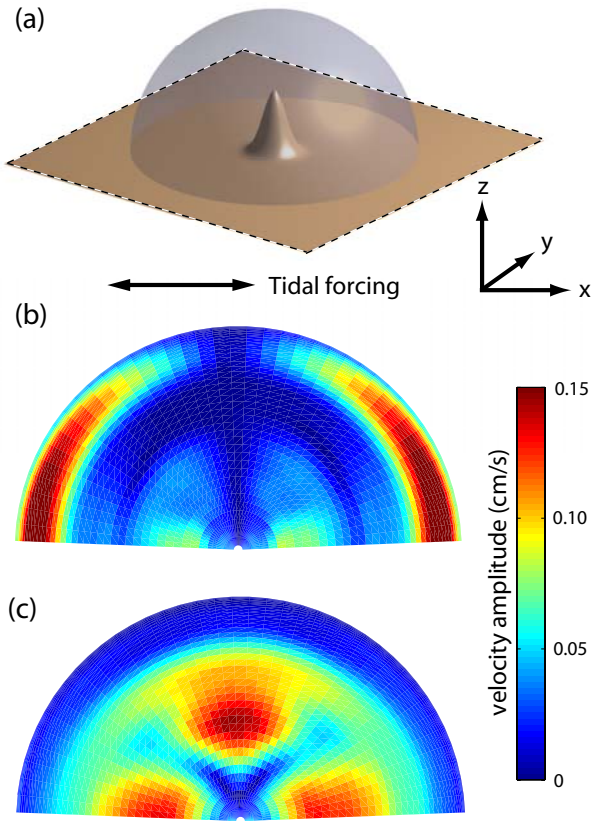

Figure 5.1: (a) A schematic diagram of the model topography, a 7 cm high Gaussian mountain with 1/e half-width $\sigma = 2.85$ cm. The transparent blue sphere with radius 15 cm is the imaginary visualization surface which is viewed from above (along the positive z-axis) in (b) and (c). (b) Fundamental and (c) second harmonic wave velocity amplitudes visualized near the topography for velocity components normal to the spherical surface depicted in (a). The out-of-forcing-plane second harmonic velocity amplitude in (c) is slightly stronger than the in-plane second harmonics, and is comparable in amplitude to the fundamental wave in (b). The dimensionless tidal forcing amplitude is $A/\sigma = 0.50$.

5.1 Results

The velocity amplitudes $A\omega$ of the internal tides crossing the spherical visualization surface in Figure 5.1a were obtained by fitting the time series of surface-normal velocity to sinusoidal components at the tidal forcing frequency ω and twice the tidal forcing frequency 2ω. The results for the ω component of the internal tide are shown in Figure 5.1b, which shows the $\cos\phi$ dependence on the azimuthal angle ϕ expected (for small forcing amplitudes) from the linear inviscid theory of *Appleby and Crighton* [1987]. Figure 5.1c shows that in addition to the expected second harmonics in the tidal forcing direction, there is also a second harmonic internal wave generated perpendicular to this direction. We will refer to internal tides in the $y = 0$ plane, which contains the tidal forcing direction, as 'in-plane' waves. Internal tides in the $x = 0$ plane, which is perpendicular to the tidal forcing direction, will be referred to as 'out-of-plane.' At high tidal forcing amplitude, the unexpected out-of-plane second harmonic wavebeam has amplitude comparable to the internal tides generated at the tidal forcing frequency.

A direct comparison between simulation and experiment is shown in Figures 5.2a-d. The comparison is made in the $x = 0$ plane, perpendicular to the forcing direction. For a quantitative comparison, Figures 5.2c and 5.2d show velocity profiles for both experiments and simulations at two phases of tidal forcing. The experimental results agree well with the simulations; both show a strong out-of-plane second harmonic wave.

Figure 5.4 at the end of this chapter shows direct *in-plane* comparisons

between experiment and simulation for 10 different forcing phases at 18° increments. Figure 5.5 shows similar comparisons at the same phases in the *out-of-plane* direction.

5.1.1 Dependence of Harmonics on Amplitude

The velocity amplitudes of the in-plane and out-of-plane second harmonic waves determined for tidal forcing amplitudes $0.0625 < A/\sigma < 1$ are shown in Figure 5.2e. The in-plane and out-of-plane harmonics both scale as the square of the forcing amplitude, as expected for a nonlinear generation process. At low forcing amplitudes, the in-plane harmonics are stronger than the out-of-plane harmonics, but the in-plane harmonics begin to saturate at a smaller forcing amplitude. At $A/\sigma \approx 0.4$, the out-of-plane harmonics become stronger, and at the highest amplitude reported here, $A/\sigma = 1$, the out-of-plane second harmonics have amplitude 36% greater than the in-plane second harmonics.

5.1.2 Dependence on Topographic Slope

Previous work has examined the effect of topographic steepness on the generation of internal tides [*Khatiwala*, 2003; *Munroe and Lamb*, 2005; *Balmforth and Peacock*, 2009]. The relevant dimensionless parameter is the ratio of maximum topographic slope to the slope of the generated internal waves. We have conducted numerical simulations for Gaussian mountains with height 7

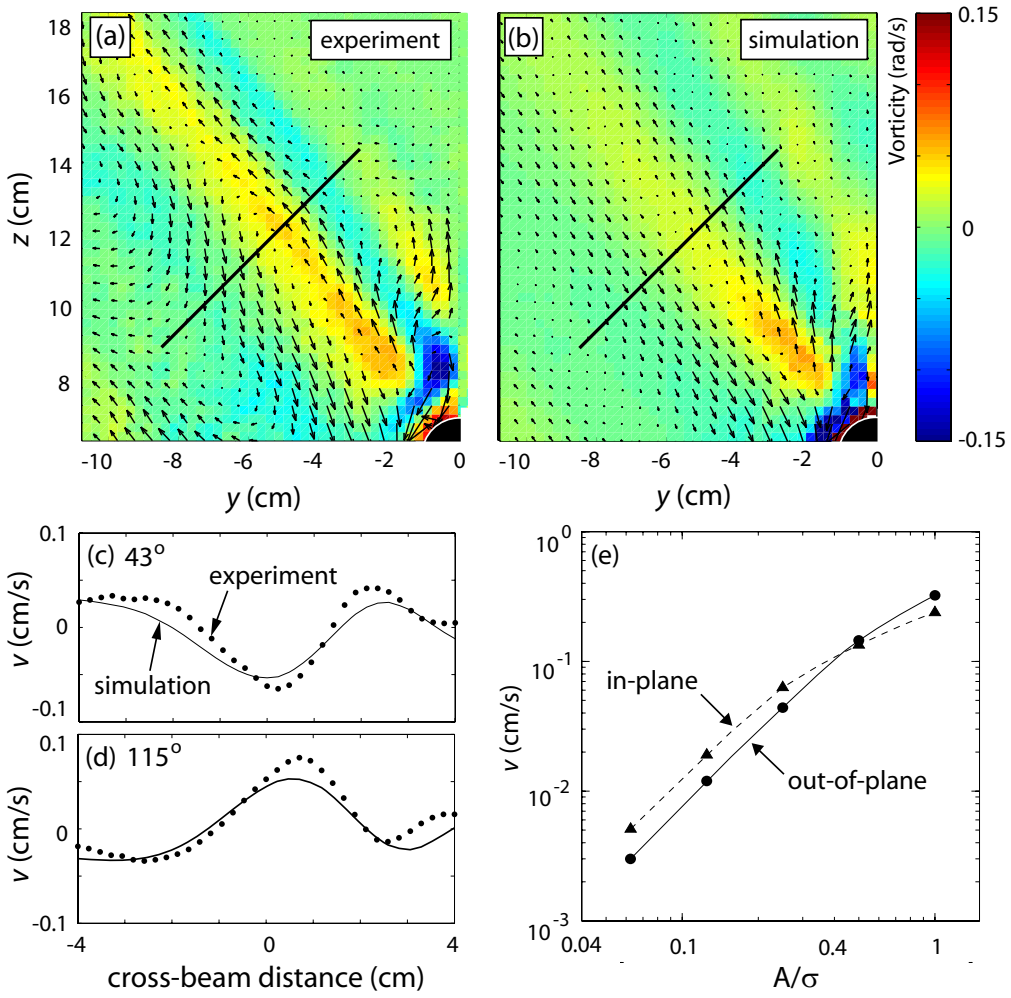

Figure 5.2: Snapshots of the out-of-plane second harmonics in (a) experiment and (b) simulation ($A/\sigma = 0.25$). The tip of the Gaussian mountain is in the lower right corner. Arrows denote instantaneous velocity, taken when the tidal flow is near its maximum, coming out of the page (phase 90°), and color represents vorticity. (c) and (d) Velocity profiles at phases 43° and 115°, respectively, along the diagonal lines in (a) and (b) (the velocity component is along the beam direction). (e) Second harmonic velocity amplitude dependence on tidal forcing amplitude at distance $r = 15$ cm from the origin. The in-plane harmonics (triangles) and out-of-plane harmonics (circles) both scale quadratically with forcing amplitude for small forcing, as expected. The in-plane harmonics begin to saturate at lower tidal forcing amplitude than the out-of-plane harmonics.

cm and three different maximum topographic slopes S_{max}. Using the relation,

$$S = \sqrt{\frac{\omega^2}{N^2 - \omega^2}}, \tag{5.1}$$

the three topographic slopes can be compared to the slopes for the fundamental wave S_1 and the second harmonic wave S_2, as shown in Figure 5.3, both in the in-plane (left-hand panels) and out-of-plane (right hand panels) directions. The topography in the top two panels (a) and (b) is the same as that used in the previous sections of this study. The maximum slope of this topography is greater than the slope of both the fundamental and second harmonic beams (i.e., the topography is 2ω-supercritical), resulting in downward-propagating internal tides at frequencies ω and 2ω, in addition to the normal upward propagating internal tides.

Fundamental waves are absent in the out-of-forcing plane direction, Figure 5.3b, as expected from linear inviscid theory [*Appleby and Crighton*, 1987]. Figures 5.3c and 5.3d show results for topography with maximum slope greater than S_1 but less than S_2 (ω-supercritical topography). As expected, there are upward and downward propagating fundamental waves but only upward propagating second harmonic waves in the forcing direction (c). Second harmonics are also generated in the out-of-forcing plane direction (d), but they only propagate upward, unlike the harmonics on the (2ω-supercritical topography (b), which has upward and downward propagating second harmonics.

Figures 5.3e and 5.3f show topography with maximum topographic slope less than both S_1 and S_2 (subcritical topography). In this case, waves

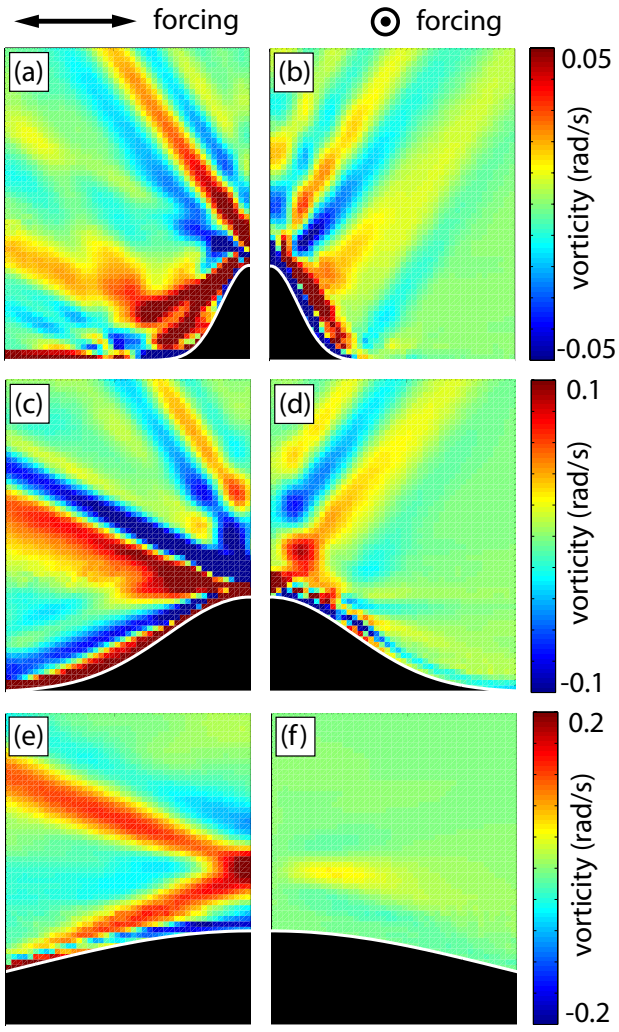

Figure 5.3: Vorticity snapshots of simulation results in the forcing plane and perpendicular to the forcing plane for (a)-(b) $S_2 < S_{max}$ (2ω-supercritical) , (c)-(d) $S_1 < S_{max} < S_2$ (ω-supercritical), and (e)-(f) $S_{max} < S_1$ (subcritical), where $S_1 = 0.436$ and $S_2 = 1.33$ are respectively the slopes of the fundamental and second harmonic, and S_{max} is the maximum topographic slope (2.11, 0.693, and 0.249 for the 7 cm high mountains with $1/e$ half-widths 2.85 cm, 8.66 cm, and 24.1 cm, respectively). The snapshots are taken when the tidal forcing flow is at its maximum, coming out of the page; note the difference in colorbars for the three different topographies. Each panel shows a fluid region 18 cm wide $\times$ 23 cm high.

at the tidal forcing frequency occur only in the forcing direction, and internal tides are absent in the out-of-forcing plane direction. As expected, more of the barotropic tide is converted to internal tides for the wider Gaussian mountains, as these mountains present a greater obstacle to the tidal flow. In the top two cases, however, the out-of-plane harmonics are comparable in strength to the in-plane harmonics and fundamental wave beams.

5.1.3 Energy Flux

To determine the internal tidal energy radiated perpendicular to the tidal forcing direction, we first separate the barotropic and baroclinic components of the pressure and velocity. The barotropic components of the pressure and velocity perturbations are obtained from the x-component of the Navier-Stokes equation and are given by:

$$p'_{bt} = -A\omega^2 x \cos \omega t, \tag{5.2}$$

$$u'_{bt} = A\omega \sin \omega t. \tag{5.3}$$

Far from the topography, where the barotropic flow can be assumed to be largely unaffected by the presence of the topography, we can subtract the above quantities from the total perturbation pressure and velocities to obtain the baroclinic perturbation quantities, p'_{bc} and u'_{bc}, associated with the internal tides. Integrating across an arbitrary surface for one tidal forcing period gives the period-averaged radiated power,

$$P = \frac{\omega}{2\pi} \iint p'_{bc} \mathbf{u}'_{bc} \cdot d\mathbf{A}\, dt, \tag{5.4}$$

To differentiate between energy contained in fundamental and second harmonic internal tides, the velocity and pressure fields from simulation results are first fit to harmonic functions of the form:

$$[u(t), v(t), w(t), p(t)] = C + \sum_{n=1}^{4} B_n sin(n\omega t + \phi_n), \tag{5.5}$$

It is necessary to include terms at three and four times the tidal forcing frequency because motions at these frequencies are produced by nonlinear interactions between the ω and 2ω flow components, especially at higher tidal forcing amplitude. Equation 5.4 is evaluated separately for the fundamental and second harmonic internal tides using the $n = 1$ and $n = 2$ (respectively) parameters obtained from the fit to Eq. 5.5. The in-plane and out-of-plane second harmonics are reasonably distinct (see Figure 5.1c), but there is a small overlap due to the finite spatial extent of the wave beams. For simplicity, we consider second harmonic waves within 45° of the tidal forcing direction to be in-plane harmonics, with the out-of-plane second harmonics being defined outside these limits. Table 5.1.3 summarizes the results for four tidal forcing amplitudes.

5.1.3.1 A refined energy flux analysis

The foregoing energy analysis makes the zeroth-order assumption that the disturbance to the background tidal flow caused by the topography is negligible far from the topography. While this is a reasonable assumption, we also briefly consider a first-order correction, where the disturbance to the

Table 5.1: Power radiated into second harmonic internal tides for four tidal forcing amplitudes. The first row gives the total power radiated into internal tides by the topography. The following rows give the percentages of the total radiated power contained in in-plane and out-of-plane second harmonics, respectively.

Tidal Amplitude (A/σ)	0.125	0.25	0.5	1
Total radiated power ($\times 10^{-7}$ W)	1.3	4.9	20	59
In-plane harmonics	1.1%	3.9%	9.8%	19%
Out-of-plane harmonics	0.70%	2.6%	8.1%	16%

background tidal flow is approximated by performing sister barotropic computations without stratification [*Khatiwala*, 2003]. All previous simulations are re-evaluated in the absence of stratification to obtain the barotropic pressure p'_{bt} and velocity u'_{bt} (rather than obtaining them from the Navier-Stokes equations, as in Equations 5.2 and 5.3), and the perturbation pressure and velocity p'_{bc} and u'_{bc} are then derived by subtracting these newly found barotropic variables from their corresponding values from the previous stratified simulations. This method of computing the barotropic pressure and velocity fields is more accurate than the previously discussed method, but operates on the assumption that the barotropic and baroclinic pressure and velocity fields are completely decoupled and do not interact. This assumption is valid as long as tidal forcing, and hence nonlinear effects, is not too large. This refined energy analysis is performed for tidal forcing amplitudes A/R= 0.25, 0.5, and 1, and the results are displayed in Table 5.1.3.1. A quick comparison between the total radiated energy figures in the two energy flux computation methods

Table 5.2: Power radiated into second harmonic internal tides for three tidal forcing amplitudes, utilizing the energy analysis method of *Khatiwala* [2003]. The first row gives the total power radiated into internal tides by the topography. The following rows give the percentages of the total radiated power contained in in-plane and out-of-plane second harmonics, respectively.

Tidal Amplitude (A/σ)	0.25	0.5	1
Total radiated power ($\times 10^{-7}$ W)	4.1	16.5	49.9
In-plane harmonics	4.7%	11.8%	22.6%
Out-of-plane harmonics	3.1%	9.7%	19.2%

shows that the two methods typically agree on the power radiated into second harmonics, but the first method tends to overestimate the total rate of energy conversion, especially at high tidal forcing amplitudes. This results in a lower percentage of the power radiated being comprised of second harmonics. This more refined method of computing energy flux shows that up to 19.2% of the radiated power is emitted as out-of-plane second harmonics (compared to 16% for the previous method).

At small tidal forcing amplitude, the power radiated as second harmonics is negligible. However, since the amplitude of the harmonic waves has a quadratic dependence on tidal forcing amplitude, their contribution to the wave field becomes significant with increasing forcing amplitude. At forcing amplitude $A/\sigma = 1$, 35% of the radiated power is in second harmonics, with 16% being radiated perpendicular to the forcing plane. These unexpected waves could be an additional source of mixing energy near bottom topography.

5.2 Discussion

Existent models for internal wave generation do not include the possibility of the generation of internal tides perpendicular to the tidal forcing direction. However, we find strong perpendicular internal tides in our laboratory experiments and direct numerical simulations of tidal flow over a Gaussian mountain. For low tidal forcing amplitudes, the fraction of energy contained in internal tides in the out-of-plane direction is very small. However, at larger forcing amplitudes, corresponding to physical cases of large tidal excursion distance or small topography, the out-of-plane internal tides become significant. These perpendicular internal tides could affect parametrizations of internal tide generation in the ocean, especially in regions of small scale topographic roughness where the excursion parameter is large and nonlinear effects such as second harmonic generation become important. Indeed, Nycander [*Nycander*, 2005] has shown that 3D roughness and small topographic features on larger topography produce stronger internal tides than previously thought. Further, *Muller and Buhler* [2009] recently found that topographic features with horizontal length scales less than 10 km have a large effect on the presence of instabilities in the internal tides that are generated. These studies indicate that the large excursion parameter (large tidal forcing amplitude) regime could be more significant in the ocean than previously thought. As a result, a significant amount of the energy converted from barotropic to baroclinic tides can be generated perpendicular to the tidal forcing direction.

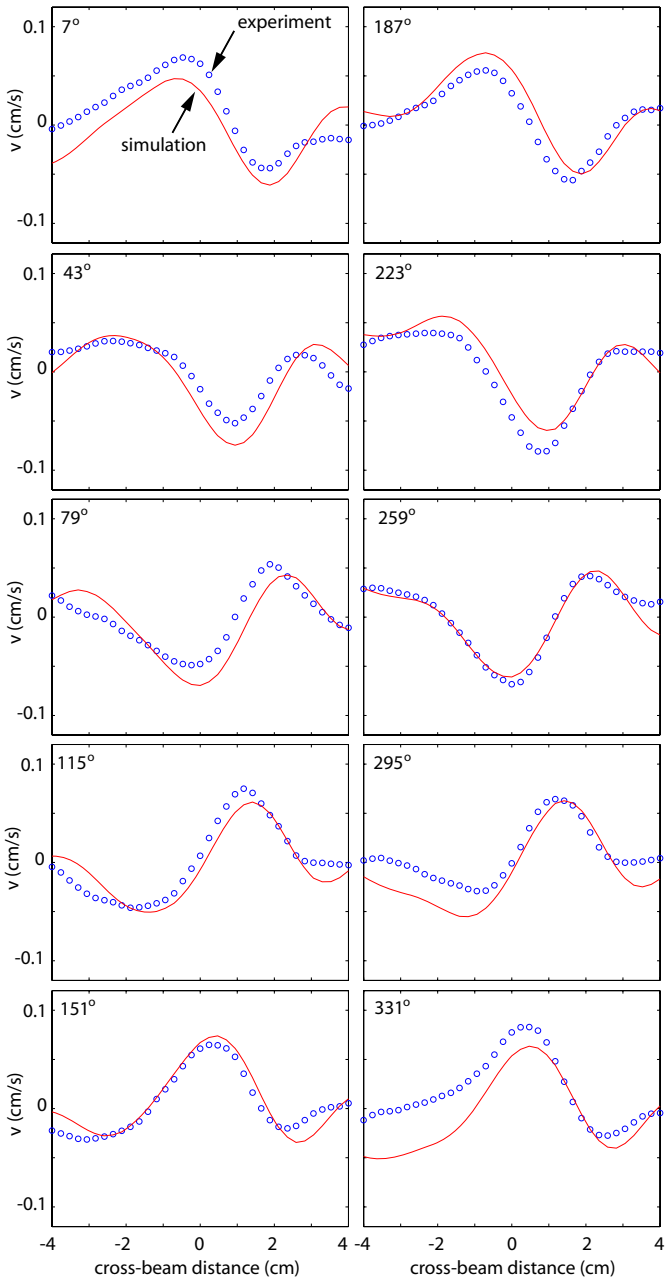

Figure 5.4: Comparison of numerical (red) and experimental (blue) data at 36° phase increments. The cross sections are taken 8 cm from the Gaussian topography, in the *in-plane direction*.

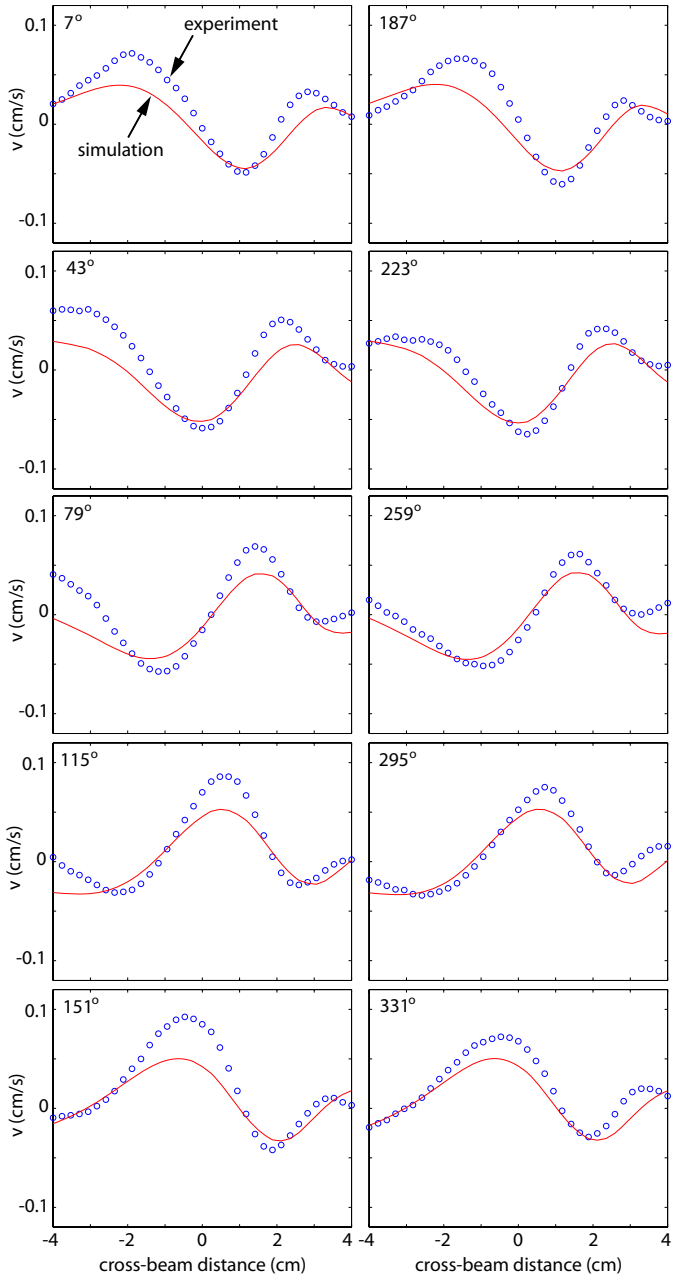

Figure 5.5: Comparison of numerical (red) and experimental (blue) data at 36° phase increments. The cross sections are taken 8 cm from the Gaussian topography, in the *out-of-plane direction*.

Chapter 6

Turning Points in the deep ocean

In certain regions of the deep ocean, it is possible that the water has been thoroughly mixed, reducing the vertical density gradient, and hence the local buoyancy frequency $N(z)$ to the point where the internal wave dispersion relation (Eq. 1.1) is undefined and an internal wave at the semidiurnal tidal frequency would be unable to propagate. Such mixed regions in the deep ocean would be bounded above by so called 'turning points,' where $N(z)$ passes through the critical value $N(z) = \omega_{M2}$. The possibility of turning points in the deep ocean has been acknowledged, most notably by *Munk* [1981], but the potential existence and consequences of turning points have not been systematically explored by examining oceanic data. We present a thorough analysis of the World Ocean Circulation Experiment data to determine if and where turning points exist, and we find that they are in fact common in many regions of the deep ocean. We also perform numerical simulations of internal waves interacting with these turning depths to shed light on the possible consequences of these well mixed regions. Before presenting the results, it is necessary to discuss a nearly universal approximation that breaks down in the case of the weak stratification which occurs near the sea floor.

6.1 Limitations of the Traditional Approximation

In many regions of the ocean, particularly at mid and high latitudes, the Coriolis force becomes a significant factor in determining internal wave dynamics. Therefore any realistic analysis of internal wave propagation in the ocean needs to account for rotational effects. To include rotational effects in the internal wave dispersion relation derived in Section 2.2.2, the full Coriolis corrections must be added to the Navier-Stokes equations (Eqs. 2.4-2.6), again written in linear inviscid form:

$$\frac{\partial u}{\partial t} - fv + \tilde{f}w = -\frac{1}{\rho_o}\frac{\partial p'}{\partial x} \tag{6.1}$$

$$\frac{\partial v}{\partial t} + fu = -\frac{1}{\rho_o}\frac{\partial p'}{\partial y} \tag{6.2}$$

$$\frac{\partial w}{\partial t} - \tilde{f}u = -\frac{1}{\rho_o}\frac{\partial p'}{\partial z} - \frac{\rho'}{\rho_o}g \tag{6.3}$$

where

$$f = 2\Omega \sin\phi, \quad \tilde{f} = 2\Omega \cos\phi \tag{6.4}$$

and Ω is the angular frequency of earth's rotation ($\Omega = 7.272 \times 10^{-5}$ rad/s), and ϕ is the latitude [*Gerkema and Zimmerman*, 2008]. Table 6.1 summarizes the new variables, along with variables that have been previously defined.

The nearly universal 'Traditional Approximation' consists of neglecting the $\tilde{f}$ terms, which involve the cosine of the latitude. This approximation can normally be made in oceanic internal wave studies because, throughout most of the water column, $N(z)$ is much greater than ω_{M2}, resulting in predominantly horizontal internal wave propagation (by the dispersion relation Eq. 1.1).

Table 6.1: Summary of variables used in this section, including the newly defined Coriolis corrections f and $\tilde{f}$.

Ω	angular velocity of earth (7.272×10^{-5} rad/s)
ϕ	latitude
ω	internal wave angular frequency ($\omega_{M2} = 1.405 \times 10^{-4}$ rad/s)
θ	internal wave propagation angle, measured from the horizontal
f	$2\Omega \sin\phi$
$\tilde{f}$	$2\Omega \cos\phi$
$\omega_{min,max}$	minimal and maximum permissible internal wave frequencies
α	wave propagation angle, measured counterclockwise from east

Since the fluid motion is then mostly horizontal, it is expected that the vertical velocity is small, and hence the $\tilde{f}$ Coriolis correction term multiplying w in Eqs. 6.1 can be neglected. In addition, the $\tilde{f}$ term in Eq. 6.3 is often neglected since stratification tends to suppress vertical motions, resulting in small vertical accelerations. This is the so-called 'Traditional Approximation,' and results in a modified dispersion relation which includes first-order rotational effects [*Gerkema and Zimmerman*, 2008]:

$$\omega^2 = N^2(z)\sin^2\theta + f^2\cos^2\theta \tag{6.5}$$

Inclusion of rotational effects places an additional bound on the internal wave frequency:

$$\omega_{min} = min(|f|, N(z)), \quad \omega_{max} = max(|f|, N(z)) \tag{6.6}$$

resulting in:

$$f < \omega < N(z) \quad or \quad N(z) < \omega < f \tag{6.7}$$

depending on if $|f|$ or $N(z)$ is larger. The first scenario of Eq. 6.7 is by far more common in the ocean, and this will be assumed to be the case in further discussion unless otherwise noted. (The second relation can occur in the deep ocean at high latitudes where $|f|$ becomes greater than $N(z)$.)

Turning points, by definition, occur when $N(z) = \omega_{M2}$, and internal wave motion is predominantly vertical as the turning point is approached. This means that the traditional approximation breaks down, and the $\tilde{f}$ terms in the governing equations can no longer be ignored. Inclusion of the full Coriolis correction results in the full internal wave dispersion relation [*Gerkema and Zimmerman*, 2008]:

$$\omega^2 = N^2(z)\sin^2\theta + 4\Omega^2(\sin\alpha\cos\phi\sin\theta + \sin\phi\cos\theta)^2, \tag{6.8}$$

where α is the angle of the internal wave vector $\vec{K}$ measured counterclockwise from the east direction. There are many consequences of inclusion of the entire Coriolis correction for various ocean flows [*Gerkema et al.*, 2008], including two effects relevant to this work: (1) ω_{min} and ω_{max} become more complicated and drastically alter the propagation regimes of internal waves in the deep ocean from that of Eq. 6.7. (2) The presence of the angle α introduces additional horizontal anisotropy into the background fluid, affecting zonally- and meridionally-propagating internal waves differently

6.1.1 Modified frequency range

Using the full Coriolis correction, the permissible frequency range for internal wave propagation (Eq. 6.7) becomes [*Gerkema and Zimmerman*, 2008]:

$$\omega_{min,max} = \frac{1}{\sqrt{2}} \left([N^2 + f^2 + f_s^2] \mp \{ [N^2 + f^2 + f_s^2]^2 - (2fN)^2 \}^{1/2} \right)^{1/2} \quad (6.9)$$

Figure 6.1 shows a comparison of ω_{min} and ω_{max} with and without the traditional approximation. N is normalized to 2Ω since 2Ω appears frequently in Eq. 6.9. The difference between ω_{min} with and without the traditional approximation only becomes apparent when $N/2\Omega \lesssim 1$, with the difference being especially pronounced at high latitudes. The difference in ω_{max} is apparent when $N/2\Omega \lesssim 2$, with the difference being more pronounced at low latitudes.

One of the main results of not using the traditional approximation is that ω_{min} goes to zero at high latitudes and where N is very small. This is in stark contrast to the traidtional approximation, which says that $\omega_{min} = min(|f|, N)$ (Eq. 6.7). The other main difference is that regardless of how small both $|f|$ and N become, ω_{max} asymptotically approaches the value 2Ω, meaning that for internal waves propagating meridionally, *there are no turning depths*. This point is also illustrated in Figure 6.2, which compares ω_{max} for a meridionally propagating internal wave at 45° latitude with and without the traditional approximation. Figure 6.3 generalizes these results to arbitrary internal wave propagation direction. ω_{max} is plotted versus latitude for many wave propagation angles α. For the case $\alpha = 0$ (east-west internal waves), the traditional approximation yields exact results, with $\omega_{max} = \omega_{M2}$ at all

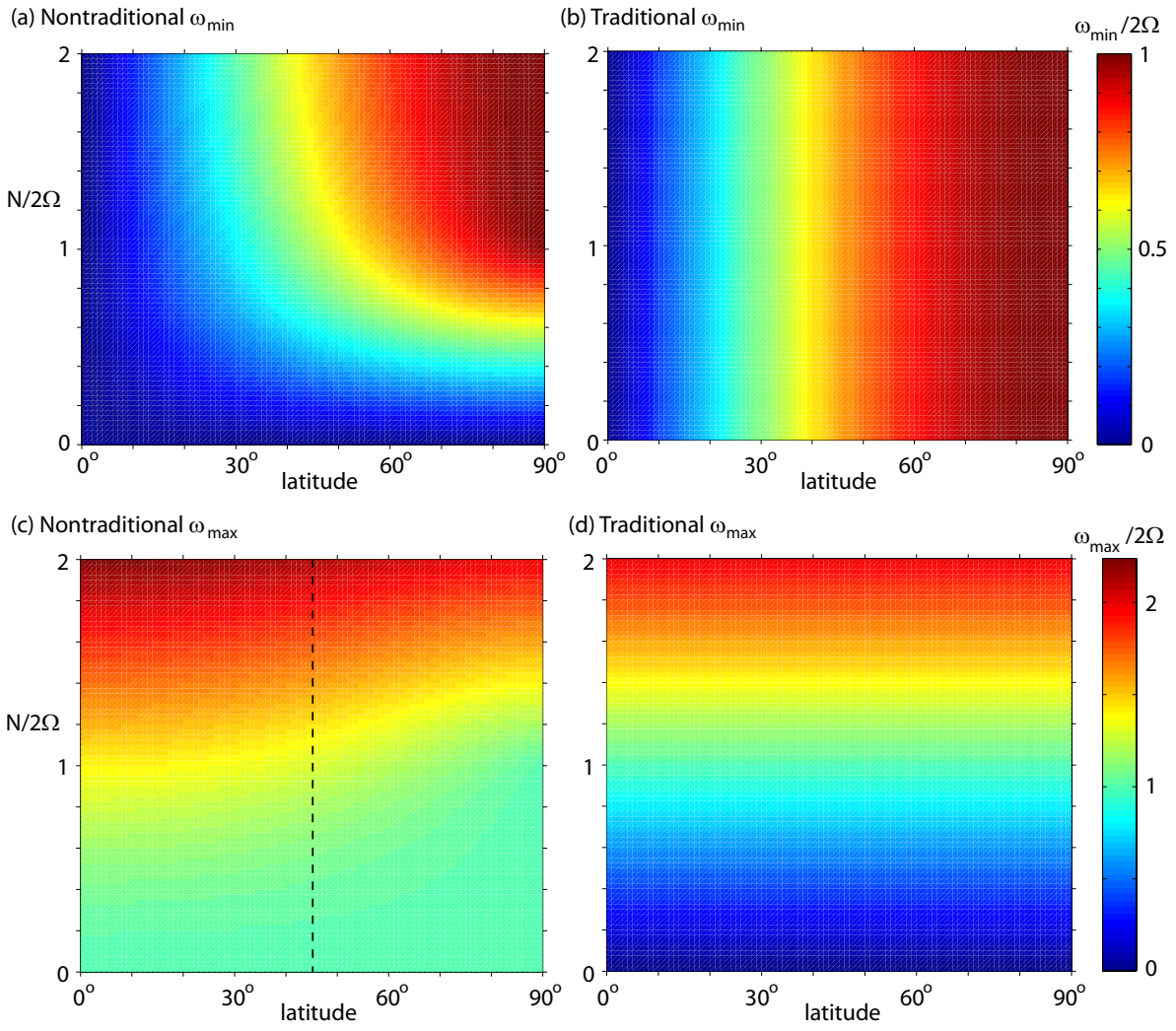

Figure 6.1: Comparison of internal wave frequency bounds for the weakly stratified deep ocean for the case of Meridional internal waves (waves propagating in the north-south direction). (a) and (b) show ω_{min} without and with making the traditional approximation, respectively. (c) and (d) show ω_{max} without and with making the traditional approximation, respectively. The dashed black line in (c) denotes the location of the cross section shown in Figure 6.2.

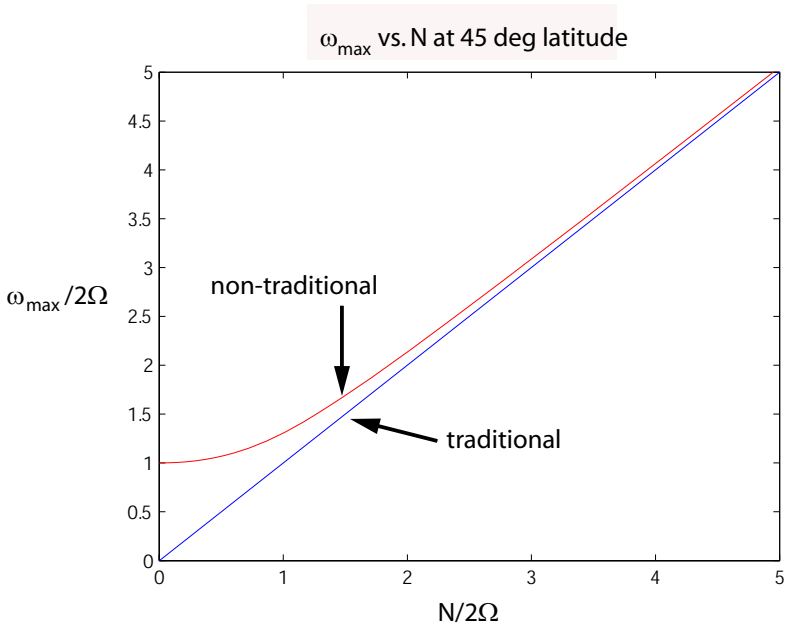

Figure 6.2: Comparison of ω_{max} with (blue) and without (red) the traditional approximation for a meridional internal wave. This indicates the absence of turning points for internal waves propagating in the north-south direction.

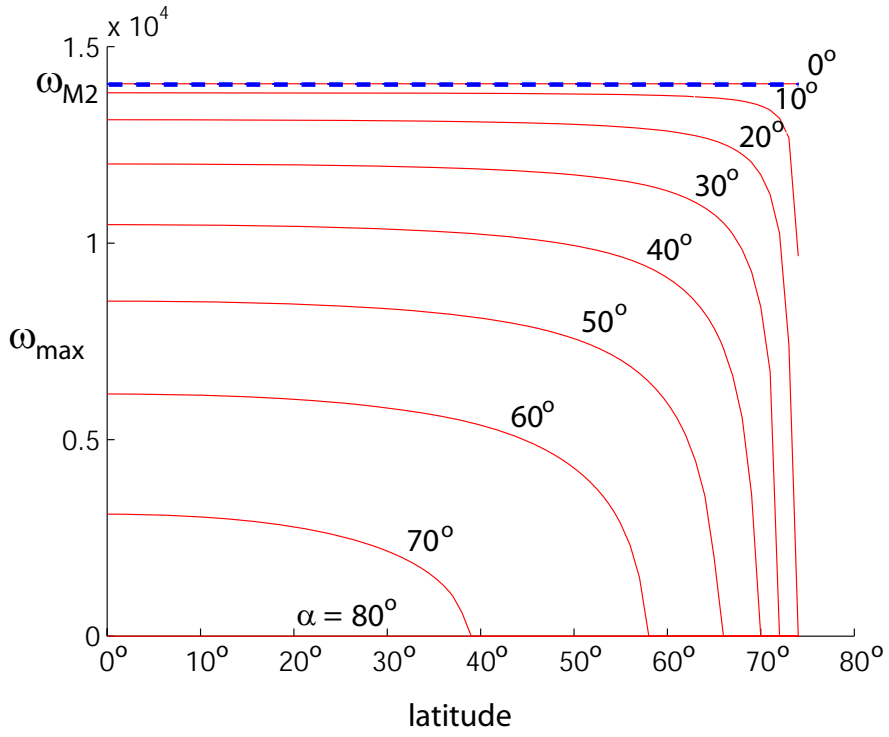

Figure 6.3: ω_{max} vs. latitude for wave propagation angles α (red lines) using the full Coriolis correction. The result from the traditional approximation is denoted with the dashed blue line. The traditional approximation is only correct for east-west propagating waves ($\alpha = 0$). Based on figure from private communication with Gerkema.

latitudes (assuming $N > |f|$). As α becomes larger (the wave vector has a larger component in the north-south direction, ω_{max} becomes continually smaller, becoming zero at higher latitudes. When $f = \omega_{M2}$ ($2\Omega \sin\phi = \omega_{M2}$), ω_{max} becomes zero at all latitudes, meaning there are no turning depths for propagation angles greater than $\alpha = 75°$.

For the purpose of simplicity, the analysis of turning points presented in the remainder of this chapter will strictly apply only to internal waves

traveling in the east-west direction, as internal waves traveling in the north-south direction cannot have turning points. As can be seen in Figure 6.3, the following simple analysis where the criterion $N(z) < \omega_{M2}$ is used to identify turning depths is also reasonably accurate for $\alpha \lesssim 30°$, since nontraditional effects don't significantly reduce ω_{max} at low and mid latitudes.

6.2 Turning depths from the simple filtering scheme

6.2.1 Individual casts

Figure 6.4 shows $N(z)$ profiles from two locations, with several individual casts being averaged to compute the profiles (with the filtering scheme described in Section 3.3.1). The casts that are averaged are located within 1° clusters. The bold black lines in (b) and (c) denote the average $N(z)$ profiles (averages are taken after all other filters have been applied), and the alternating red and blue lines show the individual casts, translated to the right for better visibility. Both examples are taken near deep trenches, as these regions consistently show turning points far above the sea floor. Recall from Section 6.1 that these turning points only apply to internal waves propagating in the east-west direction. (b) is located near the Philippine Trench, and (c) is located near the Middle America Trench. It is clear that, in these cases, $N(z)$ does not vary strongly in space below roughly 3 km depth. In addition, the first two and the last five casts in (b) were taken on separate cruises roughly two years apart, showing that, in at least this example, the $N(z)$ profile is not changing significantly over time below 3 km. Spatial variations in $N(z)$ are

discussed fully in Section 6.3.3.

6.2.2 Transects

Figure 6.5 shows three transects of WOCE cruises which contain extended regions where the local $N(z) < \omega_{M2}$. In (a), the mixed region occupies a deep basin (the Philippine Sea) and in (b), the mixed region occupies the Venezuelan Basin, which, below roughly 1500 m, is bounded on all sides by topographic features. (c) shows a mixed region in the North Pacific which is bounded on the north and south, but not on the east and west. These three examples are typical of extended mixed regions, which are often bounded by topography.

Figure 6.6a shows an unusual example (in the cruise P15) of a mixed region which is not bounded by large scale bottom topography. This mixed region is most likely contiguous with the mixed region at the same latitude in cruise P14, as cruises P14 and P15 are parallel and separated by roughly 1000 km. In the previous cases, elevated mixing could be caused when bottom currents enter a basin by flowing over bottom topography. However, this explanation is insufficient to explain the unbounded case in Figure 6.6a.

Figure 6.6b shows the A05 transect, which passes over the Mid-Atlantic Ridge. Despite the fact that much mixing in the deep ocean occurs over rough topography [*Polzin et al.*, 1997], rough topography alone does not guarantee the presence of a well mixed bottom layer, as can be verified by examining the N^2 values near the rough bottom on the Mid-Atlantic Ridge. However, there

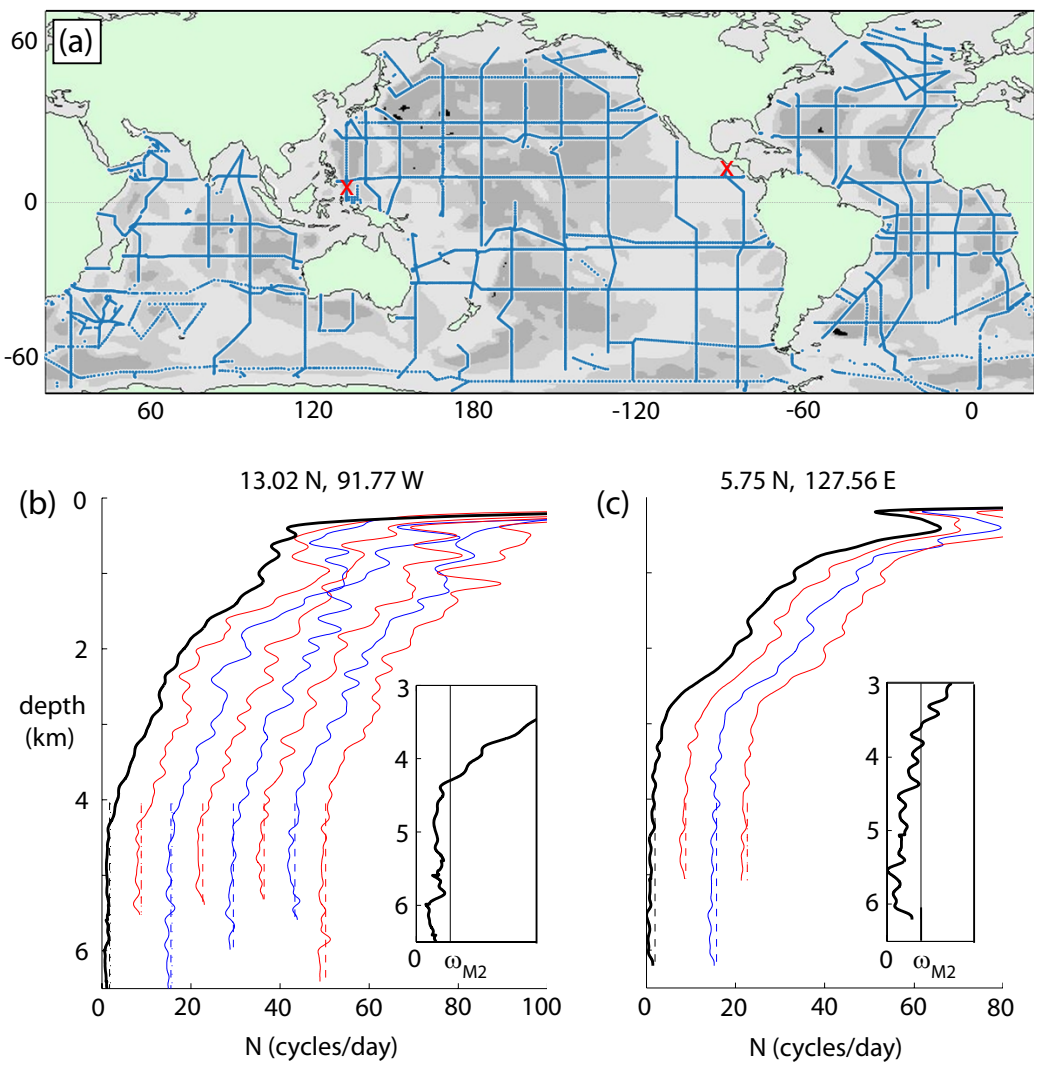

Figure 6.4: (a) The WOCE cast map, with red 'X's denoting the locations of the clusters of casts in (b) and (c). Average $N(z)$ profiles are shown with bold black lines, with individual casts in alternating red and blue. The dashed lines denote ω_{M2} for each cast. The insets of (b) and (c) are close up plots of the average $N(z)$ profiles. Small horizontal jogs occur in the average profiles wherever individual casts run out near the bottom.

are localized patches near the ridge where $N^2 < \omega_{M2}^2$, which is consistent with recent observational results of elevated mixing rates near rough topography [*Polzin et al.*, 1997; *Toole et al.*, 1997; *Ledwell et al.*, 2000].

The fact that well-mixed regions tend to be bounded by topography (often times being constrained to nearly completely enclosed basins, such as the Venezuelan Basin in Figure 6.5b), supports three possible explanations for the mixed water: (1) Elevated internal wave generation by the surrounding topographic features translates to elevated mixing within the basin. This has been documented near the Luzon Strait [*Echeverri et al.*, 2010], which is close to the transect in Figure 6.6a. (2) The mixing rate in the enclosed basin is not elevated, but due to the fact that the water mass in the basin is relatively 'old,' the normal mixing rate has had longer to homogenize the water mass. (3) The local mixing rate is not elevated, but water only enters the basin through one or more discrete locations, such as gaps in a ridge, so that the incoming water has properties that are uniform over long time periods. Due to a lack of abrupt topography, (2) or (3) are the more likely explanations for the basin-confined mixed region in Figure 6.5b.

We also utilize dissolved gas concentration data from the World Ocean Atlas 2005 (WOA2005) to show that the water masses in bounded basins have noticeably different properties than the surrounding water. The World Ocean Atlas was a project which analyzed WOCE data (including the CTD data we analyze as well as many other types of data including dissolved gas data from sample bottles), and interpolated this data to a global 1° grid having

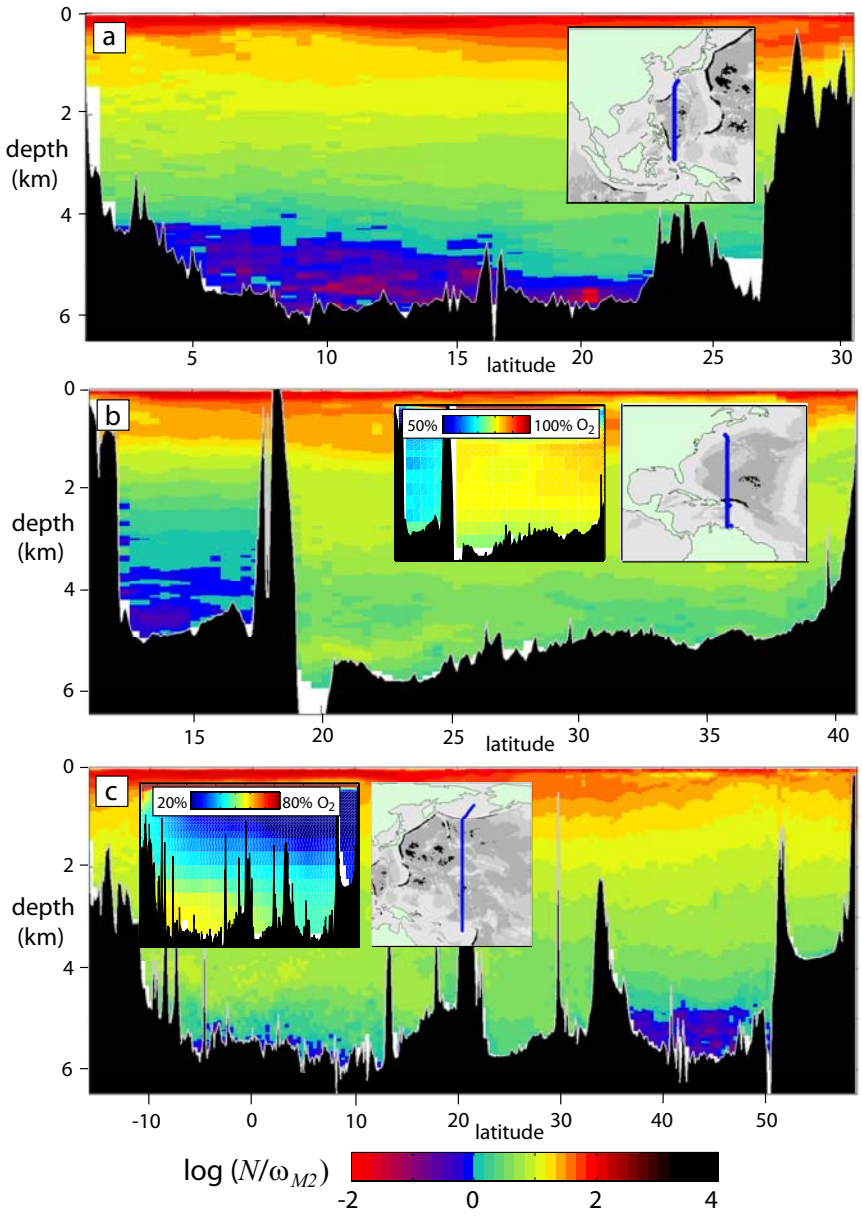

Figure 6.5: WOCE cruise transects from the (a) P08, (b) A22, and (c) P14 meriodional cruises. The mixed regions (dark blue to red in color) where eastward or westward propagating M_2 internal tides are forbidden cover large geographical areas in the deep ocean. The mixed regions in all three transects are bounded by topographic features. The inset boxes display regional maps with the cruise locations denoted by blue lines.

10 m vertical resolution near the surface and 500 m vertical resolution in the deep ocean. The simplest physical quantity to examine is the concentration of dissolved oxygen, which can be used to infer a rough 'age' of a given water mass. Water is oxygenated at the ocean surface, after which the dissolved oxygen is gradually removed. Lower dissolved oxygen content implies water that has been below the surface for a longer period of time. It is nontrivial to use dissolved oxygen to establish a quantitative age, but the relative ages of different water masses can easily be established.

The dissolved oxygen content from the World Ocean Atlas database is interpolated along the cruise tracks of interest, and the results from two cruises are displayed as insets in Figures 6.5b and 6.5c. These insets show a stark contrast between the dissolved oxygen levels observed within enclosed basins and in surrounding waters. The quantity plotted is the percent oxygen saturation, which is the percentage of the observed oxygen level relative to the saturation level at the local temperature and salinity values. In Figure 6.5b, the dissolved oxygen in the enclosed Venezuelan Basin is at roughly 70% of its saturation value, while the water outside the basin has values closer to 80%.

These differences in dissolved gases indicate that, in addition to water masses in enclosed basins being well mixed, the water is either 'older' than the surrounding water masses or comes from a different source. In either case, water properties besides the density can be used to determine how likely a given water mass is to be well mixed.

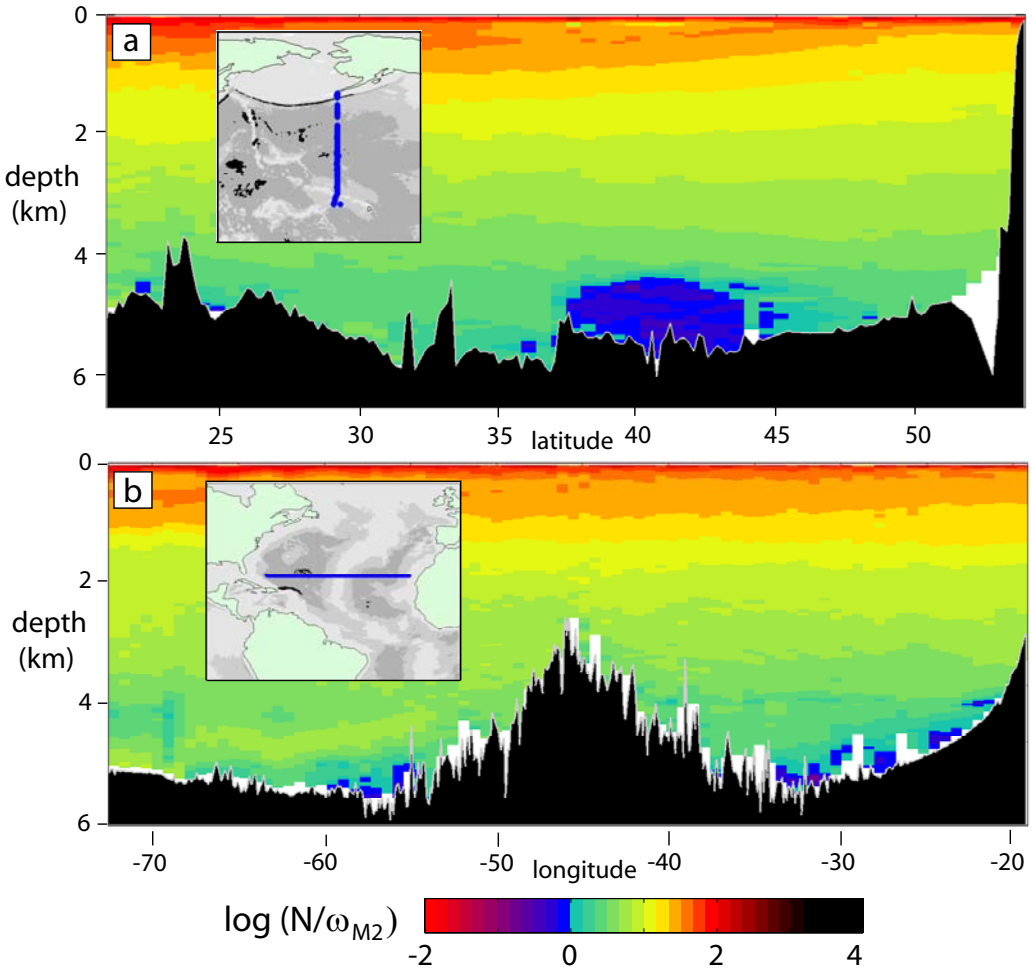

Figure 6.6: WOCE cruise transects from the (a) P15 and (b) A05 cruises. P15 is an example that contains a mixed region without bounding topography. A05 contains small pockets of well mixed fluid near the Mid-Atlantic Ridge.

6.2.3 Analysis on a global scale

We use two methods to display the results of analysis on 18,000 WOCE casts. Figure 6.7a shows the same map of the WOCE cruises as in Figure 3.13, with the individual WOCE casts now scaled in size and color saturation based on the height of the turning point (where present) above the sea floor. Casts without turning points or turning points less than 40 m from the sea floor are represented by small blue dots. Casts with turning points a minimum of 40 m above the sea floor are color coded red, with diameter proportional to the height of the turning point above the sea floor. This figure shows that there are several large regions which contain well mixed layers in the deep ocean. Particular areas of interest are the Philippine Sea, the Northern Pacific Ocean, and Venezuelan Basin. Other regions with widespread turning depths are the central Indian Ocean, the Pacific Ocean northeast of New Zealand, and various regions in the Atlantic Ocean. These all correspond to deep regions where east-west propating internal waves at the M2 tidal frequency would not propagate down to the sea floor. Important to note is that the color coding in Figure 6.7a is conservative, as the height above bottom is assumed to be equal to the height of the turning depth above the bottom of each cast. In general, however, cast data do not go all the way to the seafloor since impacting the sea bottom could damage delicate sensors. Typically, then, we expect the estimates of turning depth height above the seafloor to be low by several tens of meters.

Given the sparse coverage provided by WOCE cruises, Figure 6.7b high-

lights regions of interest in Figure 6.7a. Regions with the shallowest turning depths are denoted by dark red ovals, with less pronounced turning points shown with more faded red ovals. The most pronounced regions with elevated turning depths, and hence well mixed deep layers, are in the Philippine Sea, the North Pacific, and the southern Caribbean Sea.

For a more quantitative measure of the extent of turning points, Table 1 gives the percentages of WOCE casts which have turning points as a function of cast depth. As expected, the vast majority of turning points are in the deep ocean below 5 km depth. For a given minimum depth in the left column, the second column gives the percentage of the seafloor below this depth. The third column gives the total number of casts below the given depth, and the last column gives the percentage of the casts with turning points at least 200 m above the sea floor.

The sea floor percentage at a given depth interval was calculated by numerically integrating over the Smith and Sandwell 2 minute resolution bathymetry set [*Smith and Sandwell*, 1997]. For simplicity, the integral was performed at 2 degree intervals in both latitude and longitude (Increasing the spatial resolution to 1/3 degree changed the resulting area percentages by less than 0.5%).

Of roughly 2200 casts below 5 km depth, 16.4% have turning depths 200 m or more above the sea floor. If we make the approximation that the WOCE data gives uniform coverage of the world ocean basin, we can estimate the percentage of the ocean basin that contains turning points by simply summing over the products of the noncumulative percentages of the seafloor within a

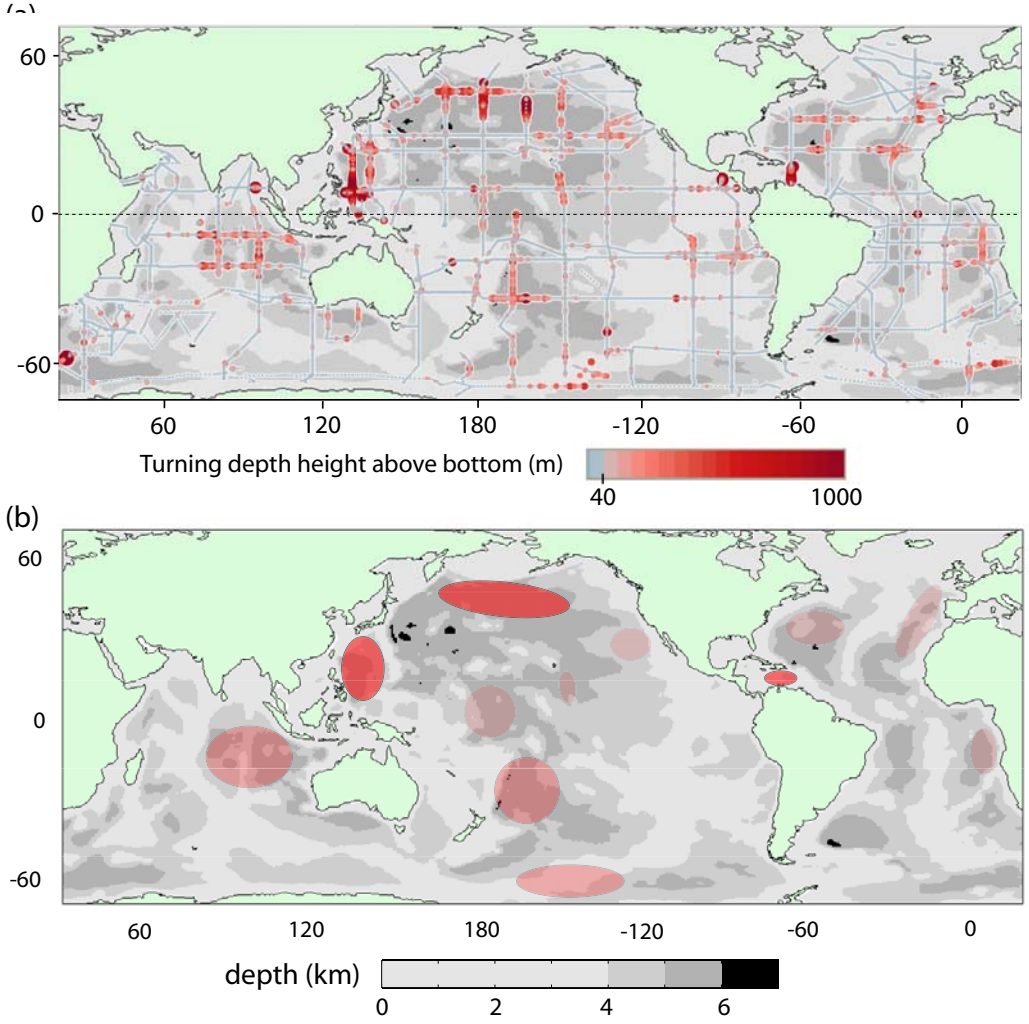

Figure 6.7: (a) A global map of turning depths in the ocean. Small, light blue circles indicate casts with either no turning depths or turning depths less than 40 m from the sea floor. Beginning with turning depths 40 m or more from the sea floor, casts are coded by size and color saturation according to the height of the turning depths above the sea bottom. (b) A global map highlighting regions from (a) with a large occurrence of turning points (red ovals). The height of the turning depths above the sea floor is roughly represented by the saturation of the red ovals.

Table 6.2: Prevalence of turning points as a function of bottom depth in the ocean. For various depths, the table gives the percentage of the seafloor below that depth, the total number of casts, the number of casts with a turning point at least 200 m above the sea floor, and the corresponding percentage of the casts with turning depths. All quantities are cumulative. To be counted, turning points must be at least 200 m above the sea floor.

Depth (km)	% seafloor	casts	Depth (km)	No. TP	% with TP
> 0	100	18087	0-1	1	0.0
> 1	89.3	14157	1-2	1	0.0
> 2	84.8	11956	2-3	2	0.1
> 3	76.3	9878	3-4	27	0.9
> 4	54.3	6850	4-5	176	3.8
> 5	21.6	2212	5-6	353	16.4
> 6	1.0	54	>6	51	94.4

given depth interval and the percentage of the casts which have turning points in the same interval. This simple approach results in the rough estimate that 5.6% of the global ocean contains turning points (for east-west propagating internal waves) at a height of at least 200 m above the sea floor.

6.3 Statistical analysis

The statistical analysis of the WOCE data is discussed in Section 3.3.2. Here we discuss the effects of bin size on the results, compare the statistical results with the results of the simpler filtering, and show how $N(z)$ varies across the world oceans.

6.3.1 Bin size effects

The size of the bins the raw data are sorted into has a large effect on the resulting resolution and error bars. Sorting into larger bins reduces error while decreasing vertical resolution, so one would expect different bin sizes to be appropriate, depending on the nature of the problem being studied. Figure 6.8 compares the N^2 profiles resulting from evaluating a sample cast using four bin sizes. For studying small-scale variability in the N^2 profile, one would typically choose smaller bins. For the turning depth results presented in the remainder of this chapter, we choose a bin size of 100 m, which makes the error bars comparable in size to ω_{M2}, without sacrificing too much vertical resolution. In many cases, this enables us to state with high confidence that the local $N(z)$ falls below ω_{M2}, resulting in turning points for east-west propagating internal waves at the semidiurnal tidal frequency.

6.3.1.1 χ^2 and information entropy

One approach to balance the tradeoff of vertical resolution versus error is to minimize a carefully chosen function that reflects the balance between vertical resolution and error. To quantify the extent to which adjacent bins are statistically distinguishable, we write a term similar to χ^2 from statistical methods.

$$\chi^2 = \frac{1}{N_b - 1} \sum_{i=1}^{N_b - 1} \frac{(\bar{x}_i - \bar{x}_{i+1})^2}{S_i^2/\Delta N_{b,i} + S_{i+1}^2/\Delta N_{b,i+1}} \tag{6.10}$$

where the summation runs over adjacent pairs of bins, and $\bar{x}_i$, S_i, and $\Delta N_{b,i}$ are the average value, the standard deviation, and the bin size of the ith bin,

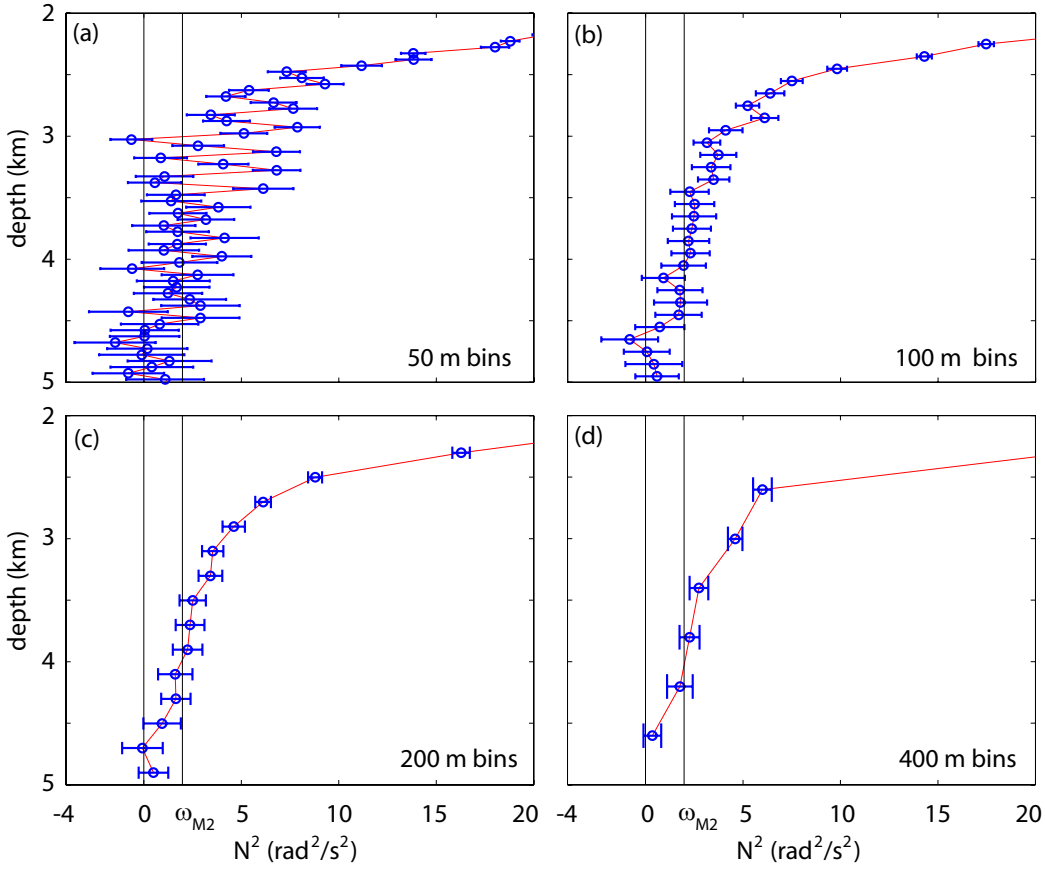

Figure 6.8: A section of a sample cast in the A22 cruise (cast A22_316N151_4_10, 13.17° N, 66.00° W, located in the Venezuelan Basin) processed with bin sizes (a) 50 m, (b) 100 m, (c) 200 m, and (d) 400 m. Smaller bins result in higher vertical resolution but large error bars. Larger bins result in smaller error bars at the cost of vertical resolution. The vertical black lines are zero and ω_{M2}. The red line connects the data points for visualization purposes.

respectively. This term is similar to an average of t-tests performed over all pairs of adjacent bins. The quantity is divided by $N_b - 1$ since there are only $N_b - 1$ *pairs* of bins. The magnitude of χ^2 is proportional to the average extent to which neighboring bins are statistically distinguishable, with $\chi^2 = 1$ when, on average, the 1σ (68% confidence interval) error bars of neighboring bins are just shy of overlapping. Increasing bin size leads to larger χ^2, but this comes at the cost of vertical resolution, which becomes progressively coarser as bin size is increased. We introduce a competing term, which we define as the information entropy Γ [*Shannon*, 1948; *Sethna*, 2006]:

$$\Gamma = N_b \ln N_b \tag{6.11}$$

This quantity is analogous to entropy in physical systems, where a larger number of possible states is energetically preferable. Figure 6.9 shows the information entropy and χ^2 terms for bin sizes ranging from 20 m to 300 m in 10 m increments. To obtain better results, χ^2 and Γ are averaged over ten adjacent casts (casts P14N_325023_1_60 - P14N_325023_1_69 from the P14 cruise) for each bin size. (Averaging more than ten adjacent casts gives a diminishing return in terms of quality of the resulting plot.) The function $\chi^2 + \Gamma$ is shown in Figure 6.10. There are two important points to note about the resulting function: (1) $\chi^2 + \Gamma$ has a local minimum, which means we expect there to be an optimum bin size. (2) The minimum is wide, meaning that a large range of bin sizes around the absolute minimum should yield reasonable results. This means that bin size can be modified within a large acceptable

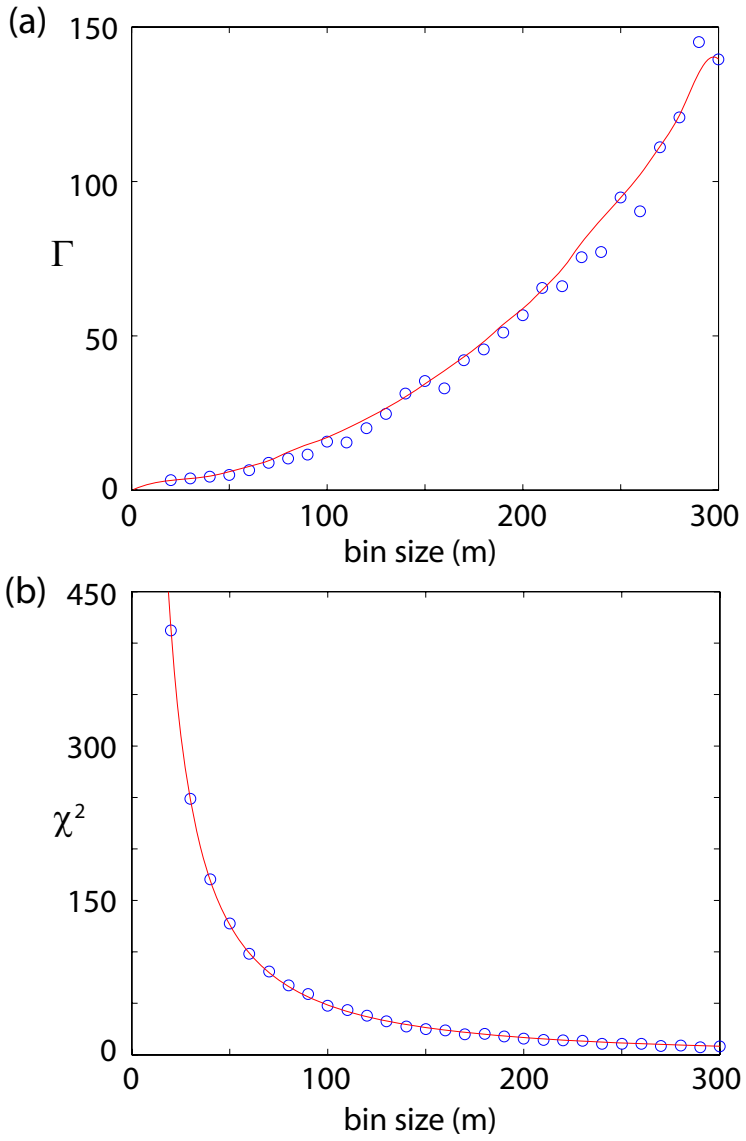

Figure 6.9: (a) information entropy Γ and (b) χ^2 vs. bin size (blue circles). The red curves are a simple smoothing and spline fit of the data in (a) and least squares fit to a log function in (b).

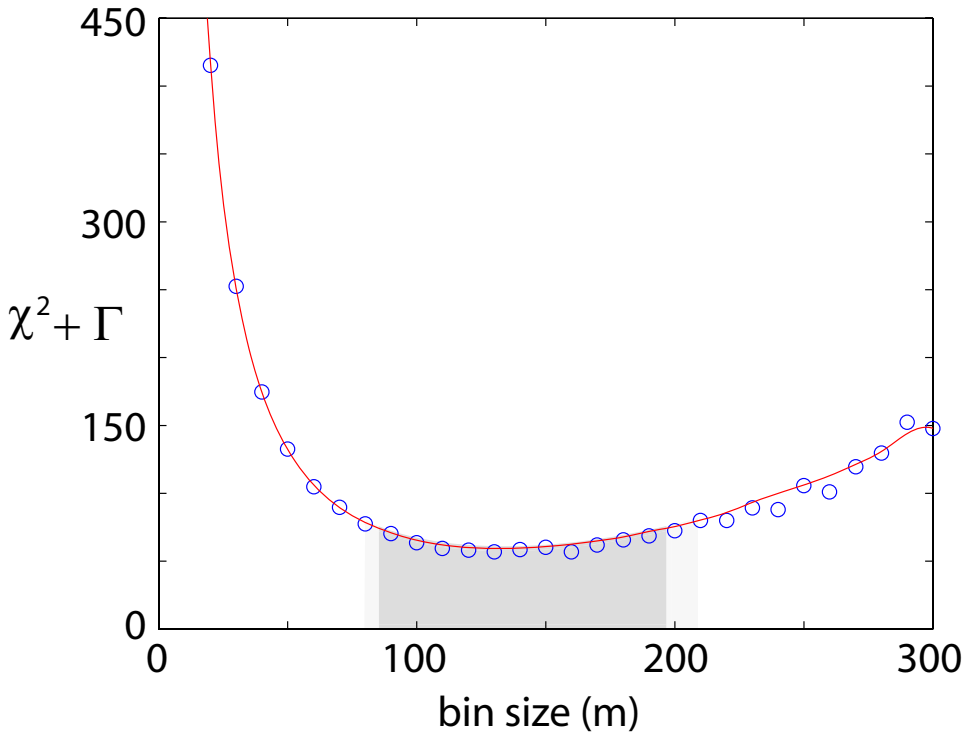

Figure 6.10: $\chi^2 + \Gamma$ as a function of bin size. The bin sizes corresponding to the local minimum of the function (arbitrarily defined to be where $\chi^2 + \Gamma$ is within 25% of the absolute minimum), which should result in a good balance between vertical resolution and low error, are highlighted in gray.

range to suit our preference for resolution or error minimization. In Figure 6.10, bin sizes ranging from 85-197 m fall within 25% of the absolute minimum.

The coefficient of the information entropy term is implicity set to 1 in Eq. 6.11. This is reasonable since the χ^2 term (Eq. 6.10) equals 1 when the adjacent bins, on average, start to become statistically significant. However, there is still a degree of arbitrariness associated with the relative weighting of the χ^2 and entropy terms. For the remainder of this chapter, we work with a

bin size of 100 m, as this results in roughly 50 data points (with acceptable error bars) throughout the water column.

6.3.2 Comparison with simpler filtering scheme

The statistical method of WOCE data analysis is more rigorous than the simpler filtering scheme, and provides error bars on the resulting $N(z)$ profiles. However, a simple comparison between the two methods shows that the resulting N^2 profiles are not significantly different. Figure 6.11 shows sample N^2 profiles resulting from the simple filtering and the statistical analysis for three different bin sizes. To enable a direct comparison of the two methods, the simple filtering scheme is slightly modified to not change negative N^2 values to zero (This was previously done so that the square root of the result could be taken and $N(z)$ could be plotted). From the direct comparison, it is clear that the two methods give similar results, with the best comparison obtained for 200 m bins. The comparison with the 40 m bin size shows that either the statistical analysis picks up more of the noise at small bin sizes, or the simpler filtering scheme is simply averaging over more signal.

6.3.3 Spatial variability of $N(z)$

To illustrate how $N(z)$ varies throughout the world ocean, we plot transects of $N(z)$ along individual cruises. These enable a quick comparison of many $N(z)$ profiles across thousands of kilometers. Three transects of interest derived from the statistical bin analysis are shown here, and the reader

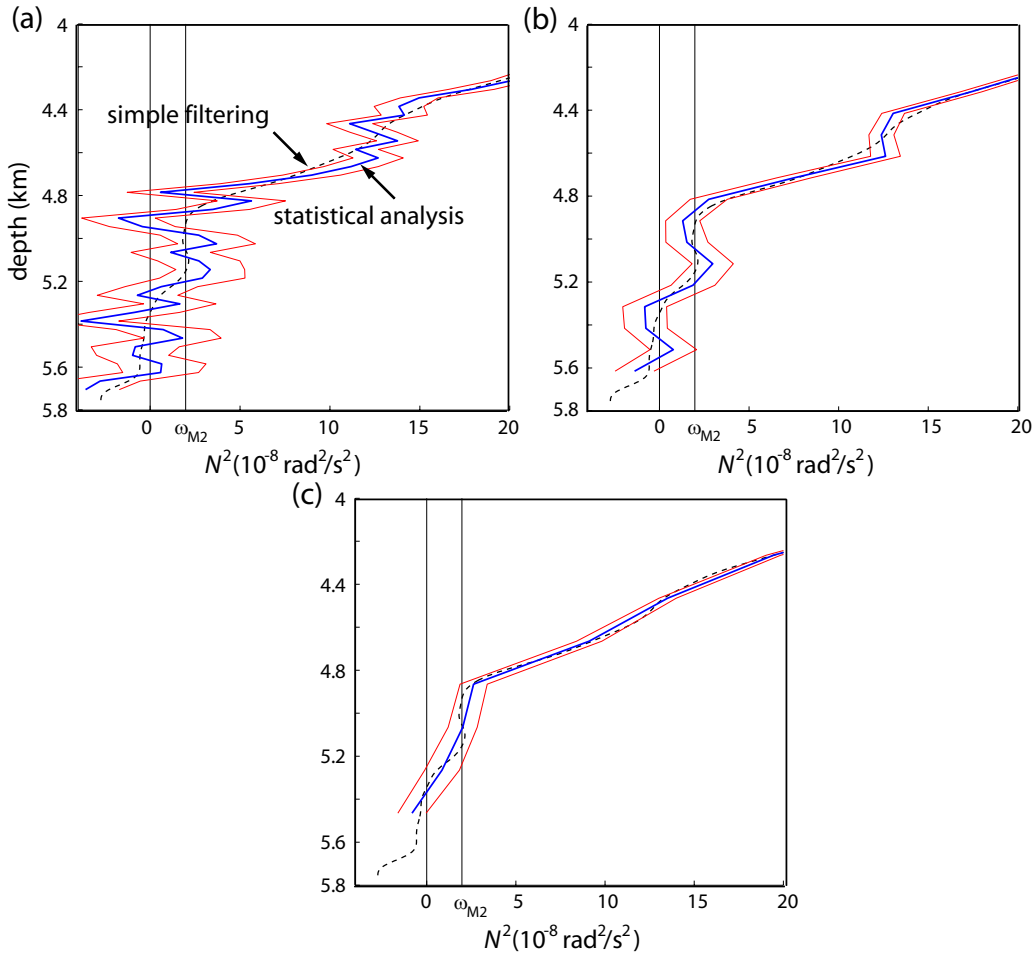

Figure 6.11: Comparison of the simpler filtering scheme and the statistical bin analysis on a sample cast in the P14 cruise (cast P14N_325023_1_32, 46.50° N, 179.01° E). The N^2 profile derived from the simple filtering scheme is shown with a dashed black line, and the statistical analysis with a blue line. The red lines on either side of the blue line denote the standard error resulting from the bin averaging. The red lines are not continuous curves, but the connecting lines are drawn between the discrete points for an easier comparison with the filtering scheme profile.

is referred to Appendix 1 for many more transect figure. Figures 6.12-6.14 show three of the transects which contain the most pronounced turning points. These figures can be compared to the same transects derived from the simpler filtering scheme (Figure 6.5). As discussed in Section 6.3.2, the differences are not substantial, but the figures produced using the statistical analysis are more rigorously derived using bin averaging rather than filters with arbitrary length scales. As will be shown in Appendix 1, the spatial variability is itself highly variable. In many locations, especially on the open ocean, the $N(z)$ doesn't change substantially (at least below the thermocline) over distances of thousands of kilometers. However, in many other regions, especially regions containing large topographic features, the differences in $N(z)$ can be large over distances of only tens or hundreds of kilometers.

6.3.4 Turning points revisited

One of the primary motivations for studying the WOCE data was to determine if there are regions in the deep ocean where the stratification is too weak to support internal waves at the semidiurnal tidal frequency. We now return briefly to this point to discuss how the statistical analysis enables us to assert with much greater confidence that turning depths exist in the ocean. The (b) and (c) panels in Figures 6.12-6.14 show N^2 profiles averaged over regions specified in the corresponding (a) panels. Of special interest are the (c) panels, which show, for these three examples, the averaged N^2 values along with 68% confidence intervals. In all three examples, there are regions

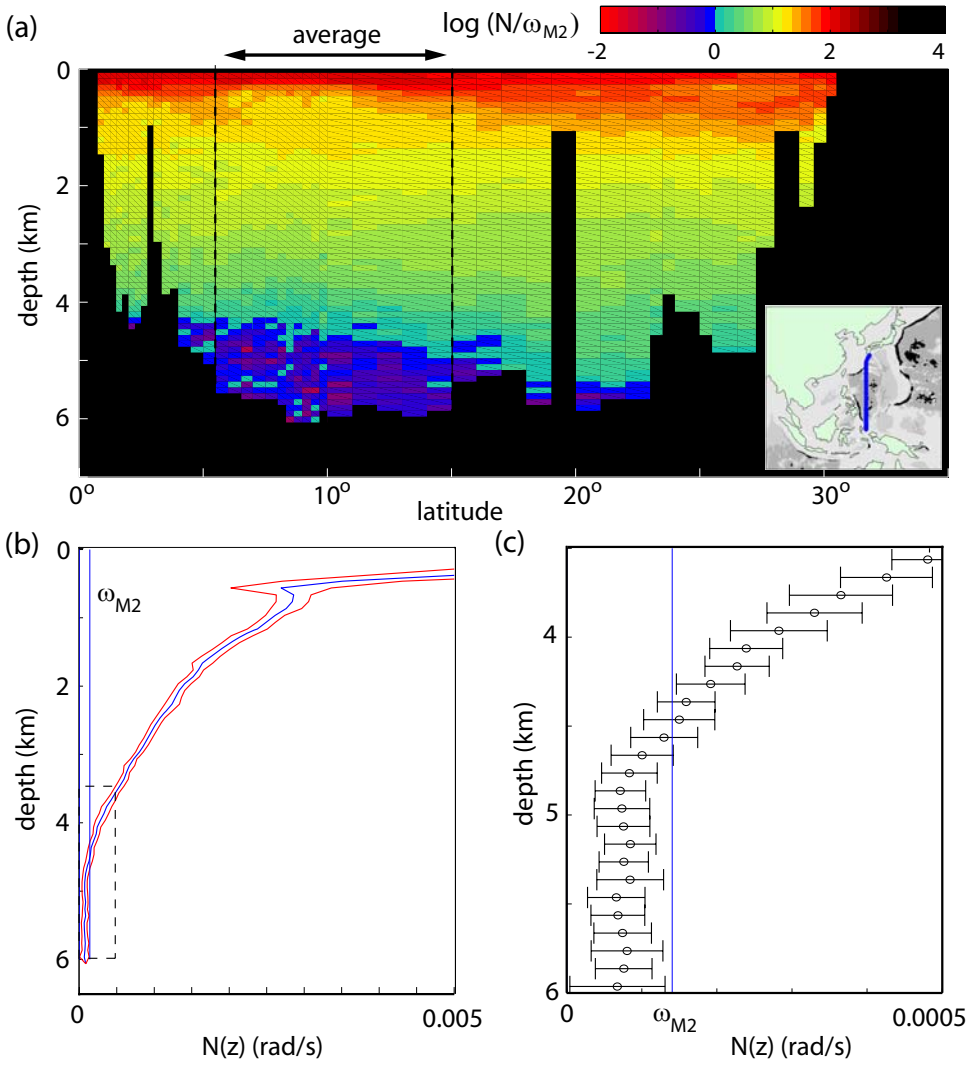

Figure 6.12: (a) Transect of $N(z)/\omega_{M2}$ along the P08 WOCE cruise. Note the logarithmic colorbar, with an abrupt change from light green to dark blue where turning depths occur. Horizontal resolution corresponds exactly to the spacing of casts along the cruise, and verical resolution is determined by the bin size (100 m). The inset of (a) shows the location of the cruise. (b) N(z) profile obtained from averaging 16 similar casts in the region bounded by vertical lines in (a). The blue line is the average value of $N(z)$, and the red lines on either side give the 68% confidence interval. (c) A closeup of the region bounded by the dashed box in (b). In this case, each data point has error bars obtained from the cast averaging procedure.

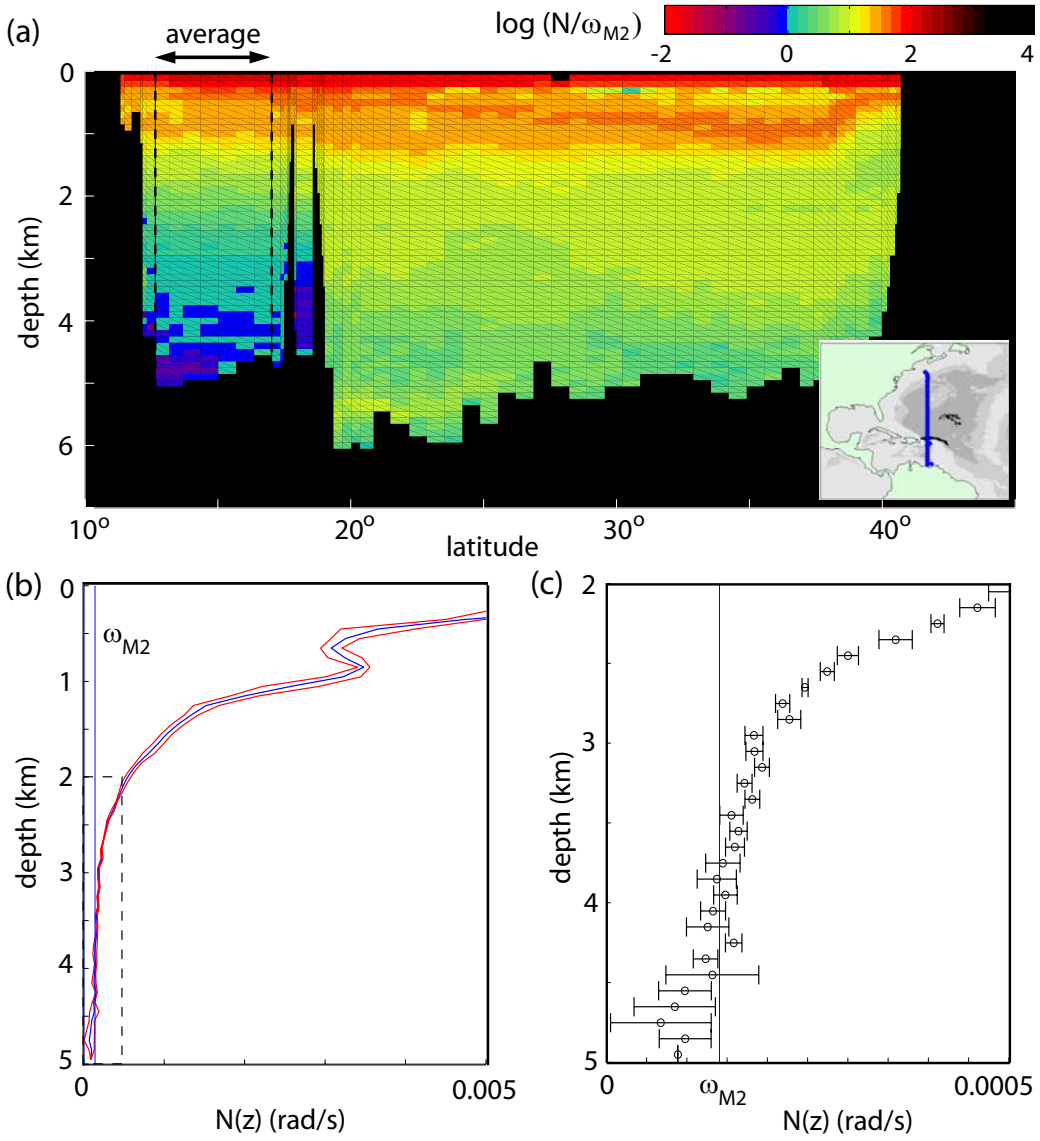

Figure 6.13: (a) Transect of $N(z)/\omega_{M2}$ along the A22 WOCE cruise. (b) N(z) profile obtained from averaging 7 similar casts in the region bounded by vertical lines in (a). (c) A closeup of the region bounded by the dashed box in (b).

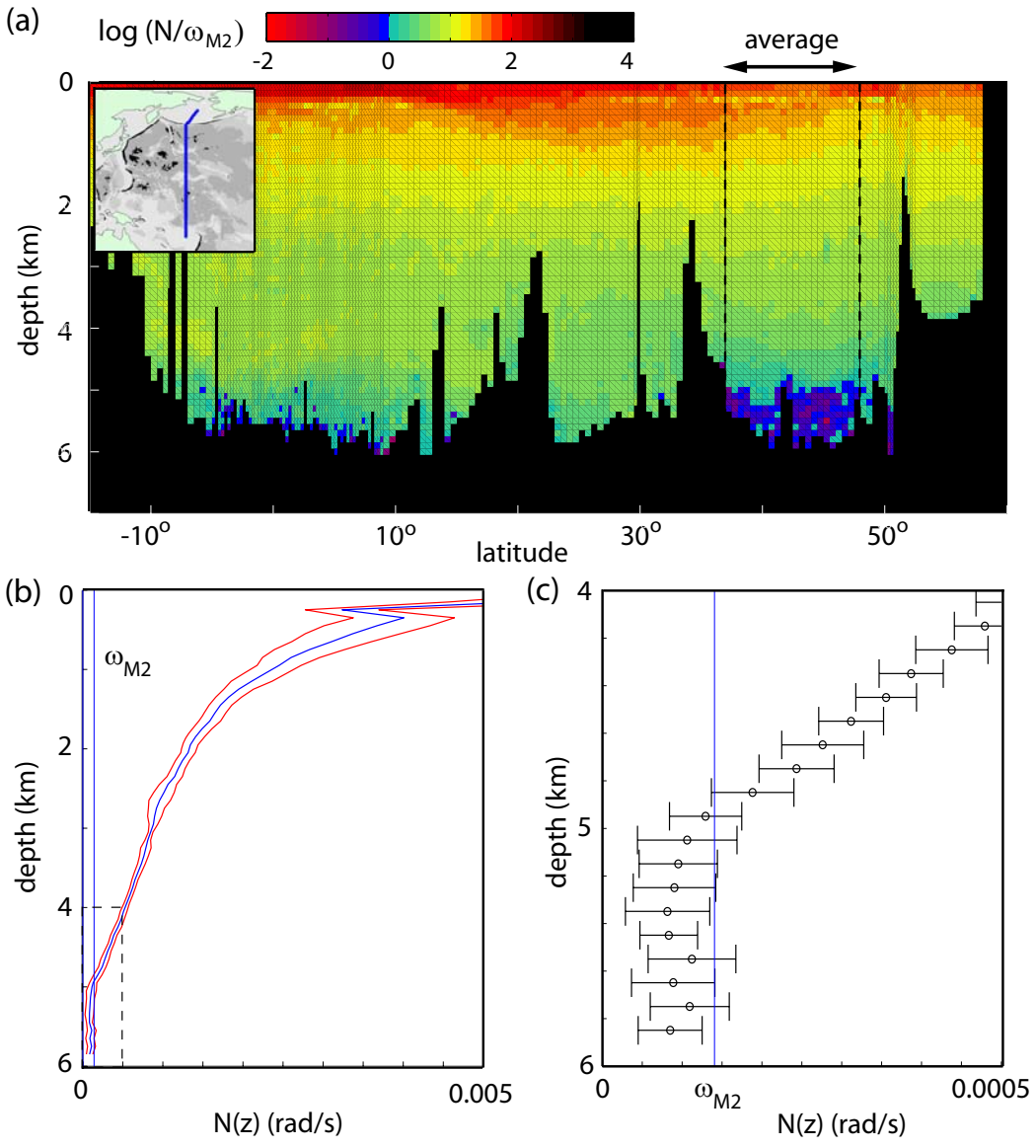

Figure 6.14: (a) Transect of $N(z)/\omega_{M2}$ along the P14 WOCE cruise. (b) N(z) profile obtained from averaging 22 similar casts in the region bounded by vertical lines in (a). (c) A closeup of the region bounded by the dashed box in (b).

in the deep where $N^2 < \omega_{M2}^2$ and east-west propagating waves would not be allowed to propagate. The best example is Figure 6.12, which has a turning depth at roughly 4.5 km depth, over 1.5 km above the sea floor. Although turning depths this far from the sea floor are not common, the global map (Figure 6.7) shows that turning depths on the order of hundreds of meters from the sea floor are commonplace. For more specific results obtained using the statistical analysis of the WOCE data, see the additional transects located in the Appendix.

6.4 Internal wave interaction with turning points

Since internal waves are thought to be ubiquitous throughout the world ocean [*Garrett and Munk*, 1972], we anticipate two important consequences if there are previously unknown regions in the deep ocean where internal waves at the semidiurnal tidal frequency cannot propagate.

The more obvious consequence is the fact that in well-mixed regions with a turning point above the seafloor, incident internal waves would be reflected back upward from the turning point, rather than impinging on the seafloor. Scattering from the seafloor, especially where the seafloor is rough, is an important mechanism by which internal wave energy is transferred to higher wave numbers [*Muller and Xu*, 1992; *Staquet and Sommeria*, 2002], and eventually leads to mixing. If internal waves impinge on a turning point and reflect back toward the surface, they never interact with the bottom topography below the turning point, and hence their wavenumber spectrum will

remain unchanged after the reflection. (Note that we expect that internal waves might interact weakly with the seafloor if the height of the turning point above the sea bottom is smaller than the dominant vertical length scale of the internal wave.) In this way, turning points could function to insulate internal waves from interaction with the rough sea floor, enabling them to propagate further across the ocean before dissipating.

The other consequence is more relevant to the internal wave generation problem discussed in Chapters 4 and 5, wherein oscillating tidal flow over a topographic feature on the seafloor generates internal wave beams. If a topographic feature is below a turning point, we would expect that internal wave generation at frequency ω_{M2} would be much weaker than for the correponding case without a turning point. Therefore, global internal wave generation models that don't take into account very weak stratification near the seafloor in certain regions may overestimate the rate of energy conversion from the surface tides to internal waves.

Numerical simulations of internal wave reflection from a turning point will be discussed below. Internal wave generation below a turning depth will be discussed in future work.

6.4.1 A generalized $N(z)$ profile

In order to perform numerical simulations relevant to the ocean, it is necessary to determine a buoyancy frequency profile that is representative of many of the regions in the ocean with turning points. We choose an example

with a relatively shallow turning point, so that the height of the turning point above the sea floor is greater than the typical width of the internal wave beams being simulated. This helps to ensure that the sea floor is well below the penetration depth of the internal wave below the turning point. Another requirement for convenience reasons is that the $N(z)$ chosen for numerical simulations be easily expressed as a simple function in closed form, preferably an exponential, as this is fairly common practice in fitting oceanographic $N(z)$ profiles. An excellent example of a cast with a roughly exponential $N(z)$ profile is located over the Middle America Trench in the cruise P19. (The cast is just off the Pacific coast of Central America.) Figure 6.15 shows the $N(z)$ profile, along with the rough fit to an exponential function:

$$N(z) = 0.006 \exp(0.001z) \text{ rad/s}, \quad z \in (-6000, 0) \text{ m} \tag{6.12}$$

The fit was performed by eye as opposed to a least squares fit because we are primarily concerned with the $N(z)$ profile near the turning depth. A simple least squares fit does not emphasize the quality of fit near the bottom, and would thus follow the noisier region between 1 km and 2.5 km, at the expense of the quality of fit near the turning depth. This rough fitting procedure is acceptable in this instance because we are not concerned here with exact quantitative prediction of internal wave behavior at this particular location, but are interested in the general interaction of internal waves and turning depths in an ocean-like $N(z)$ profile. The $N(z)$ profile Eq. 6.12 is used in all of the following numerical studies.

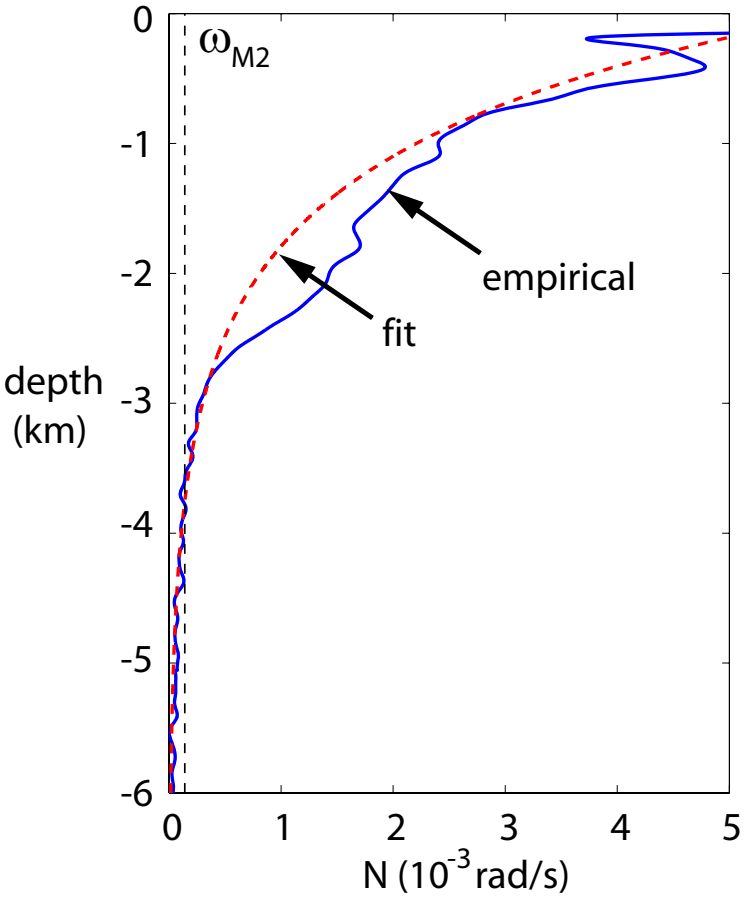

Figure 6.15: $N(z)$ profile from a cast near the Middle America Trench (blue line) as determined using the filter discussed in Section 3.3.1.1. The exponential fit (red dashed line) used in numerical simulations of internal wave interaction with a turning depth is superimposed. The vertical dashed black line denotes the semidiurnal tidal frequency. Note that the exponential $N(z)$ has turning depth at roughly 3750 m depth.

6.4.2 Direct numerical simulations

The simplest way to study internal wave interaction with a turning point is to characterize the reflection of a downward propagating internal wave beam from the turning point. *Munk* [1981] speculated that an internal wave beam incident upon a turning point should simply reflect back toward the surface. In the inviscid the limit, the reflection should not cause a loss of energy, and therefore no internal wave energy would be lost during the reflection process. However, if some fraction of the internal wave energy were lost upon reflection, this extracted energy could be used to further mix the fluid below the turning point, with the result that the turning point might gradually shift upward.

We present the results of several ocean-scale simulations of internal wave beams reflecting from turning points to quantify the amount of energy lost in the reflection process. We expect that the energy loss might depend on both the viscosity and the height of the turning point above the sea floor. Figure 6.16 shows an instantaneous vorticity plot of simulation results for a reflecting internal wave beam, using the generalized $N(z)$ profile derived in Section 6.4.1 and an effective viscosity $\nu_{eff} = 1.2 \times 10^{-3} m^2/s$. (Using an effective viscosity 1000 times greater than the molecular viscosity of water, which enables a coarser computational grid to be used, is the only way an ocean scale simulation can be performed; see Section 3.2.8) The internal wave was produced utilizing the body forcing term discussed in Section 3.2.3 (Eqs. 3.18 and 3.19 with parameters $A = 0.7$ cm/s, $\sigma_x = 1$, $\sigma_z = 2$, $x_o = 0$ m,

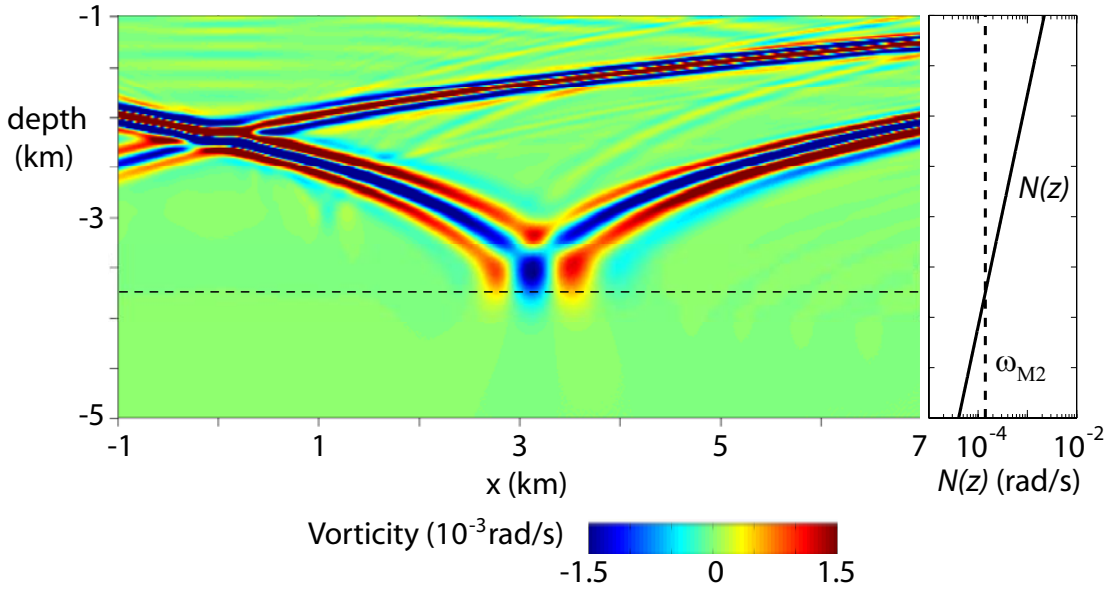

Figure 6.16: Instantanous snapshot of vorticity for simulation (1) discussed in Section 6.4.2.1. The wavemaker is located at $x = 0$ km, $z = -2.184$ km, with the wave beam of interest propagating downward from the generation region. The internal wave is reflected from the turning point, denoted by a horizontal dashed line. The $N(z)$ profile is plotted to the right. Note that the steepening of the wave beam is gradual until it reaches an angle of roughly 45°, after which the wave beam bends sharply downward toward the turning point. This abrupt curvature is a general feature of exponential $N(z)$ profiles.

$z_o = -2184$ m and rotation angle -78°. These parameters result in a relatively low amplitude internal wave (0.3 cm/s maximum velocity), and Reynolds number $Re \approx 1000$. The results presented in this section are preliminary, and rigorous grid convergence studies have not yet been performed.

6.4.2.1 Energy loss vs. turning point height

The generalized $N(z)$ profile (Eq. 6.12) has a turning point at 3756 m depth, which in a 6 km deep ocean, corresponds to a turning point 2244 m above the sea floor. This baseline simulation is hereafter referred to as simulation (1). Two similar simulations are performed with the $N(z)$ profile shifted vertically to change the height of the turning point above the sea floor. Simulation (2) has a turning point 300 m above the sea floor, and simulation (3) has no turning point. The internal wave beam reaches an angle of 65.5° from the horizontal before it reflects from the sea floor. The width of the internal wave beam is roughly 300 m, so (1) has a turning point height above the sea floor which is much greater than the wave beam width. Simulation (2) has a turning point height which is roughly equal to the wave beam width, which means that, due to a finite penetration depth, we expect that the wave beam may be able to interact weakly with the sea floor even though the wave beam cannot technically reach the bottom boundary. For comparison purposes, simulation (3) corresponds to the more common case of wave beam reflection from a solid surface in the absence of turning points.

Energy loss upon reflection from the turning point (or the solid bottom

boundary in the case of simulation (3)) is quantified by fitting the velocity and pressure fields along wave beam cross sections to sinusoidal functions at the wave frequency both immediately to the left and the right of the reflection. Cross section locations are illustrated for simulation (3) in Figure 6.17. The cross sections are placed as close as possible to the actual reflection to minimize the extent to which viscous dissipation is also reflected in the energy loss figures. (We are only concerned with energy loss due to the reflection process.) Energy flux through the cross sections is then computed using:

$$E = \int_{cs} p\mathbf{u} \cdot \hat{\mathbf{n}}\, dx' \tag{6.13}$$

where the 'cs' denotes the integral being taken over the cross section, p is the pressure, $\mathbf{u}$ the wave velocity interpolated to the cross section, $\hat{\mathbf{n}}$ the unit vector normal to the cross section and in the direction of wave propagation, and dx' the along cross section coordinate. This integation results in a power per unit span (where the spanwise direction is the third dimension, which is not simulated), with integrated wave beam powers typically on the order of 1 W/m for the parameters examined here. (Note, however, that we are interested primarily in energy lost upon reflection, which is computed as a ratio of power before and after reflection, not the actual power figures themselves.) In simulation (1), there is a 6.16% energy loss during the reflection process. Simulations (2) and (3) have 6.14% and 5.32% energy losses, respectively. Two conclusions can be drawn from these results. The first is that only a small fraction of the energy is lost upon reflection of an internal wave beam from a turning point, meaning that the inviscid prediction of *Munk* [1981]

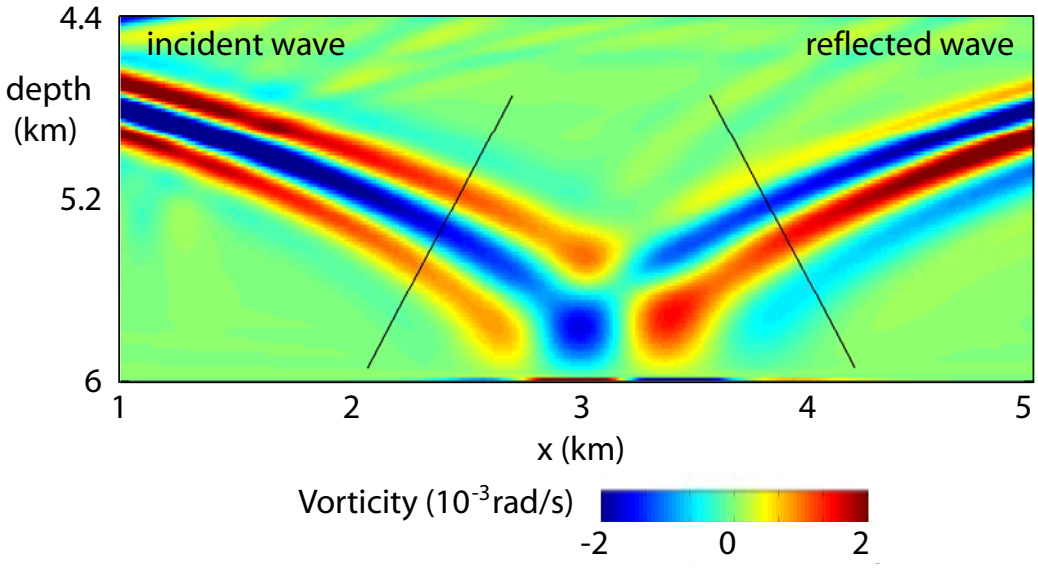

Figure 6.17: Vorticity snapshot from simulation (3), with black lines denoting cross section locations, along which energy is computed.

likely holds reasonably well in the ocean. Second, the slight energy loss does not appear to be a strong function of the height of the turning point above the sea floor. Therefore internal wave tunneling effects [*Brown and Sutherland*, 2007] are unlikely to play an important role in the relfection process.

6.4.2.2 Energy loss vs. viscosity

A similar energy analysis is performed for two more simulations with varying viscosity: in simulation (4), the effective viscosity ν_{eff} is reduced from $1.2 \times 10^{-3}\mathrm{m}^2/\mathrm{s}$ to $0.6 \times 10^{-3}\mathrm{m}^2/\mathrm{s}$. In simulation (5), the effective viscosity is increased to $\nu_{eff} = 6 \times 10^{-3} m^2/s$, so that effective viscosity is varied by an order of magnitude. In both simulations, the turning point is identical to

Table 6.3: Summary of simulation results for internal wave interactions with a turning point (TP). The first three rows are from simulations where the turning point height above the sea floor is varied. In the following three rows, results from a varied effective viscosity are presented. Note the baseline case (1) is present in both sets of rows for comparison purposes.

Simulation (A/σ)	TP height (m)	ν_{eff} (10^{-3} m^2/s)	% loss
1	2244	1.2	6.16%
2	300	1.2	6.14%
3	N/A	1.2	5.32%
4	2244	0.6	10.7%
1	2244	1.2	6.16%
5	2244	6.0	5.24%

that in simulation (1). In the case of increased effective viscosity, the energy loss upon reflection from the turning point is 10.74%. In the case of decreased effective viscosity, the energy loss is reduced to 5.24%. Based on these results, it appears that the energy loss is decreasing rapidly as a function of effective viscosity, and in the ocean case (with viscosity 10^{-6}m^2/s), very little energy is likely lost due to reflection of an internal wave beam from a turning point.

The results of the wave beam reflection analyses are summarized in Table 6.4.2.2.

6.4.3 Vertical mode approach

We also briefly present results from a similar analysis utilizing the vertical mode formalism for describing internal waves (for a thorough description of vertical modes, see Section 2.2.4).

Modes 1, 3, and 5 are shown in Figure 6.18 along with the buoyancy

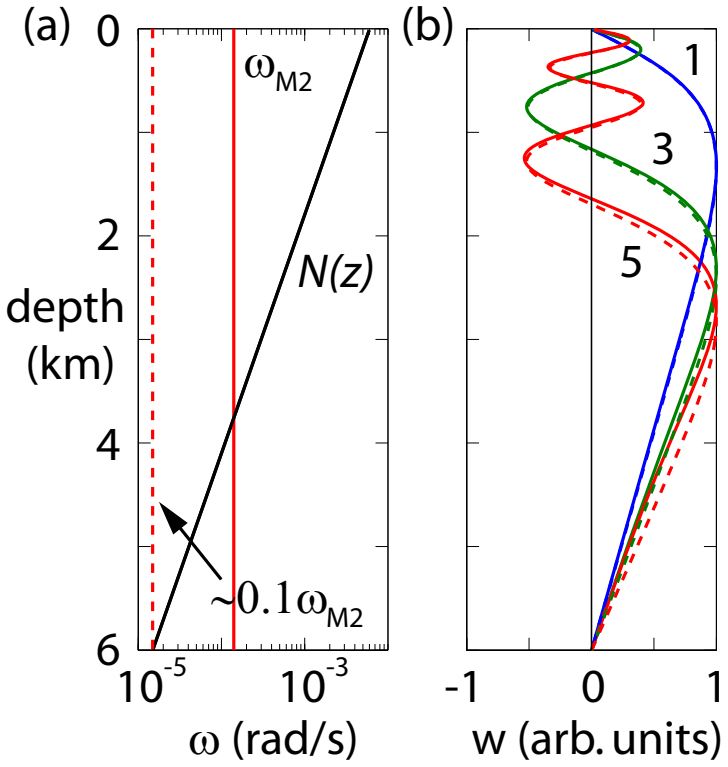

Figure 6.18: (b) Modes 1, 3, and 5 for the general $N(z)$ profile Eq. 6.12 (plotted in (a)). The vertical velocity is plotted for two cases. The solid curves denote the vertical velocity for the case of a turning point at roughly 4 km depth. The dashed lines correspond to a similar case where the wave frequency has been reduced by a factor of 10 (see the vertical dashed line in (b)), resulting in the absence of a turning point. The effect of a turning point 2 km above the sea floor on the vertical mode structure is small.

frequency profile $N(z)$ (Eq. 6.12) on the left. The solid red vertical line in (a) denotes the M2 tidal frequency, which crosses $N(z)$ at depth 3750 m. The three solid curves in (b) are the vertical velocities of the three modes normalized to 1. To illustrate the effect of the turning point on the form of the vertical modes, the eigenvalue problem is solved for the same $N(z)$ but with a reduced tidal frequency ω (dotted red line) such that $N(z) = \omega$ at the bottom of the ocean, resulting in a system with no turning point. The vertical modes are given for this scenario by the dashed curves in (b). Visual inspection shows that the presence of a turning point more than 2 km from the seafloor has little effect on the low vertical modes. This contrasts strongly with the drastic effect of the turning point on internal wave beams discussed in Section 6.4.2. These different behaviors can be accounted for by the fact that internal wave *beams* are comprised of higher vertical modes, which have smaller characteristic vertical length scales, and are more strongly affected by the presence of large mixed regions in the deep ocean. To demonstrate the effect of turning points on higher vertical modes, Figure 6.19b shows a similar plot with modes 1 and 40. The effect on the higher mode is more pronounced, with a rapid decay in vertical velocity below the turning point. Figure 6.20 shows the penetration depth below the turning point as a function of vertical mode number. Vertical modes are plotted in intervals of 5 from modes 1 to 151 on a log-log plot to show the power law behavior of the penetration depth. A least squares fit (beginning with mode 16, as the first three plotted modes deviate from power law behavior) is used to determine the functional form of

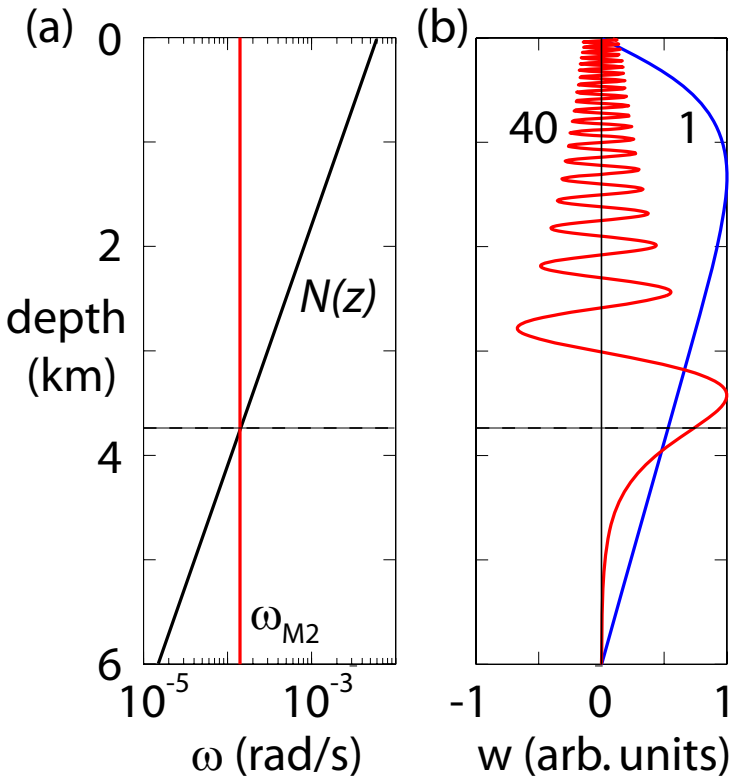

Figure 6.19: Modes 1 and 40. (a) shows the $N(z)$ profile, and (b) shows modes 1 and 40. The horizontal line depicts the turning point. Low modes are largely unaffected by the presence of the turning depth, but higher vertical modes decay quickly below the turning depth.

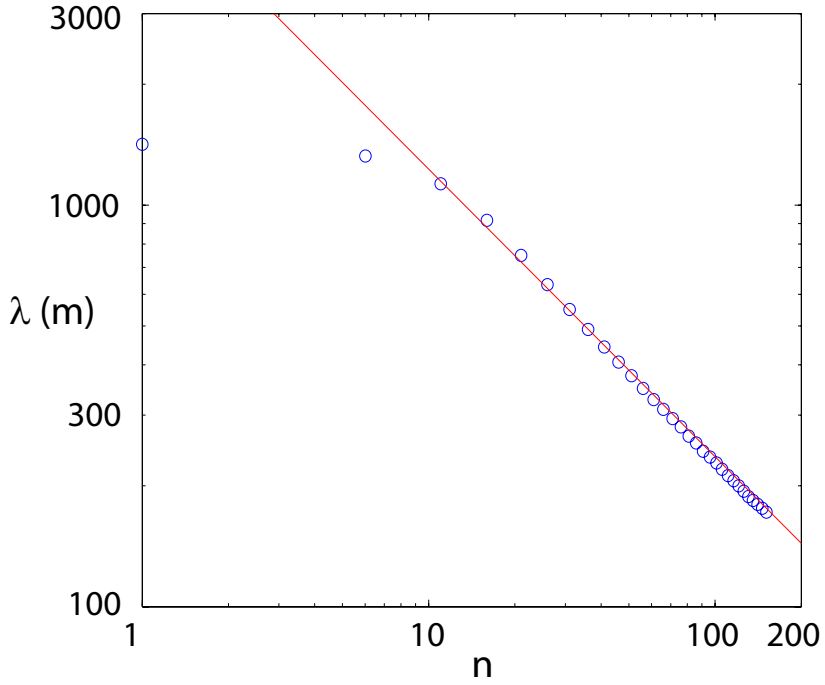

Figure 6.20: Penetration depth below the turning point vs. vertical mode number (blue circles). The penetration depth is described well by a power law, with decay exponent -0.72, for modes greater than roughly 10.

the penetration depth below the turning point:

$$\lambda = 6400 n^{-0.72} \tag{6.14}$$

where λ is the penetration depth, defined to be the depth below the turning point where the vertical velocity amplitude is reduced by a factor of e, and n is the vertical mode number. The decay exponent is less than 1, meaning that even though the turning depth falls off for high vertical modes, modes over $n = 100$ still have a finite penetration depth of over 100 m.

The primary result is that turning points present a much greater bar-

rier to higher vertical modes, with the very low modes being mostly unaffected. Since high vertical modes tend to dissipate close to their generation sites [*Munk and Wunsch*, 1998], it is then unlikely that the turning depths have a substantial effect on many of the low modes that propagate across the open ocean. However, turning points located close to sites of intense internal wave generation, such as the Hawaiian Ridge [*Nash et al.*, 2006], might play an important role in preventing the higher vertical modes from scattering from the sea floor, enabling these high modes to propagate further horizontally than would otherwise be possible.

Chapter 7

Discussion

7.1 Primary results

This work has in many ways spanned the large scale efforts of scientists to understand how internal waves fit into the larger picture of the ocean circulation and earth's climate. Before significant improvements to global models can be made, the internal wave generation process must be more fully understood at a fundamental level. Computational resources have increased by orders of magnitude in recent decades, but simulating tidal flow and internal waves accurately throughout the entire ocean will likely remain inconceivable for the foreseeable future without the use of wave generation and propagation models.

The first part of this work focused on expanding previous internal wave generation studies to include 3D and nonlinear effects, which we have shown to have significant ramifications for the wave generation process. In particular, for large tidal forcing amplitudes, which are common in shallow seas or near small bottom roughness, nonlinear effects play a large role in the dynamics of internal wave generation. The nonlinear effects have different manifestations depending on the relative values of the buoyancy frequency N and twice the

tidal forcing frequency 2ω. For $2\omega > N$, second harmonic internal waves are damped since $\sin\theta = 2\omega/N$ is undefined, and we discovered a mean flow perpendicular to the tidal forcing direction. This mean flow results in a large scale horizontal circulation near the topography [*King et al.*, 2009]. When $2\omega < N$, second harmonic internal waves are generated, and a significant fraction of the energy converted from the barotropic to internal tides (up to 19%, as discussed in Section 5.1.3.1) is radiated in the direction *perpendicular* to the tidal forcing direction [*King et al.*, 2010]. These unanticipated, inherently 3D nonlinear, results will require modelers to reconsider the previous assumptions of a 2D, linear ocean. As discussed in Chapter 2, only 6×10^{19} J of mixing energy per year (estimated from an average global mixing rate of 2×10^{12} W times 3×10^{7} s/yr), mostly from breaking internal waves, is required worldwide to moderate the 2×10^{25} J of energy tied up in the general ocean circulation, so the accurate characterization of the relatively small internal wave energy could have important effects on the physical understanding the larger ocean circulation. And with the global ocean's substantial heat capacity, small improvements in ocean modeling can lead to significant changes in climate models.

The second part of this study carefully examined one aspect of the evolution of the tidally-generated internal waves. Although the possibility of 'turning points,' boundaries of well mixed regions which reflect incident internal waves, has been mentioned in the literature [*Munk*, 1981], no systematic study has previously been undertaken to determine how common they might be in the deep ocean. The World Ocean Circulation Experiment database, which

is a catalog of more than 18,000 individual data sets (casts) spread across the world oceans, has provided an opportunity to study the buoyancy frequency $N(z)$ in the ocean far more thoroughly than would have been possible only two decades ago. From a climatological standpoint, the ten year timeframe over which the data were taken is a mere snapshot compared to the ocean circulation timescale (10^3 years), but this ten year window was sufficient to give us significant insight into the temporal variability of $N(z)$ worldwide. Understanding how $N(z)$ changes both temporally and spatially will ultimately enable turning points to be incorporated into global ocean models, where they can affect the distance internal waves propagate before breaking and releasing their energy to small scale mixing. The most prominent effect these turning points likely have on propagating internal waves is the insulating effect they provide from the sea floor, which can be a very efficient scatterer of internal waves in many regions. Understanding how internal waves might be prevented from interacting with the sea floor will help pinpoint where internal waves deposit their energy, resulting in local mixing and a corresponding increase in the potential energy of the water column. The other likely effect well mixed regions in the deep ocean could have is the reduction in internal wave energy radiated by rough topography fully or partially below a turning depth. Topographic features that would otherwise be very efficient scatterers of energy might not contribute to the global internal wave field as much as would otherwise be expected in the absence of turning points. Recent global internal tide generation models, such as *Nycander* [2005], do not take this effect into

account.

7.2 Future directions

This work raises as many new questions as it's answered. Primary among these is how significant the out-of-plane second harmonics generated by tidal flow over 3D topography might actually be. The tidal excursion parameter range we studied is similar to values encountered in the ocean, but by using direct numerical simulations (DNS), we were limited to Reynolds numbers smaller than those found in the ocean by many orders of magnitude. The most difficult component of extrapolating laboratory and DNS simulation results to ocean flows is bridging the enormous gap in Reynolds number. However, as computational resources steadily increase, the Re which can be obtained in DNS simulations will steadily rise as well, slowly closing the gap between simulations and reality. Studying 2D problems, where the lack of the third dimension enables much higher Re to be reached, is tempting, but we showed that several phenomena, including a mean flow (when $2\omega > N$) and out-of-plane second harmonics (when $2\omega < N$) can only be characterized by studying the full 3D problem.

Sub-grid scale (SGS) modeling has not been used in this work, but with great care, could probably be used to obtain similar results for ocean-scale flows.

There are several additional logical extensions of this work:

(1) Realistic tidal forcing, with tidal orbits being comprised of ellipses, and inclusion of the Coriolis force in the flow solver could be used to examine how 3D nonlinear effects might depend on latitude.

(2) Simulations of 3D internal wave generation should use a realistic $N(z)$ profile, such as Eq. 6.12. This would cause distortion of the characteristic cones, and perhap have unanticipated results.

(3) Of primary interest to oceanographers is the 'conversion efficiency' of a particular topographic shape, or what fraction of the impinging surface tide energy is converted into internal waves. The energy radiated as internal waves has been computed in this work, and a reasonable extension would be to compute the available surface tide energy, most likely by integrating the pressure-velocity work at the forcing boundaries in the simulations. The ratio of the two energies, the conversion efficiency, could then be computed for varying parameters.

(4) This work has focused on the small excursion parameter regime $\epsilon < 1$, where the tidal excursion is smaller than the typical horizontal length scale of bottom topography. However, the regime $\epsilon > 1$, called the quasisteady state, is also applicable in many areas of the ocean, and results in the generation of lee waves instead of internal waves [*Garrett and Kunze*, 2007].

(5) 3D studies presented here focused on *axisymmetric* topography. As shown by *Holloway and Merrifield* [1999], the horizontal aspect ratio of bottom topography can have a substantial impact on tidal conversion. This work could

be generalized by studying 3D and nonlinear effects of internal tide generation by non-axisymmetric topography.

(6) Most work is confined to a single tidal forcing frequency (in this case the dominant lunar semidiurnal (M2) forcing frequency), but other tidal components, especially the solar semidiurnal component (S2), can also have significant amplitudes. In the low amplitude limit, the internal wave solutions from various tidal frequency components can be linearly superposed, but in general, there are nonlinear interactions between waves of different frequencies [*Tabaei et al.*, 2005]. A generalized study of flow over 3D topography could incorporate multiple forcing frequencies, and determine how the resulting waves interact.

(7) Incorporation of a free-surface. This would probably require the use of a different flow solver, but in general, internal waves cause a displacement of the free surface, and can couple with surface waves, so it would be useful to extend the present works on the rigid lid case to the more general case with a free surface.

(8) The presence of turning points could have significant effects on internal wave generation in the deep ocean. Since M2 internal waves cannot propagate below turning depths, they could also not be generated below turning points, with the result that topographic features below turning points, which might otherwise be efficient wave generators, would not radiate internal waves. A numerical or experimental study could be undertaken to quantify the effects of turning points on wave generation, with internal wave amplitude

being determined for bottom topography both fully and partially submerged beneath a turning point.

(9) Quantifying the effects of turning points on propagating internal waves remains another interesting and open problem. As internal waves traverse the oceans, they reflect back and forth between the ocean surface or thermocline and the ocean bottom, resulting in many opportunities for internal wave to interact with turning points above the sea floor. Further DNS simulations could further examine the role of the height of the turning point above the seafloor in determining the nature of internal wave interactions with the turning points. In addition, 3D simulations of internal wave reflections from turning points could be useful if performed with sufficiently high spatial resolution to determine if the internal waves can break or undergo instability as they approach the turning points. There would be great interest if internal wave reflection created a positive feedback loop, where energy loss from a reflecting internal wave further mixed the region below the turning depth, causing the turning depth to gradually rise in the water column.

(10) An ideal way to expand the study of turning points would be to obtain observational data from a region that contains turning points. For the purpose of minimizing uncertainty in the $N(z)$ profiles, it would be useful to have multiple CTD casts at the same location on the same day, so that averaging could be used to reduce noise and determine the amount of the noise in the data. Measurements of this kind were not performed as part of the WOCE project because the primary objective was to obtain data at as

many locations as possible, not to carefully quantify measurement error.

In addition, if careful current velocity measurements could be taken above and below a suspected turning point, and an algorithm could be developed for subtracting the barotropic tide, an internal wave spectrum could be derived as a function of depth, and the effects of a turning point on internal waves at different frequencies could be directly observed. There are, in fact, mooring profilers scattered throughout the ocean, but the sensors are sparse. Also, there are very few measurements deep enough (below 5 km) to be below turning points. In addition, the barotropic tide turns out to be a large signal which is difficult to subtract from the raw data (preliminary results were very sensitive to the method used to subtract the barotropic tide signal), and many of the presently used sensors have stall speeds, where they incorrectly read zero for current speeds below some threshold velocity (typically 1 cm/s). The current velocity meters are being gradually replaced by Acoustic Doppler Current Profilers (ADCPs), so higher quality data will eventually be available.

Besides understanding how internal waves interact with turning points, the origin of the turning points themselves would also be a worthwhile pursuit. Do the well mixed regions result from elevated rates of internal wave breaking in the vicinity? Do deep ocean basins slowly fill with uniform water from external sources? These are open questions, and any explanations for their presence are speculation at the current time.

The problems of internal wave generation and turning points discussed in this work could have a substantial impact on future studies of ocean circu-

lation, and ultimately, earth's climate. The general picture of internal waves in the ocean has progressed greatly in the past several decades, but much work remains to be done, especially when it comes to extending the simplistic models currently in use to the complex, dynamic ocean. We have utilized laboratory experiments, numerical simulations, and analysis of observational data to shed light on several aspects of the internal wave problem. We hope that future studies will place increased emphasis on understanding processes that are inherently 3D and nonlinear, and take into account the complex and variable stratification found in the ocean basins.

Appendix

Appendix 1

Additional WOCE Transects

This appendix contains addition transects derived from the statistical analysis of the World Ocean Circulation Experiment data (see Section 3.3.2 for details). The transects are sorted by ocean, and each section begins with a map of the relevant ocean showing the locations of the cruises. Not all of the cruises are plotted here, but there are enough plots to obtain a representative cross section of the world ocean. Each transect is labeled with its name and the time interval over which the data was obtained. The WOCE labeling system has some irregularities, but in general, the prefixes 'A,' 'I,' 'P', and 'S' denote cruises in the Atlantic, Indian, Southern, and Pacific oceans, respectively. The following two digits denote the number of the cruise, which was arbitrarily assigned when the cruise paths were planned. The commonly encountered suffixes 'E,' 'W,' 'N,' 'S,' and 'C' denote the four cardinal directions and 'center,' respectively. Many cruises in the WOCE dataset are broken into subsections. For example, the Pacific zonal cruise P04 contains three subcruises: P04W, P04C, and P04E, representing the west, center, and east legs, respectively. For each cruise, detailed information about dates, measurements, and individual data files can be found at http://whpo.ucsd.edu.

All transects were derived using a bin size of 100 m, which, as shown in Section 6.3.1.1, is a reasonable size to balance the desire for vertical velocity and minimal error. The transects are plotted along uniform longitudinal or latitudinal axes. Since the spatial interval between WOCE casts can change markedly over the course of a cruise (with large gaps in the data being common), this results in varying horizontal resolutions in the following figures. The horizontal resolution is representative of the actual spacing of the individual casts, as no interpolation has been performed. In certain figures (such as the I01 transect at 76° longitude), this results in artifacts that appear to be flat-topped topography. However, these features are simply the result of a single cast that has been stretched to cover a large area so that the horizontal axis remains uniform.

One general trend is that variations in $N(z)$ are more pronounced when looking at meridional transects, meaning that the stratification of the global ocean tends to vary more with changes in latitude than with changes in longitude. This is most pronounced when looking at the depth of the thermocline for the meridional transects. In addition, there tends to be much greater variation in many of the $N(z)$ isosurfaces in the North-South plots. $N(z)$ isosurfaces are not plotted directly, but the eye can easily trace the transitions in the discrete color map to observe the slope of the lines of constant $N(z)$.

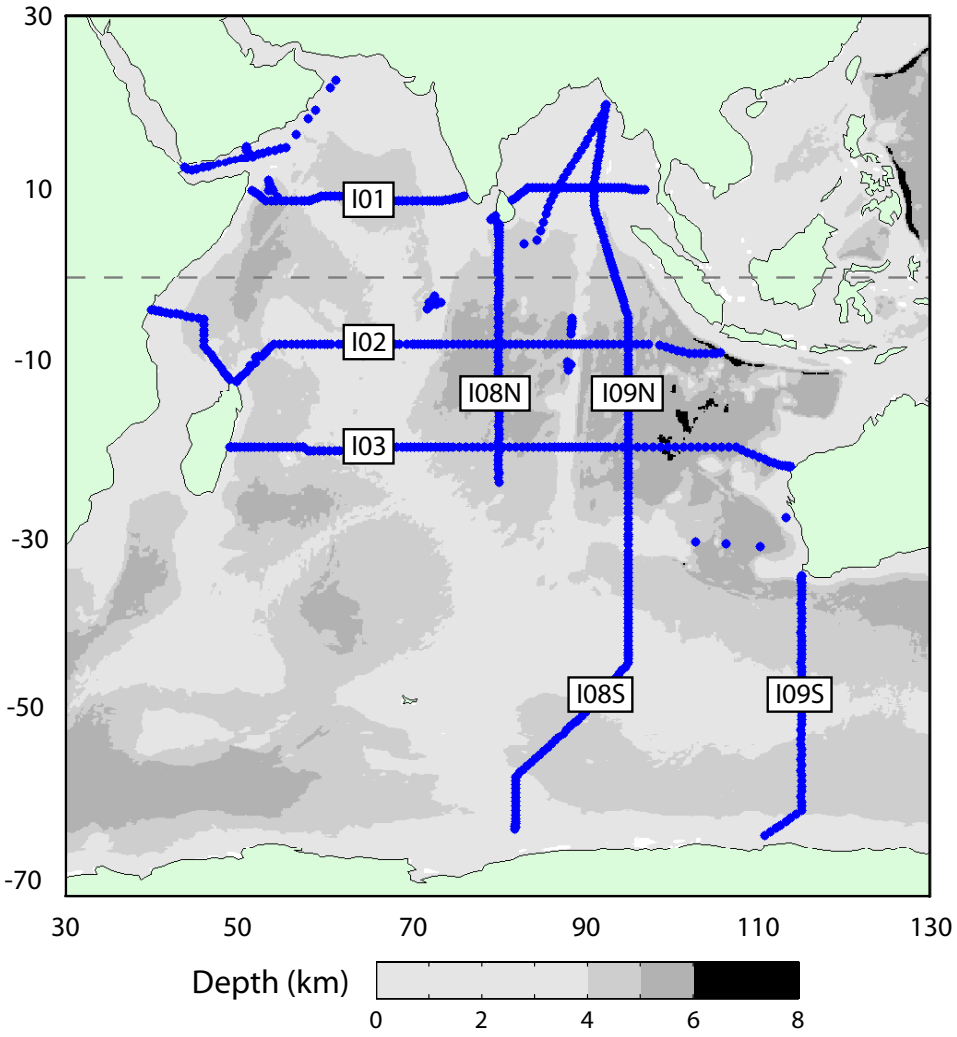

Figure 1.1: Map of the Indian Ocean denoting the locations of cruises I01, I02, I03, I08, and I09. Cruises I08 and I09 are split into disjointed north and south segments, denoted by an 'N' and 'S' suffix after the labeled cruise name. All cruises are on the following pages.

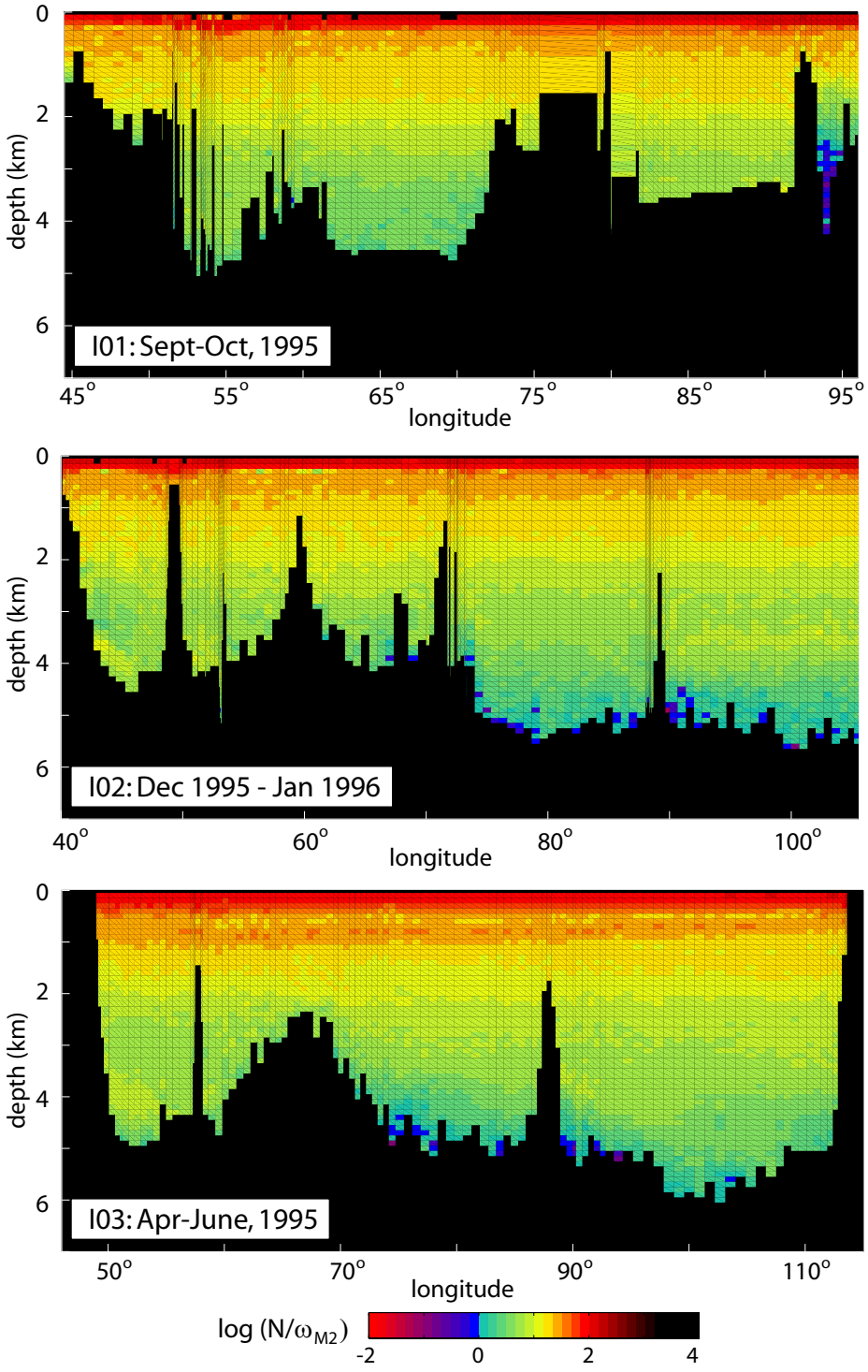
depth (km)
0
2
4
6
I01: Sept-Oct, 1995
45°
55°
65°
75°
85°
95°
longitude
depth (km)
0
2
4
6
I02: Dec 1995 - Jan 1996
40°
60°
80°
100°
longitude
depth (km)
0
2
4
6
I03: Apr-June, 1995
50°
70°
90°
110°
longitude
log (N/ω_M2)
-2
0
2
4

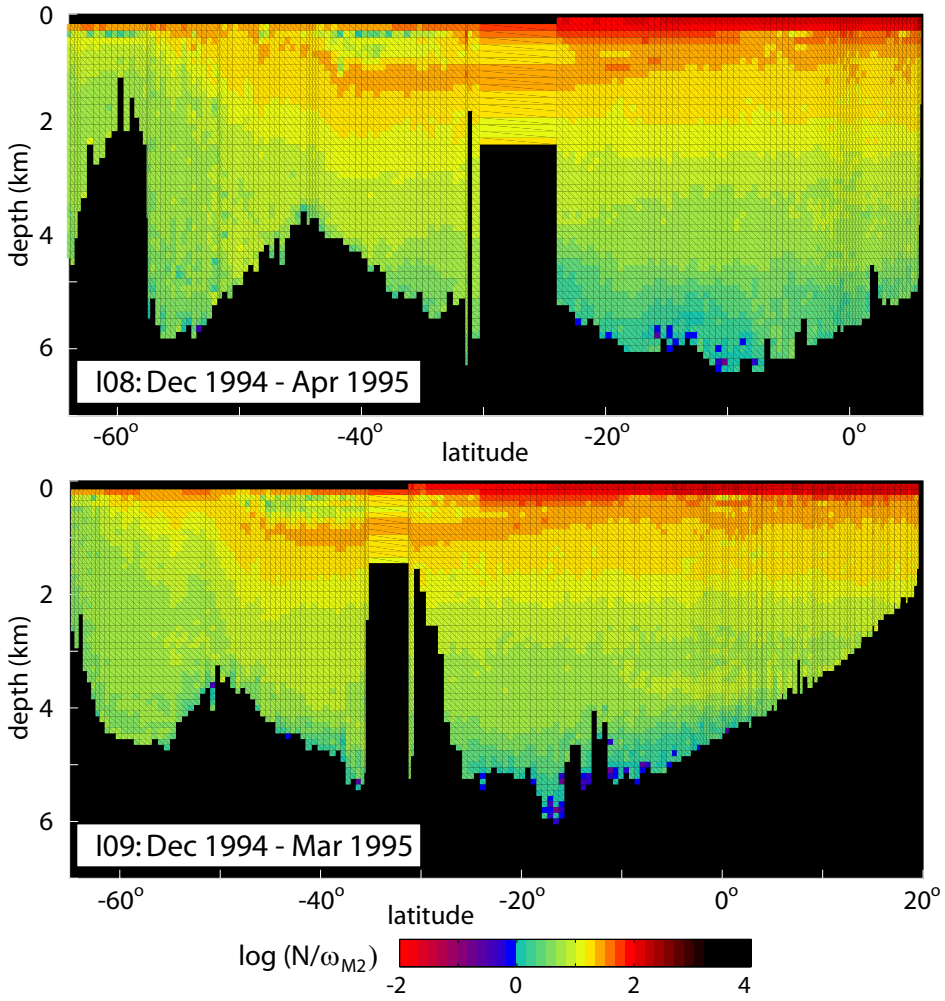
0
2
4
6
depth (km)
I08: Dec 1994 - Apr 1995
-60°
-40°
-20°
0°
latitude
0
2
4
6
depth (km)
I09: Dec 1994 - Mar 1995
-60°
-40°
-20°
0°
20°
latitude
log (N/ω_M2)
-2
0
2
4

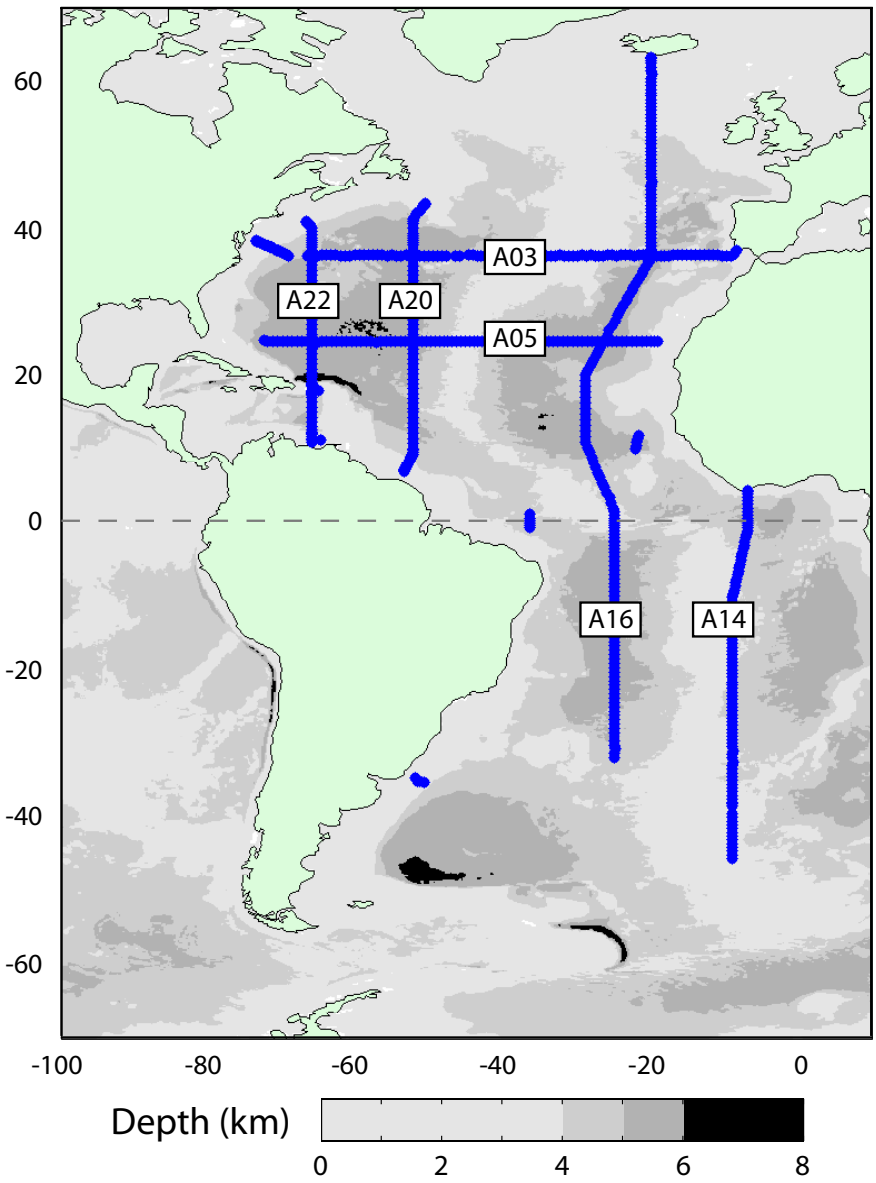

Figure 1.2: Map of the Atlantic Ocean denoting the locations of cruises A03, A05, A14, A16, A20, and A22. The A22 transect is displayed in Figure 6.13. The remaining cruises are on the following pages.

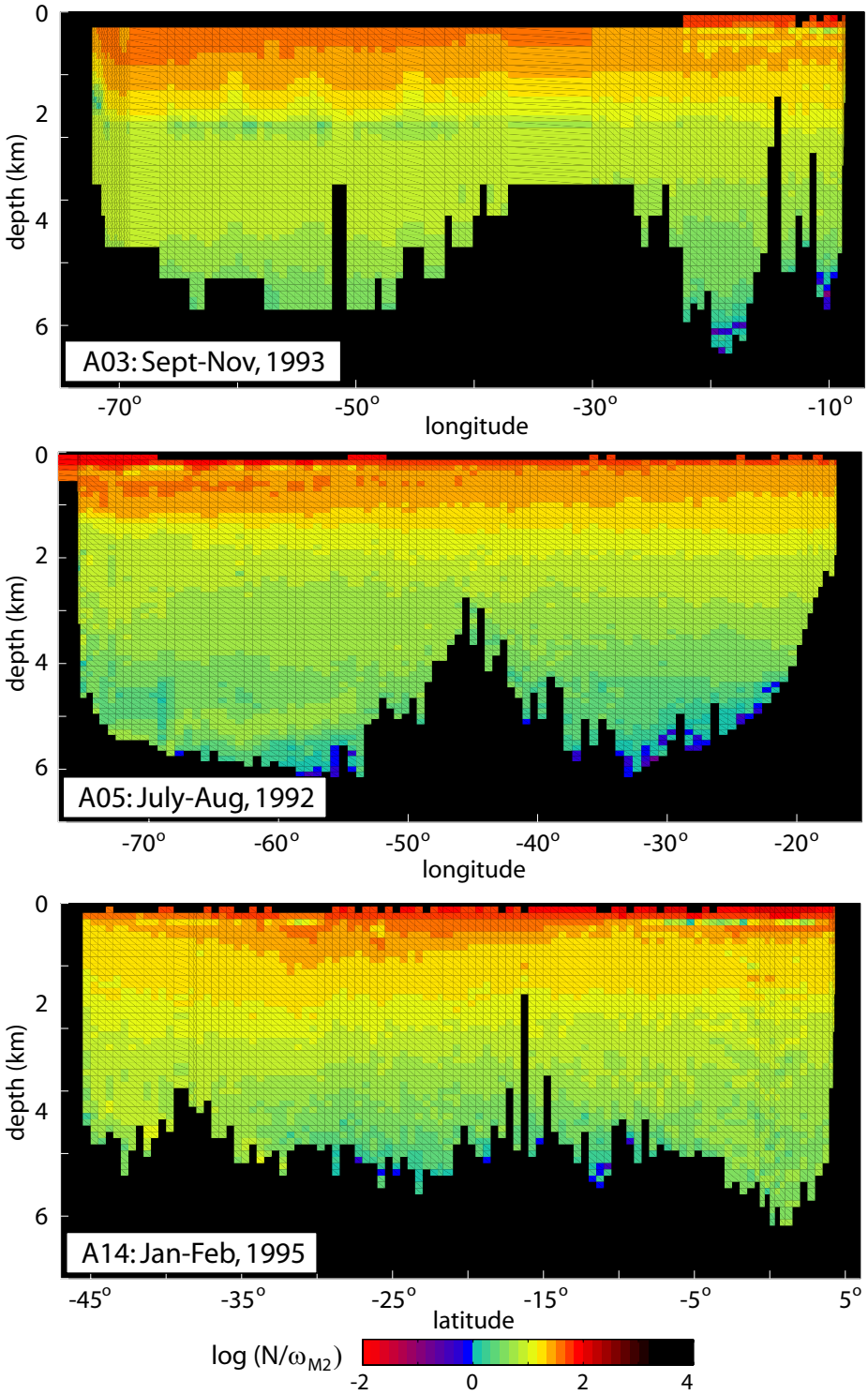
depth (km)
0
2
4
6
A03: Sept-Nov, 1993
-70°
-50°
-30°
-10°
longitude
depth (km)
0
2
4
6
A05: July-Aug, 1992
-70°
-60°
-50°
-40°
-30°
-20°
longitude
depth (km)
0
2
4
6
A14: Jan-Feb, 1995
-45°
-35°
-25°
-15°
-5°
5°
latitude
log (N/ω_M2)
-2
0
2
4

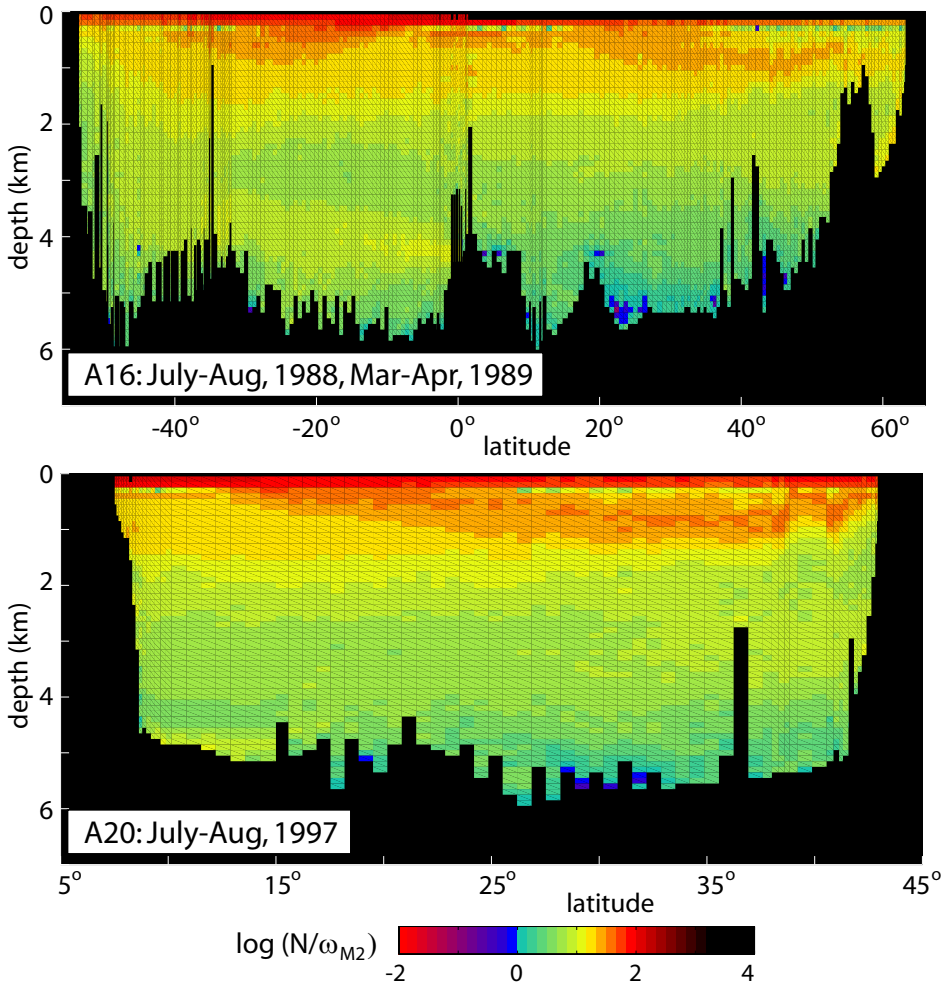
depth (km)
0
2
4
6
A16: July-Aug, 1988, Mar-Apr, 1989
-40°
-20°
0°
20°
40°
60°
latitude
depth (km)
0
2
4
6
A20: July-Aug, 1997
5°
15°
25°
35°
45°
latitude
log (N/ω_M2)
-2
0
2
4

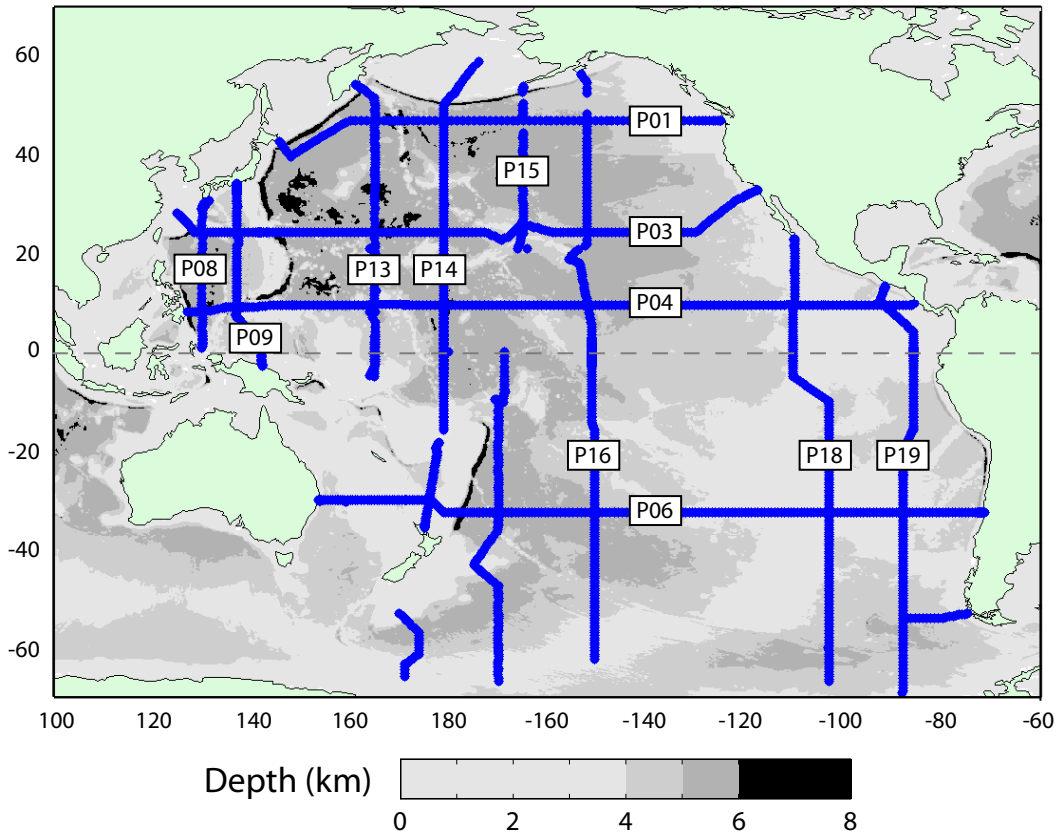

Figure 1.3: Map of the Pacific Ocean denoting the locations of cruises P01, P03, P04, P06, P08, P09, P13, P14, P15, P16, P18, and P19. The P08 and P14 transects are displayed in Figures 6.12 and 6.14, respectively. The remaining cruises are on the following pages.

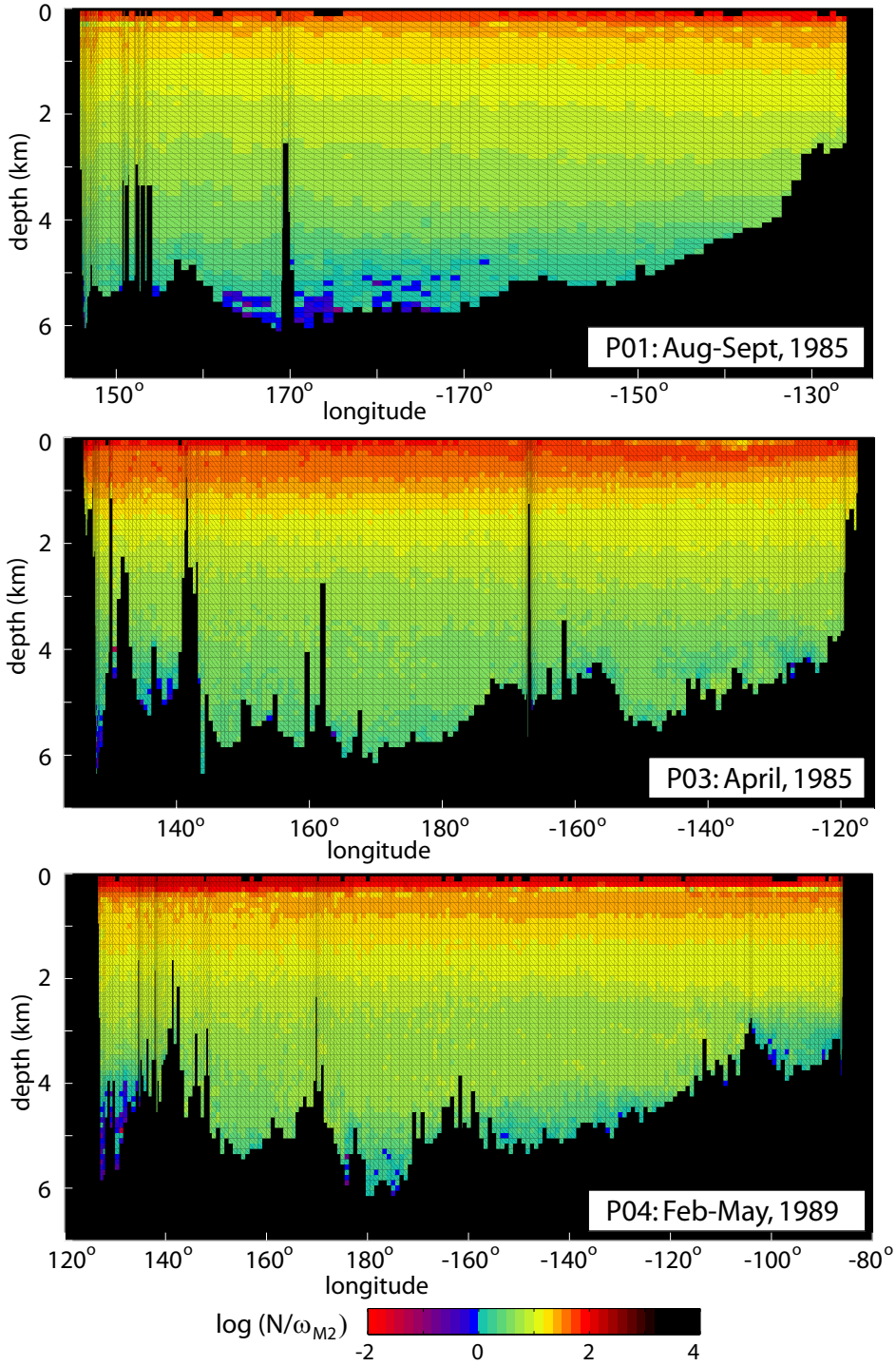
depth (km)
0
2
4
6
P01: Aug-Sept, 1985
150°
170°
-170°
-150°
-130°
longitude
P03: April, 1985
140°
160°
180°
-160°
-140°
-120°
P04: Feb-May, 1989
120°
-100°
-80°
log (N/ω_M2)
-2
0
2
4

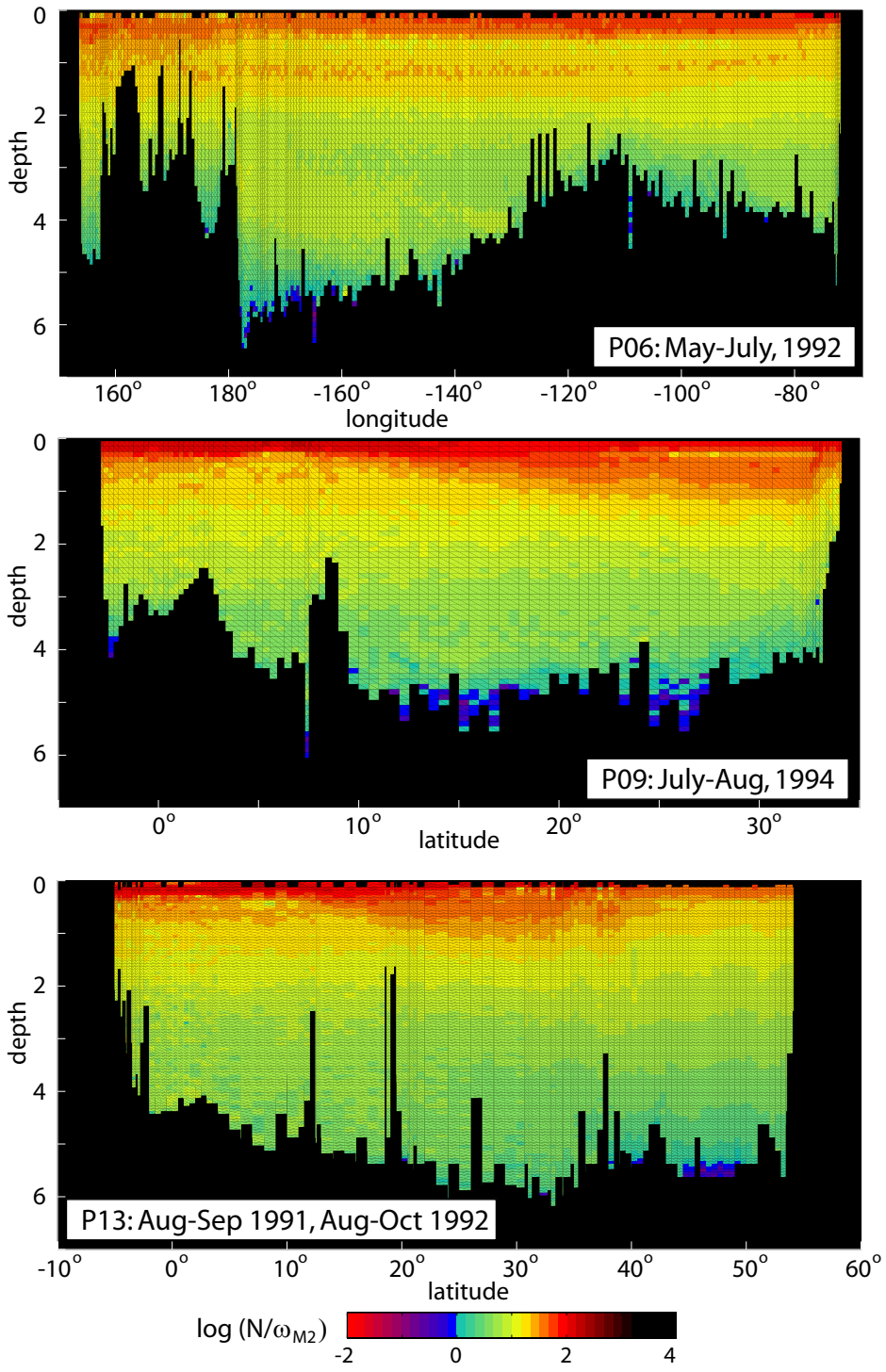
depth
0
2
4
6
P06: May-July, 1992
160°
180°
-160°
-140°
-120°
-100°
-80°
longitude
depth
0
2
4
6
P09: July-Aug, 1994
0°
10°
20°
30°
latitude
depth
0
2
4
6
P13: Aug-Sep 1991, Aug-Oct 1992
-10°
0°
10°
20°
30°
40°
50°
60°
latitude
log (N/ω_M2)
-2
0
2
4

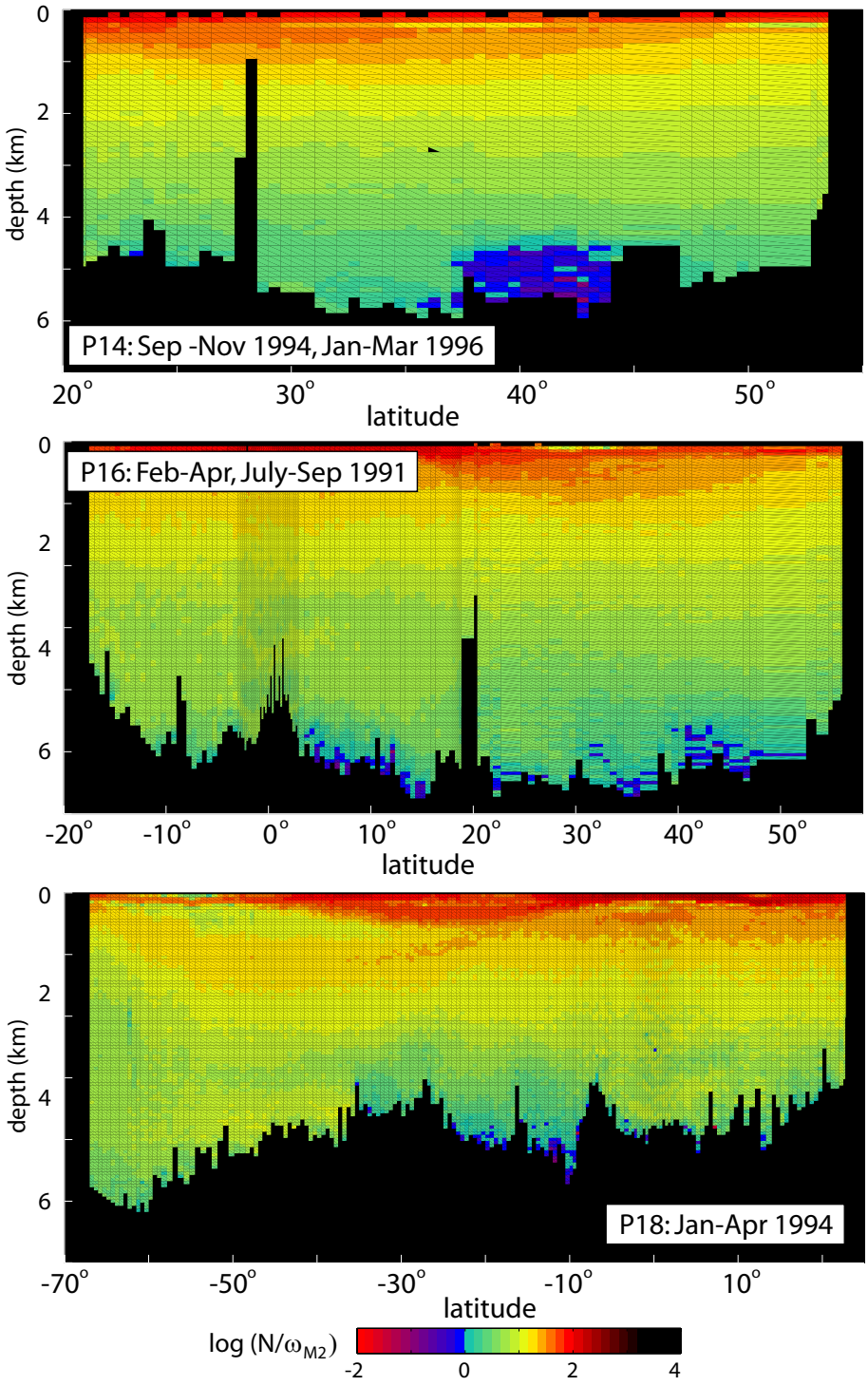
depth (km)
0
2
4
6
P14: Sep -Nov 1994, Jan-Mar 1996
20°
30°
40°
50°
latitude
P16: Feb-Apr, July-Sep 1991
-20°
-10°
0°
10°
20°
30°
40°
50°
P18: Jan-Apr 1994
-70°
-50°
-30°
-10°
10°
log (N/ω_M2)
-2
0
2
4

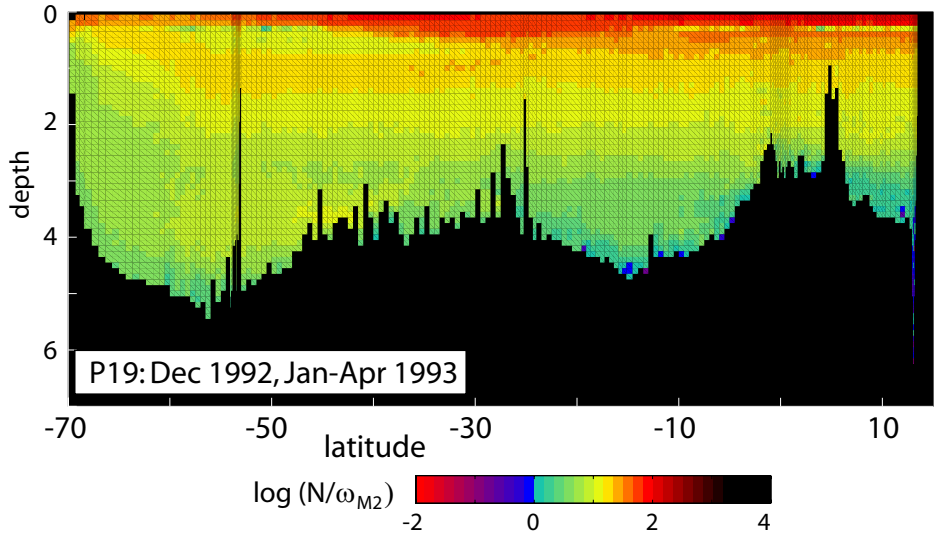
0
2
4
6
depth
P19: Dec 1992, Jan-Apr 1993
-70
-50
-30
-10
10
latitude
log (N/ω_M2)
-2
0
2
4

Bibliography

Aguilar, D. A., and B. R. Sutherland, Internal wave generation from rough topography, *Physics Of Fluids*, *18*(6), 066,603, 2006.

Aguilar, D. A., B. R. Sutherland, and D. J. Muraki, Laboratory generation of internal waves from sinusoidal topography, *Deep-Sea Research Part Ii-Topical Studies In Oceanography*, *53*(1-2), 96–115, 2006.

Althaus, A. M., E. Kunze, and T. B. Sanford, Internal tide radiation from mendocino escarpment, *Journal Of Physical Oceanography*, *33*(7), 1510–1527, 2003.

Appleby, J. C., and D. G. Crighton, Internal gravity-waves generated by oscillations of a sphere, *Journal Of Fluid Mechanics*, *183*, 439–450, 1987.

Baines, P. G., Generation of internal tides by flat-bump topography, *Deep-Sea Research*, *20*(2), 179–205, 1973.

Baines, P. G., On internal tide generation models, *Deep-Sea Research Part A-Oceanographic Research Papers*, *29*(3), 307–338, 1982.

Baines, P. G., Internal tide generation by seamounts, *Deep-Sea Research Part I-Oceanographic Research Papers*, *54*(9), 1486–1508, 2007.

Baines, W. D., and J. S. Turner, Turbulent buoyant convection from a source in a confined region, *Journal Of Fluid Mechanics*, *37*, 51–&, 1969.

Balmforth, N. J., and T. Peacock, Tidal conversion by supercritical topography, *Journal Of Physical Oceanography*, *39*(8), 1965–1974, 2009.

Balmforth, N. J., G. R. Ierley, and W. R. Young, Tidal conversion by subcritical topography, *Journal Of Physical Oceanography*, *32*(10), 2900–2914, 2002.

Becker, J. J., et al., Global bathymetry and elevation data at 30 arc seconds resolution: Srtm30$_p lus$, *Marine Geodesy*, *32*(4), 355 – −371, 2009.

Bell, T. H., Topographically generated internal waves in open ocean, *Journal Of Geophysical Research*, *80*(3), 320–327, 1975.

Blumberg, A. F., and G. L. Mellor, *A description of a three-dimensional coastal ocean circulation model*, American Geophysical Union, 1987.

Brown, G. L., and B. R. Sutherland, Internal wave tunnelling through non-uniformly stratified shear flow, *Atmosphere-Ocean*, *45*(1), 47–56, 2007.

Buhler, O., and C. J. Muller, Instability and focusing of internal tides in the deep ocean, *Journal Of Fluid Mechanics*, *588*, 1–28, 2007.

Cacchione, D., and C. Wunsch, Experimental study of internal waves over a slope, *Journal Of Fluid Mechanics*, *66*(NOV6), 223–&, 1974.

Chang, M. H., R. C. Lien, T. Y. Tang, E. A. D'Asaro, and Y. J. Yang, Energy flux of nonlinear internal waves in northern south china sea, *Geophysical Research Letters*, *33*(3), L03,607, 2006.

Cole, S. T., D. L. Rudnick, B. A. Hodges, and J. P. Martin, Observations of tidal internal wave beams at kauai channel, hawaii, *Journal Of Physical Oceanography*, *39*(2), 421–436, 2009.

Cox, C. S., and H. Sandstrom, Coupling of surface and internal waves in water of variable depth, *Journal of the Oceanographic Society of Japan 20th Anniversary Volume*, pp. 499–513, 1962.

Dalziel, S. B., G. O. Hughes, and B. R. Sutherland, Whole-field density measurements by 'synthetic schlieren', *Experiments In Fluids*, *28*(4), 322–335, 2000.

Dewar, W. K., Oceanography a fishy mix, *Nature*, *460*(7255), 581–582, 2009.

Di Lorenzo, E., W. R. Young, and S. L. Smith, Numerical and analytical estimates of m-2 tidal conversion at steep oceanic ridges, *Journal Of Physical Oceanography*, *36*(6), 1072–1084, 2006.

Dickey, J. O., et al., Lunar laser ranging - a continuing legacy of the apollo program, *Science*, *265*(5171), 482–490, 1994.

Duda, T. F., and L. Rainville, Diurnal and semidiurnal internal tide energy flux at a continental slope in the south china sea, *Journal Of Geophysical Research-Oceans*, *113*(C3), C03,025, 2008.

Echeverri, P., T. Yokossi, N. J. Balmforth, and T. Peacock, Internal tide attractors in double ridge systems, *submitted to Journal of Fluid Mechanics*, 2010.

Egbert, G. D., and R. D. Ray, Significant dissipation of tidal energy in the deep ocean inferred from satellite altimeter data, *Nature*, *405*(6788), 775–778, 2000.

Egbert, G. D., and R. D. Ray, Semi-diurnal and diurnal tidal dissipation from topex/poseidon altimetry, *Geophysical Research Letters*, *30*(17), 1907, 2003.

Eriksen, C. C., Implications of ocean bottom reflection for internal wave spectra and mixing, *Journal Of Physical Oceanography*, *15*(9), 1145–1156, 1985.

Ermanyuk, E. V., and N. V. Gavrilov, On internal waves generated by large-amplitude circular and rectilinear oscillations of a circular cylinder in a uniformly stratified fluid, *Journal Of Fluid Mechanics*, *613*, 329–356, 2008.

Filonov, A. E., and M. F. Lavin, Internal tides in the northern gulf of california, *Journal Of Geophysical Research-Oceans*, *108*(C5), 3151, 2003.

Fincham, A., and G. Delerce, Advanced optimization of correlation imaging velocimetry algorithms, *Experiments In Fluids*, *29*, S13–S22, 2000.

Flynn, M. R., K. Onu, and B. R. Sutherland, Internal wave excitation by a vertically oscillating sphere, *Journal Of Fluid Mechanics*, *494*, 65–93, 2003.

Fringer, O. B., M. Gerritsen, and R. L. Street, An unstructured-grid, finite-volume, nonhydrostatic, parallel coastal ocean simulator, *Ocean Modelling*, *14*(3-4), 139–173, 2006.

Garabato, A. C. N., K. L. Polzin, B. A. King, K. J. Heywood, and M. Visbeck, Widespread intense turbulent mixing in the southern ocean, *Science*, *303*(5655), 210–213, 2004.

Garrett, C., Internal tides and ocean mixing, *Science*, *301*(5641), 1858–1859, 2003.

Garrett, C., and E. Kunze, Internal tide generation in the deep ocean, *Annual Review Of Fluid Mechanics*, *39*, 57–87, 2007.

Garrett, C., and W. Munk, Space-time scales of internal waves - progress report, *Journal Of Geophysical Research*, *80*(3), 291–297, 1975.

Garrett, C. J. R., and W. H. Munk, Space-time scales of internal waves, *Geophysical Fluid Dynamics*, *3*, 225–264, 1972.

Gerkema, T., and J. T. F. Zimmerman, *An Introduction to Internal Waves*, Unpublished, 2008.

Gerkema, T., J. T. F. Zimmerman, L. R. M. Maas, and H. van Haren, Geophysical and astrophysical fluid dynamics beyond the traditional approximation, *Reviews Of Geophysics*, *46*(2), RG2004, 2008.

Gilbert, D., and C. Garrett, Implications for ocean mixing of internal wave scattering off irregular topography, *Journal Of Physical Oceanography*, *19*(11), 1716–1729, 1989.

Gortler, H., Uber eine schwingungserscheinung in flussigkeiten mit stabiler dichteschichtung, *Z. Angew. Math. Mech.*, *23*, 65–71, 1943.

Gostiaux, L., and T. Dauxois, Laboratory experiments on the generation of internal tidal beams over steep slopes, *Physics Of Fluids*, *19*(2), 028,102, 2007.

Ham, F., and G. Iaccarino, Energy conservation in collocated discretization schemes on unstructured meshes, *Tech. rep.*, Center for Turbulence Research, Annual Research Briefs, 2004.

Ham, F., K. Mattsson, and G. Iaccarino, Accurate and stable finite volume operators for unstructured flow solvers, *Tech. rep.*, Center for Turbulence Research, Annual Research Briefs, 2006.

Hendershott, C., M., Impulsively started oscillations in a rotating stratified fluid, *Journal Of Fluid Mechanics*, *36*(10), 513–527, 1969.

Hofmann, M., and M. A. M. Maqueda, Geothermal heat flux and its influence on the oceanic abyssal circulation and radiocarbon distribution, *Geophysical Research Letters*, *36*, L03,603, 2009.

Holloway, G., Oceanic internal waves are not weak waves, *Journal Of Physical Oceanography*, *10*(6), 906–914, 1980.

Holloway, P. E., and M. A. Merrifield, Internal tide generation by seamounts, ridges, and islands, *Journal Of Geophysical Research-Oceans*, *104*(C11), 25,937–25,951, 1999.

Huang, R. X., Mixing and energetics of the oceanic thermohaline circulation, *Journal Of Physical Oceanography*, *29*(4), 727–746, 1999.

Hurley, D. G., The generation of internal waves by vibrating elliptic cylinders. part 1. inviscid solution, *Journal Of Fluid Mechanics*, *351*, 105–118, 1997.

Hurley, D. G., and G. Keady, The generation of internal waves by vibrating elliptic cylinders. part 2. approximate viscous solution, *Journal Of Fluid Mechanics*, *351*, 119–138, 1997.

Ivey, G. N., and R. I. Nokes, Vertical mixing due to the breaking of critical internal waves on sloping boundaries, *Journal Of Fluid Mechanics*, *204*, 479–500, 1989.

Jachec, S. M., O. B. Fringer, M. G. Gerritsen, and R. L. Street, Numerical simulation of internal tides and the resulting energetics within monterey bay and the surrounding area, *Geophysical Research Letters*, *33*(12), L12,605, 2006.

Javam, A., J. Imberger, and S. W. Armfield, Numerical study of internal wave reflection from sloping boundaries, *Journal Of Fluid Mechanics*, *396*, 183–201, 1999.

Johnston, T. M. S., and M. A. Merrifield, Internal tide scattering at seamounts, ridges, and islands, *Journal Of Geophysical Research-Oceans*, *108*(C6), 3180, 2003.

Johnston, T. M. S., M. A. Merrifield, and P. E. Holloway, Internal tide scattering at the line islands ridge, *Journal Of Geophysical Research-Oceans*, *108*(C11), 3365, 2003.

Kantha, L. H., C. Tierney, J. W. Lopez, S. D. Desai, M. E. Parke, and L. Drexler, Barotropic tides in the global oceans from a nonlinear tidal model assimilating altimetric tides .2. altimetric and geophysical implications, *Journal Of Geophysical Research-Oceans*, *100*(C12), 25,309–25,317, 1995.

Katsumata, K., Two- and three-dimensional numerical models of internal tide generation at a continental slope, *Ocean Modelling*, *12*(1-2), 32–45, 2006.

Khatiwala, S., Generation of internal tides in an ocean of finite depth: analytical and numerical calculations, *Deep-Sea Research Part I-Oceanographic Research Papers*, *50*(1), 3–21, 2003.

King, B., H. P. Zhang, and H. L. Swinney, Tidal flow over three-dimensional topography in a stratified fluid, *Physics Of Fluids*, *21*(11), 116,601, 2009.

King, B., H. P. Zhang, and H. L. Swinney, Tidal flow over three-dimensional topography generates out-of-forcing-plane harmonics, *In press, Geophysical Reseach Letters*, 2010.

Kitade, Y., and M. Matsuyama, Semidiurnal internal tide observed over ohmuro-dashi, the northern part of the izu ridge, *Deep-Sea Research Part I-Oceanographic Research Papers*, *49*(8), 1309–1320, 2002.

Klymak, J. M., R. Pinkel, and L. Rainville, Direct breaking of the internal tide near topography: Kaena ridge, hawaii, *Journal Of Physical Oceanography*, *38*(2), 380–399, 2008.

Kundu, P. K., and I. M. Cohen, *Fluid Mechanics*, Elsevier, New York, 2004.

Kunze, E., J. F. Dower, R. Dewey, and E. A. D'Asaro, Mixing it up with krill, *Science*, *318*(5854), 1239–1239, 2007.

Lai, R. Y. S., and C. M. Lee, Added mass of a spheroid oscillating in a linearly stratified fluid, *International Journal Of Engineering Science*, *19*(11), 1411–1420, 1981.

Lamb, K. G., Nonlinear interaction among internal wave beams generated by tidal flow over supercritical topography, *Geophysical Research Letters*, *31*(9), L09,313, 2004.

Laurent, L. S., S. Stringer, C. Garrett, and D. Perrault-Joncas, The generation of internal tides at abrupt topography, *Deep-Sea Research Part I-Oceanographic Research Papers*, *50*(8), 987–1003, 2003.

Ledwell, J. R., A. J. Watson, and C. S. Law, Mixing of a tracer in the pycnocline, *Journal Of Geophysical Research-Oceans*, *103*(C10), 21,499–21,529, 1998.

Ledwell, J. R., E. T. Montgomery, K. L. Polzin, L. C. St Laurent, R. W. Schmitt, and J. M. Toole, Evidence for enhanced mixing over rough topography in the abyssal ocean, *Nature*, *403*(6766), 179–182, 2000.

Lee, C. M., E. Kunze, T. B. Sanford, J. D. Nash, M. A. Merrifield, and P. E. Holloway, Internal tides and turbulence along the 3000-m isobath of the hawaiian ridge, *Journal Of Physical Oceanography*, *36*(6), 1165–1183, 2006.

Legg, S., and A. Adcroft, Internal wave breaking at concave and convex continental slopes, *Journal Of Physical Oceanography*, *33*(11), 2224–2246, 2003.

Legg, S., and K. M. H. Huijts, Preliminary simulations of internal waves and mixing generated by finite amplitude tidal flow over isolated topography, *Deep-Sea Research Part Ii-Topical Studies In Oceanography*, *53*(1-2), 140–156, 2006.

Legg, S., and J. Klymak, Internal hydraulic jumps and overturning generated by tidal flow over a tall steep ridge, *Journal Of Physical Oceanography*, *38*(9), 1949–1964, 2008.

Lien, R. C., T. Y. Tang, M. H. Chang, and E. A. D'Asaro, Energy of nonlinear internal waves in the south china sea, *Geophysical Research Letters*, *32*(5), L05,615, 2005.

Lueck, R., and R. Reid, On the production and dissipation of mechanical energy in the ocean, *Journal Of Geophysical Research-Oceans*, *89*(NC3), 3439–3445, 1984.

Maas, L. R. M., and F. P. A. Lam, Geometric focusing of internal waves, *Journal Of Fluid Mechanics*, *300*, 1–41, 1995.

Macdonald, A. M., and C. Wunsch, An estimate of global ocean circulation and heat fluxes, *Nature*, *382*(6590), 436–439, 1996.

Mahesh, K., G. Constantinescu, and P. Moin, A numerical method for large-eddy simulation in complex geometries, *Journal Of Computational Physics*, *197*(1), 215–240, 2004.

Mahesh, K., G. Constantinescu, S. Apte, G. Iaccarino, F. Ham, and P. Moin, Large-eddy simulation of reacting turbulent flows in complex geometries, *Journal Of Applied Mechanics-Transactions Of The Asme*, *73*(3), 374–381, 2006.

Manders, A. M. M., L. R. M. Maas, and T. Gerkema, Observations of internal tides in the mozambique channel, *Journal Of Geophysical Research-Oceans*, *109*(C12), C12,034, 2004.

Marder, M. P., *Research Methods for Science*, 2009.

Marshall, J., A. Adcroft, C. Hill, L. Perelman, and C. Heisey, A finite-volume, incompressible navier stokes model for studies of the ocean on parallel computers, *Journal Of Geophysical Research-Oceans*, *102*(C3), 5753–5766, 1997.

Mauritzen, C., K. L. Polzin, M. S. McCartney, R. C. Millard, and D. E. West-Mack, Evidence in hydrography and density fine structure for enhanced vertical mixing over the mid-atlantic ridge in the western atlantic, *Journal Of Geophysical Research-Oceans*, *107*(C10), 3147, 2002.

Moin, P., *Fundamentals of Engineering Numerical Analysis*, Cambridge University Press, 2001.

Morozov, E. G., Semidiurnal internal wave global field, *Deep-Sea Research Part I-Oceanographic Research Papers*, *42*(1), 135–148, 1995.

Mowbray, D. E., and B. S. H. Rarity, A theoretical and experimental investigation of the phase configuration of internal waves of small amplitude in a density stratified liquid, *Journal of Fuid Mechanics*, *28*, 1, 1967.

Muller, C. J., and O. Buhler, Saturation of the internal tides and induced mixing in the abyssal ocean, *Journal Of Physical Oceanography*, *39*(9), 2077–2096, 2009.

Muller, P., and N. Xu, Scattering of oceanic internal gravity-waves off random bottom topography, *Journal Of Physical Oceanography*, *22*(5), 474–488, 1992.

Munk, W., *Evolution of Physical Oceanography*, chap. Internal Waves and Small-Scale Processes, pp. 264–291, MIT Press, 1981.

Munk, W., and C. Wunsch, Abyssal recipes ii: energetics of tidal and wind mixing, *Deep-Sea Research Part I-Oceanographic Research Papers*, *45*(12), 1977–2010, 1998.

Munk, W. H., and D. E. Cartwright, Tidal spectroscopy and prediction, *Philosophical Transactions Of The Royal Society Of London Series A-Mathematical And Physical Sciences*, *259*(1105), 533–&, 1966.

Munroe, J. R., and K. G. Lamb, Topographic amplitude dependence of internal wave generation by tidal forcing over idealized three-dimensional topography, *Journal Of Geophysical Research-Oceans*, *110*(C2), C02,001, 2005.

Nakamura, T., and T. Awaji, Scattering of internal waves with frequency change over rough topography, *Journal Of Physical Oceanography*, *39*(7), 1574–1594, 2009.

Nash, J. D., E. Kunze, J. M. Toole, and R. W. Schmitt, Internal tide reflection and turbulent mixing on the continental slope, *Journal Of Physical Oceanography*, *34*(5), 1117–1134, 2004.

Nash, J. D., E. Kunze, C. M. Lee, and T. B. Sanford, Structure of the baroclinic tide generated at kaena ridge, hawaii, *Journal Of Physical Oceanography*, *36*(6), 1123–1135, 2006.

Niwa, Y., and T. Hibiya, Numerical study of the spatial distribution of the m-2 internal tide in the pacific ocean, *Journal Of Geophysical Research-Oceans*, *106*(C10), 22,441–22,449, 2001.

Niwa, Y., and T. Hibiya, Three-dimensional numerical simulation of m-2 internal tides in the east china sea, *Journal Of Geophysical Research-Oceans*, *109*(C4), C04,027, 2004.

Nycander, J., Generation of internal waves in the deep ocean by tides, *Journal Of Geophysical Research-Oceans*, *110*(C10), C10,028, 2005.

Oster, G., Density gradients, *Scientific American*, *213*, 70, 1965.

Peacock, T., M. J. Mercier, H. Didelle, S. Viboud, and T. Dauxois, A laboratory study of low-mode internal tide scattering by finite-amplitude topography, *Physics Of Fluids*, *21*(12), 121,702, 2009.

Petrelis, F., S. L. Smith, and W. R. Young, Tidal conversion at a submarine ridge, *Journal Of Physical Oceanography*, *36*(6), 1053–1071, 2006.

Pingree, R. D., and A. L. New, Downward propagation of internal tidal energy into the bay of biscay, *Deep-Sea Research Part A-Oceanographic Research Papers*, *36*(5), 735–758, 1989.

Pingree, R. D., and A. L. New, Abyssal penetration and bottom reflection of internal tidal energy in the bay of biscay, *Journal Of Physical Oceanography*, *21*(1), 28–39, 1991.

Pingree, R. D., G. T. Mardell, and A. L. New, Propagation of internal tides from the upper slopes of the bay of biscay, *Nature*, *321*(6066), 154–158, 1986.

Polzin, K. L., J. M. Toole, J. R. Ledwell, and R. W. Schmitt, Spatial variability of turbulent mixing in the abyssal ocean, *Science*, *276*(5309), 93–96, 1997.

Rahmstorf, S., Ocean circulation and climate during the past 120,000 years, *Nature*, *419*(6903), 207–214, 2002.

Ray, R. D., Inversion of oceanic tidal currents from measured elevations, *Journal Of Marine Systems*, *28*(1-2), 1–18, 2001.

Ray, R. D., R. J. Eanes, G. D. Egbert, and N. K. Pavlis, Error spectrum for the global m-2 ocean tide, *Geophysical Research Letters*, *28*(1), 21–24, 2001.

Sarma, L. V. K. V., and D. V. Krishna, Oscillation of axisymmetric bodies in a stratified fluid, *Zastasow. Matem.*, *13*, 109–121, 1972.

Sethna, J. P., *Statistical Mechanics: Entropy, Order Parameters and Complexity*, Oxford University Press, 2006.

Shannon, C. E., A mathematical theory of communication, *Bell System Technical Journal*, *27*, 379–423, 1948.

Shunn, L., and F. Ham, Method of manufactured solutions applied to variable-density flow solvers, *Tech. rep.*, Center for Turbulence Research, Annual Research Briefs, 2007.

Simmons, H. L., S. R. Jayne, L. C. St Laurent, and A. J. Weaver, Tidally driven mixing in a numerical model of the ocean general circulation, *Ocean Modelling*, *6*(3-4), 245–263, 2004.

Slinn, D. N., and J. J. Riley, Turbulent mixing in the oceanic boundary layer caused by internal wave reflection from sloping terrain, *Dynamics Of Atmospheres And Oceans*, *24*(1-4), 51–62, 1996.

Slinn, D. N., and J. J. Riley, Turbulent dynamics of a critically reflecting internal gravity wave, *Theoretical And Computational Fluid Dynamics*, *11*(3-4), 281–303, 1998.

Smith, S. G. L., and W. R. Young, Conversion of the barotropic tide, *Journal Of Physical Oceanography*, *32*(5), 1554–1566, 2002.

Smith, S. G. L., and W. R. Young, Tidal conversion at a very steep ridge, *Journal Of Fluid Mechanics*, *495*, 175–191, 2003.

Smith, W. H. F., and D. T. Sandwell, Global sea floor topography from satellite altimetry and ship depth soundings, *Science*, *277*(5334), 1956–1962, 1997.

Song, H. B., Y. Bai, C. Z. Dong, and Y. Song, A preliminary study of application of empirical mode decomposition method in understanding the features of internal waves in the northeastern south china sea, *Chinese Journal Of Geophysics-Chinese Edition*, *53*(2), 393–400, 2010.

St Laurent, L., and C. Garrett, The role of internal tides in mixing the deep ocean, *Journal Of Physical Oceanography*, *32*(10), 2882–2899, 2002.

Staquet, C., Gravity and inertia-gravity internal waves: Breaking processes and induced mixing, *Surveys In Geophysics*, *25*(3-4), 281–314, 2004.

Staquet, C., Internal gravity waves: parametric instability and deep ocean mixing, *Comptes Rendus Mecanique*, *335*(9-10), 665–678, 2007.

Staquet, C., and J. Sommeria, Internal gravity waves: From instabilities to turbulence, *Annual Review Of Fluid Mechanics*, *34*, 559–593, 2002.

Stevenson, B. J. N., T. N., and H. H. Thomas, An internal wave in a viscous heat-conducting isothermal atmosphere, *Journal of Fluid Mechanics*, *65*, 315–323, 1974.

Stommel, H., and A. B. Arons, On the abyssal circulation of the world ocean - ii. idealized model of the circulation pattern and amplitude in oceanic basins, *Deep-Sea Research*, *6*, 217–233, 1960.

Su, F. C., C. R. Ho, Q. Zheng, and N. J. Kuo, Estimating amplitudes of internal waves using satellite ocean colour imagery of the south china sea, *International Journal Of Remote Sensing*, *29*(21), 6373–6380, 2008.

Sutherland, B. R., S. B. Dalziel, G. O. Hughes, and P. F. Linden, Visualization and measurement of internal waves by 'synthetic schlieren'. part 1. vertically oscillating cylinder, *Journal Of Fluid Mechanics*, *390*, 93–126, 1999.

Tabaei, A., T. R. Akylas, and K. G. Lamb, Nonlinear effects in reflecting and colliding internal wave beams, *Journal Of Fluid Mechanics*, *526*, 217–243, 2005.

Thomas, N. H., and T. N. Stevenson, Similarity solution for viscous internal waves, *Journal Of Fluid Mechanics*, *54*(AUG8), 495–&, 1972.

Thrope, S. A., *The Turbulent Ocean*, Cambridge University Press, 2005.

Toole, J. M., K. L. Polzin, and R. W. Schmitt, Estimates of diapycnal mixing in the abyssal ocean, *Science*, *264*(5162), 1120–1123, 1994.

Toole, J. M., R. W. Schmitt, K. L. Polzin, and E. Kunze, Near-boundary mixing above the flanks of a midlatitude seamount, *Journal Of Geophysical Research-Oceans*, *102*(C1), 947–959, 1997.

UNESCO, Background papers and supporting data on the international equation of state of sea water, 1980, *Unesco Tech. Pap. in Mar. Sci.*, *38*, 192, 1981.

Visser, A. W., Biomixing of the oceans?, *Science*, *316*(5826), 838–839, 2007a.

Visser, A. W., Mixing it up with krill - response, *Science*, *318*(5854), 1239–1239, 2007b.

Voisin, B., Internal wave generation in uniformly stratified fluids .1. green-function and point sources, *Journal Of Fluid Mechanics*, *231*, 439–480, 1991.

Voisin, B., Limit states of internal wave beams, *Journal Of Fluid Mechanics*, *496*, 243–293, 2003.

Wu, Z. K., X. Q. Lu, and J. W. Tian, Simulation of barotropic and baroclinic tides in the south china sea, *Acta Oceanologica Sinica*, *24*(2), 1–8, 2005.

Wunsch, C., and R. Ferrari, Vertical mixing, energy and thegeneral circulation of the oceans, *Annual Review Of Fluid Mechanics*, *36*, 281–314, 2004.

Zhang, H. P., B. King, and H. L. Swinney, Experimental study of internal gravity waves generated by supercritical topography, *Physics Of Fluids*, *19*, 2007.

Zhang, H. P., B. King, and H. L. Swinney, Resonant generation of internal waves on a model continental slope, *Physical Review Letters*, *100*(24), 2008.

Zhao, Z. X., and M. H. Alford, Source and propagation of internal solitary waves in the northeastern south china sea, *Journal Of Geophysical Research-Oceans*, *111*(C11), C11,012, 2006.

Zhao, Z. X., V. Klemas, Q. N. Zheng, and X. H. Yan, Remote sensing evidence for baroclinic tide origin of internal solitary waves in the northeastern south china sea, *Geophysical Research Letters*, *31*(6), L06,302, 2004.

Zilberman, N. V., J. M. Becker, M. A. Merrifield, and G. S. Carter, Model estimates of m-2 internal tide generation over mid-atlantic ridge topography, *Journal Of Physical Oceanography*, *39*(10), 2635–2651, 2009.

Vita

Benjamin Thomas King was born in Fort Worth, Texas in 1983. He attended high school in Haltom City, Texas, and began undergraduate study at Texas A&M University, College Station in 2001. He completed a Bachelor of Science degree in 2005, and began graduate studies at the University of Texas at Austin

Permanent address: 2501 Wickersham Lane Apt 2331
Austin, Texas 78741

This dissertation was typeset with LaTeX[†] by the author.

[†]LaTeX is a document preparation system developed by Leslie Lamport as a special version of Donald Knuth's TeX Program.